DEFORMATION AND FRACTURE STUDIES

IN ALUMINIUM ALLOYS.

Miss J. M. DOWLING, B. A.,
ST. ANNE'S COLLEGE,
OXFORD.

A dissertation submitted for the Degree of Doctor of Philosophy at the University of Oxford in November, 1975.

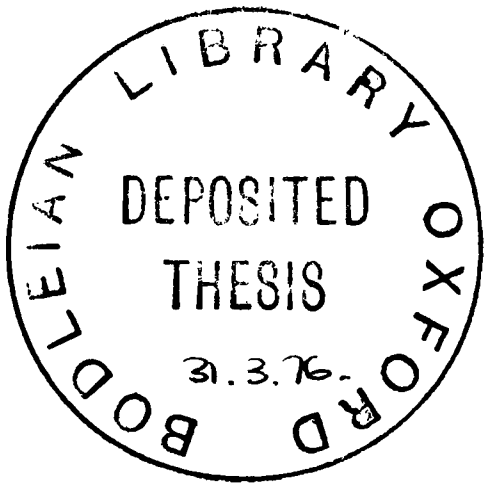

"The more innocuous a design change appears,
the further its influence will extend."

(An extract from 'The Contributions of Edsel Murphy to the Understanding of the Behaviour of Inanimate Objects' - D. L. Klipstein, 1967, EEE, 15, 91).

CONTENTS

		Page No.
Acknowledgements		i
Preface		ii
Abstract		iii
CHAPTER 1	Introduction	1
1.1.	Outline of Research Problem.	2
1.2.	Age-Hardening in Al-Mg-Si Alloys.	2
1.3.	Two Step Ageing in Al-Mg-Si Alloys.	7
1.4.	Formation of Precipitate Free Zones (P.F.Z.).	13
1.5.	Effect of Alloying Elements on the Ageing of Al-Mg-Si Alloys.	15
1.6.	Deformation Mechanisms in Two-Phase Alloys.	17
1.6a	F.C.C. Single Crystals.	18
1.6b	F.C.C. Polycrystals.	23
1.7.	Transgranular versus Intergranular Fracture.	25
1.8	Objects of the Present Research	27
Figures for Chapter 1.		
CHAPTER 2	Materials, Apparatus and Experimental Techniques.	28
2.1.	Materials.	29
2.2.	Heat Treatment Methods.	29
2.3.	Optical Metallographic Techniques.	30
2.3a	Polishing Procedure.	30
2.3b	Grain Size Determination	31

2.4.	Transmission Electron Microscopy (T.E.M.).	33
2.4a	Thin Foil Preparation.	33
2.4b	Particle Analysis.	34
2.4c	Slip Band Analysis.	39
2.5.	Mechanical Testing.	42
2.5a	Compression Tests.	42
2.5b	Tensile Tests.	42
2.5c	Notch Bend Testing.	43

Figures for Chapter 2.

CHAPTER 3	Metallography.	45
3.1.	Introduction.	46
3.2.	Age-Hardening Curves.	46
3.3.	Microstructure of Solution Heat Treated State.	47
3.4.	Metallography after Ageing at $185^{o}C$	48
3.4a	Electron Microscopy	49
3.5.	Preliminary Discussion of Microstructures.	52
3.6.	Precipitation Studies of $\alpha(Al_{12}Mn_3Si)$.	54
3.7.	Recrystallisation and Grain Growth Experiments.	61
3.7a	Effect of Annealing Temperature on Grain Size.	61
3.7b	Effect of Prior Strain on Recrystallised Grain Size.	63
3.7c	Effect of Heating Rate on Grain Size.	63
3.8.	Summary of Precipitation and Recrystallisation Kinetics.	64

Figures and Plates for Chapter 3.

CHAPTER 4	Deformation Mechanisms.	66
4.1.	Introduction.	67
4.2.	Compression Tests.	67
4.2a	Results and Discussion of Work-Hardening Behaviour.	67
4.2b	Transmission Electron Microscopy of Deformed Alloys.	68
4.2c	Observations and Discussion of Slip Distribution.	69
4.2d	Fracture Processes in BD3.	72
4.2e	Inducing Intergranular Failure in BD6 and BD8.	74
4.3.	Tensile Tests	75
4.3a	Ductility and Deformation Structure.	75
4.3b	Discussion of Conventional Stress-Strain Curves.	78
4.3c	Discussion of Fracture Stresses.	81
4.4.	Metallography of Fracture.	83
4.4a	Optical Metallographic Observations.	83
4.4b	Discussion of Metallographic Observations.	84
4.4c	Inhibition of Ductile Fracture Propagation by Small Particles.	86
4.4d	Proposed Fracture Processes in BD6 and BD8.	88
4.4e	Fractography of BD3, BD6 and BD8.	91
4.4f	Crack Propagation in Notch-Bend Tests.	94

Figures and Plates for Chapter 4.

CHAPTER 5	Summary, Final Discussion and Conclusions.	97
5.1.	Relation of Microstructure to the Thermo-mechanical Processing of the Alloys.	98
5.2.	Deformation and Fracture Mechanisms in BD3.	99
5.3.	Microstructure of BD6 and BD8.	100
5.4.	Deformation Structures of BD6 and BD8 at Low Strains.	101
5.5.	Void Nucleation in BD6 and BD8.	102
5.6.	Fracture Processes in BD6 and BD8.	103
5.7.	Final Discussion and Conclusions.	105
References		108

ACKNOWLEDGEMENTS

It gives me great pleasure to express my gratitude to the many people who have assisted me during the course of this project. In particular,

Professor Sir Peter Hirsch, F.R.S., for providing the laboratory facilities and the Scientific Research Council for their financial aid.

Dr. J. W. Martin, who supervised this research and gave me help, advice and encouragement throughout the project and who also supervised my undergraduate studies at Oxford.

Messrs. Alcan International Limited for providing the alloys. I am especially grateful to Messrs. A. T. Thomas and B. Dunwoody for their helpful discussions.

Drs. D. Gould and A. Lasalmonie for their advice on experimental techniques. Thanks are also given to Messrs. Alan Fairless, John Short and Graham Dixon-Brown and all members of the laboratory workshops for their assistance.

Mrs. Helen Suggett for deciphering the handwritten script of the thesis and typing the text. Messrs. Andrew McKnight and Chris Bacon for the photographic work.

In conclusion, I would like to thank my fellow post-graduate research students who have been called upon for their muscular strength in certain experiments and who have been cheerful company at all times.

J. Dowling

J. M. Dowling
St. Anne's College,
Oxford.

November, 1975.

PREFACE

This thesis is an account of work performed in the Department of Metallurgy and Science of Materials in the University of Oxford, between October 1972 and September 1975. The work reported is original and is not substantially the same as any thesis submitted elsewhere. Where the work of other authors has been included in the text this has been acknowledged, and its source given in the reference list at the end of this thesis.

Part of the present work has been presented at the Third International Conference on the Strength of Metals and Alloys, Cambridge, England, 1973 as 'The Influence of Manganese Addition on the Deformation and Fracture Behaviour of an Al-Mg-Si Alloy' by J. M. Dowling and J. W. Martin

ABSTRACT

The research is concerned with the problem of embrittlement in fully aged alloys of the H.30 type (Al-Mg-Si). These alloys fracture in a brittle intergranular fashion at low strains but when small amounts of manganese (~ 0.5wt%) are added, intergranular failure is suppressed and the ductility of the alloys is increased.

Previous work performed by Messrs. Alcan International Limited has shown that the manganese-bearing alloys contain incoherent intermetallic particles of the $\alpha(Al_{12}Mn_3Si)$ phase. The particles have a diameter of ~ 0.1μm and are rod-shaped. It was considered that these particles might be responsible for the improved mechanical behaviour of the manganese bearing alloys, but the mechanism involved was not known. Earlier work by the author has indicated that the manganese-bearing particles can modify the surface slip line distribution and it was suggested that this effect of slip homogenization might prevent intergranular failure. The present work investigates the extent to which these 0.1μm particles influence the nucleation and propagation of fracture and explores the mechanisms involved.

Three Al-Mg-Si alloys were selected - BD3(Al-0.58wt%Mg - 1.02wt%Si), BD6(Al-0.58wt%Mg - 0.99wt%Si - 0.21wt%Mn) and BD8(Al-0.57wt%Mg - 0.95wt%Si - 0.50wt%Mn). After casting, the alloys were thermo-mechanically processed into sheet form before solution heat treatment at 560°C and artificial ageing at 185°C.

The alloy microstructures were examined using optical and transmission electron microscopy. The grain size of the alloys were measured and the dispersion parameters of 0.1μm α phase particles

were determined. These measurements show that the grain size of the brittle alloy BD3 is ~ 400μm while that of BD6 and BD8 is ~ 100μm. When fully aged, three alloys contain a fine ageing precipitate of Mg_2Si, grain boundary precipitates and precipitate free zones adjacent to the grain boundaries. The manganese bearing alloys additionally contain the 0.1μm $\alpha(Al_{12}Mn_3Si)$ phase particles and also coarser, 5μm particles of the same phase.

An investigation of the precipitation kinetics of $\alpha(Al_{12}Mn_3Si)$ particles from a chill cast alloy was made, and also attempts were made to increase the grain size of BD8. It is shown that above 530°C, the α phase particles grow very quickly. Below 530°C, their growth is slower, but the kinetics are complicated by the onset of precipitation of Mg_2Si phase particles which coarsen rapidly. The subsequent grain growth experiments indicate that both these precipitate phases are effective in inhibiting extensive grain growth in the manganese-bearing alloys. Within the scope of the present research, it was thus not possible to produce comparable grain sizes in BD3, BD6 and BD8 and to compare their mechanical properties at constant grain size.

The mechanical properties of the three alloys were studied using compression tests and tensile tests and their deformation structures were examined using both optical and electron microscopy.

In compression, BD3 can withstand larger strains before fracture than in tensile deformation. This enables an analysis of its structure after plastic deformation to be made. It is found that at compressive strains up to 9%, BD3 contains well defined slip bands and these can produce distortion at the grain boundaries. At low compressive strains, BD6 and BD8 also contain slip bands but these are closer together and their spacing decreases with increasing strain;

eventually, the deformation structure consists of homogeneous arrays of dislocations. No local grain boundary distortion was observed in BD6 or BD8.

It is concluded that the slip bands produce stress concentrations at the grain boundaries. In BD3, these are large because (a) the grain size is large and (b) the slip band width is narrow. It is proposed that intergranular decohesion occurs at small tensile strains, because the stress concentrations are large enough to nucleate voids at the grain boundary precipitates and fracture proceeds by coalescence of these voids. This is supported by scanning electron microscopy of fracture surfaces at room temperature; the grain boundary surfaces are covered with fine dimples whose size corresponds to the observed spacing of the grain boundary precipitates. It is also concluded that intergranular decohesion in BD6 and BD8 is suppressed at low strains because the stress concentrations at the head of the slip bands are reduced by (a) the smaller grain size and (b) the broadening of the slip band width by the 0.1μm α phase particles.

Tensile tests at 20°C, 150°C and 185°C show that the fracture processes in BD6 and BD8 are controlled by the presence of both the coarse, ~ 5μm α phase particles and the 0.1μm particles. The coarse, ~ 5μm, particles nucleate voids shortly after yield and the coarsening of these voids determines the start of localised plastic deformation. Fracture does not occur at the U.T.S., but only after large amounts of localised plastic deformation. Scanning and transmission electron microscopy indicate that in these alloys, fracture takes place when voids are formed at the 0.1μm particles and the voids coalesce. It is proposed that this void formation requires conditions of high stress and strain such that void formation and coalescence occur virtually simultaneously. The difficulty of void

formation at these particles is related to the high matrix-particle binding energy and the particle shape. Because of these latter properties, the 0.1μm particles inhibit the spread of voids formed at the coarse particles and so fracture is delayed until a very late stage of deformation.

In conclusion, it is proposed that the 0.1μm particles in the manganese-bearing alloys are important in controlling the deformation mechanisms. Not only do these particles disperse slip, thus preventing intergranular failure at low strains, but they also appear to be effective in impeding crack propagation. Their efficacy in both these processes depends on their dispersion parameters, shape and binding energy with the matrix. These parameters are discussed in relation to the production of an alloy with optimum mechanical properties.

CHAPTER 1

INTRODUCTION

1.1. OUTLINE OF THE RESEARCH PROBLEM

The research is concerned with the problem of embrittlement in fully aged alloys of the H.30 type (Al-Mg-Si). These alloys fracture in a brittle intergranular fashion, but when small amounts of manganese (~ 0.5wt%) are added, this brittle fracture is suppressed.

Previous work carried out by Messrs. Alcan International Limited has shown that the manganese is present in the form of a 0.1μm dispersion of an incoherent intermetallic phase in the manganese-bearing alloys. A preliminary survey (Dowling, 1972) of the manganese-free alloy and manganese-bearing alloy has indicated that the manganese particles can modify the surface slip line distribution. It was suggested that this effect of slip homogenization might prevent intergranular failure.

The present work investigates the extent to which these 0.1μm particles influence the nucleation and propagation of fracture and explores the mechanisms involved.

1.2. AGE-HARDENING IN Al-Mg-Si

Investigations by several authors (see below) have established that the general ageing sequence in pseudo binary Al-Mg_2Si alloys is as follows: Needle shaped G.P. zones along <100> matrix (β") → rod-shaped precipitates along <100> matrix (β') → plate shaped equilibrium precipitates of Mg_2Si (β).

Some of the earliest work on this precipitation system was carried out by Guinier and Lambot in 1948, by studying the diffuse

X-ray scattering from Al-Mg-Si alloys after different ageing treatments. They deduced that at room temperature a clustering process took place, since there was no abnormal diffuse scattering but the hardness of the alloys increased with ageing time. At higher ageing temperatures (< 200°C), streaks appeared on the X-ray photographs and these corresponded to zones lying along matrix <100> with a periodicity equal to d_{100} of the solid solution. Between 200°C and 250°C, the zones persisted, but there were intensity variations in the streaks. In conclusion a model for the Mg_2Si precipitates was proposed; the β" zones consisted of two rows of magnesium atoms parallel to a row of silicon atoms and these lay along <100> of the matrix. Guinier (1952 and 1956) later suggested that the zones initially have an irregular or non-periodic structure and with increasing ageing time the structure slowly changes towards a crystalline structure.

A thorough investigation in an Al-1.58% Mg_2Si alloy by Thomas (1961) using transmission electron microscopy confirmed Guinier's hypothesis. Thomas found that there were no anomalous features in diffraction patterns of the alloy after quenching from solution treatment, so that the β" zones are not formed immediately after quenching. On ageing below 204°C, streaks were observed along <100> directions on [100] diffraction patterns and these implied a <100> growth direction for the β" zones. (100) reflections are forbidden for the F.C.C. lattice, so he concluded that the β" zones were a superlattice of Mg_2Si. The corresponding transmission micrographs showed that the matrix contained β" needles along <100> . After prolonged ageing at temperatures below 204°C, the diffraction pattern streaks became more pronounced; the β" needles then reached a maximum

length (200Å → 1000Å, depending on ageing temperature) and there was no further growth. It was observed that a precise orientation was required to give sharp images of the β" needles, either [100] or [110] and that there were no contrast effects around the needles which suggested that no coherency strains were present. (Later work by Jacobs, 1972 and Pashley et al, 1967 shows that coherency strains do exist around the β" needles).

Examination of {100} sections showed that the number of black spots (assumed to be needles parallel to the electron beam) was half the number of observed lines (β" needles perpendicular to the beam). This confirmed that the precipitates were needles lying along the three <100> directions in the matrix. Further, the density of the β" needles was always in excess of the number of condensed vacancy loops observed in the as quenched alloys, so that the zones could not have been nucleated on these loops. Thomas (1959) has shown that the vacancy concentration in loops in the as quenched Al-Mg-Si alloys is only ~ 3×10^{-6} compared with the normal quenched in vacancy concentration of 10^{-4} in aluminium. Therefore in the alloys, most of the vacancies must be retained in solution by some solute-vacancy interaction. It is probable that these solute-vacancy pairs form clusters from which the β" zones are formed, (Federighi and Thomas, 1962). Lutts, 1961, in X-ray diffraction work of pre-precipitation in Al-Mg-Ge and Al-Mg-Si alloys supports this hypothesis.

After ageing at temperatures above 200°C, the β" needles change in situ to β' rods, which still lie along <100> matrix and have a diameter of 1000Å. According to Thomas (1961) these rods give an F.C.C. diffraction pattern with a = 6.42Å (a = 6.39Å for equilibrium Mg_2Si). Finally after 3 hours at 260°C, the equilibrium (β) Mg_2Si

phase is formed.

Apart from examining the ageing precipitates within the grains, Thomas has also followed precipitation in the grain boundaries during ageing of the alloys. The grain boundary precipitate forms initially as silicon and is still predominantly silicon after 10 minutes at 288°C, but with longer ageing the precipitates eventually transform to Mg_2Si.

Several other authors have reported on the precipitation system in Al-Mg-Si alloys. Most of these are agreed that the basic ageing sequence is continuous, (Brichet et al, 1970 and Jacobs, 1972) and the fact that the needle shaped zones are responsible for strengthening the matrix.

More recently, Jacobs, 1972, working with an Al-1.2% Mg_2Si alloy has questioned the structure of the β' phase proposed by Thomas. Jacobs shows that rods have a hexagonal structure with a = 7.04Å and c = 4.05Å with the orientation:

$$(001)_{rod} \;//\; (100)_{matrix}$$

$$[100]_{rod} \;//\; [01\bar{1}]_{matrix}$$

These rods were about 0.25μm in length after 10 minutes at 250°C. After longer ageing times at this temperature, the rods grow to a length of 2μm and were no longer coherent with the matrix; the unit cell was now a = 7.04Å and c = 12.15Å. The hexagonal diffraction patterns were then used to explain the origin of the intensity maxima seen in the streaks produced by the coherent β" needles, assuming that they had a unit cell similar to that of the rods. In conclusion,

Jacobs proposes a more quantiiative description of the basic ageing process:

a) Needle-shaped β" G.P. zones form randomly in the matrix; they are only partially coherent and have a hexagonal structure.

b) The zones develop into β' rod-shaped metastable precipitates with a hexagonal unit cell, a = 7.05Å and c = 4.05Å.

c) When the β' rods lose coherency with the matrix along their length, modification may occur leading to a hexagonal unit cell with a = 7.05Å and c = 12.15Å.

d) Finally, platelets of equilibrium β Mg_2Si are formed.

Wahi and Von Heimendahl, 1974, report that the β" needle-shaped phase has a monoclinic structure, a = c = 6.16Å, b = 7.1Å and β = 82° and further that the β' phase (rods) may have a cubic structure as described by Thomas (1961). The work of both Jacobs and Thomas was carried out on pseudo-binary alloys of Al-Mg_2Si without excess silicon, but the alloy investigated by Wahi had a large excess silicon content of about 11.5wt%. He maintains that this excess precipitates directly from the melt as pure silicon and that the alloy should age in the same way as the balanced alloys.

Despite these differences in the reported structures of the intermediate phases, the ageing sequence described at the beginning of this section seems to be well supported in the literature.

1.3. TWO STEP AGEING IN Al-Mg-Si ALLOYS

In the commercial processing of age hardened alloys, there is generally a delay between quenching and artificial ageing treatment. This delay can produce mechanical properties which are inferior to those produced by immediate ageing (Harris and Varley, 1953/54). Depending on the time and temperature of this storage (pre-ageing), the final precipitate structure can be either finer or coarser than that produced without pre-ageing. Since in the present research, the alloys are given a standard age at room temperature for 5 minutes prior to artificial ageing, it is important to understand how such delays alter the final microstructure.

A preliminary investigation on Al-1.2%Mg_2Si (Pashley et al, 1966) showed that when the alloy was artificially aged at 160°C, the average β" needle size was ~ 220Å. With delays of three hours and three days at room temperature, the average needle sizes were 410Å and 490Å respectively. In contrast to this, pre-ageing at 120°C gave very different results, (Pashley et al, 1967). Here, a pre-age of approximately twenty minutes produced a very coarse precipitate structure at 160°C, the average needle length being 1300Å. Pre-ageing shorter or longer than this gave a finer structure with an average needle length of 250Å.

The room temperature pre-ageing effects were tentatively explained in terms of a clustering mechanism which had been proposed earlier by Hardy, 1948/49. He suggested that zones formed during storage could act as nuclei for precipitates at higher temperatures. In the alloy under consideration, the authors had observed considerable strengthening during storage at room temperature which seemed to confirm this

clustering mechanism.

They proposed that immediately after quenching to a low temperature from the solution temperature, spherical clusters formed. The actual clustering process was assumed to involve a magnesium-silicon-vacancy complex, so that as clustering proceeds, the supersaturation in the matrix decreases. Initially, the numbers increase with time, but there then follows a period of time when the number remains constant and cluster growth occurs. At a later stage, a process similar to Ostwald ripening takes place. When the alloy is raised to the artificial ageing temperature, the supersaturation is even less and the size at which a cluster becomes stable is increased. Those clusters below this initial size will dissolve and the others grow. Therefore the longer the alloy is at room temperature, the lower is the supersaturation at the start of artificial ageing and the fewer are the number of stable clusters and hence the precipitate structure is coarser.

A more quantitative explanation was made in a later paper, (Pashley et al, 1967). Various parameters were identified as being important in the process of two-step ageing. The excess vacancy concentration, which depends on the solution temperature T_s, the quench rate, and the pre-ageing temperature T_1 and T_c, above which supersaturation is insufficient for homogeneous nucleation. T_c will vary with the alloy composition and also with excess vacancy concentration. In general, T_c increases with increase in the excess vacancy concentration.

A model was developed and extended for various ageing conditions and it was shown how the experimental results could be interpreted

from the theory, even though some of the parameters could not be determined.

The influence of clustering at some pre-ageing temperature T_1 on the artificial ageing temperature T_2 was considered as follows. If W (wt./unit vol.) is the average solute concentration in the matrix at a solution temperature T_s and n_r clusters form of radius r at T_1, then the total fraction of solute, α, in the clusters after this pre-age is

$$\alpha W = \sum_r \frac{4}{3} \pi r^3 n_r \rho \qquad 1.1$$

where ρ is the density of solute.

When the alloy is taken up to T_2, there will be a supersaturation S dependent on the concentration of solute, C_2, in equilibrium with a cluster of planar interface.

$$S = \frac{W(1-\alpha)}{C_2} \qquad 1.2$$

For a cluster of radius r to grow at T_2, the rate of arrival of solute must be greater than the solute leaving the cluster. The concentration of solute, C, in equilibrium with a spherical cluster is greater than C_2.

$$\log_e \left(\frac{C}{C_2}\right) = \frac{2\gamma V}{rRT} = \frac{k}{r} \qquad 1.3$$

(This is the Gibbs-Thomson relation; γ is the surface energy of the cluster and V is an atomic volume).

The rate of arrival of solute at the cluster surface is AC_2S/ unit area, where A is a constant incorporating the temperature and diffusion coefficients for the solute. The rate at which solute

leaves the cluster is $BC_2 \exp\frac{k}{r}$ so for the cluster to grow

$$AC_2S > B\,C_2 \exp \frac{k}{r} \qquad 1.4$$

or, when there are no excess vacancies

$$r\log_e S > k$$

Taking the simple case when all the clusters, N, have an average size $\bar{r}$,

$$\alpha W = \frac{4}{3}\pi \bar{r}^{3} N \rho \qquad 1.5$$

A critical value of α, $\alpha_{\bar{r}}$, can be found for the stability of the clusters, by plotting graphs of $\bar{r}$, $\bar{r}\log_e S$ and k as functions of α, Fig.1.1. Once the clusters have reached a size $\bar{r}$ at $\alpha_{\bar{r}}$, the clusters will be stable at T_2 if $T_2 < T_c$. From this it is obvious that if T_1 is decreased, the value of $\alpha_{\bar{r}}$ must increase because N increases with decreasing temperature. Because of this the graphs of $\bar{r}$ and $\bar{r}\log_e S$ are lowered, see Fig.1.1. For this lower temperature, no clusters formed during pre-age at T_1 are stable at T_2, because $\bar{r}\log_e S$ is always less than k.

A temperature $T_{1(min)}$ can then be defined below which clusters cannot be stabilised at T_2; above $T_{1(min)}$, the average sized clusters are stabilised are T_2 (provided $T_2 < T_c$).

If this general case is extended to include the size distribution of the clusters and the dependence of $\bar{r}$ and k upon T_1, two important cases arise corresponding to a pre-age above $T_{1(min)}$ and below $T_{1(min)}$. These are shown in Figs.1.2a and 1.2b. In both these cases, T_2 is assumed to be below T_c and the alloy is quenched to T_1.

The first case, where $T_1 > T_{1(min)}$, N is relatively small and $\bar{r}$ large, so that k is decreased. When the pre-age is sufficiently long,

all the clusters, even those with radius r_{min}, will be stabilized at T_2. The final precipitate distribution will be characteristic of the pre-ageing temperature, T_1. After shorter times at T_1, the size distribution will be to the left of that shown in Fig.1.2a, so that no clusters (or very, very few) are stable at T_2. The solute supersaturations have been much reduced at T_1 and at the start of ageing at T_2, the clusters will dissolve, until S increases to a value at which some of the dissolving clusters are stable. At this point, the larger ones will start to grow. The actual number will depend on the value of S and this is determined by the rate of cluster dissolution and cluster growth. Therefore this pre-age will produce a coarse precipitate structure after ageing at T_2. When the pre-age at T_1 is very short, or omitted, there is insufficient time for extensive cluster nucleation and growth, so that subsequent ageing at T_2 will give a microstructure characteristic of T_2.

This case describes the behaviour of the Al-1.2% Mg_2Si when it is pre-aged at 120^oC. Pashley et al (1967) determined T_c for this alloy and found it to be $190^oC \pm 10^oC$. This temperature is correct for an alloy without excess vacancies. With excess vacancies, T_c is increased to $T_{c'}$, $225^oC \pm 5^oC$. $T_{1(min)}$ was not determined, but even so it was possible to judge from the observed microstructures if a pre-ageing temperature was below $T_{1(min)}$. This is clearly seen when considering the case for $T_1 < T_{1(min)}$.

Here, N is now very large, $\bar{r}$ small and k large, Fig.1.2b. When the size distribution is studied, it is seen that even after a long pre-age only a small proportion of clusters will be stabilized at T_2. The definition of $T_{1(min)}$ should now be modified to that temperature below which complete stabilization of clusters can never occur at T_2.

If the pre-age is long enough the particle distribution will be to the right of that shown in the diagram and a large number of clusters will be stable at T_2. Since only some fraction of clusters formed are stabilized, the final microstructure will never have the fineness which is theoretically associated with the pre-ageing temperature.

As in the previous case, no pre-ageing or a very short pre-age will result in a fine microstructure at T_2; longer pre-ageing will produce a coarse microstructure.

Pre-ageing at room temperature seems to obey this second case; the β" needles are still very coarse after three days pre-ageing. → The authors extended the pre-ageing time beyond this point to see if the coarse precipitate structure was ever refined. After several weeks, a finer microstructure was produced, but the average needle size was never less than that observed after pre-ageing at 120°C (250Å). This agrees with the predictions of the second model.

Even though the above theory is simplified (varying quench rates, quenching temperature and excess vacancy concentration will change the critical parameters), it would appear to provide a model which should be applicable to other alloy systems. It demonstrates how critical the pre-ageing treatment is for age-hardening alloys; careless selection of storage conditions can so easily lead to coarse precipitates and poor mechanical properties.

In respect of the present research, it is now evident why the standard storage of five minutes at room temperature should be strictly adhered to. After this short time, a fine precipitate should be formed after artificial ageing, but if the pre-age were increased there is the possibility that coarsening will take place.

However intermediate pre-ageing times at $T_1 < T_{1(min)}$ are not always deleterious. The kinetics of pre-ageing are influenced by the presence of additional elements in solid solution. These can improve the hardenability of aged alloys.

1.4. FORMATION OF PRECIPITATE FREE ZONES (P.F.Z.)

Precipitate free zones are often observed adjacent to grain boundaries in age-hardened alloys. Originally these zones were thought to be associated with local depletion of solute because of precipitation at the grain boundaries, Geisler 1951. Thomas and Nutting, 1959-60, suggested that vacancy depletion might control P.F.Z. width and Embury and Nicholson, 1965, working on Al-Mg-Zn alloys proposed that the grain boundary acted as a sink for vacancies during the quench and that a vacancy concentration profile was formed adjacent to the grain boundary. For nucleation of precipitates at a higher temperature, a critical minimum vacancy concentration was required. This condition would be satisfied in the centre of the grains, but adjacent to the grain boundaries, the vacancy concentration would eventually fall below the critical value. Beyond this point no precipitates would form.

Lorimer and Nicholson, 1966, extended this model to include the solute-vacancy clustering processes in age-hardened alloys. They found that pre-ageing had a marked effect on the particle distribution and P.F.Z. A long pre-ageing time produced a narrow P.F.Z., while after a short pre-age a wide P.F.Z. was formed, provided the pre-ageing temperature was below the homogeneous nucleation temperature for the system. This was explained in terms of the formation of clusters during the pre-age; these would have a maximum size, d_{max},

proportional to the ageing time and temperature. In the gradient condition near the grain boundaries, where the as-quenched vacancy concentration was reduced and bulk diffusion slower, the clusters would reach a maximum size less than d_{max} and would decrease in size towards the grain boundary. At the higher ageing temperature, there was a critical size, d_{crit}, below which clusters dissolved. Provided d_{max} was greater than d_{crit}, the clusters would continue to grow within the grains, but towards the grain boundary a point would be reached where the maximum cluster size was less than d_{crit} and this marked the beginning of the P.F.Z. As pre-ageing time increases and d_{max} increases, this point will move towards the grain boundary and so a narrower P.F.Z. is formed after longer pre-ageing times.

Jacobs and Pashley, 1968, have applied the model described in section 1.3 to P.F.Z. formation. The predicted results are essentially the same as the above, but they also show that solute depletion can still be an important factor. For example, when T_2 (the artificial ageing temperature) is below T_c, clusters formed during pre-ageing ($T_1 < T_c$) are only stabilized at T_2 if they have a certain size. Assuming the pre-age is long enough, the clusters in the body of the grain will continue to grow, but the smaller ones near the boundary will dissolve until the local supersaturation is high enough to restabilize them. The larger ones will start to grow again to produce a precipitate region of low density near the grain boundaries and so there is no true P.F.Z. This assumes that there is no solute depletion, which will not be true where there is grain boundary precipitation. With the Jacobs model, reducing the solute concentration effectively lowers T_c. If, due to grain boundary precipitation, T_c is lowered below T_2 in the adjacent region, then precipitation can only occur by heterogeneous nucleation or if the cluster size is large.

Therefore a narrow P.F.Z. is formed. Unwin et al, 1969, have observed local broadening of the P.F.Z. in the region of grain boundary precipitates in Al-Zn alloys. Together with Jacobs theory, this would imply that solute depletion as well as vacancy depletion should be taken into account when considering the formation of P.F.Z.

1.5. EFFECT OF ALLOYING ELEMENTS ON THE AGEING OF Al-Mg-Si ALLOYS

In their studies of pre-ageing, Pashley et al, 1966, also investigated the effects of alloying additions on the ageing kinetics. They found that an addition of 0.24% copper to the basic alloy produced beneficial effects. The copper reduced the pre-ageing rate at room temperature and after artificial ageing at 160°C or 175°C, the copper containing alloy always had a finer precipitate distribution than the copper free alloy and also better mechanical properties.

They proposed that the copper atoms were somehow associated with the magnesium-silicon-vacancy complexes such that the migration rate was slowed down. This was not due just to strong binding between copper atoms and vacancies, because Thomas, 1959, had shown that copper atoms had very little affinity for vacancies. Therefore some other factor must determine whether an alloying addition will reduce the pre-ageing rate in Al-Mg-Si alloys.

From the theory discussed in the previous section, the beneficial effect of the copper can be interpreted. If the copper reduces the rate of cluster growth at T_1, then a much longer storage time will be required before a coarse precipitate structure is produced. Alternatively, the copper might increase the average cluster size $\underline{r}$ for a given pre-age at room temperature. If this is true, then the copper bearing alloy is behaving as though it were being pre-aged at a higher

temperature, very close to $T_{l(min)}$ or maybe above it. The former suggestion is more likely as indicated by the pre-ageing results and is also supported by the experimental results of Chatterjee and Entwhistle, 1973. How the pre-ageing rate is reduced by the copper is not fully understood.

Excess silicon in Al-Mg_2Si alloys can also alter the precipitation kinetics. Using resistivity measurements, (Ceresara et al, 1969/70), the ageing of a stoichiometric alloy, Al-0.8%Mg_2Si, has been followed at room temperature and at 175°C. The results were then compared with those from the alloy containing increasing amounts of excess silicon.

When the alloys are aged at room temperature, the change in resistivity increases with increasing silicon content. Further, the resistivity starts to increase after a shorter time in the latter alloys. The resistivity curves can be superimposed by using a normalization factor, allowing for the different rates of the processes, and this leads to the conclusion that the density of the zones or clusters in the high silicon alloys is larger than in the stoichiometric alloy. This is supported by T.E.M. of the alloys after ageing at 175°C; increasing the silicon content leads to a progressively finer β" needle structure.

The increased cluster density is probably a direct consequence of the fact that the solution temperature for the Mg_2Si phase is raised as the silicon content increases, (Phillips, 1961). Thus an alloy with a high silicon content will have a higher solute supersaturation after quenching than the stoichiometric alloy and consequently the density of clusters will be greater.

The authors also deduce that apart from increasing the cluster

density, the excess silicon will also enhance the rate of the pre-precipitation process, but does not affect the nature of the process. Unfortunately, two step ageing in the excess silicon alloys was not investigated, so that one can only speculate on the effects of pre-ageing in excess silicon alloys.

If the pre-ageing rate at room temperature is increased, this might lead to stable clusters being formed at short ageing times, so a fine precipitate structure will be produced after artificial ageing. Of course, this assumes that the solute and vacancy super-saturation remains high enough after nucleation to allow rapid growth.

The above results show how easily the precipitation kinetics can be changed and hence how sensitive are the parameters T_c, $T_{1(min)}$ and k to microstructural variables. For an Al-Mg-Si alloy containing several alloying additions, excess magnesium or silicon, it is obviously very difficult to predict the response to two-step ageing. It would seem that a careful investigation of pre-ageing conditions must be carried out for such alloys to ensure selection of the optimum two-step ageing conditions.

1.6. DEFORMATION MECHANISMS IN TWO-PHASE ALLOYS

As discussed in the opening section of this chapter, commercial aluminium alloys can have complex microstructures. Apart from being polycrystalline the alloys contain several types of particles some of which will lie in the grain boundaries. All of these features will contribute to the deformation behaviour, so a theoretical description of the latter would be very complicated indeed. For simplicity the role of second phases in the deformation of F.C.C. single crystals will be described first and then how this is modified by the intro-

duction of grain boundaries into the structure.

1.6a F.C.C. Single Crystals

In general, the main effect of alloying is to raise the yield stress and alter the rate of work hardening in comparison with that of the pure metal. The extent to which an alloying addition can change these mechanical properties will depend on the form in which it is present. Coarse, widely spaced particles tend to produce the least change in yield stress, but may increase the work hardening rate appreciably. On the other hand, a matrix with a very fine precipitate structure will show a large increase in yield stress while the work-hardening rate may be similar to that of the pure metal. However, particle size and spacing are not sufficient criteria; the ease of deformation of the particles themselves may also be an important parameter in determining the deformation mode of a two-phase alloy.

When the particles are deformable and have a fine distribution, yield will take place by dislocations shearing the particles. This is the case where an alloy has been age hardened to produce a fine dispersion of precipitates which are coherent or partially coherent with the matrix (Nicholson et al, 1960). The critical resolved shear stress τ_y at yield of a two-phase alloy, can be expressed as a sum of shear terms:

$$\tau_y = \tau_m + \Delta\tau_p \qquad 1.6$$

where τ_m is the shear stress of the matrix and $\Delta\tau_p$ is the additional stress required due to the particles.

For particle shear, this extra stress will be influenced by several factors, such as chemical strengthening, modulus effects,

coherency strains and ordering. There are many quantitative assessments of these and they have been well reviewed in the literature (see for example, Brown and Ham, 1971 or Kelly, 1973). In any alloy system, some of the above will be more dominant than others and $\Delta\tau_p$ cannot usually be ascribed to one particular strengthening mechanism. In an Al-Mg_2Si alloy, it is likely that the effects of coherency strains and the work of shearing the β" needles and β' rods will dominate.

The equations for $\Delta\tau_p$ used to account for the different strengthening mechanisms all have the general form

$$\Delta\tau_p = K\, r^a\, F_V^{\,b}\, (\Delta E)^c \qquad 1.7$$

where K is a constant term for the process, (ΔE) an irreversible energy change associated with cutting of the particle, r is the particle radius (spheres) and F_V the volume fraction. The power indices reflect the degree to which any mechanism contributes to the process. Typically, their values are:

$$0 < a < \tfrac{1}{2},\ \tfrac{1}{3} < b < \tfrac{2}{3},\ 1 < C < \tfrac{3}{2}.$$

Kelly and Fine, 1957, have shown that the shearing occurs in alloys containing zones, but when the alloy is overaged the process is replaced by looping of dislocations between the particles. In this situation, the particles are usually no longer coherent with the matrix, are larger and more widely spaced so that now

$$\Delta\tau_{\text{cutting}} > \Delta\tau_{\text{looping}} \qquad 1.8$$

$\Delta\tau_{\text{looping}}$, as originally formulated by Orowan, is defined by the critical shear stress required to bow a dislocation of line tension, T, and Burger's vector, $\underline{b}$, through an array of obstacles

a distance L apart.

$$\Delta\tau_{looping} = \frac{2T}{bL} \simeq \frac{\mu b}{L} \qquad 1.9$$

where μ is the shear modulus of the matrix.

This equation has since been modified to allow for the effective spacing of a random array of particles and their size, (Kocks, 1966, Foreman and Makin, 1966) and the variation of line tension with the shape of the loop, (Ashby, 1966) to give the general formula for dislocation looping

$$\Delta\tau_{looping} = \frac{\mu b}{2\pi(1-\nu)^2} \cdot \frac{B}{(L-2r)} \cdot \ln \frac{2r}{r_o} \qquad 1.10$$

where ν is Poisson's ratio, r_o is the dislocation core radius and B is a geometrical factor related to the particle distribution. This process of looping has been observed by many authors, though the mechanism has been adapted to allow for cross slip and the formation of prismatic loops which are seen, Humphreys and Martin, 1967. Even when cross slip takes place at yield, the yield stress is still given by the Orowan bypass stress as indicated by Hirsch and Humphreys, 1969.

The rate of work hardening in a single crystal containing a second phase will also be governed by particle-dislocation interaction. When the particles are sheared at yield, the dislocations cut through the precipitates intersecting the slip plane and continue to move through the crystal, and the work hardening rate is expected to be similar to that in single-phase crystals, (Price and Kelly, 1964).

When the single crystals yield by the dislocation looping mechanism, the work hardening rate is much higher than in the pure metal. The increased hardening rate in such materials arises from the dislocation debris which accumulates at the particles after repeated

dislocation looping and cross slip. Ashby, 1970, has shown that such dislocations are geometrically necessary because a two-phase material does not deform homogeneously. Deformation gradients are set up between the rigid particles and dislocations are required to accommodate the regions of different strain. By assuming a random array of prismatic loops around the particles, he relates the average dislocation density $\bar{\rho}$ and particle size, r, to the flow stress using a forest model for the interaction of the gliding dislocations with the dislocation debris. The applied stress τ to force a dislocation through the debris is then

$$\tau = \tau_0 + C_1 \mu \underline{b} (\bar{\rho})^{\frac{1}{2}} \qquad 1.11$$

where τ_0 is a frictional stress, taken as the flow stress of the matrix, and $\underline{b}$ is the average Burger's vector for the material. The density $\bar{\rho}$ is taken to be the density of the geometrically necessary dislocations ρ^G which is dependent on the geometric slip distance λ^G.

$$\rho^G = \frac{1}{\lambda G} \quad \frac{4\gamma}{\underline{b}} \qquad 1.12$$

γ is the shear strain imposed on the material. For well spaced, equiaxed particles, λ^G is given by r/f, when there is no recovery, so

$$\tau = \tau_0 + C_1 \mu \left(\frac{f \underline{b} \gamma}{2r} \right)^{\frac{1}{2}} \qquad 1.13$$

which gives a parabolic relationship between τ and γ. It should be noted that this model is based on a random array of prismatic loops with random Burger's vectors, which is not true of real materials where the loops are often lined up in rows and have primary Burger's vectors. However equation 1.13 does show how the hardening rate can be raised by the presence of second phase particles and its dependence on the particle volume fraction.

It is clear that particle shear should produce a different dislocation distribution and slip band distribution from dislocation looping. Nicholson et al, 1960, have studied the dislocation-particle interactions in several alloys. They showed that G.P. zones in Al-Zn alloys and θ" precipitates in Al-Cu alloys were cut by dislocations; the deformation was concentrated in widely separated slip bands. When the precipitates were large and non-coherent, dislocation debris was observed around the particles; there was, as well, a uniform dislocation distribution within the grains, i.e. slip was more uniform when a dislocation looping mechanism was operating.

Optically, the slip distributions have been followed by surface slip line observations. Greetham and Honeycombe, 1959-60, found that when an Al-Cu single crystal contained θ" precipitates, the surface slip lines were sharp, but as ageing proceeded the slip lines became finer and fainter until they were hardly visible at peak hardness. This suggests that the particle shear associated with coherent precipitates produces highly localized slip. As the particles coarsen and the looping mechanism takes over slip becomes more homogeneous. When the alloy was over aged and contained θ' and precipitates, evidence of slip could only be seen at high magnifications.

With such differences in slip distribution, it is to be expected that the fracture modes will also differ. Beevers and Honeycombe, 1959, observed that extensive necking occurs in pure aluminium and failure occurs when the crystal has necked down by 100%. The authors found that necking disappeared when the aluminium was alloyed with 5% copper and aged to peak hardness. Coarse slip bands were seen prior to fracture and the crystal sheared parallel to an active set of

slip planes. The fracture surfaces were not smooth like a cleaved surface, but covered with fine cusps which were elongated in the direction of shear.

For an Al-Cu single crystal containing non-deformable particles, Dew-Hughes and Robertson, 1960, found that fracture was 'cup and cone' and similar to that in fine grain polycrystals and was thus characteristic of slip on several systems. The authors did not describe the fracture surface of the single crystal, but it is likely that ductile rupture occurred. The fracture surface would then consist of equiaxed dimples due to coalescence of voids nucleated at the particles. These processes have been described and reviewed by Brock, 1972.

1.6b F.C.C. Polycrystals

In general, commercially important materials are in polycrystalline form and often contain second phase particles, thus these alloys owe their strength to a combination of strengthening mechanisms. Particle strengthening has already been described and it is now instructuve to consider the effect of grain boundaries.

Grain boundaries must provide resistance to dislocation glide at yield; additional stresses will be needed to nucleate and propagate slip in an adjacent grain.

The Hall-Petch equation

$$\sigma_y = \sigma_i + k_y d^{-\frac{1}{2}} \qquad 1.14$$

(σ_y = yield stress, σ_i = lattice friction stress, k_y = constant) originally proposed as the relationship between the lower yield stress, σ_y, in carbon steels and the grain diameter, d, is also valid for

yielding of F.C.C. metals (Armstrong, 1962). The lattice friction term which is essentially a function of the grain matrix will be determined by the matrix strengthening mechanisms. For a particular alloy, σ_i is expected to be large where the particles are sheared and smaller where the particles are by-passed. The constant k_y is related to the difficulty of spreading slip from one grain to another and incorporates the continuity conditions necessary to maintain contiguous grains.

The importance of the grain size depends on the value of σ_i. In high strength materials, σ_i is very large, so that $k_y d^{-\frac{1}{2}}$ is negligible in comparison. In age hardened alloys, where σ_i is smaller the grain size makes a relatively larger contribution to the yield stress and thus can be a source of strengthening.

The effect of grain size is probably more noticeable when work hardening and slip distribution are considered. Using Ashby's equation (1.12) for work hardening

$$\tau = \tau_o + C_1 \mu b \underline{\quad} \left(\frac{1}{\lambda^G} \; \frac{4\gamma}{b} \right)^{\frac{1}{2}} \qquad 1.15$$

we can obtain an idea of the work hardening rate in single phase polycrystals. The geometric slip distance, λ^G, will be the grain diameter D.

$$\tau = \tau_o + C_1 \mu \left(\frac{4\gamma b}{D} \right)^{\frac{1}{2}} \qquad 1.16$$

This predicts a parabolic stress-strain curve for polycrystals. Since age hardened single crystals work harden at a similar rate to single-phase metal crystals, equation 1.16 must describe the behaviour of age hardened polycrystals. This means that deformation will essentially be Stage III. For a polycrystal containing non-deformable

particles, the work hardening behaviour will still be described by equation 1.13, but because r/f is smaller than D, these polycrystals will still show a higher work hardening rate. This will probably be more than that of the single crystal, because of the additional constraints imposed by the grain boundaries.

Polycrystals with small, non-coherent particles initially work harden more than the matrix material without a dispersion, but after a few percent strain, the work hardening decreases and the stress strain curve becomes parallel with the matrix curve, (Hart, 1953). At this stage, some additional mechanism must take place, probably one of cross slip in F.C.C. metals with high stacking fault energy.

The slip dispersion within the grains will still be controlled by the operative deformation mechanism, but many more slip systems should be activated due to grain rotation relative to the tensile axis and grain boundary constraints.

1.7. TRANSGRANULAR VERSUS INTERGRANULAR FRACTURE

Many high strength polycrystals of precipitation hardened aluminium alloys show little ductility and are susceptible to intergranular fracture. This phenomenon is observed in the fully heat-treated H.30 alloys without a manganese addition. It is therefore instructive to consider the factors which encourage intergranular failure. To understand this it is necessary to consider the two competing processes at the grain boundary. Firstly, there is the process of yield, where slip must be transmitted across the boundary. This is described by the Hall-Petch equation. Then there is the initiation of fracture and propagation along the boundary. From the theory of Cottrell for cleavage, the stress σ_F required for fracture can be expressed in terms of γ, the total work done per unit area for continued crack growth

$$\sigma_F = \frac{4\mu\gamma}{k_f} d^{-\frac{1}{2}} \qquad 1.17$$

It is seen that intergranular fracture will predominate if k_f is very high or γ is very low in the region of the grain boundaries.

Now k_f is a measure of the difficulty of transmitting slip from one grain to another. k_f can be increased by alloying and dislocation pinning (Armstrong, 1962) or where cross slip is inhibited and slip is localised into bands, (Embury, 1971).

Alternatively, γ can control the fracture mechanics. It is not necessarily a measure of the surface energy of the fracture path but may also include a plastic work term. One way of reducing γ arises when there is solute segregation in the boundary. If this lowers the surface energy of the boundary, then intergranular fracture will take place. Segregation can also reduce γ in respect of the P.F.Z. in age-hardened alloys. The P.F.Z. will be softer than the grain matrix and will provide a low energy path for crack propagation. Here γ will include a plastic work term. Associated with the P.F.Z. are grain boundary precipitates; these can act in the same way as solute segregation in the boundaries and change the local cohesive strength or voids could nucleate at the particles, which will aid crack propagation in the P.F.Z.

It would seem that intergranular fracture can be avoided by reducing k_f and thus encouraging homogenized slip. Certainly the intergranular brittleness associated with peak aged Ti-Al alloys is suppressed when the alloy is aged such that the matrix contains coarse particles and deformation is by dislocation looping and thus homogeneous, (Lutjering and Weissman, 1970). If γ has a high value this would be equally effective but this is difficult to achieve in age-

hardened alloys where grain boundary precipitates and P.F.Z. are inherent in the microstructure.

1:8. OBJECTS OF THE PRESENT RESEARCH

From the fore going, it is seen that localised slip in age hardened alloys is extremely relevant to the deformation mechanisms which produce intergranular failure. The H.30 alloy system containing non-coherent manganese intermetallic particles does not fracture intergranularly. The effect of these particles on fracture nucleation in Al-Mg-Si alloys will be studied with special reference to the slip distribution. It was also decided that some direct metallographic observations of fracture propagation would also be made, using a bending jig which could be fitted to an optical microscope.

Fig.1.1

Variation of $r \log_e S$ for a temperature T_2 as clustering occurs at T_1, plotted as a function of the fraction of solute in clusters, α.

(The full line corresponds to a case where clusters formed at T_1 are stable at T_2; the broken line represents the case where the clusters are not stable at T_2).

FIG. 1.1

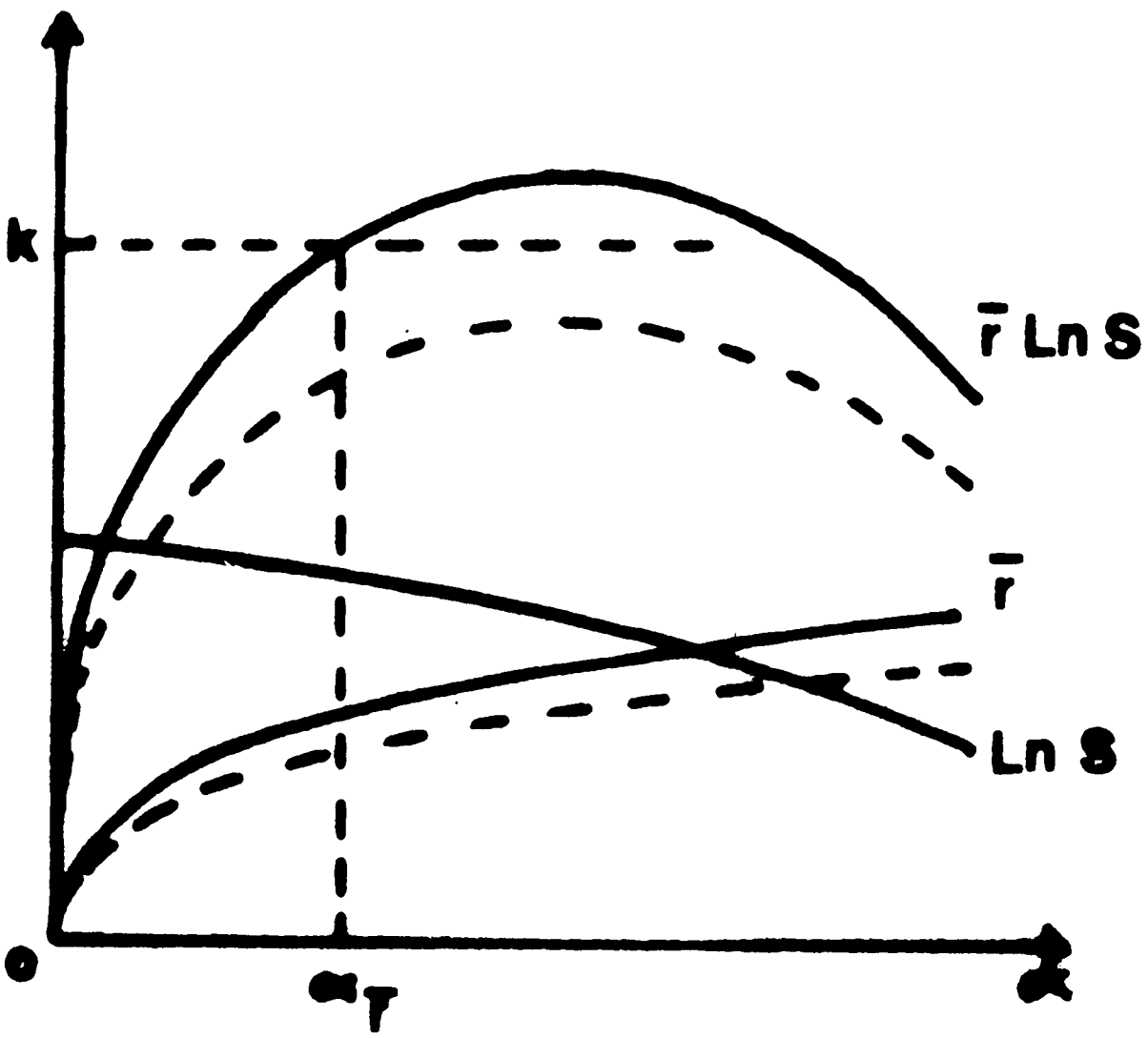

Fig.1.2

The general stability curve when the cluster sizes are distributed between r_{min} and r_{max}

(a) Full stabilization at T_2 is possible

(b) Only a small proportion of clusters are stable at T_2

FIG. 1.2

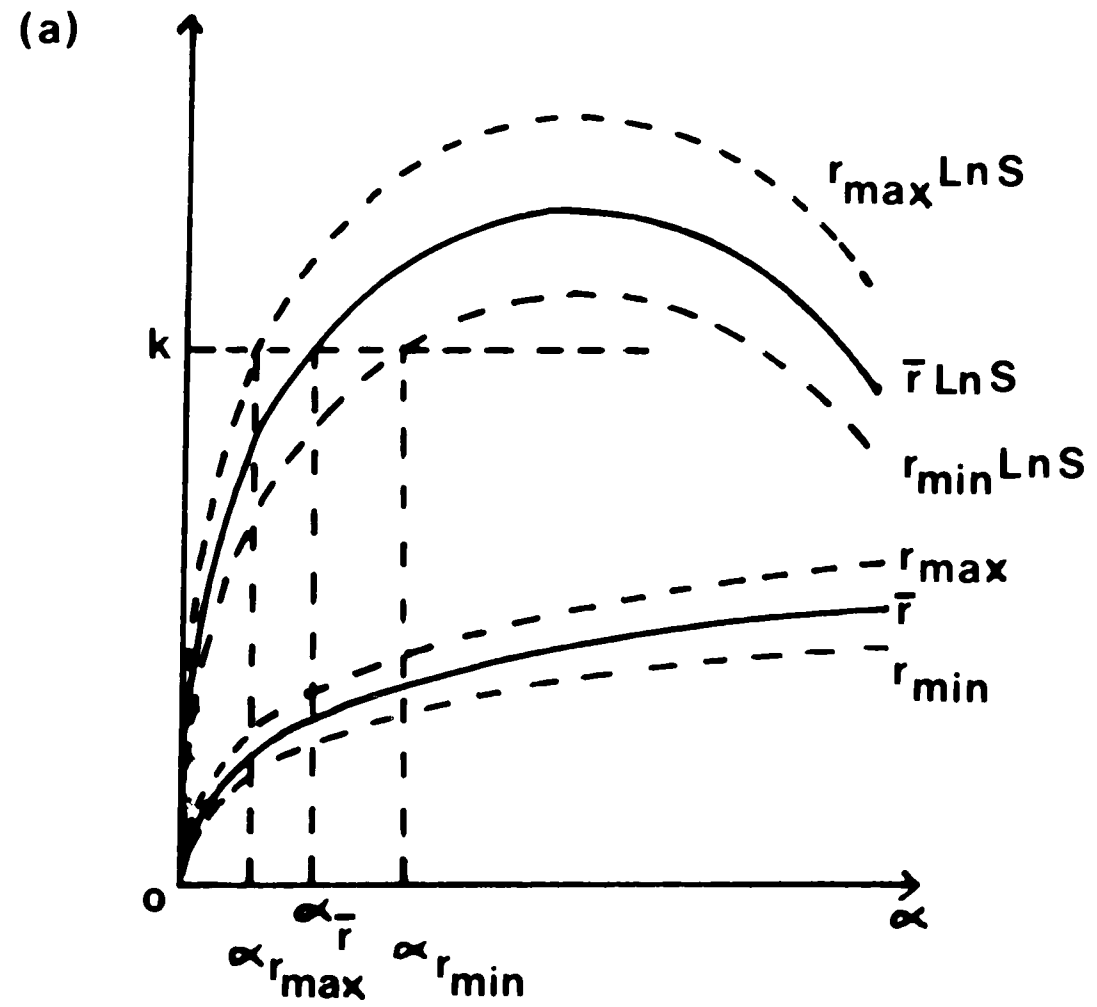
(a)
k
o
r_{max} Ln S
$\bar{r}$ Ln S
r_{min} Ln S
r_{max}
$\bar{r}$
r_{min}
$\propto_{\bar{r}}$
$\propto_{r_{max}}$
$\propto_{r_{min}}$
$\propto$

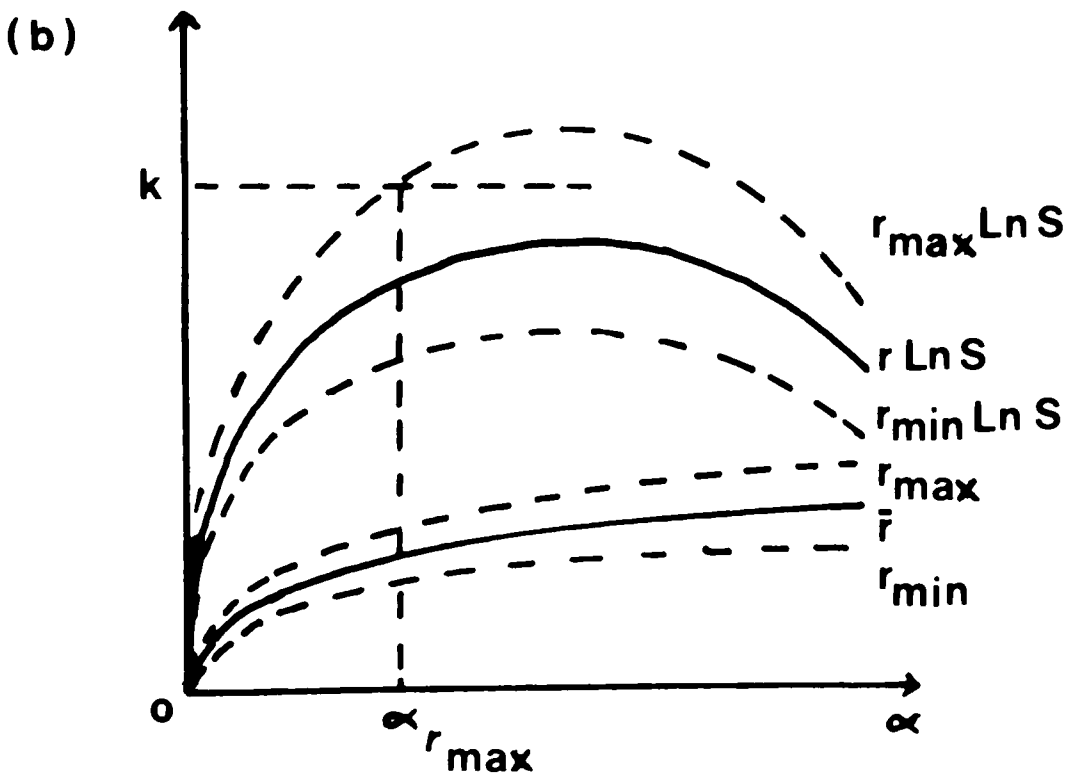
(b)
k
o
r_{max} Ln S
r Ln S
r_{min} Ln S
r_{max}
$\bar{r}$
r_{min}
$\propto_{r_{max}}$
$\propto$

CHAPTER 2

MATERIALS, APPARATUS AND EXPERIMENTAL TECHNIQUES.

2.1. MATERIALS

A selection of aluminium alloys from the H30 series were made available by Alcan International Limited. All the alloys contained magnesium, silicon and iron in varying amounts; in addition to these elements, different amounts of manganese were present in some of the alloys. The presence of iron in the alloys has a deleterious effect on the toughness; coarse particles (>1μm) of $FeAl_3$ and α-AlFeSi are formed during casting and these tend not only to reduce the toughness of the manganese bearing alloys, but also encourage intergranular fracture (Dunwoody et al., 1973), thus masking the effects of the manganese additions. Therefore, alloys of low iron content, less than 0.01wt%, were selected in order to simplify the research investigations. Three alloys were used, one manganese-free and two of different manganese content; the alloy compositions are given in Fig.2.1.

2.2. HEAT TREATMENT METHODS

After casting, the aluminium alloys undergo a sequence of heat treatments and rolling processes to produce sheet material 3mm. thick. The process carried out in the Alcan Laboratories is as follows:

i) Casting homogenized at 530°C for 16 hours,

ii) Casting hot rolled at 530°C from 25mm. to 10mm. thickness,

iii) Billet cold rolled from 10mm. to 3mm. thickness,

iv) Sheet solution heat treated in air at 560°C for 30 minutes; water quenched,

v) Standard age at room temperature for 5 minutes,

vi) Aged in oil at 185°C to peak hardness; water quenched.

Alcan International Limited supplied the alloys in the cold rolled state. In the present work, solution heat treatment was carried out in

air using a platinum-wound, resistance furnace in conjunction with a Eurotherm temperature controller. After insertion of a sample into the pre-heated furnace, there was always a period of a few minutes before the furnace reached temperature again. This 'warming-up' time was not included in the solution heat treatment time, nor in the heat treatments used later in the precipitation and grain growth studies. Ageing was carried out using a bath of low melting point salt.

The age-hardening curves of the three alloys were determined by Vickers Hardness measurements of the alloys after different ageing times at 185°C.

2.3. OPTICAL METALLOGRAPHIC TECHNIQUES

2.3a Polishing Procedure

Specimens for optical examination were prepared as follows:

i) Wet ground on silicon carbide papers, 220, 320, 400 and 600,

ii) Metal polish on a soft cloth,

iii) Diamond paste polish with 6μm and $\frac{1}{4}\mu$m.

Chemical etches failed to reveal the grain structure of the manganese bearing alloys, BD6 and BD8; the etchants tended to stain the surface so that the grain boundaries were not detectable. This effect was not observed in the manganese-free alloy, BD3, nor in the as cast alloys, so the staining must be produced by chemical attack on the ~ 0.1μm, manganese-bearing particles present in BD6 and BD8. However, this phenomenon was useful in the optical detection of the presence or absence of the α-phase particles in the precipitation and recrystallization studies described in Chapter 3. Keller's reagent

was used for this purpose.

An electro-chemical etch was used to reveal the grain structures of the alloys in both the deformed and undeformed states. The solution used was 49% methanol, 49% nitric acid, 2% hydrochloric acid cooled with liquid nitrogen with a cathode of commercial aluminium. With a specimen to cathode distance of 5cm, a current of 0.2 to 0.3 amp. at 5 volts produced a highly polished surface with good grain boundary etching. Some pitting occurred in BD6 and BD8; this was due to localized chemical attack at the coarse residual casting precipitates, which lay in strings parallel to the rolling direction.

Metallographic specimens were examined on a Vickers 505 microscope or a Reichart Microscope both before and after etching.

2.3b Grain Size Determination

The manganese-free alloy, BD3, has a regular, equiaxed grain size, but BD6 and BD8 have grain structures consisting of regions of small grains, adjacent to the residual casting precipitates, and larger grains which are elongated along the rolling direction and lie between the strings of coarse particles.

The Jeffries procedure (a planimetric method) was used to measure the grain size of the three alloys (Jeffries et al., 1916 and Dehoff and Rhines, 1968). This is a counting method which determines the arithmetic mean size. Measurement is carried out by counting the number of grains which lie inside a circle of known area and half the number of those that intersect the circumference of the circle.

If R is the radius of the circle and n_1 is the number of grains lying completely within the circle and n_2 the number intersecting the

circumference, M the magnification and $\bar{A}$ the mean area of a grain, then

$$A = \frac{\pi R^2}{M^2} \left(\frac{1}{n_1 + \frac{n_2}{2}}\right) \qquad 2.1$$

$$\text{Mean grain size } \sqrt{\bar{A}} = \frac{R}{M} \left(\frac{\pi}{n_1 + \frac{n_2}{2}}\right)^{\frac{1}{2}} \qquad 2.2$$

Strictly speaking this formula applies only to equiaxed structures where the count can be made on any planar section. For non-equiaxed grains, measurements should be made on three mutually perpendicular planes (ASTM Designation E112-60T) and the mean calculated from

$$N_V = 0.7 \; N_A(\ell).N_A(t).N_A(n) \qquad 2.3$$

where N_V is the number of grains per mm^3 and $N_A(\ell)$, $N_A(t)$ and $N_A(n)$ are the numbers of grains per mm^2 in the three sections. The ratios $N_A(\ell)/N_A(t)$ and $N_A(\ell)/N_A(n)$ give an indication of the grain shape.

Since the purpose of the grain size analysis was mainly to determine the ratios of grain size between BD3, BD6 and BD8, equation 2.2 was used for counts on just the rolling plane of the alloys. This gives valid results for BD3, which is equiaxed. In the recrystallization and grain growth experiments performed on BD8 (described in Chapter 3), the aim was to produce an equiaxed grain structure of size similar to that of BD3. Hence the use of equation 2.2 was considered sufficiently accurate.

For the above analysis, a plane, polished surface is required and strongly etched grain boundaries. The rolling plane of each alloy was prepared as described in Section 2.3a and the grains counted

by inscribing a circle of radius 4cm on the projected image screen of the Vickers 505 microscope. Magnifications which gave a grain count of 30 were selected and fifty such counts were made for each alloy. The mean grain diameters were calculated and the results plotted as histograms.

2.4. TRANSMISSION ELECTRON MICROSCOPY (T.E.M.)

2.4a Thin Foil Preparation

For the examination of the alloys, after solution treatment and ageing, the sheet material was slit into two and ground down before the final heat treatments. The bulk material was mounted on a brass block with high conductivity silver paint and 3mm discs were trepanned by spark erosion. The resulting discs, which were approximately 0.5mm thick, were lightly rubbed on 600 emery paper to a thickness of 0.4mm.

A two stage technique was used for thinning and polishing. The discs were initially thinned by jet machining. Discs were centred 8mm below a stainless steel jet nozzle (0.8mm bore) and dished on each side for 30 seconds with a current of 0.2 amp. and a voltage of ~ 70 volts; the electrolyte was 15% nitric acid. For deformed material, the above conditions produced a non-uniform dish. By increasing the current to 0.4 amp. and the voltage to 130 volts. a smooth polished dish was obtained after a jetting time of 18 seconds per side. The latter conditions were used to prepare discs cut from specimens which had been tested in compression or tension.

For the final polish, a circular electrolytic cell was used;

the cathode being made of commercial aluminium and the electrolyte a solution of 49% methanol, 49% nitric acid, 2% hydrochloric acid cooled with liquid nitrogen. The discs were polished to perforation using 0.2 amp. and 5 volts and the process was observed with a telescope.

The thin foils were examined using either a Phillips EM300 electron microscope or a JEOL JEM100C electron microscope, which were both operated at 100kV.

2.4b Particle Analysis

Particle size distributions for spherical particles can be determined by various methods. For precipitates which are rod shaped and have random orientation, a rigorous analysis of the distribution in opaque materials is possible, provided the rods are of uniform size (Fullman, 1953). Alloys BD6 and BD8 contain $\alpha(Al_{12}Mn_3Si)$ in the shape of rods of various diameters and even allowing for the random orientation there was not a constant aspect ratio ℓ/d (d and ℓ are the particle diameter and length respectively) for the system. With such a complicated distribution, its size distribution analysis can only be approximate.

As the particles have a mean diameter of $0.1\mu m$, counting and sizing was performed using T.E.M. Particle diameters can be measured accurately by this method, but complications may arise from overlapping particles and surface effects. As Ashby and Ebeling, 1966, have shown, these factors lead to an inaccurate measurement of particle volume fraction.

Fullman, 1953, has derived several formulaefor rod shaped

particles as viewed on a polished plane. His results are used in the following analysis, but Underwood's (1970) notation is used.

For a rod at any orientation, the diameter is easily identified, so the following analysis is based on the measured mean diameter of the rods. The diameter distribution was investigated by direct measurement from electron micrographs using a hand lens with a graticule. The results were plotted as a histogram, from which the mean particle diameter was determined.

Using Fullman's method, the mean projected length, $\bar{\ell}_p$, of a rod is given by

$$\bar{\ell}_p = \frac{\pi \ell}{4} \qquad 2.4$$

This assumes that the rods have a constant length, ℓ, for a radius r. In this analysis, $\bar{\ell}_p$ was calculated using

$$\bar{\ell}_p = \frac{1}{n} \sum_{i=1}^{n} \ell_{pi} \qquad 2.5$$

where n is the number of particles with a mean diameter $\bar{d}$. Therefore the actual mean length, $\bar{\ell}$, of the particles will be

$$\bar{\ell} = \frac{4}{n\pi} \sum_{i=1}^{n} \ell_{pi} \qquad 2.6$$

There is some evidence that α phase particles in BD6 and BD8 are rods with faceted ends (see Plate 3.19). In this analysis the particle shape was assumed to be that of a regular rod, so the volume of an individual particle, V, is given by

$$V = \pi r^2 \ell \qquad 2.7$$

If there are n particles on a micrograph of unit foil area and thickness t, then the number of particles per unit volume, N_V, will be

$$N_V = \frac{n}{t} \qquad 2.8$$

and the volume fraction, F_V, is

$$F_V = V N_V \qquad 2.9$$

or

$$F_V = \pi r^2 \ell N_V \qquad 2.10$$

Equations 2.7 and 2.10 hold for rods with a constant length ℓ and radius r. For rods of non uniform size, ℓ and r must be replaced by $\bar{\ell}$ and $\bar{r}$.

Interparticle spacing can be described in terms of the mean free path, λ, or the nearest neighbour distance, Δ_3. The mean free path, λ, is defined as the average distance between the surfaces of the particles along any random straight line in the structure. λ may be calculated using the reciprocal of the linear particle density, N_L. N_L along a vertical line in the structure will be N_V times the probability that the line hits a single rod. Fullman equates this probability to the average area, $\bar{A}p'$, presented by the rods where viewed from the direction of the line, i.e. $\bar{A}p'$ is the mean projected area on the horizontal plane.

For rods,

$$\bar{A}p' = \frac{\pi r \ell}{2} \qquad 2.11$$

$$N_L = \bar{A}p' N_V = \frac{\pi r \ell}{2} \cdot N_V \qquad 2.12$$

Underwood, 1970, has shown that $(N_L)^{-1}$, the random particle centre to centre distance, exceeds the mean free path path, λ, by the average particle intercept length, $\bar{L}_3$.

$$\frac{1}{N_L} - \lambda = \bar{L}_3 \qquad 2.13$$

Fullman calculates $\bar{L}_3$ for rods from the equality

$$N_V V = N_L \bar{L}_3 \qquad 2.14$$

and by substituting for N_V/N_L (equation 2.12) and V

$$\bar{L}_3 = 2r \qquad 2.15$$

Hence the mean free path, λ, can be calculated. Again, for the present system, the mean values $\bar{\ell}$ and $\bar{r}$ were used.

Finally, the nearest neighbour distance, Δ_3, which is the average centre to centre distance between nearest neighbours, was determined using

$$\Delta_3 = 0.554\ N_V^{-\frac{1}{3}} \qquad 2.16$$

(Gurland, 1968).

To calculate N_V and F_V, the foil thickness, t, must be known. The most convenient method for BD6 and BD8 was the planar trace technique. At low plastic strains, their deformation structure consisted of slip bands perpendicular to <111>. The foil thickness, t, is given by

$$t = \omega \tan\theta \qquad 2.17$$

where ω is the projected width of the slip band and θ is the angle between the foil surface and the slip band. This equation is only

valid when the foil normal is parallel to the electron beam.

There is a number of inaccuracies associated with this calculation and derive from the accompanying trace analysis, (Hirsch et al, 1965). The main one occurs when the foil is tilted and θ should be replaced by θ' (ibid).

$$\theta' = \theta + \cos^{-1}\left[\frac{\text{Cos } \psi}{(1 - \text{Cos}^2\omega\text{Sin}^2\psi)^{\frac{1}{2}}}\right] \qquad 2.18$$

where ψ is the angle of tilt of the foil and ω is the angle between the tilt axis and the projected length of the planar feature.

The other important source of error lies in the determination of the crystallographic orientation of the foil. In general, a diffraction pattern corresponding to [uvw] does not mean that the electron beam is parallel to [uvw], which may be off-axis by an angle α. An exact determination of the orientation can be made from the position of the Kikuchi lines on the diffraction pattern. As the foil is tilted, the Kikuchi lines move as though fixed to the crystal, but the diffraction spots just change in intensity. For a tilt of α, the Kikuchi lines will move a distance $L\alpha$, where L is the diffraction camera length. If L is known, α can be calculated.

In the polycrystalline materials used, the electron beam was rarely parallel to any [uvw] and frequently off-axis by several degrees. Added to this, the slip bands only came into sharp contrast at the two beam diffraction condition. The orientation of a grain was determined by plotting this diffraction direction (and two others), relative to the tilt axis, on a stereographic projection in terms of the angles of tilt. By replotting the projection to the required diffraction condition, θ, ω and ψ were measured and the foil thickness

determined.

2.4c Slip Band Analysis

The purpose of the slip band analysis was to compare the slip band spacings in BD3, BD6 and BD8 after various plastic strains.

Normally BD3 fractures in tension at 1% elongation compared with ~ 17% for BD6 and BD8. By using compressive stresses, reductions of at least 10% could be achieved in BD3 without fracture. Rod specimens of the three alloys were prepared by swageing the sheet material prior to the final heat treatments and plastically deformed in compression using an Instron Mechanical Testing Machine. The deformation structures of the alloys were examined after compressive reductions of ~ 1.5%, ~ 2.5%, ~ 4.0% and ~ 9.0%. Thin foils were prepared from sections cut perpendicularly to the compressive axes of the rod specimens.

The orientation of the slip bands within the deformed grains was found using the method described in section 2.4b. In single crystals, where foils can be cut from sections of an orientation where the slip bands are known to be visible, the slip band spacing, p, is easily calculated using

$$p = q \sin\theta \qquad 2.19$$

where q is the projected repeat distance of the slip band traces and θ is the angle the slip band makes with the foil surface (see Fig.2.2). This equation holds for polycrystals, where the slip traces are visible when the foil surface is normal to the electron beam.

When the foil is tilted, this equation must be assumed to be no

longer valid. Since nearly all the trace analyses were necessarily performed after several degrees of tilt, a technique had to be devised to take the latter into account. Firstly, it was deduced that the measured repeat distance for a set of traces would vary in magnitude as the foil was tilted. Secondly, it was assumed that the variation would be dependent on the angle the slip trace made with the tilt axis. Thirdly, after tilt about two axes, the variation was found to be dependent on the relative orientations of the foil surface normal, F.N., and slip plane normal, <111>, to the direction of the electron beam. It was found that there were only four distinct tilt conditions and a simple mathematical formula could be derived in each case. In conjunction with the stereographic projection for the tilted condition, the slip band spacing for any angle of tilt was calculated.

The models for the four different tilt situations are shown in Figs.2.3, 2.4, 2.5 and 2.6; these will be referred to as Cases 2,3,4 and 5, respectively, Case 1 being for the non tilted foil. Only Cases 2 and 3 will be explained fully; the derivation of the formulae for Cases 4 and 5 is similar to that for 3.

Case 2 is the simple case where the slip trace is parallel to one of the tilt axes and the foil is tilted by an angle ψ about the axis, Fig.2.3. If θ is the angle the slip plane makes with the foil surface, then the slip band spacing, p, is

$$p = q \frac{\text{Sin } \theta}{\text{Cos } \psi} \qquad 2.20$$

It is worth pointing out that this calculation is made for the vertical plane containing the direction of the electron (the vertical) and the slip plane normal and, in this case, the foil normal, F.N.; in the other three cases, the foil normal does not lie in this

vertical plane. Note that the slip band spacing is independent of the foil thickness in all four cases.

Case 3 is illustrated in Fig.2.4a. Here the foil is tilted about one axis or both axes; the slip trace is not parallel to either tilt axis. The stereographic projection shown is for a tilt ψ with the following restrictions.

i) The angle vertical, <111>, F.N. (foil normal is less than 90°.

ii) F.N. and <111> lie on the same side of the slip trace projection (111).

The plane of the foil normal has been drawn in, as has the vertical plane containing the vertical direction and <111>, the slip plane normal. The section through this vertical plane is shown in Fig.2.4b. From this it can be seen that the slip band spacing is given by

$$p = AC \text{ Sin } (\beta - S) \qquad 2.21$$

where S is the angle the foil surface makes with the horizontal.

$$AC = \frac{q}{\text{Cos } S} \qquad 2.22$$

$$p = q \frac{\text{Sin } (\beta - S)}{\text{Cos } S} \qquad 2.23$$

β and S are measured from the stereographic projection as shown, q is measured directly from the electron micrograph in a direction perpendicular to the projected images of the slip bands, hence p, the slip band spacing can be calculated.

2.5. MECHANICAL TESTING

An Instron Mechanical Testing Machine was used for compressive and tensile tests of alloys BD3, BD6 and BD8. The specimens used were in the form of rods which were prepared by swageing the sheet material in a direction parallel to its rolling direction. Prior to solution treatment and ageing, the rod was cut into specimens with the dimensions:

i) 3.88mm. diameter, 10mm. long for compression,

ii) 3.88mm. diameter, 5cm. long for tension.

For all the tests, a load cell of 500kg was used with a cross head speed of 1mm. per minute. The recorded load-extension curves were replotted in terms of conventional stress and per centage reduction or elongation.

2.5a Compression Tests

For each alloy, a range of reductions were carried out at room temperature, the maximum being 10%. Thin foils were prepared from sections cut perpendicularly to the compressive axes of the rod specimens. The deformation structures were examined as described in section 2.4c.

2.5b Tensile Tests

Specimens of each alloy were pulled to fracture at room temperature, 150°C and 185°C. Friction grips were used and the gauge length was 2cm.

The high temperature tests were carried out by immersing the straining rig into a bath of oil, previously heated to the required temperature. After immersion, there was a period of two minutes

before the oil bath reached temperature again, after which the test was started.

Thin foils were prepared from sections from the fractured test pieces. These were cut perpendicular to the tensile axis and close to the fracture surface. In BD6 and BD8, the zone of high plastic deformation extends several millimetres from the fracture surfaces, but in BD3 the plastic zone is concentrated in a very small region close to the fracture path. Thus in BD3 only thin foils prepared from sections in this area are likely to show a deformation structure especially as the total elongation is only ~ 1%.

It should be noted that the high temperature test pieces underwent some annealing. This was inherent in the method of testing; there was usually a time lapse of two minutes between removal of the testing rig from the hot oil and the quenching of the specimen halves.

The fractured tensile specimens were also examined optically using longitudinal sections.

2.5c Notch Bend Testing

Notched specimens were cut from the cold rolled sheet and their dimensions are shown in Fig.2.7a. These were fully heat treated, polished and etched in the normal way before deformation in a three point bending jig seen in Fig. 2.7b. This jig was rigidly mounted on the specimen platform of a Reichart microscope which enabled the deformation processes to be examined optically in situ.

Small increments of strain were introduced into the specimen by

an applied load at point X (see Fig. 2.7b). The notch area of the specimen was examined after each strain increment and once a crack had been nucleated its path was followed across the specimen.

Fig.2.1

Composition of the three alloys (H.30 type) selected for the research.

(BD3 - manganese free; BD6 and BD8 - manganese bearing).

Fig.2.1

ALLOY COMPOSITION IN WT%

(Determined by Spectrographic Analysis).

ALLOY	Mg	Si	Fe	Mn	TRUE EXCESS Si *
BD3	0.58	1.02	<0.01	0.001	0.68
BD6	0.58	0.99	<0.01	0.21	0.61
BD8	0.57	0.95	<0.01	0.50	0.52

* Assuming only Mg_2Si and $\alpha(Al_{12}Mn_3Si)$

Fig.2.2

Slip Band Spacing - Condition 1

Where slip bands are visible when the foil is not tilted; the foil normal (F.N.) is parallel to the direction of the electron beam

The slip band spacing, ρ, is given by

$$AB = AC \sin \theta$$

or

$$\rho = q \sin \theta$$

where θ is the angle between the slip plane normal, <111>, and F.N.

FIG. 2.2

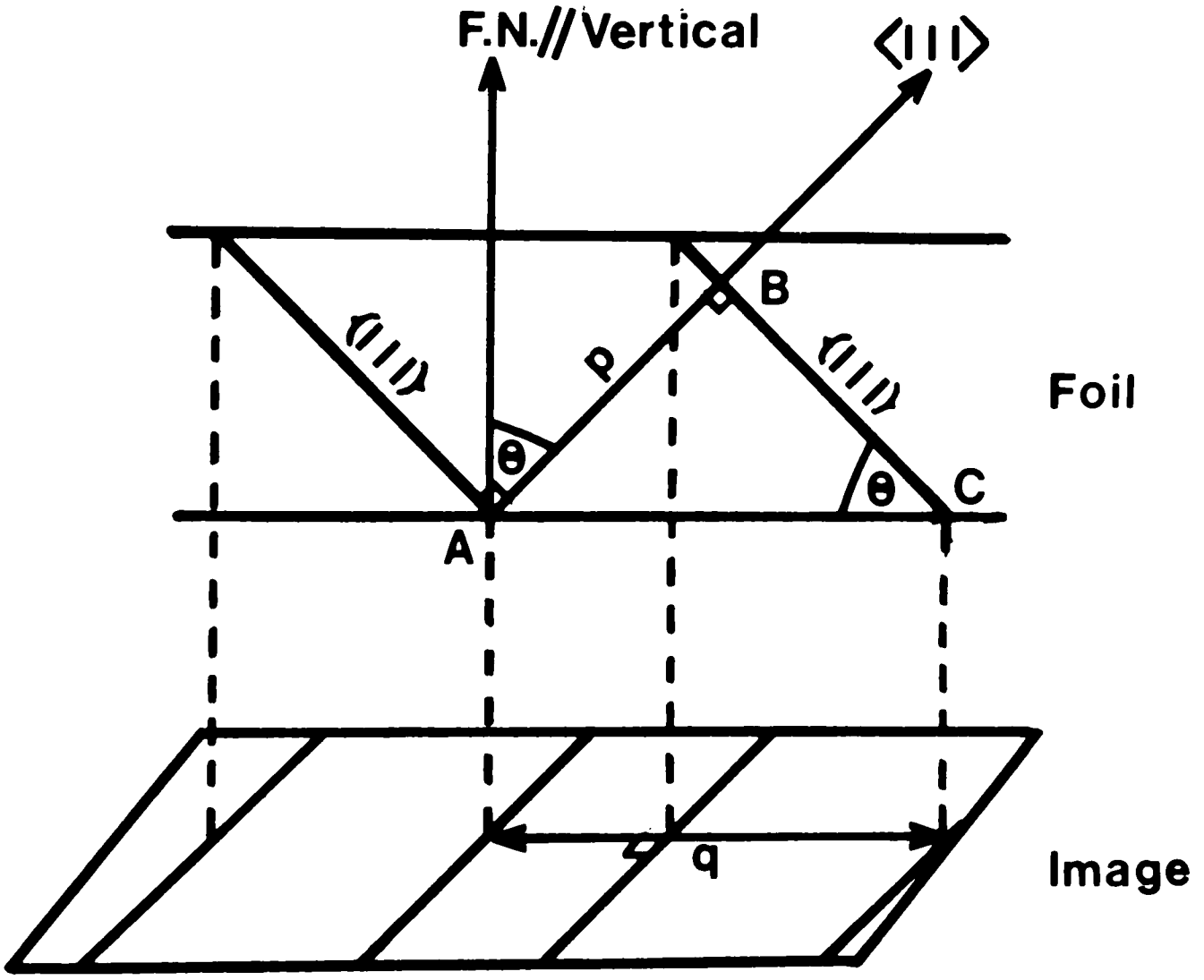

Fig.2.3

Slip band spacing - Condition 2, where slip bands are visible after tilting about <u>one axis only</u> and the <u>tilt axis is parallel to the slip band trace</u>.

i) The vertical is parallel to the electron beam direction,

ii) The angle between the vertical and the foil normal (F.N.) is the true angle of tilt, ψ, about the tilt axis; β is the angle between <111> and the vertical,

iii) Measurements made in the plane perpendicular to the tilt axis.

Slip band spacing:

$$AB = AC \sin\theta$$

$$AC = \frac{DC}{\cos\psi} = \frac{q}{\cos\psi}$$

$$AB = \rho = q\,\frac{\sin\theta}{\cos\psi}$$

FIG. 2.3

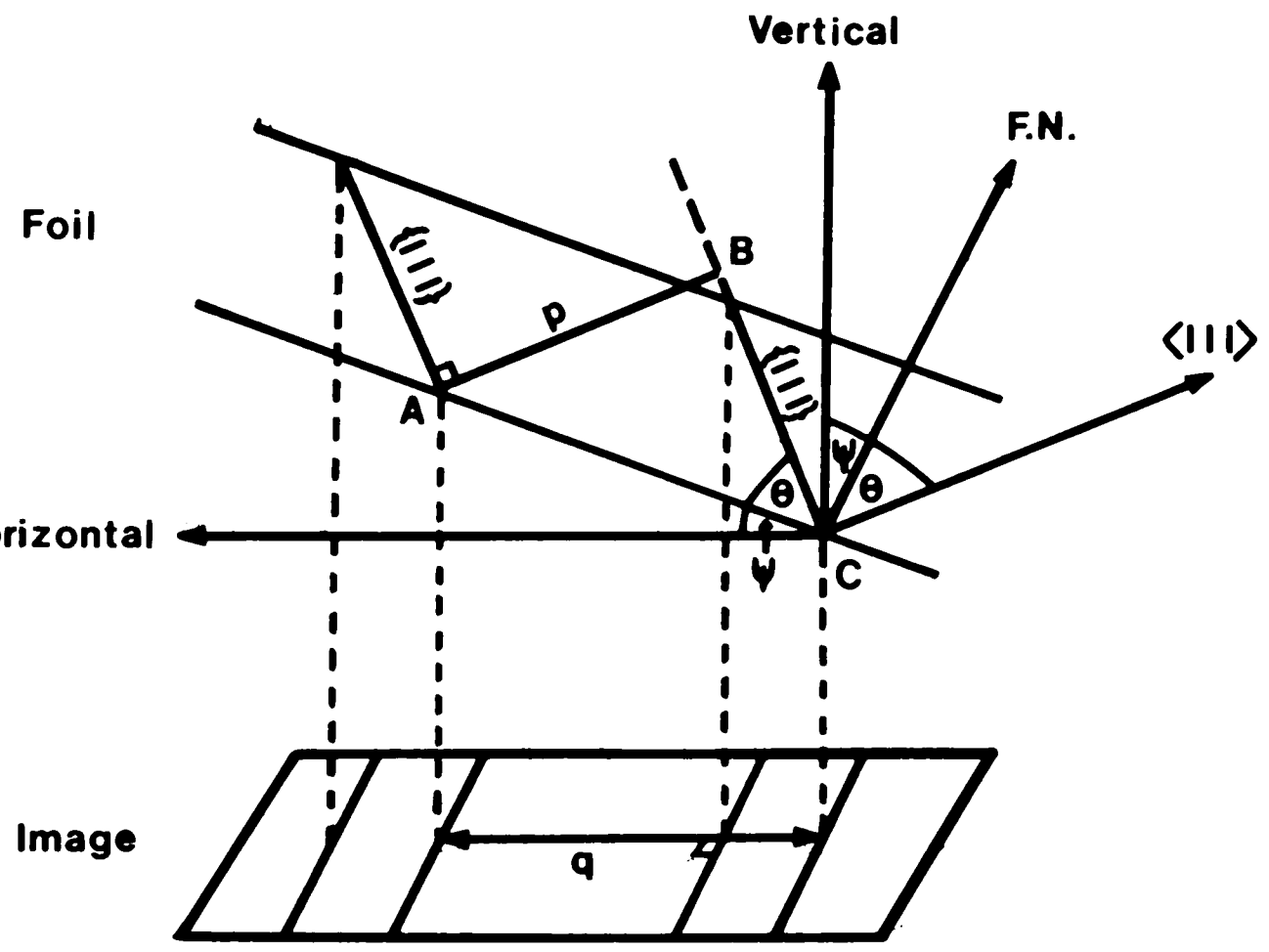

Fig.2.4

Slip Band Spacing - Condition 3, (the more general case of condition 2). The foil has been tilted about one or two axes and the foil normal (F.N.), the vertical (// electron beam) and <111> have the following orientation relationships

i) F.N. and <111> lie on the same side of the slip trace (see Fig.2.4a).

ii) The angle vertical, <111>, F.N. < 90°.

iii) The angle of tilt is ψ = F.N. ^ vertical; β is the angle between vertical and 111 .

Slip band spacing determined from the vertical sectional plane which lies at right angles to the slip band traces; the foil normal does not lie in this vertical plane.

Slip band spacing, AB:

$$AB = AC \, Sin \, (\beta - s)$$

$$AC = \frac{DC}{CosS}$$

$$AB = \rho = q \, \frac{Sin \, (\beta - s)}{CosS}$$

FIG. 2.4

(a)

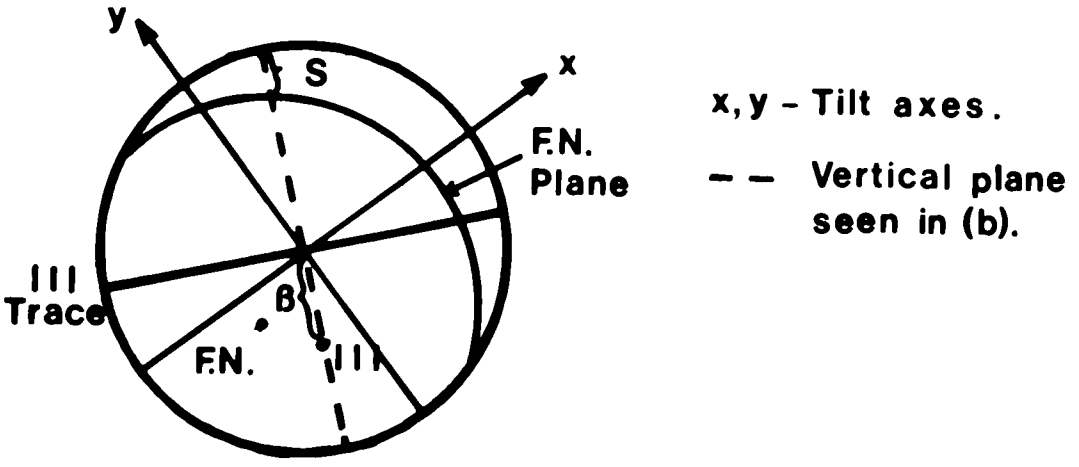
y
x
S
F.N.
Plane
III
Trace
β
F.N.
III
x, y - Tilt axes.
– – Vertical plane
seen in (b).

(b)

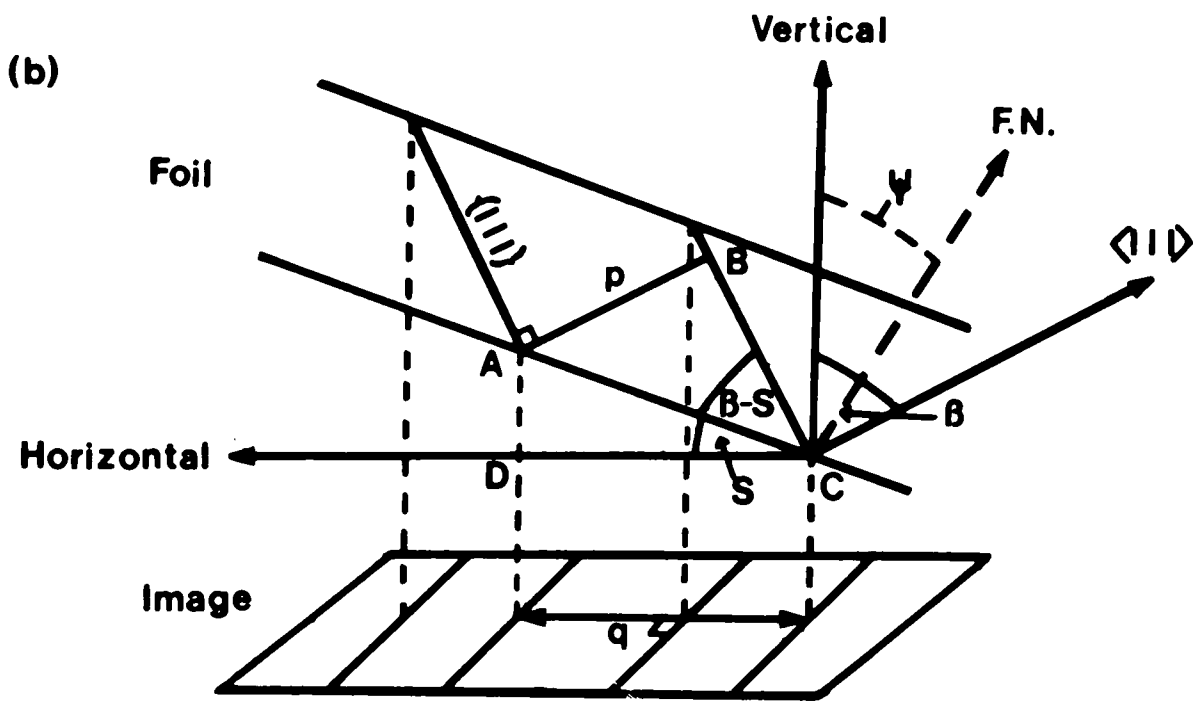
Vertical
F.N.
Foil
p
B
A
B-S
β
Horizontal
D
S
C
Image
q

Fig.2.5

Slip band spacing - Condition 4
(Another general case of condition 2). The foil has been tilted about one or two axes and the foil normal (F.N.), the vertical (// electron beam) and <111> have the following orientation relationships.

i) F.N. and <111> lie on opposite sides of the slip band trace (see Fig.2.5a).

ii) The angle <111>, vertical, F.N. > 90°.

iii) The angle of tilt is ψ = F.N. $\hat{}$ vertical.

Slip band spacing determined from the vertical sectional plane which lies at right angles to the slip band traces; F.N. does not lie in this vertical plane.

Slip band spacing, AB:

$$AB = AC \ Sin \ (\beta+s)$$

$$AC = \frac{DC}{Cos \ S} = \frac{q}{Cos \ S}$$

$$AB = \rho = q \ \frac{Sin \ (\beta+s)}{CosS}$$

FIG. 2.5

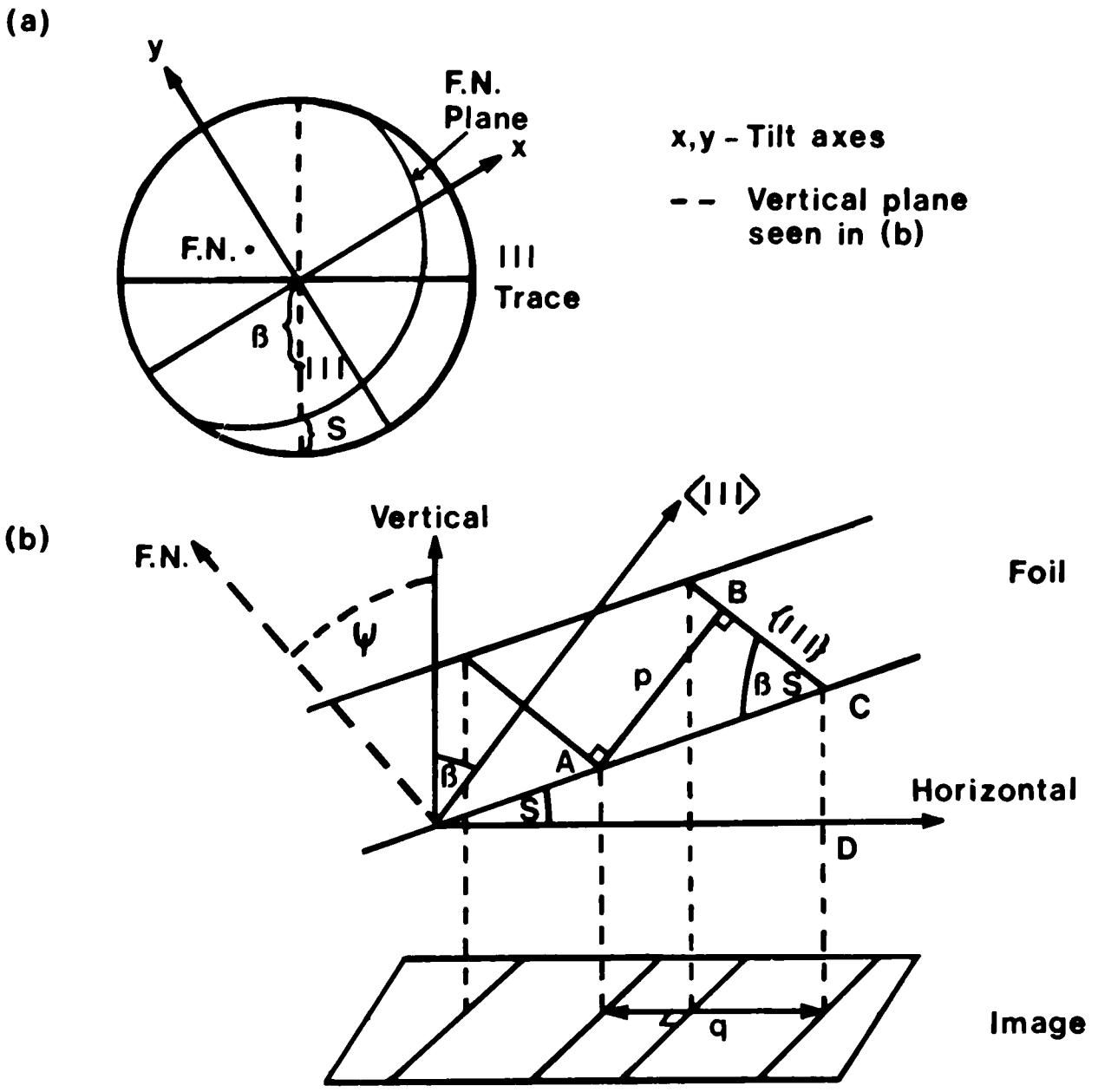
(a)
y
F.N.
Plane
x
F.N.
III
Trace
ß
111
S
x,y - Tilt axes
-- Vertical plane
seen in (b)
(b)
F.N.
Vertical
⟨111⟩
Foil
B
{111}
ψ
p
ß S
C
A
ß
Horizontal
S
D
q
Image

Fig.2.6

Slip band spacing - Condition 5
(An extreme case of Condition 3). The foil has been tilted about one or two axes and the foil normal (F.N.), the vertical (// electron beam) and <111> have the following orientation relationships

i) F.N. and <111> lie on the same side of the the slip trace.

ii) The angle Vertical, <111>, F.N. > 90°.

iii) The angle of tilt is ϕ = F.N.$^{\wedge}$ vertical.

Slip band spacing determined from the vertical sectional plane which lies at right angles to the slip band traces; F.N. does not lie in this vertical plane.

Slip band spacing, AB:

$$AB = AC \ Sin \ (S-\beta)$$

$$AC = \frac{AD}{CosS} = \frac{q}{CosS}$$

$$AB = \rho = q \frac{Sin \ (S-\beta)}{CosS}$$

FIG. 2.6

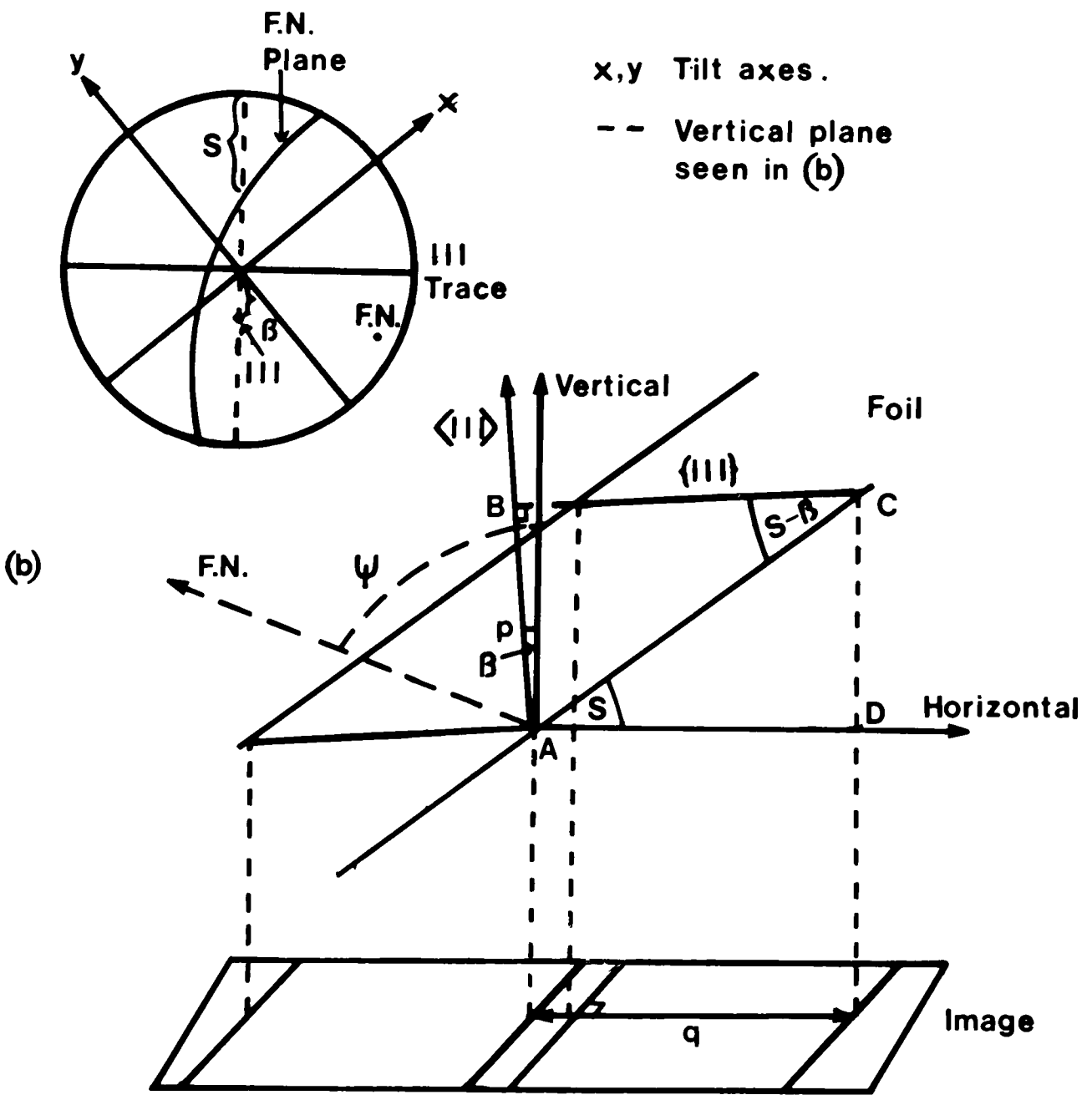
(a)
F.N.
Plane
y
x
S
III
Trace
F.N.
β
III
x,y Tilt axes.
– – Vertical plane
seen in (b)
(b)
Vertical
Foil
⟨11⟩
⟨111⟩
B
C
S-β
F.N.
ψ
p
β
S
D
Horizontal
A
q
Image

Fig.2.7

(a) Notch Bend Test Piece

(b) Plan of Bending Jig

FIG. 2.7

(a)

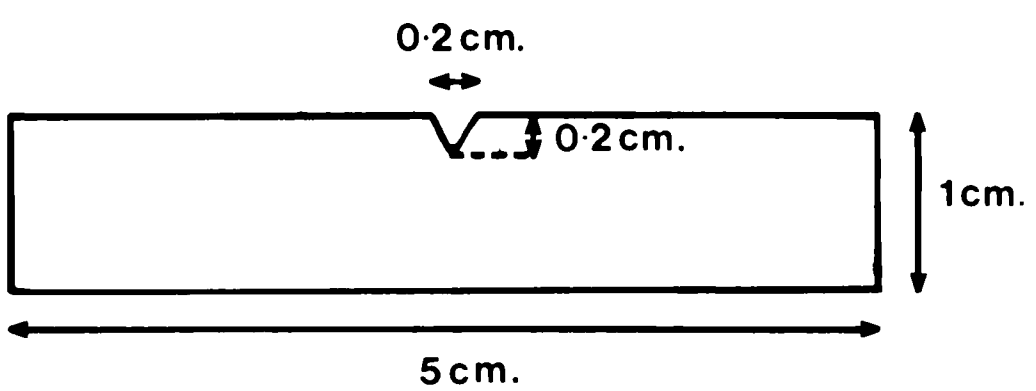
0·2 cm.
0·2 cm.
1 cm.
5 cm.

(b)

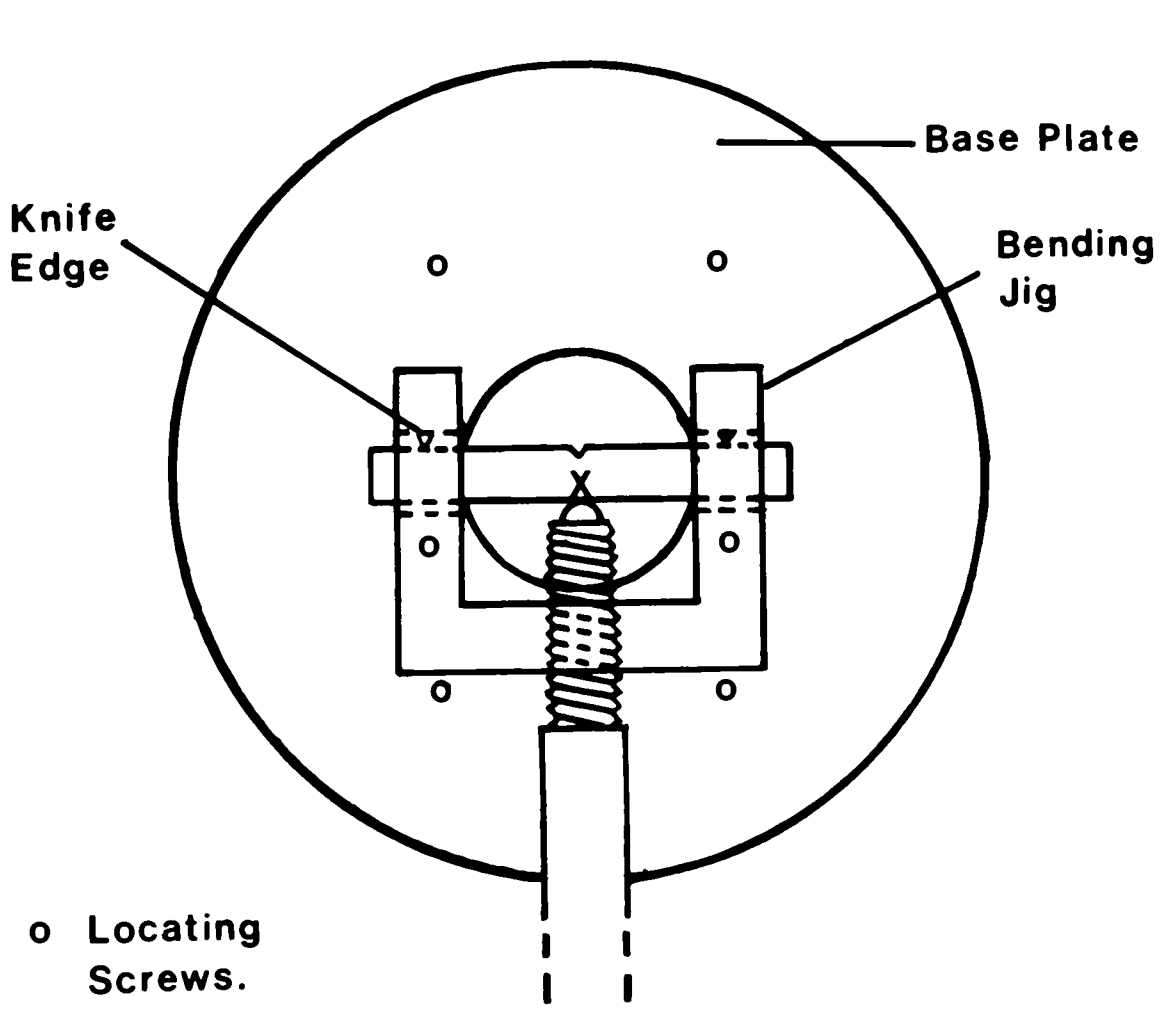
Base Plate
Knife Edge
Bending Jig
o Locating Screws.

CHAPTER 3

METALLOGRAPHY.

3.1. INTRODUCTION

In this chapter, the microstructures of the peak-aged alloys will be described. From this, questions concerning the precipitation of the ~ 0.1μm $\alpha(Al_{12}Mn_3Si)$ intermetallic particles in BD6 and BD8 will be discussed and an account given of the investigations which ensued. In the light of these observations, recrystallisation and grain growth is examined in the manganese-bearing alloys. The relevance of these experiments to the investigations of mechanical behaviour is explained and the microstructures of the three alloys are discussed.

3.2. AGE-HARDENING CURVES

The age-hardening curves of BD3, BD6 and BD8 at 185°C are shown in Figs.3.1, 3.2 and 3.3. Peak hardness for BD3 (135 V.P.N.) is reached after four hours which is nearly twice the times for BD6 and BD8 ($2\frac{1}{2}$ hours and 2 hours respectively) with maxima of 125 V.P.N. and 115 V.P.N. Comparison of the alloy compositions, Fig.2.1, shows that the excess silicon content is greatest in BD3 and lowest in BD8, assuming that all manganese is out of solution before ageing starts. However, the difference in excess silicon content is small and so it is difficult to account for the slower ageing kinetics of BD3 just in terms of the excess silicon. It is concluded that this compositional effect is not important in this context.

It might be suggested that manganese in solution may affect the ageing rate in the manganese alloys by enhanced vacancy diffusion. However, Chatterjee and Entwhistle, 1973, have shown that, when copper is added to an Al-Mg-Si alloy, the ageing kinetics are slower in the copper bearing alloy. Since manganese is also a transition element, one would expect it to behave in a similar way in solid solution.

3.3. MICROSTRUCTURE OF THE SOLUTION HEAT TREATED STATE

Optical examination of polished sections of BD6 and BD8, after solution treatment at 560°C, showed the presence of coarse particles between 1 and 5μm in size which are smaller and more widely spaced in BD6 than in BD8. These were arranged in 'strings' parallel to the rolling direction and were grey in colour. Since no such coarse particles were observed in manganese-free BD3, it was assumed that these were manganese-bearing particles, which were probably formed in casting. (Examination of the cast structure confirmed this.) By comparison with the etching characteristics of micro constituents listed by Smithells, 1967, and Mondolfo, 1943, the particles were identified as the α intermetallics. Polished sections of cold rolled BD6 and BD8 contained similar strings of particles, but with additional blue coloured precipitates which were found to be Mg_2Si. Plate 3.1 shows the microstructure of cold rolled BD8 after a light etch with Keller's reagent. The coarse particles are visible in the light band; the mottled region indicates the presence of fine scale α precipitation, see section 2.3. During the heat treatment at 560°C, the Mg_2Si precipitates dissolve and hence are absent in the solution heat treated material.

Electro-chemical etching of the solution treated material revealed the grain structures of the alloys. The grain boundaries were only lightly etched, due to the absence of any grain boundary precipitates, and are more clearly seen in the peak aged alloys, Plates 3,4, 3.5 and 3.6, where ageing has produced grain boundary precipitates.

T.E.M. of thin foils of solution heat treated BD3 showed that there were no Mg_2Si precipitates in the grain boundaries or within the grains. BD6 and BD8 were also free of Mg_2Si precipitates, but the α

($Al_{12}Mn_3Si$), incoherent, intermetallic particles, were present, Plates 3.2 and 3.3. These were rod shaped with a diameter of 0.1μm and had a random orientation and distribution, which results from the rolling procedures used in processing the alloys. The density of the α phase particles is low in BD6 (0.20 wt.%Mn); BD8, containing 0.50 wt.%Mn, has a higher density.

3.4. METALLOGRAPHY AFTER AGEING AT 185°C

The optical metallography of the peak aged alloys is similar to that of the solution heat treated material. There is no grain growth during ageing, but the grain boundaries are more sharply etched.

Plate 3.4 shows the large, equiaxed grain structure of BD3, the manganese-free alloy. In comparison, the grain size of BD6 and BD8 is very small and the grain shape quite irregular, Plates 3.5 and 3.6. The rolling direction of the sheet is indicated on the two micrographs and the strings of coarse particles can be seen to lie parallel to this direction. In the vicinity of these particles in BD6 and BD8, the grains are very small; those lying between the strings are large and tend to be elongated in the rolling direction. For BD3, the grain diameter is of the order of 400μm while for BD6 and BD8, the values are only 100μm and 70μm respectively. This small grain size is a direct consequence of adding manganese to the alloys and is done deliberately in industrial practice (Dunwoody et al, 1973).

In general, recrystallisation is inhibited by the presence of small, closely spaced, immobile particles which exert a retarding force on the grain boundaries. There are numerous reports on this and are adequately reviewed by Higgins, 1974 and Köster, 1974. Examination of BD6 and BD8 has shown that the 0.1μm intermetallics are present in the

solution heat treated material after 30 minutes at 560°C. Therefore these must prevent extensive grain growth. Using Zener's equation (Gleiter and Chalmers, 1972) for the retarding force, P_r, exerted on a grain boundary, of energy σ_b, by spheres with a radius r and volume fraction F_V.

$$P_r = \frac{3 F_V \sigma_b}{2r} \qquad 3.1$$

it is seen that for a small, constant value of r, the degree of retardation depends on the volume fraction, F_V. Now as Plates 3.2 and 3.3 show, BD6 contains fewer 0.1μm particles than BD8 and, as expected, has a larger grain size than BD8 because of the smaller retarding force, P_r. Scharf and Gruhl, 1969, examining the effect of precipitation in Al-Mg-Mn-Si alloys on recrystallisation have obtained similar results.

3.4a Electron Microscopy

After ageing to peak hardness, a fine precipitate of Mg_2Si was seen within the grains of all three alloys. Plate 3.7 is a typical area from a thin foil of BD8; the ageing precipitate, even at this low magnification, is clearly much finer than the intermetallic particles and no denudation adjacent to the particles is apparent. At higher magnifications, Plate 3.8, the ageing precipitate can be distinguished as fine needles which lie along a preferred crystallographic direction. Thomas, 1966, has, from streaks on diffraction patterns, identified this direction as <100>. This method was used to confirm the Mg_2Si orientation in the present work, since the α ($Al_{12}Mn_3Si$) particles had a characteristic diffraction pattern. In agreement with Thomas, the Mg_2Si needles were found to lie along <100> with a length of approximately 0.01μm.

Ageing also produced precipitates (assumed to be Mg_2Si) in the grain boundaries and a precipitate free zone (P.F.Z.). The width of the P.F.Z. was similar in all three alloys - ~ 0.1μm (1000Å). This small value is typical of an alloy which has been rapidly quenched from solution temperature prior to ageing. Plate 3.9 shows such a P.F.Z. in aged BD8, where the zone width is 0.125μm (1250Å). The grain boundary precipitates are only visible here by fringe displacement effects as the boundary is nearly vertical to the plane of the micrograph. The size and distribution is best seen when the boundary plane is visible, Plate 3.10. The precipitates are small rods or lathes 0.05μm in size and about 0.15μm apart. BD6 has a similar distribution of grain boundary precipitates.

In contrast, the grain boundary precipitates in BD3 are coarser and more widely spaced, Plates 3.11 and 3.12. The first plate is of a section of grain boundary containing coarse precipitates. Here the grains are out of contrast, but the Mg_2Si precipitates can be seen growing into the grains. Plate 3.12 is more typical of the manganese-free alloy; both coarse and fine precipitates lie in the boundary. The fine precipitates have a diameter of 0.05μm and the larger ones, 0.10μm with a spacing of ~ 0.50μm. The coarse precipitates are probably the result of the longer ageing of 4 hours used for BD3. BD6 and BD8 are aged for half this time, so that the precipitates will be expected to be more finely distributed.

The appearance of the intermetallic particles in the manganese-bearing alloys was not affected by ageing. There was no evidence that the Mg_2Si nucleated preferentially on these incoherent particles and the size and distribution of the latter were the same as for the solution heat treated material. The data from the particle analysis

for BD6 and BD8 are given in Fig.3.4 and the results are the average of several determinations in each case. As is expected from its higher manganese content, BD8 has a higher volume fraction F_V, 1.1 x 10^{-2}, than BD6, only 0.4 x 10^{-2}.

It should be noted that the values for F_V cannot be found very accurately for rods of random orientation with a non-uniform size, as the calculation always involves ℓ, the length of the particles, (Fullman, 1953). This is illustrated by consideration of a typical frequency histogram of particle diameter, Fig.3.5, which has a Gaussian distribution. From this the mean diameter is ~0.125μm. Using equations 2.4 and 2.5, viz.

$$\bar{\ell}_p = \frac{\pi\bar{\ell}}{4}$$

$$\bar{\ell}_p = \frac{1}{n}\sum_{i=1}^{n} \bar{\ell}_{pi}$$

the length, $\bar{\ell}$, of the particles is 0.327μm for this diameter range. The total particle count is 171 and, if the mean values for length and diameter are used, the total particle volume is ~ 5.8 x 10^{-19} m^3. When individual calculations are made for each diameter range with the appropriate value of $\bar{\ell}$, the total particle volume is nearer 8.0 x $10^{-19} m^3$ which gives a discrepancy of 30%. But even this second calculation is inaccurate because the lengths determined for the larger diameters are not statistically valid when the numbers involved are small. If the density of the intermetallic phase,α ($Al_{12}Mn_3Si$) and the number of atoms per unit cell were known, an estimate of F_V (allowing for the coarse 5μm intermetallic particles) could be made, assuming no manganese in solution. So far, no such information has been found.

Similar accuracy considerations apply to λ, the volumetric mean

free path, but not to Δ_3, the nearest neighbour distance, which is dependent only on the density of particles, N_V. Consideration of the values of λ and Δ_3 shows that the mean free path is larger than the nearest neighbour distance in both alloys: λ is 27.7 μm and 8.9 μm, Δ_3 0.5 μm and 0.3 μm in BD6 and BD8 respectively. This is true for any particle distribution as shown by Corti et al., 1972, and arises from the fact that the mean free path is the average distance between a particle and all its neighbours, whereas the nearest neighbour distance is the average centre to centre distance between any particle and its closest neighbour.

In the following discussions on recrystallization and dispersion hardening mechanisms, Δ_3 is used being the more suitable parameter according to the review of the above authors. The mean free path, λ, is not to be ignored because, in conjunction with Δ_3, it gives a more complete description of the intermetallic particle distribution in the alloys.

3.5. PRELIMINARY DISCUSSION OF THE MICROSTRUCTURES

At this stage it is profitable to summarize the information of the previous sections and to discuss its implications.

i Alloy BD3

This manganese free alloy has a large, equiaxed grain structure with a grain size of 400μm. The microstructure of the peak aged material contains grain boundary precipitates of Mg_2Si, fine needles of Mg_2Si (0.01μm) within the grains and a narrow P.F.Z. at the grain boundaries.

ii Alloys BD6 and BD8

These contain additions of manganese. There are coarse inter-

metallic particles visible in the cold rolled material which are not removed by solution heat treatment or ageing. The grain structures are not uniform; the grains are smaller adjacent to the coarse particles, larger elsewhere, and all tend to be elongated parallel to the rolling direction. The average grain size is smaller than that of BD3, being only ~ 100μm. In addition to the Mg_2Si precipitates within the grains, the peak aged material contains 0.1μm, incoherent, $\alpha(Al_{12}Mn_3Si)$ particles which are rod shaped. (These are also present in the solution heat treated material). Their volume fraction is 1.1 x 10^{-2} in BD8 and 0.4 x 10^{-2} in BD6. There are P.F.Z. near the grain boundaries and there are grain boundary, Mg_2Si precipitates, which are smaller than those in BD3.

From the above, several questions arise concerning the intermetallic precipitates of $\alpha(Al_{12}Mn_3Si)$. Firstly, at what stage in the processing of the alloy do they start to form? The coarse ones (5μm) are visible in the cold rolled material and the relatively fine, 0.1μm, ones exist in the solution heat treated state. Precipitation could occur during casting or homogenization at 530°C or hot rolling at 530°C or, for the fine particles, during solution heat treatment at 560°C. Consultation of the only existing phase diagram for this system, Plate 3.13, suggests that precipitation of $\alpha(Al_{12}Mn_3Si)$ can occur at 460°C (Phillips, 1961 and Van Horn, 1967). It is therefore probable that the intermetallics are produced before solution treatment.

Secondly, if precipitation occurs during heat treatment at 530°C, what are the growth kinetics? As already shown, such particles of this 0.1μm size range are very good inhibitors of grain growth. In addition to this, Scharf and Gruhl, 1969, have shown that manganese intermetallics are just as effective in this respect even if they precipitate during

the recrystallization anneal. If there is a temperature range where particle precipitation is slow, say 30 minutes, then it might be possible by appropriate mechanical-thermal treatment to achieve a larger and more equiaxed grain size in BD6 and BD8 before precipitation starts. In this way, it would be possible to compare the mechanical properties of the brittle, manganese-free alloy, BD3, with these ductile alloys without the complication of different grain sizes, which might contribute to the differences in fracture behaviour. Of course, this assumes that altering the precipitation temperature does not change the α-phase distributions in BD6 and BD8. If the α-phase distribution is altered, this alone may cause the previously ductile alloys to become brittle, thus masking the grain size effect.

The ideal situation would be to produce BD8 and BD6 with a grain size comparable with BD3, without changing α-phase distribution. If with this new microstructure BD6 and BD8 were still highly ductile, this would prove that the grain size does not determine the ductility of the alloys. From there, the effect of particle distribution on ductility could be investigated, since there may be a critical distribution for high ductility.

Before any attempts to change the grain size and particle distribution could be made, the precipitation kinetics of $\alpha(Al_{12}Mn_3Si)$ had to be investigated, since there was little if no information on the subject in the literature.

3.6. PRECIPITATION STUDIES OF $(Al_{12}Mn_3Si)$.

To study the precipitation kinetics of the manganese-bearing alloys, a chill cast ingot of BD8 was subjected to heat treatments at different temperatures for various times.

An ingot of BD8 was provided by Alcan International Limited. Because of the large size of the casting, there was some doubt about the rapidity of the chill away from the edges. If the central portion had not received a rapid chill, some precipitation of the fine scale α-intermetallics might have taken place in these areas. Since it was not known whether the particles were produced during casting or during homogenization at 530°C or hot rolling, it was important that the entire casting should be rapidly chilled to prevent such slow cooling effects.

Initially, the structure of the Alcan casting was compared with that of a small ingot which was prepared by the author in the research laboratory. This was produced by melting a sample of BD8 and rapidly chilling the melt in a thick walled copper finger mould (internal diameter 1.5cm). The metallography of both ingots was examined using optical and electron microscopy and re-examined after homogenization at 530°C to detect any segregation differences.

Polished sections of the castings contained long precipitates which lay predominantly along the grain boundaries. Some spherical particles were observed within the grains, Plate 3.14. The latter particles were blue in colour, while the precipitates in the boundary were predominantly blue with some grey particles in between. Using the constituent etches mentioned in section 3.3, the grey particles were identified as the α-intermetallics and the blue ones as particles of Mg_2Si. The grain size of the casting was estimated to be between 50 and 100μm.

Prolonged etching with Keller's reagent revealed a dendritic structure within the grains, Plate 3.15. Examination at high magnific-

ation showed that this was only visible in relief; there were no precipitates within or between the dendrite arms except for the coarse round particles of Mg_2Si seen in the unetched section.

T.E.M. of thin foils confirmed that the matrix in both castings was precipitate free, except for the coarse residual casting precipitates in the grain boundaries. Plate 3.16 shows an example of these. The spherical particles within the grains were also seen in some of the foils.

Homogenization of the castings at 530°C revealed more clearly the dendritic structure observed in the castings. Plate 3.17 shows that the dendritic microstructure is full of regions of fine scale precipitation with light areas in between containing relatively coarse needle-shaped precipitates with some preferred orientation. The grain boundaries lie within the narrow light bands bounded by a fine continuous line of darkened precipitates. Within these bands can be seen some coarse particles, but these are less numerous than in the casting. The large spherical particles within the grains are also absent and this would imply that a certain amount of Mg_2Si has gone back into solution during homogenization. From the phase diagram of solid-solubility for Al-Mg-Si, Plate 3.18, it can be seen that the homogenization temperature, 530°C, is just below the solvus, 540°C, for Mg_2Si in BD8, which contains 0.57 wt.%Mg and 0.95 wt.%Si. Thus during soaking for 16 hours at 530°C, most of the precipitates of Mg_2Si, formed in casting, will dissolve to restore phase equilibria. This would imply that the observed staining in the dendritic structure is predominantly due to the formation of the manganese intermetallics. Indeed, rod-shaped precipitates were observed in thin foils of BD8, Plate 3.19. Again, the particles seem to have no preferred orientation,

though a few are seen to lie parallel to each other, but in fact these may be Mg_2Si precipitates. An attempt was made to obtain diffraction patterns from the particles in order to identify them. As can be seen, however, most of them are highly opaque to the electron beam and this, together with their size, makes a structural analysis almost impossible.

As a check on the random orientation of the α-intermetallics, homogenized material was solution heat treated at $560^{o}C$ to remove the Mg_2Si precipitates. As before, the thin foils contained rod-shaped particles of random orientation, and as in the homogenized material, the precipitation occurred in patches, Plate 3.20. Optically, the microstructure was no different from the homogenized material. After etching, the dendritic structure was still visible and in between the mottled areas there were still the aligned, needle-shaped particles, Plate 3.21.

From this it is concluded that the α-intermetallics are produced during homogenization at $530^{o}C$. The distribution is not uniform and occurs in areas where there is segregation of manganese in solid solution. The coarse needles, seen in the optical micrographs,are also of the intermetallic phase and their size is probably a reflection of the lower supersaturation of manganese in these areas.

The next step was to determine how quickly the intermetallic particles precipitated out at $530^{o}C$. Samples of the casting were heated for various times ranging from 1 minute to 5 minutes and thin foils were examined from each sample.

Plate 3.22 shows BD8 after 1 minute at $530^{o}C$. In the right hand corner of the micrograph, there are a few small precipitates. After

3 minutes, precipitation is well established in the alloy, Plates 3.23 and 3.24. These two micrographs show clearly the different particle densities which were observed within a single grain and which results from the inter dendritic segregation apparent in the optical micrographs. The large black shapes seen in these electron micrographs are the remains of the residual casting precipitates.

Plates 3.25 and 3.26 are electron micrographs of BD8 after 5 minutes at 530°C; already there are signs of particle coarsening, the particle diameter being 0.05μm. After 30 minutes at 530°C, Plate 3.27, the particle diameter is already 0.09μm.

Since the particles nucleated and grew rapidly at 530°C, similar investigations were carried out at temperatures near 580°C and 450°C. At 580°C, the alloy is well within the region of solid solubility for Mg_2Si, so that, if there is precipitation at this temperature, the precipitating phase will be $(Al_{12}Mn_3Si)$. The precipitation system at 450°C will be more complex, because both Mg_2Si and the intermetallic phase can be precipitated. This was in fact the case as Plate 3.28 shows. The alloy has been held at 447°C for 30 minutes and clearly two types of particles have been precipitated. There are long, fine needles which lie parallel to three directions within the foil and many have a surrounding, strain contrast fringe. The other precipitates are on the whole rod-shaped, though some appear truncated probably due to surface effects. When such a specimen is heat treated at 560°C for 30 minutes, the long fine needles are absent and only the rod precipitate remains, Plate 3.29. This implies that the needles are the Mg_2Si phase. These will nucleate and grow quickly at 447°C which is ~ 100°C below the solvus temperature for Mg_2Si with excess Si in BD8. At 560°C, the Mg_2Si

will dissolve leaving only the rod precipitates, which are α ($Al_{12}Mn_3Si$). The diameter of the latter is 0.04μm after 30 minutes at 447°C and after 2 hours at this temperature, the diameter is 0.07μm.

Finally, the effect of a higher temperature heat treatment was investigated to see if precipitation of α $Al_{12}Mn_3Si$ was suppressed. After 10 minutes at 581°C, precipitation of the intermetallic phase was well established, Plate 3.30, and the particle size already 0.1 μm in diameter.

All the above data are summarized in Fig.3.6, which shows the particle diameters attained after the different heat treatments of cast BD8. Inspection of the 530°C diameters suggests that the particles have an asymptotic growth curve, because there is very little change in size beyond 30 minutes at this temperature. These results are expressed on a log-log plot in Fig.3.7 together with the data from 447°C isotherm.

Ignoring the 960 minute point, there is a linear relationship between log particle diameter and log time for short precipitation times at 530°C. The slope of the graph is approximately $\frac{1}{3}$. A line of similar slope can be drawn through the points at 447°C. The particle growth thus seems to be a process of Ostwald ripening, which implies that precipitation is complete at an early stage and the changes in microstructure observed are taking place at constant volume fraction and are driven by a reduction in interfacial energy. However, there are other processes taking place while the α phase is growing, i.e. residual casting precipitates are going into solution and at temperatures below 540°C, growth of Mg_2Si precipitates Both of these processes will affect the growth kinetics of the phase.

If a slope of $\frac{1}{3}$ is assumed for log d/log t at all temperatures, particle growth graphs can be drawn in for the higher temperatures of 560°C and 581°C. By extrapolation, the times to achieve a diameter of 0.05μm at the latter can be plotted on the graph in Fig.3.6 and also the times to reach 0.10μm at 447°C and 530°C. Isometric lines for particle diameters of 0.05μm and 0.10μm can then be sketched in.

From this set of data and the metallographic observations, a number of conclusions can be drawn about the precipitation systems in the manganese-bearing alloys.

First, there is manganese segregation in the cast material and after heat treatment the α phase is precipitated in these areas, while adjacent regions are particle free. Consequently the particle densities observed in the micrographs appear higher than the density in the commercially processed alloy, where rolling has produced a more uniform distribution.

Secondly, $\alpha(Al_{12}Mn_3Si)$ is precipitated over a wide range of temperatures.

Thirdly, at temperatures above the Mg_2Si solvus, nucleation and growth of the α particles is rapid so that a particle diameter of 0.05μm is reached within a time between 1 and 4 minutes.

Finally, below the Mg_2Si solvus temperature, there is precipitation of Mg_2Si in addition to the α intermetallics. The former will grow very rapidly at temperatures near the solvus where the diffusion rate is high. Consequently, though it takes a longer time at these temperatures to produce coarse particles of α-phase, the Mg_2Si precipitates will coarsen in a very short time, probably only

a few minutes.

It is apparent from these four points that it will be difficult by controlled recrystallization to produce a large grain size in BD6 or BD8. No matter what recrystallization temperature is selected, there will always be rapid precipitation of coarse particles of one phase or the other, which is likely to inhibit recrystallization as previously mentioned.

Since changing the recrystallization annealing temperature is probably insufficient to increase the grain size of BD8, other methods must be devised to produce the desired grain diameter while retaining the original particle distribution seen in the commercially processed material. Several methods were devised and investigated and in the next section these are described and explained in relation to the above precipitation kinetics.

3.7. RECRYSTALLIZATION AND GRAIN GROWTH EXPERIMENTS

When the as-provided alloys are normally heat treated, the manganese-free alloy, BD3, has large equiaxed grains which are nearly four times the size of those in BD6 and BD8. Preliminary work showed that the grain size of BD3 could not be significantly reduced, since it is determined by the solution heat treatment, so that the recrystallization experiments concentrated on attempting to change the elongated grain structure of BD8 to an equiaxed one.

3.7a Effect of Annealing Temperature on Grain Size

Chadwick et al, 1953/54, have shown in a cold rolled Al-0.74% Mg-0.6% Mn-1.06% Si alloy that the elongated structure can be removed by soaking at 600°C. They maintain that after 120 hours at 600°C, the

banded structure is removed and is apparently replaced by a large equiaxed grain structure. Subsequent ageing of the alloy at 160°C was found to render the material brittle. However, when Keller's etch is used on this microstructure, there is no staining and, as the author has observed already, this only occurs when the manganese is in solid solution. This would indicate that the prolonged soaking at 600°C produces a microstructure without any 0.1μm intermetallic particles. Nevertheless, this method was worth investigating.

Samples of cold rolled BD8 were held for 30 minutes at different temperatures between 560°C and 630°C and their grain size measured in each case. The grain boundaries in each specimen were closely examined for signs of grain boundary melting; this was first observed in specimens heat treated at 595°C. Below this temperature, there was very little change in the grain size, but above this temperature, the grain size increased sharply and had doubled after annealing at 614°C. Fig.3.8 gives a graphical account of this grain size variation with temperature.

This experiment was then repeated with a holding time of 3 hours to see if there was any further grain growth. The measured grain sizes were not appreciably different from the first results, but the grain boundary melting seemed more extensive. Chadwick's micrographs show signs of grain boundary melting which is apparently removed by long soaking, 120 hours at 600°C. A longer anneal was investigated. After 6 hours at 617°C and 631°C, though a large grain size, 350μm, was reached, the grain boundary melting was not improved. These results are also plotted in Fig.3.8.

In all cases where there was extensive grain boundary melting, the

microstructure, when etched with Keller's reagent, showed no signs of mottling and hence an absence of the 0.1μm particles. In view of the grain boundary melting, it was not considered fruitful to pursue this method further as a means of grain-size control.

3.7b Effect of Prior Strain on Recrystallized Grain Size

Prior to solution treatment, the H.30 alloys provided had been reduced by 75% in hot rolling and a further 70% in cold rolling. The amount of deformation in a material is one important factor which influences the ultimate grain size. In an attempt to explore this effect samples of the cast alloy BD8 were cold rolled between 10% and 90% and heat treated at 560°C for 30 minutes, quenched, and the grain sizes determined.

This technique was not successful in producing coarse grains. The grains, though equiaxed were only 50μm in diameter at low strains and at higher strains, the grains were too small to measure. Referring back to the precipitation studies, these results are easily explained since the 0.1μm intermetallic particles precipitate out quickly and so prevent extensive grain growth.

3.7c Effect of Heating Rate on Grain Size

From the precipitation studies, it is known that the 0.1μm particles start to precipitate after a few minutes at normal recrystallization temperatures. It was considered that if the cold worked ingot was slowly taken up to 560°C, the α intermetallics would come out as fine precipitates at low temperatures and would be less efficient at pinning the grain boundaries. At higher temperatures, the latter could then move relatively easily through the matrix and a larger grain size would result.

Cast BD8 was cold rolled by 60% and slowly heated in air up to 560°C. A heating rate of 26°C/hour was achieved using a Sirect Proportional Controller in conjunction with a worm drive and motor. Once at 560°C, the alloy was held at temperature for 30 minutes, quenched, and the grain size determined. Again there was little improvement in the grain diameter, the average grain size being only 75μm.

This can be explained in terms of the precipitation kinetics of the α intermetallic particles. At some low temperature, these will nucleate as fine precipitates and begin to grow slowly. As the temperature is raised, the larger particles will continue to grow, but small ones will tend to shrink and dissolve. Therefore during the slow heating up to 560°C, the α phase becomes coarser and reaches a size sufficient to prevent grain growth, before recrystallization can occur. Because of this, extensive grain growth is prevented.

3.8. SUMMARY OF PRECIPITATION AND RECRYSTALLIZATION KINETICS

From the previous metallographic observations, it is clear that the α intermetallic particles are very effective grain refiners, as they grow very rapidly at high temperatures and at lower temperatures, where their growth is delayed, rapid precipitation and growth of Mg_2Si occurs and is likely to be an equally efficient grain refiner.

An upper temperature limit for recrystallization and grain growth is imposed by the onset of melting in the alloy. There appears to be no region of solid solubility for $\alpha(Al_{12}Mn_3Si)$; the intermetallics are stable up to the solidus temperature of the alloy, which is around 595°C. Referring to the phase diagram of the solidus in Al-Mg-Si alloys, Plate 3.31, the melting point for an alloy containing 0.57wt%

Magnesium and 0.95wt% silicon (which are the proportions in BD8) is approximately 590°C. This implies that it is the magnesium and silicon content which is controlling the melting point of the alloy system. As the plot of grain size against annealing temperature, Fig.3.8 shows, there is extensive grain growth at temperatures above the solidus point and this indicates that the region of solid solubility for $\alpha(Al_{12}Mn_3Si)$ has been reached.

It is therefore concluded that, within the scope of the present research, it does not seem possible to alter the grain size of BD6 or BD8.

Fig.3.1

Age Hardening Curve of BD3 at $185^{o}C$.

FIG. 3.1

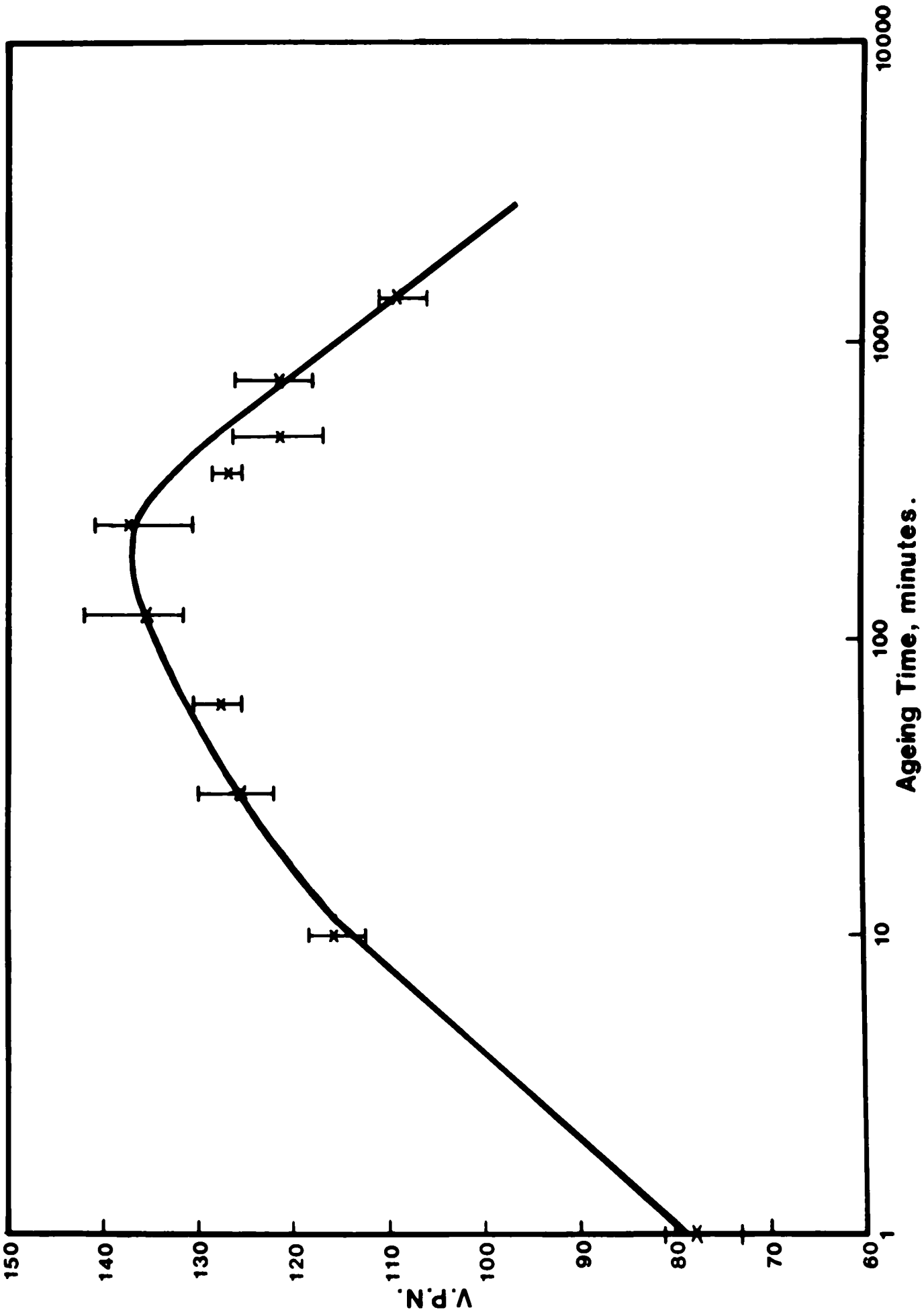
V.P.N.
150
140
130
120
110
100
90
80
70
60
1
10
100
1000
10000
Ageing Time, minutes.

Fig.3.2

Age Hardening Curve of BD6 at 185°C.

FIG. 3.2

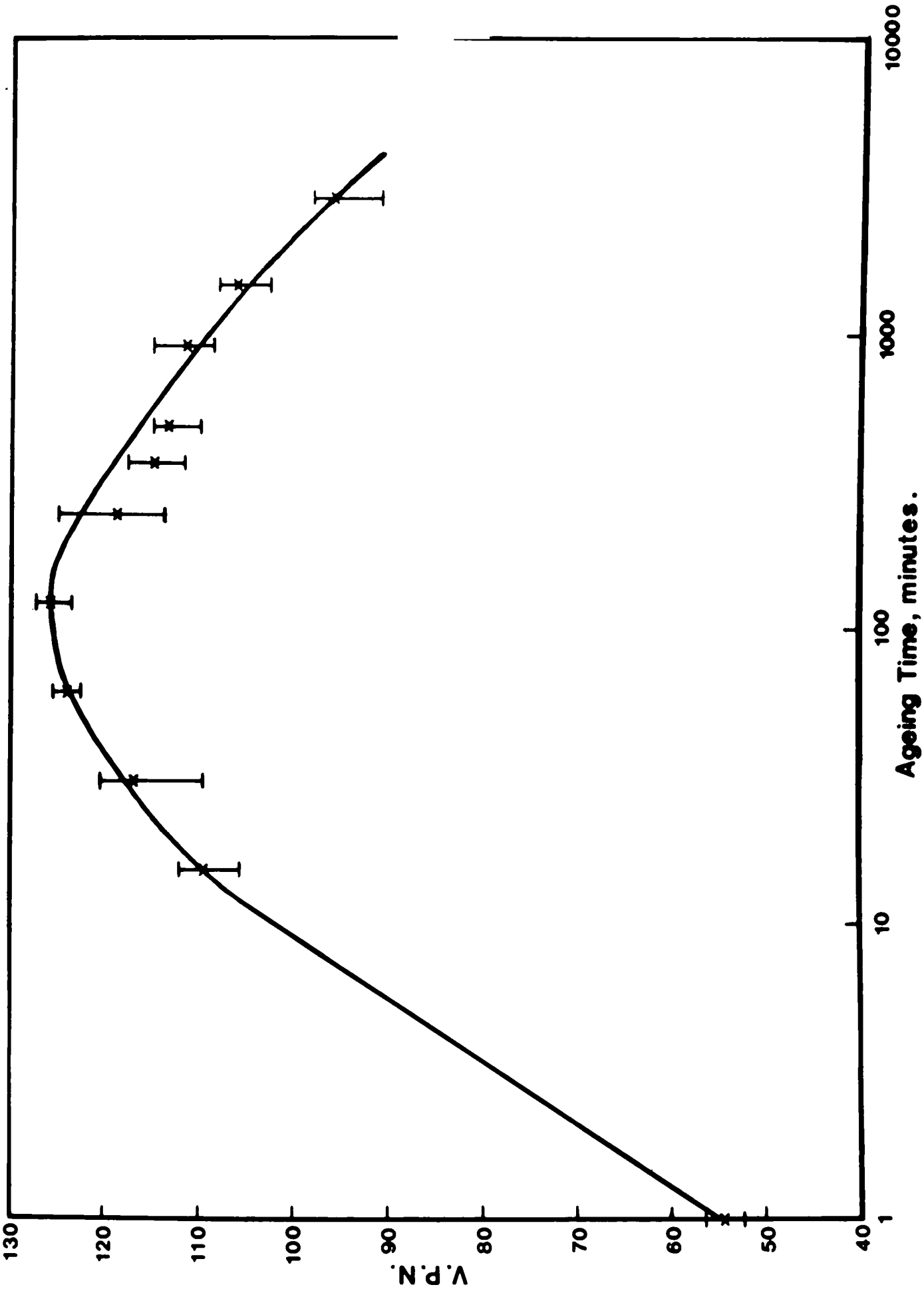
V.P.N.
130
120
110
100
90
80
70
60
50
40
1
10
100
1000
10000
Ageing Time, minutes.

Fig.3.3

Age Hardening Curve of BD8 at 185°C.

FIG. 3.3

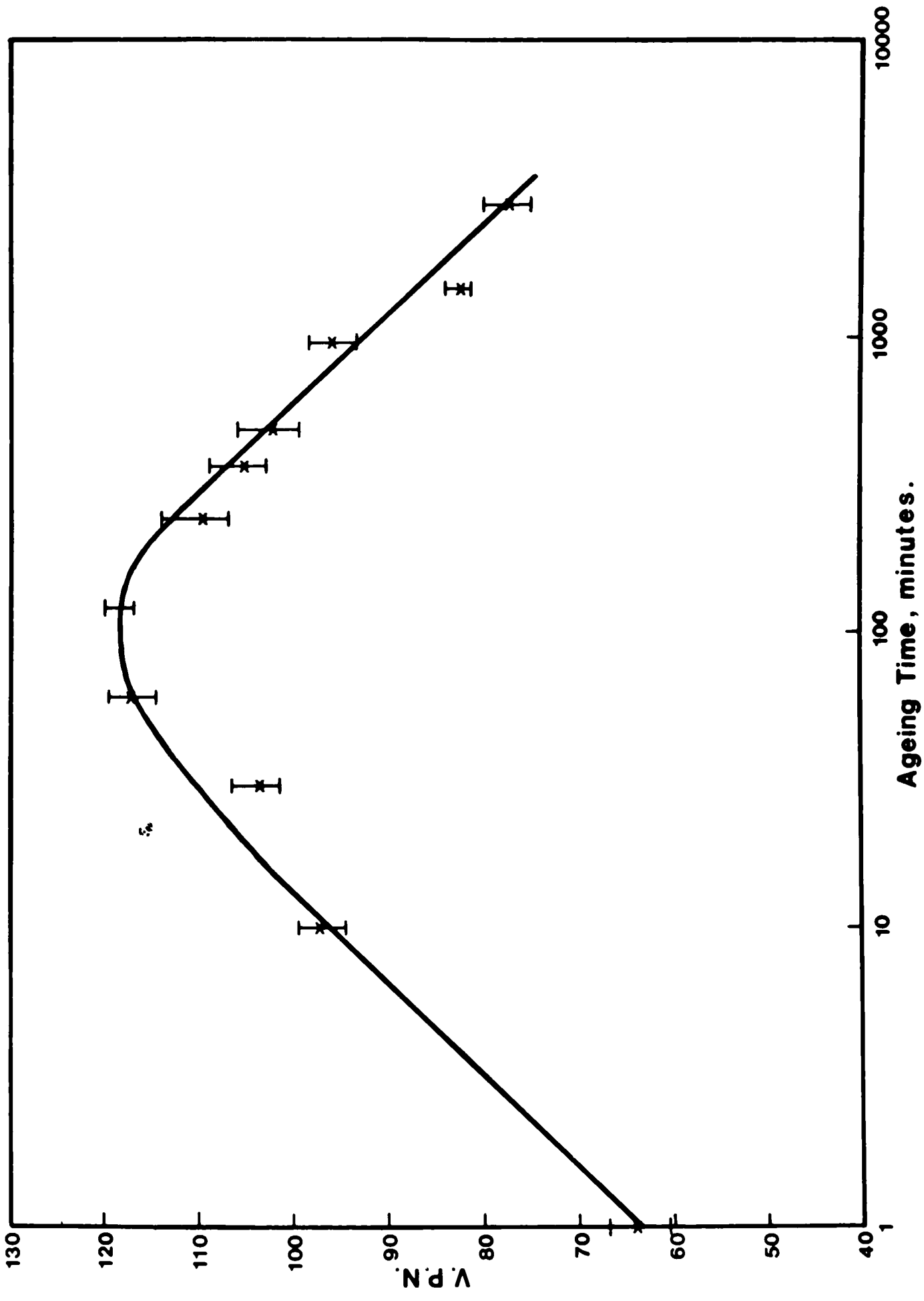
V. P.N.
130
120
110
100
90
80
70
60
50
40
1
10
100
1000
10000
Ageing Time, minutes.

Fig.3.4

Dispersion Parameters for ~ 0.1μm $\alpha(Al_{12}Mn_3Si)$ particles in Alloys BD6 and BD8.

Fig.3.4

*Particle Parameter	ALLOY BD6	ALLOY BD8
Particle Diameter in μm	0.1	0.1
Particle Length in μm	0.3	0.3
Volume Fraction, Fv	0.4×10^{-2}	1.1×10^{-2}
No./unit volume, Nv, in m^{-3}	1.8×10^{18}	7.8×10^{18}
No./unit length, N_L, in m^{-1}	0.4×10^{4}	1.1×10^{4}
Mean Free Path, λ, in μm	27.7	8.9
Nearest Neighbour Distance, Δ_3, in μm	0.5	0.3

*Average values

Fig.3.5

Frequency Histogram of Particle Diameter for ~ 0.1μm $\alpha(Al_{12}Mn_3Si)$ particles in BD8.

FIG. 3.5

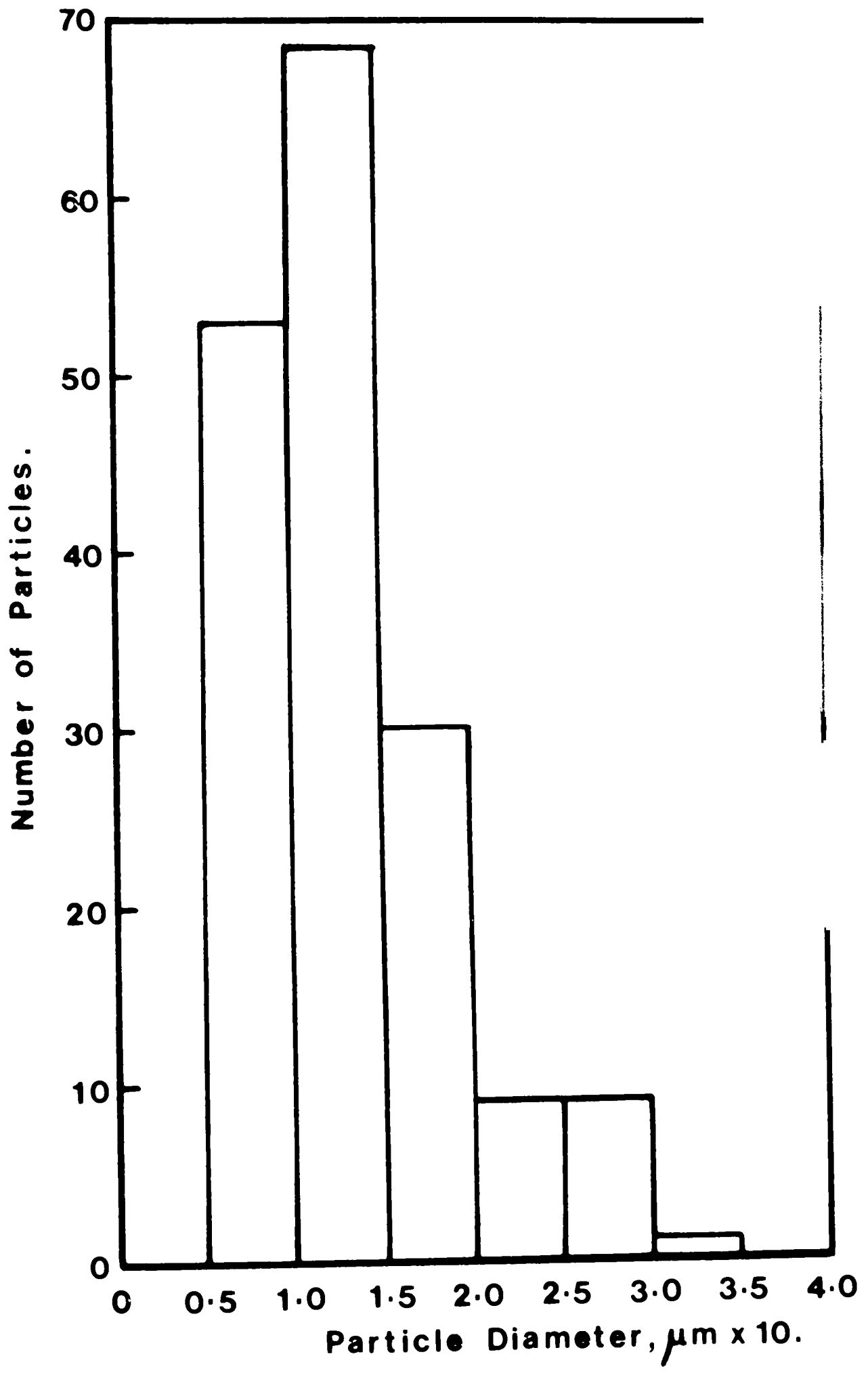
70
60
50
40
30
20
10
0
Number of Particles.
0
0·5
1·0
1·5
2·0
2·5
3·0
3·5
4·0
Particle Diameter, μm x 10.

Fig.3.6

Plot of Diameter of $\alpha(Al_{12}Mn_3Si)$ Particles as a Function of Annealing Time and Temperature.

(i) Experimental data are shown as circles on the graph with the corresponding particle diameters adjacent to them; the particle diameters are in μm.

(ii) The squares indicate data extrapolated from Fig.3.7.

(iii) The diagonal lines are the isometric lines for particle diameters of 0.05μm and 0.10μm.

FIG. 3.6

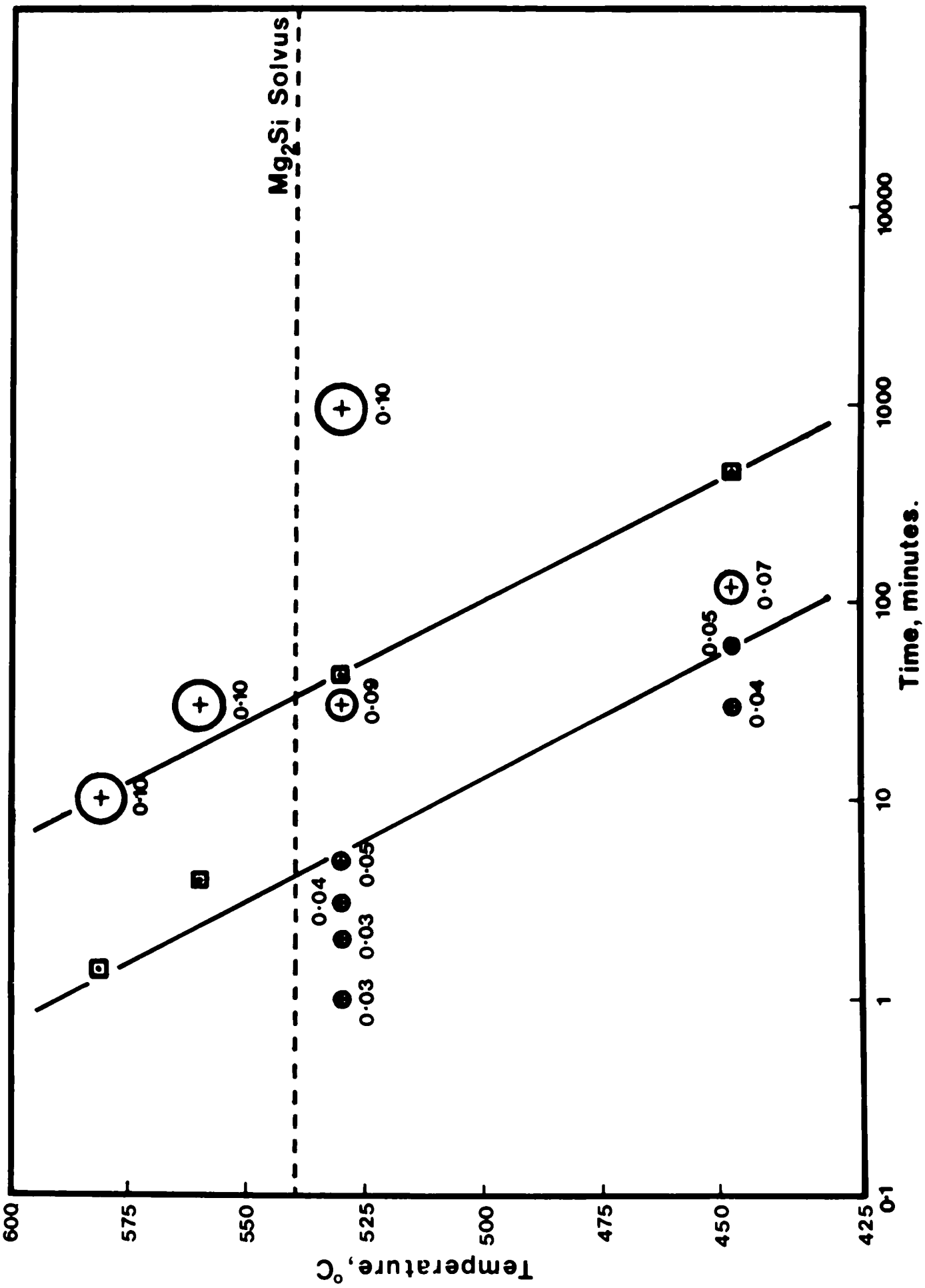
Mg_2Si Solvus
0·10
0·10
0·10
0·09
0·07
0·05
0·04
0·05
0·04
0·03
0·03
600
575
550
525
500
475
450
425
Temperature, °C
10000
1000
100
10
1
0·1
Time, minutes.

Fig.3.7

Log-Log Plot of Particle Diameter against Annealing Time Using the Experimental Data shown in Fig.3.6.

(The squares indicate the extrapolated data used in Fig.3.6. These correspond to the time taken to achieve a particle diameter of 0.05μm at 560°C and 581°C and a particle diameter of 0.10μm at 447°C and 530°C).

FIG. 3.7

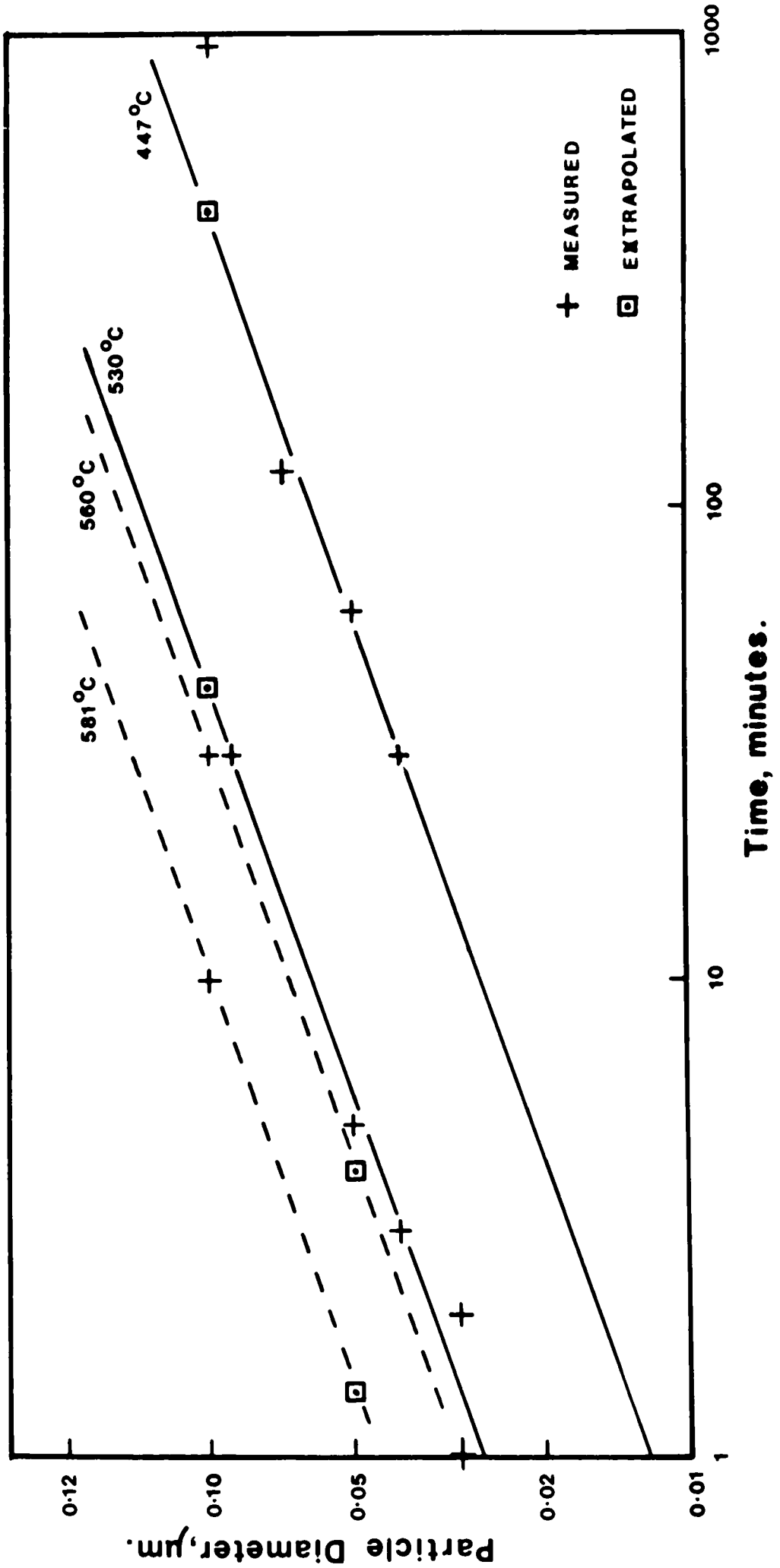
Particle Diameter, μm.
0·12
0·10
0·05
0·02
0·01
1
10
100
1000
Time, minutes.
MEASURED
EXTRAPOLATED
447°C
530°C
560°C
581°C

Fig.3.8

Variation of Grain Size of Cold Worked BD8 after Annealing at Temperatures between 560°C and 630°C.

(Grain boundary melting occurs at temperatures of 590°C and above).

FIG. 3.8

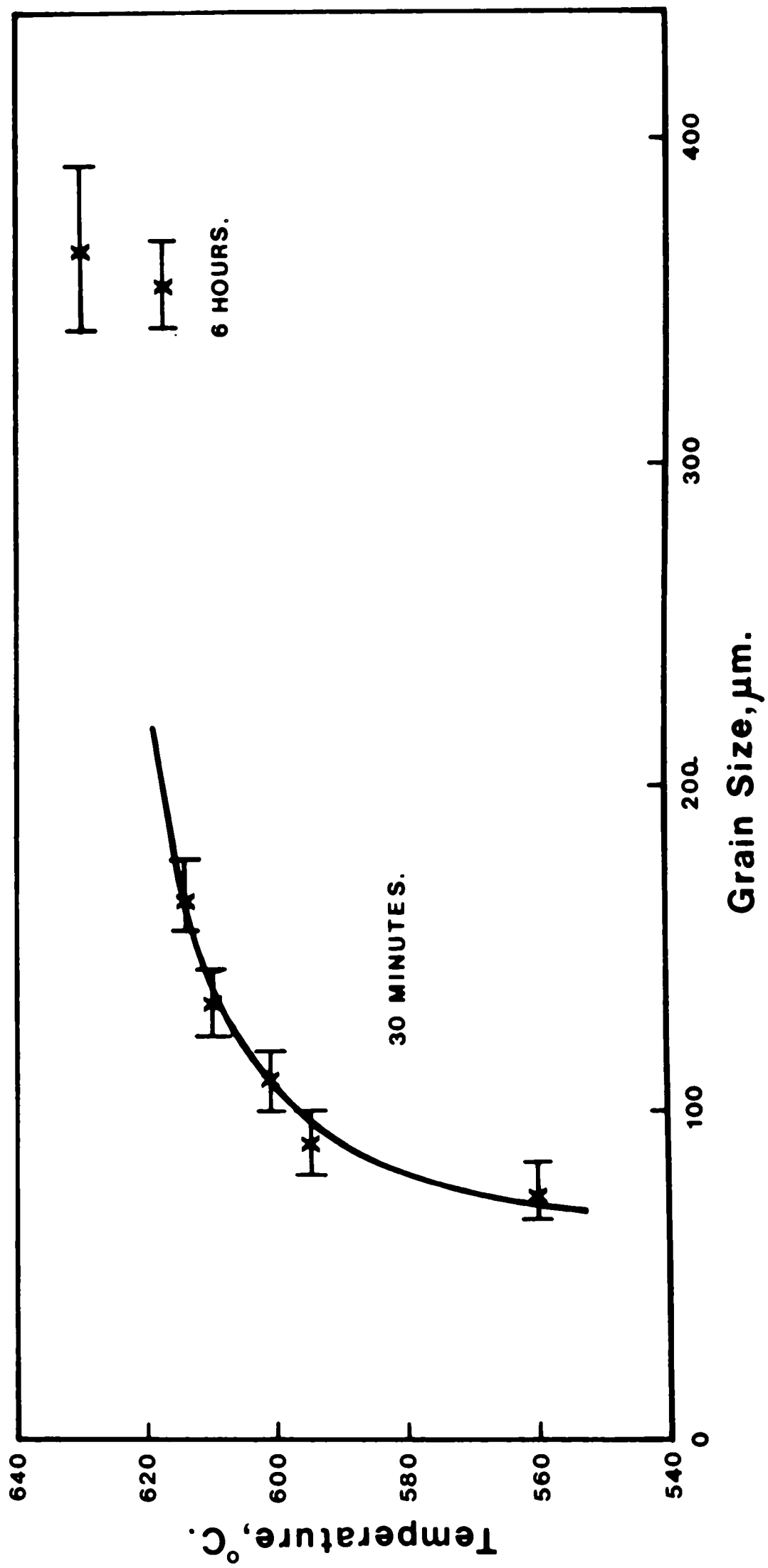
6 HOURS.
30 MINUTES.
Temperature, °C.
640
620
600
580
560
540
0
100
200
300
400
Grain Size, μm.

Plate 3.1

Residual Casting Precipitates in BD8, Homogenized and Cold Rolled (Keller's Etch).

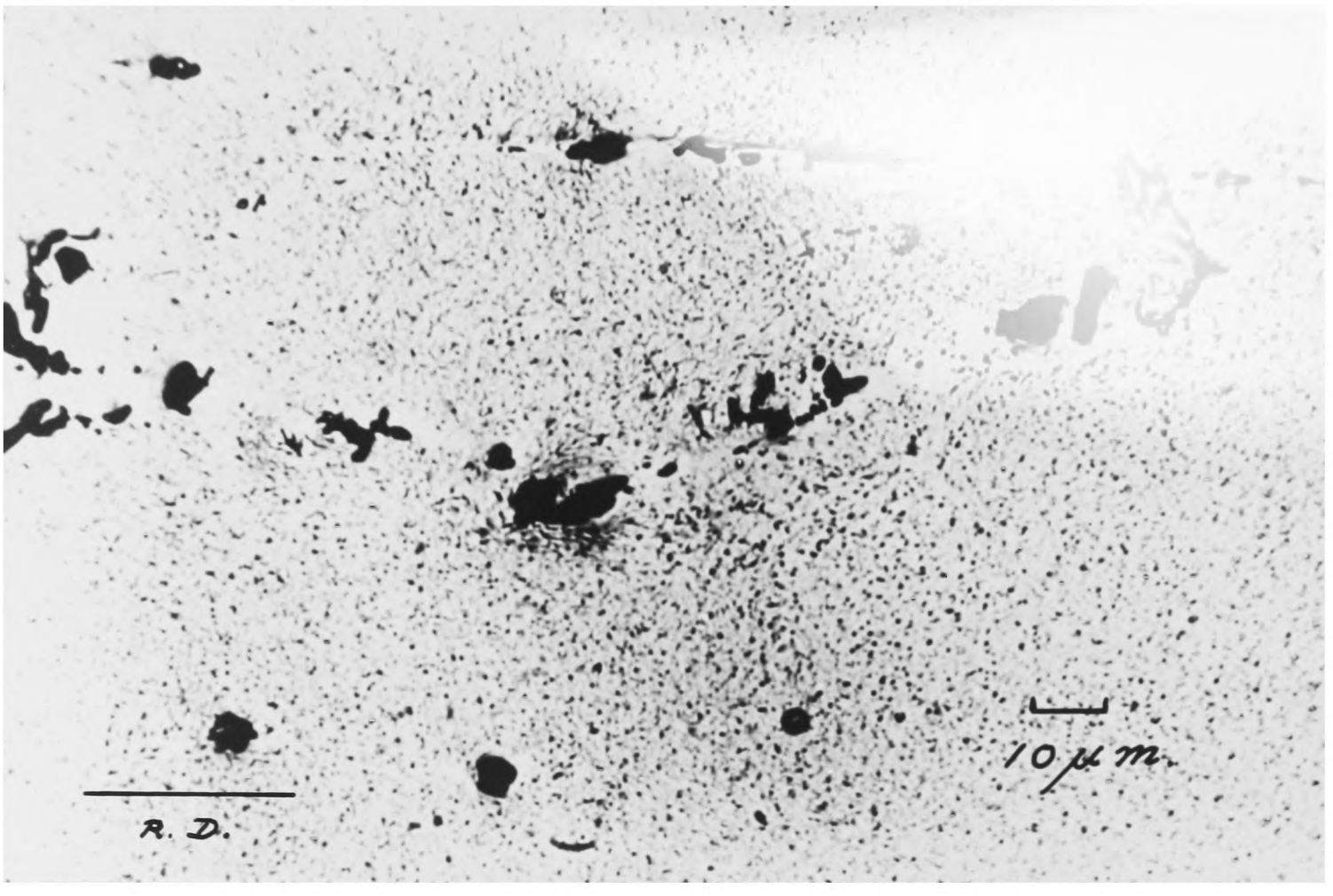
10 μm
R. D.

Plate 3.2

T.E.M. of Solution Heat Treated BD6

Plate 3.3

T.E.M. of Solution Heat Treated BD8.

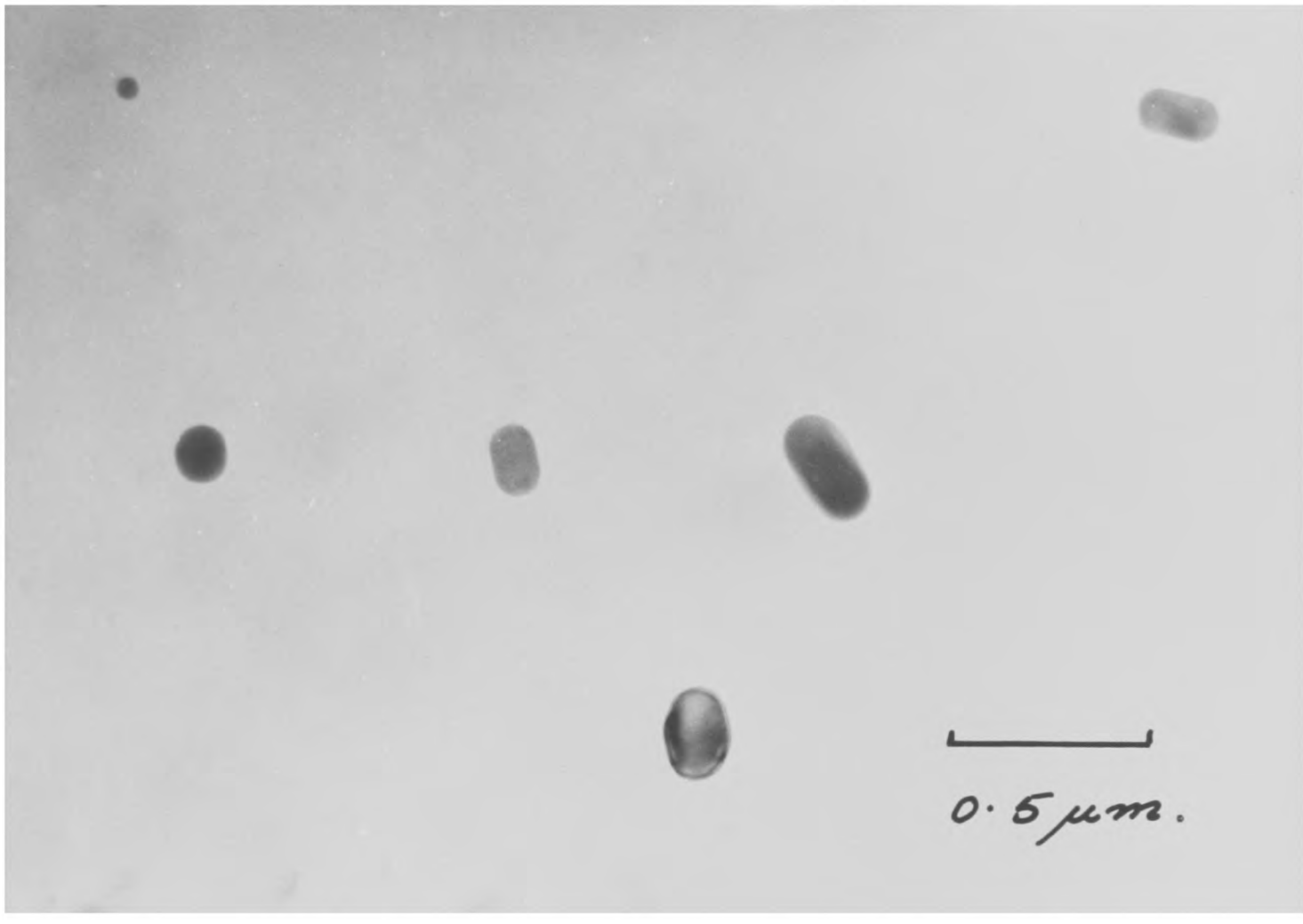
0·5 μm.

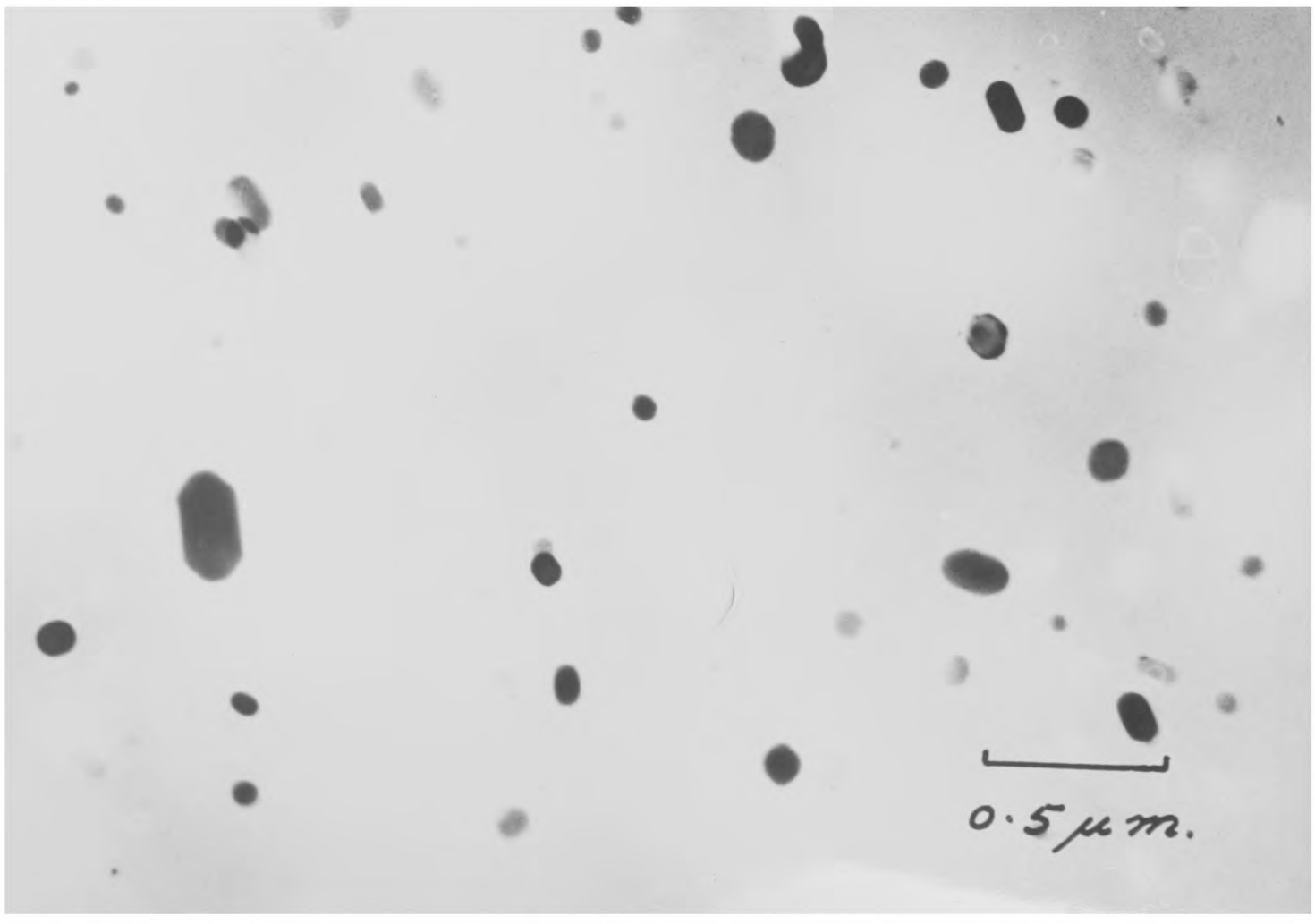
0·5 μm.

Plate 3.4

Optical Micrograph of the Grain Structure in Peak-Aged BD3.

Plate 3.5

Optical Micrograph of the Grain Structure in Peak-Aged BD6.

Plate 3.6

Optical Micrograph of the Grain Structure in Peak-Aged BD8.

(Electro-Chemical Etch).

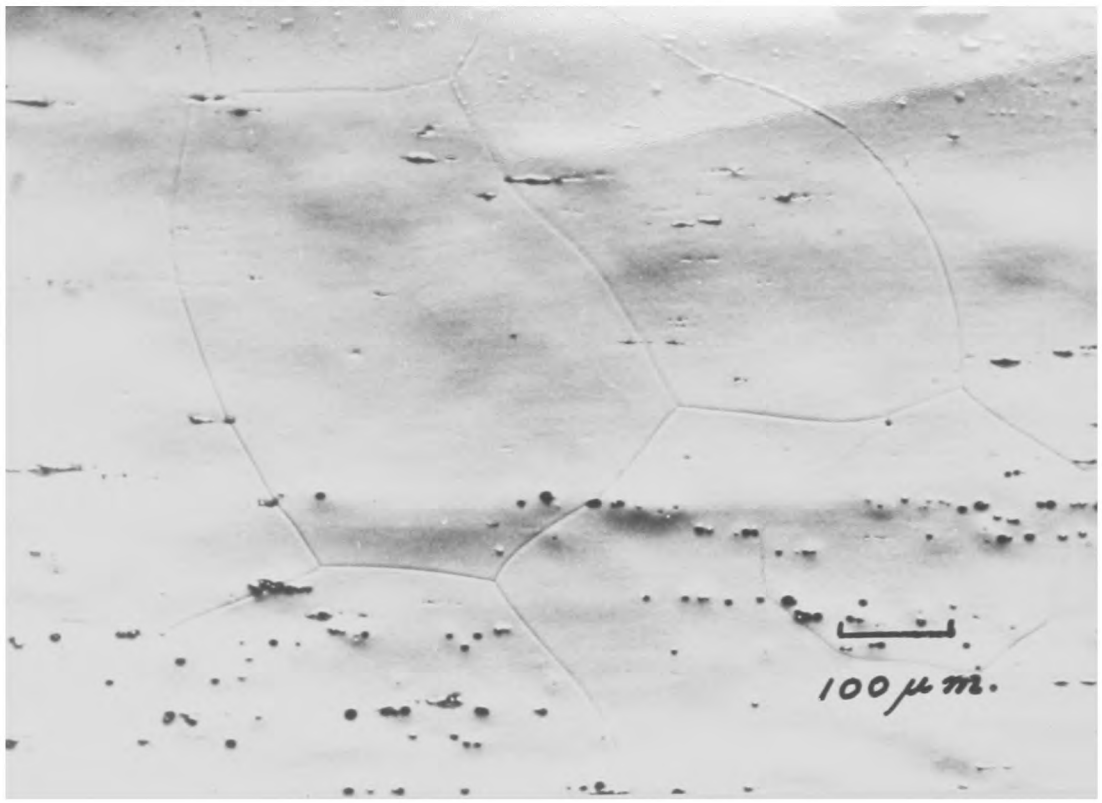
100 μm.

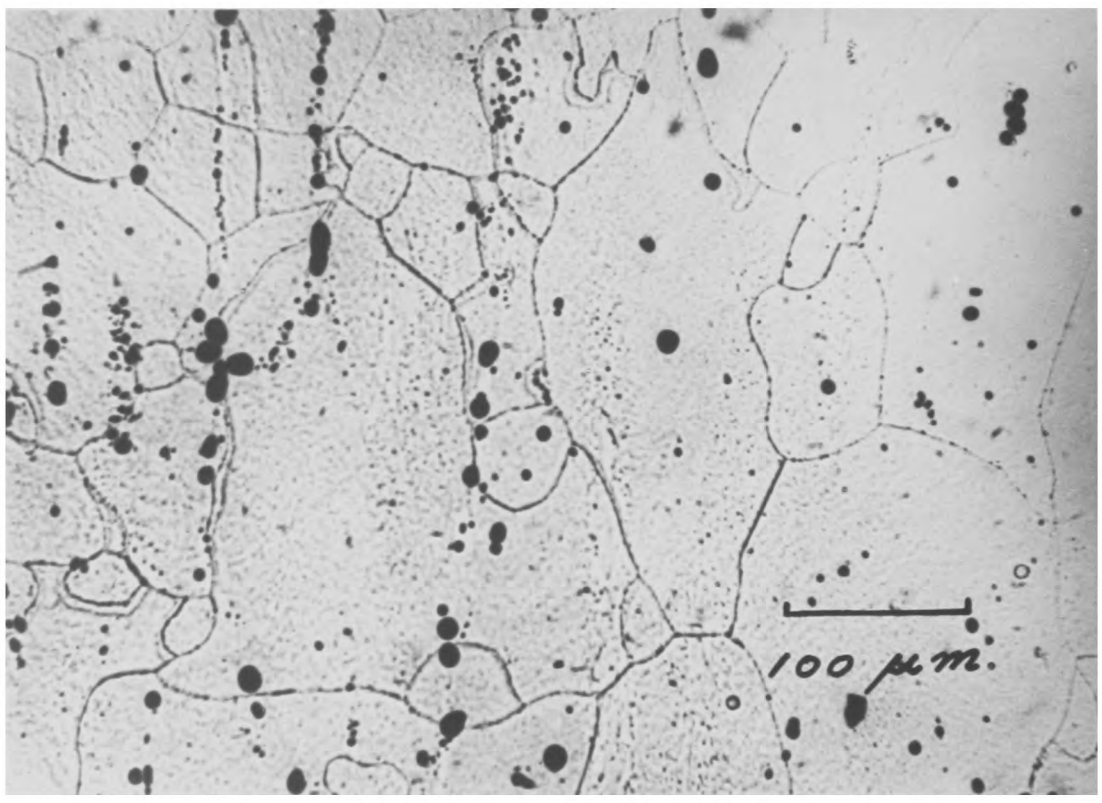
100 μm.

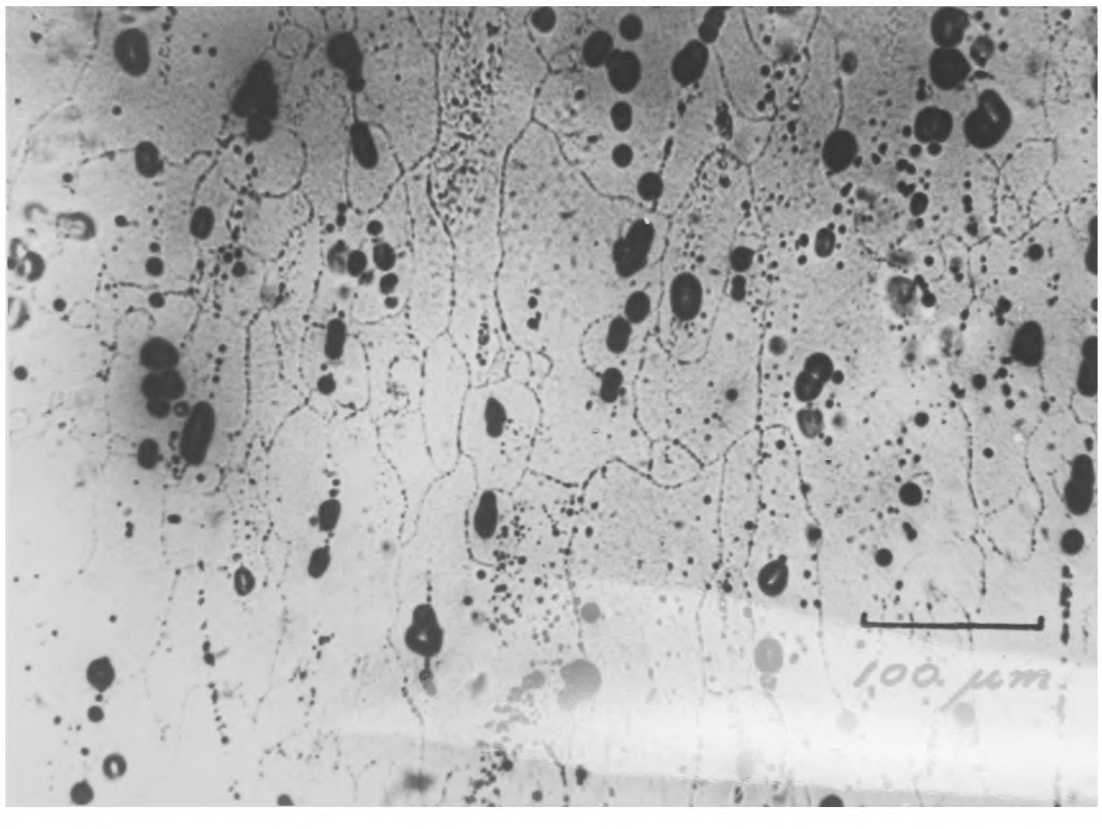
100 μm.

Plate 3.7

T.E.M. of Peak-Aged BD8.

Plate 3.8

T.E.M. of Peak-Aged BD8. (Mg_2Si ageing precipitate visible as needles).

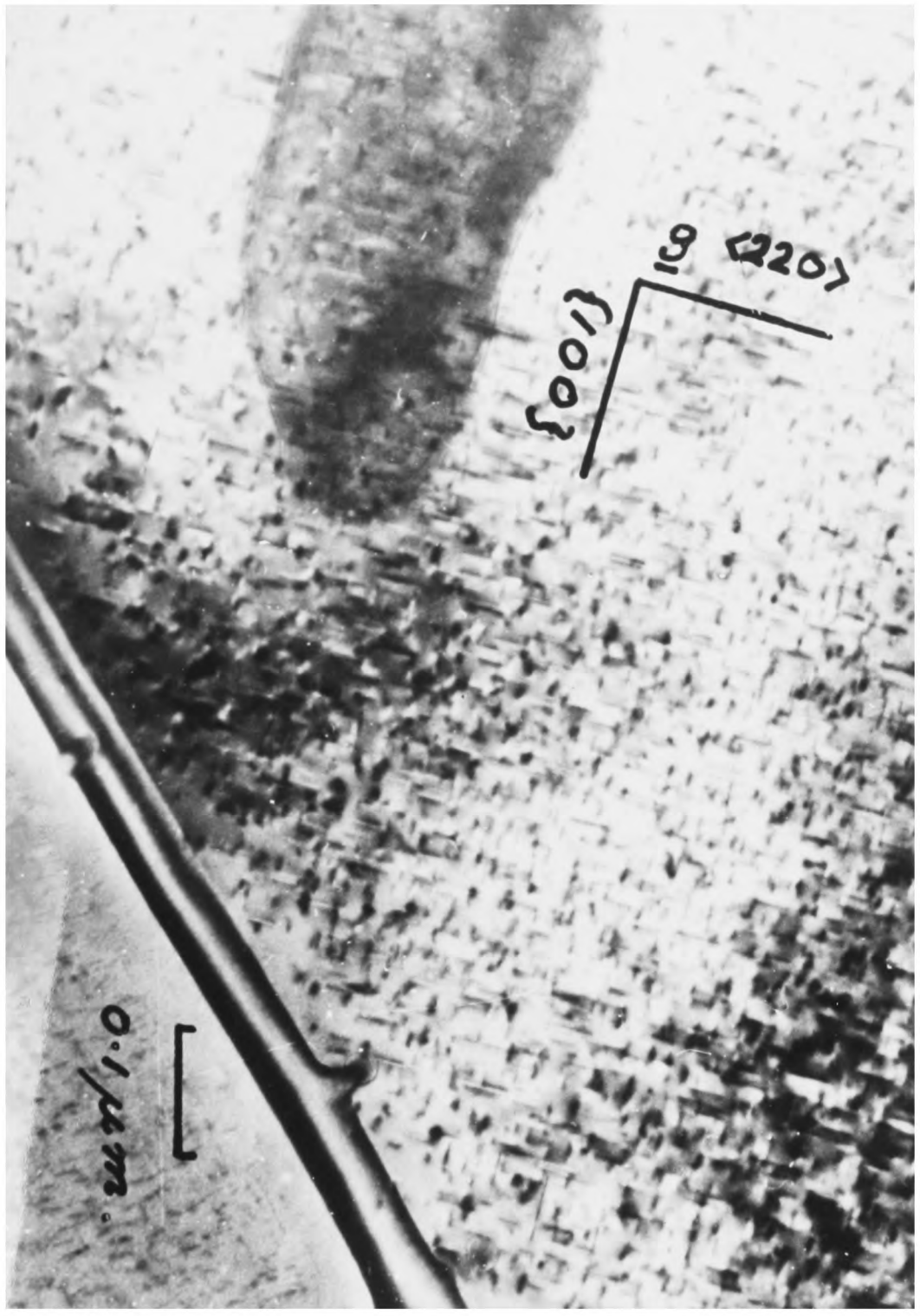
{001}
19 ⟨220⟩
0.1 μm.

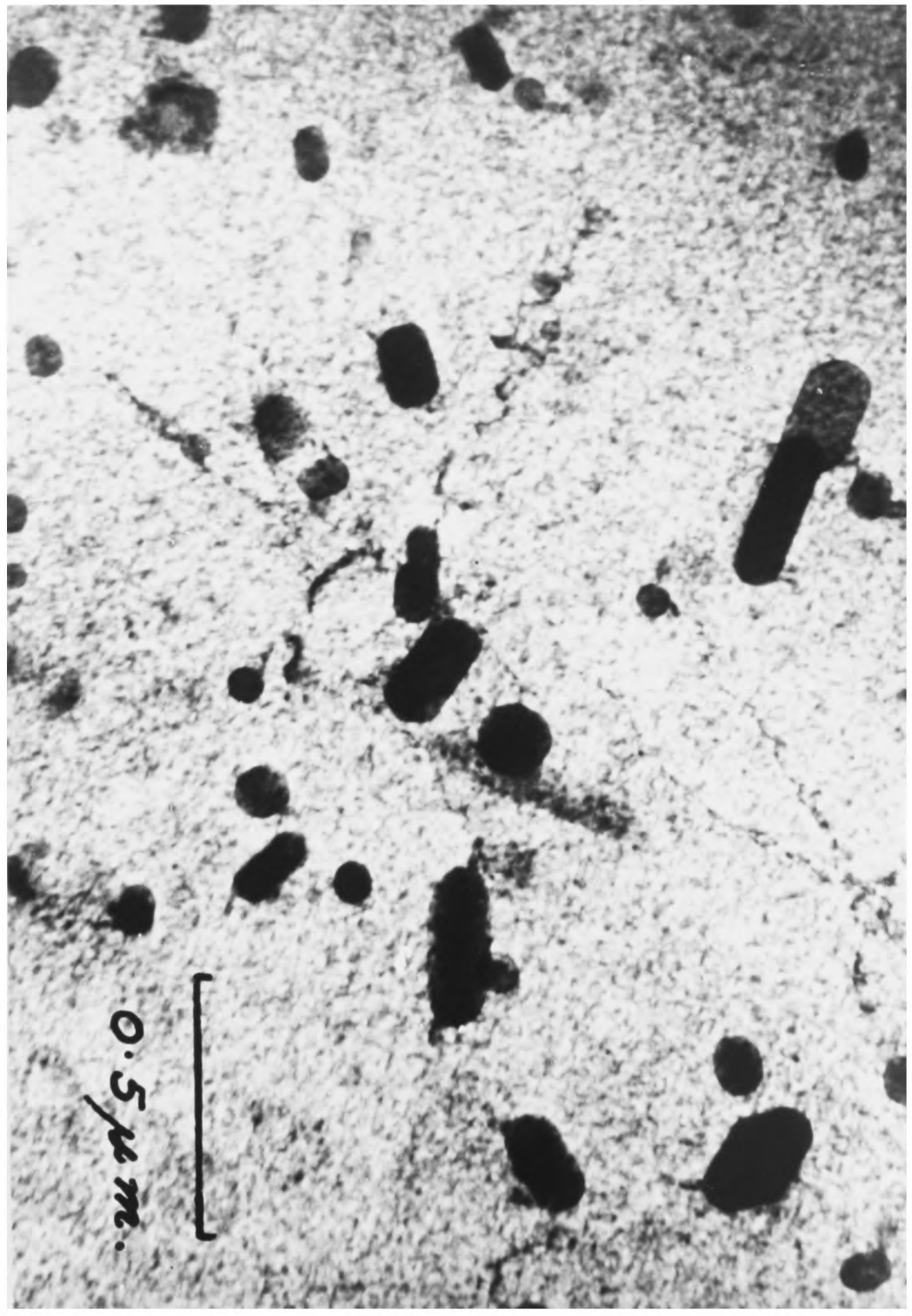
0.5 μm.

Plate 3.9

T.E.M. of Peak-Aged BD8, showing P.F.Z.

Plate 3.10

T.E.M. of Peak-Aged BD8, showing Grain Boundary Precipitates.

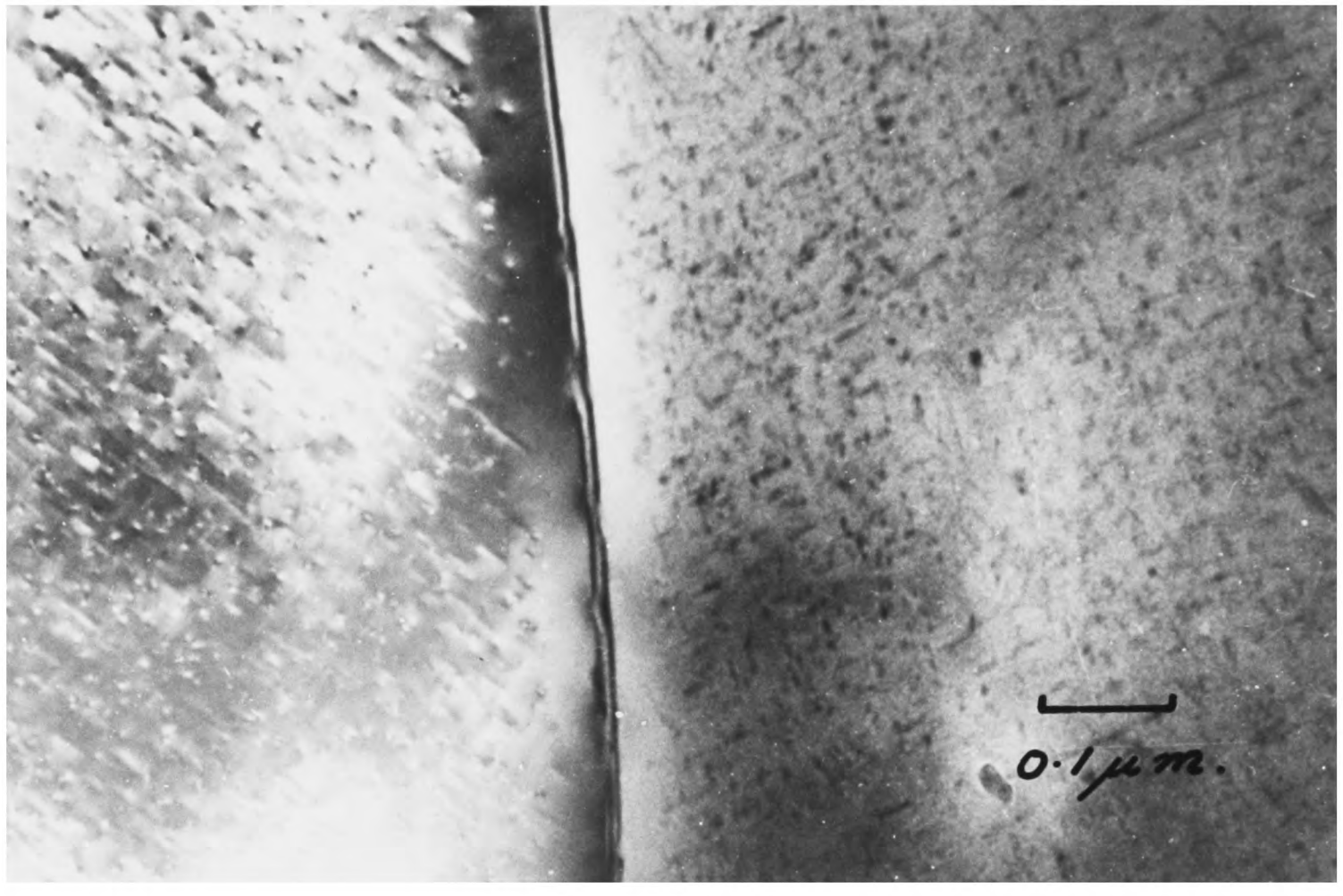
0·1μm.

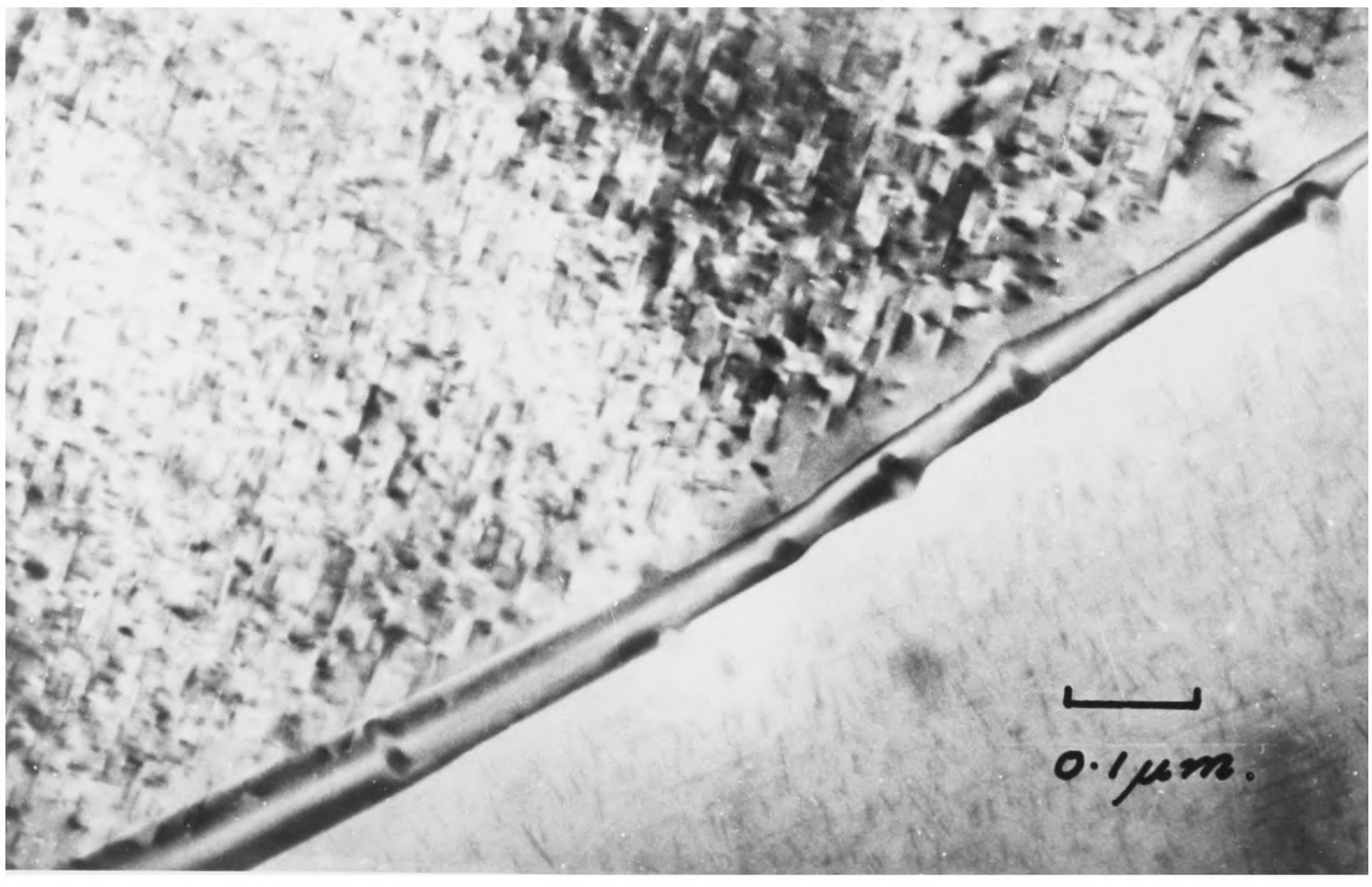
0·1μm.

Plate 3.11

T.E.M. of Peak-Aged BD3, Grain Boundary Precipitates.

Plate 3.12

T.E.M. of Peak-Aged BD3, Grain Boundary Precipitates.

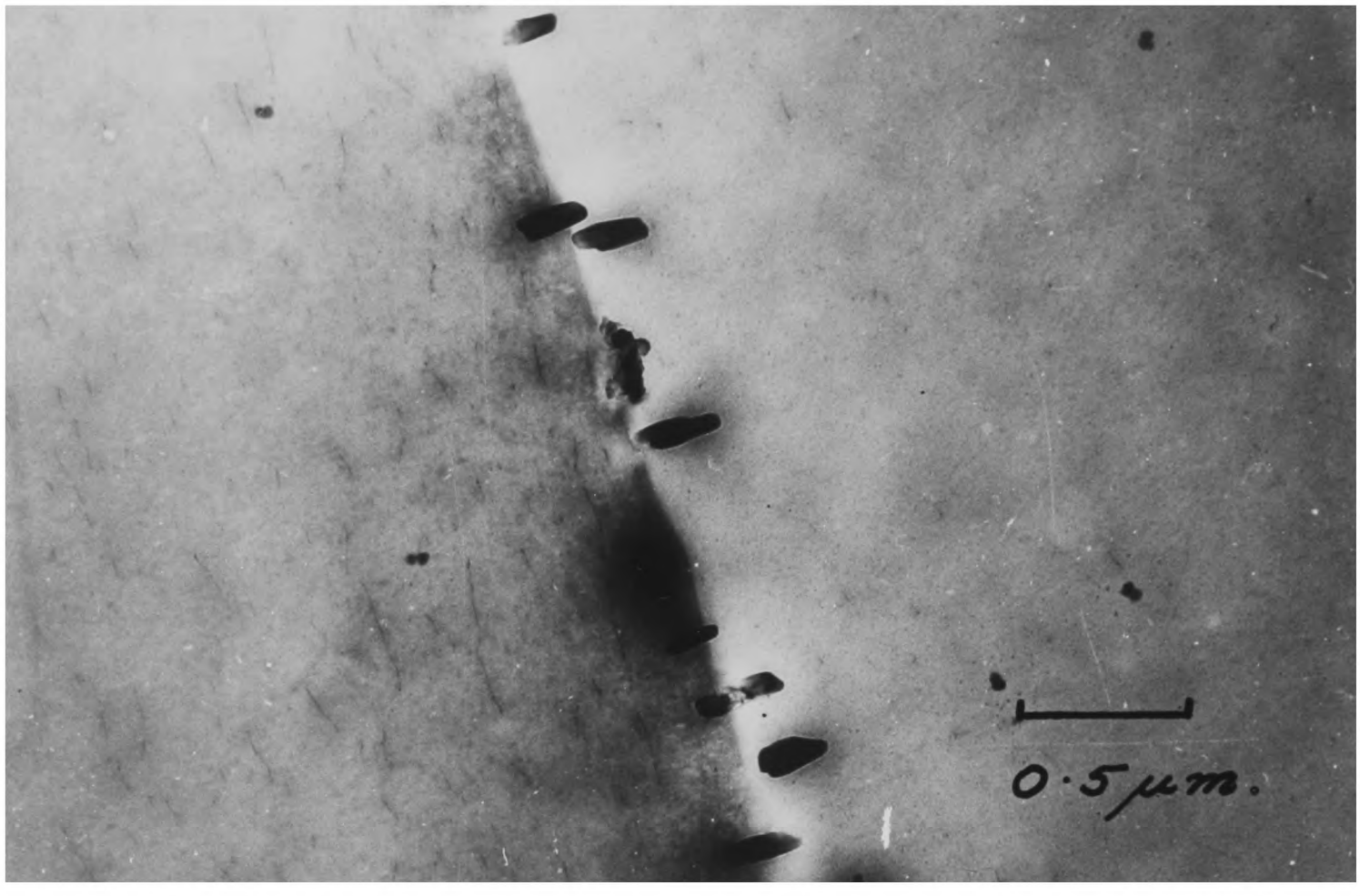
0·5μm.

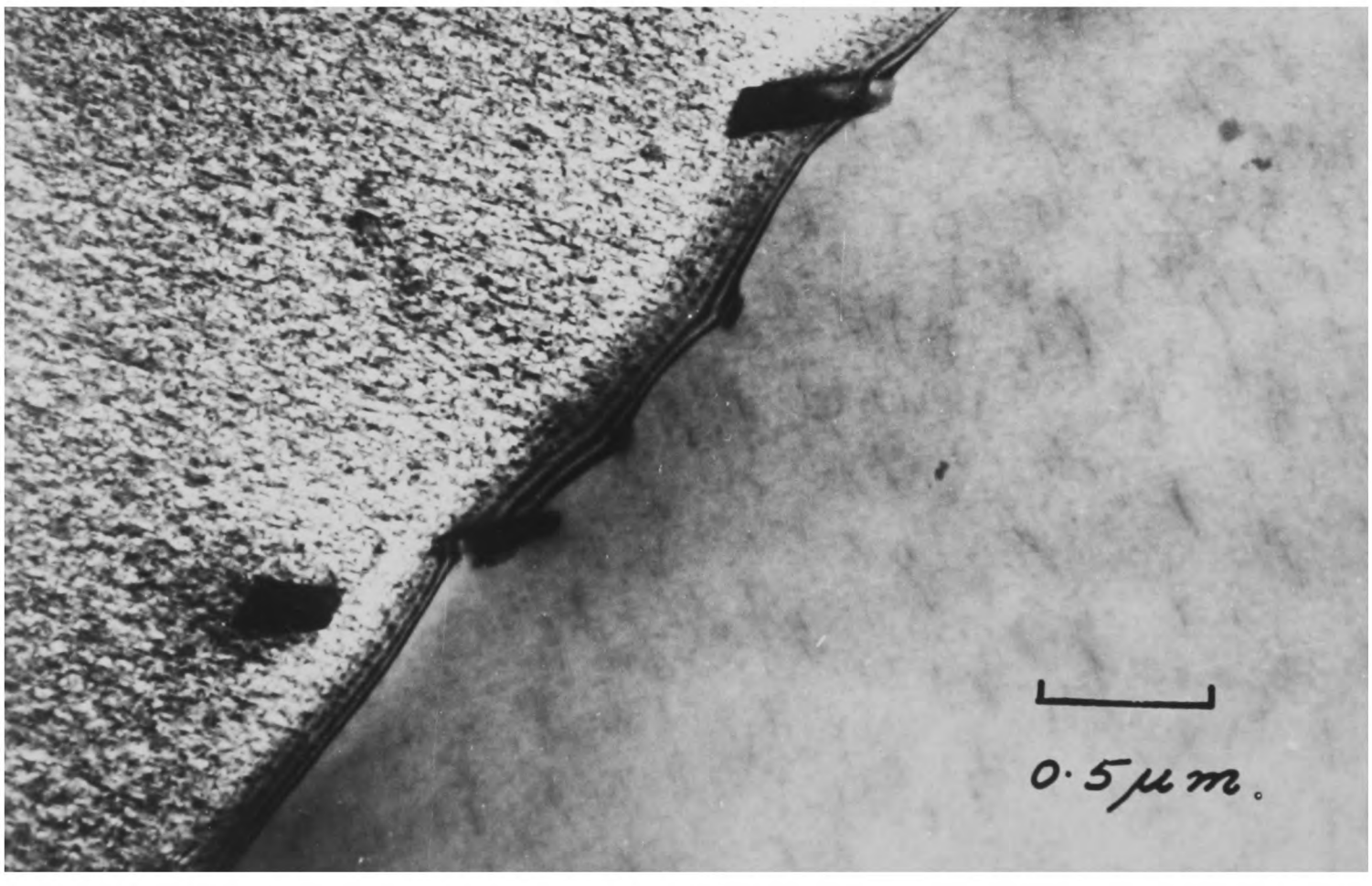
0·5μm.

Plate 3.13

Phase Diagram for Al-Mg-Mn-Si at 1wt%Si.
Isothermal diagram at 460°C.

(Reproduced from 'Equilibrium Diagrams of Al-Alloy Systems' (A.D.A.) edited by H. W. L. Phillips, 1961).

Van Horn, 1967, has since identified the α phase as $\alpha(Al_{12}Mn_3Si)$.

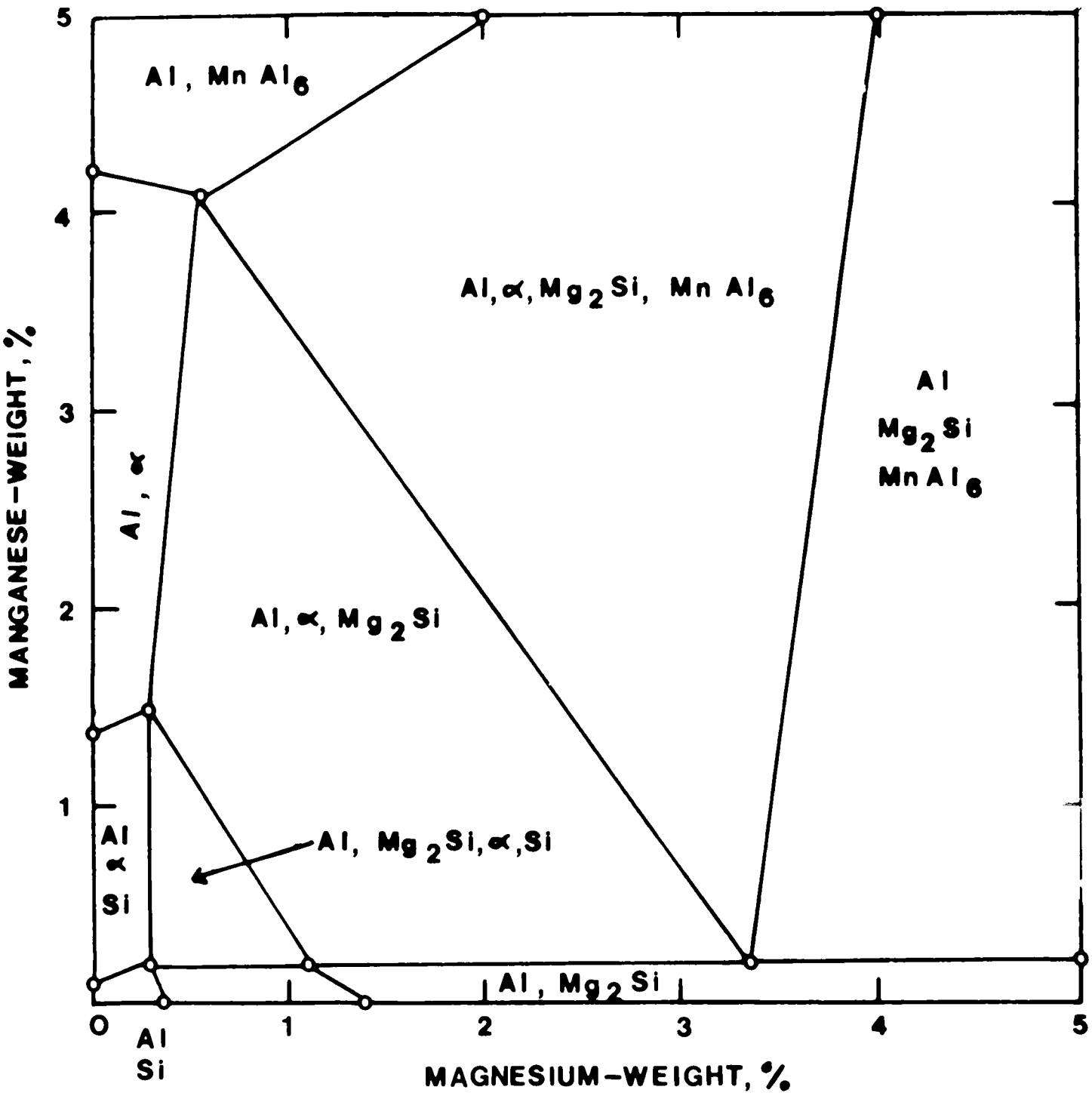
Al , Mn Al6
Al,α,Mg2Si, Mn Al6
Al
Mg2Si
Mn Al6
Al, α
Al, α, Mg2Si
Al
α
Si
Al, Mg2Si,α,Si
Al, Mg2Si
Al
Si
MANGANESE-WEIGHT, %
MAGNESIUM-WEIGHT, %
0
1
2
3
4
5

Plate 3.14

As Cast BD8, unetched. (Optical Micrograph).

Plate 3.15

As Cast BD8. (Optical Micrograph; Keller's Etch).

Plate 3.16

T.E.M. of As Cast BD8.

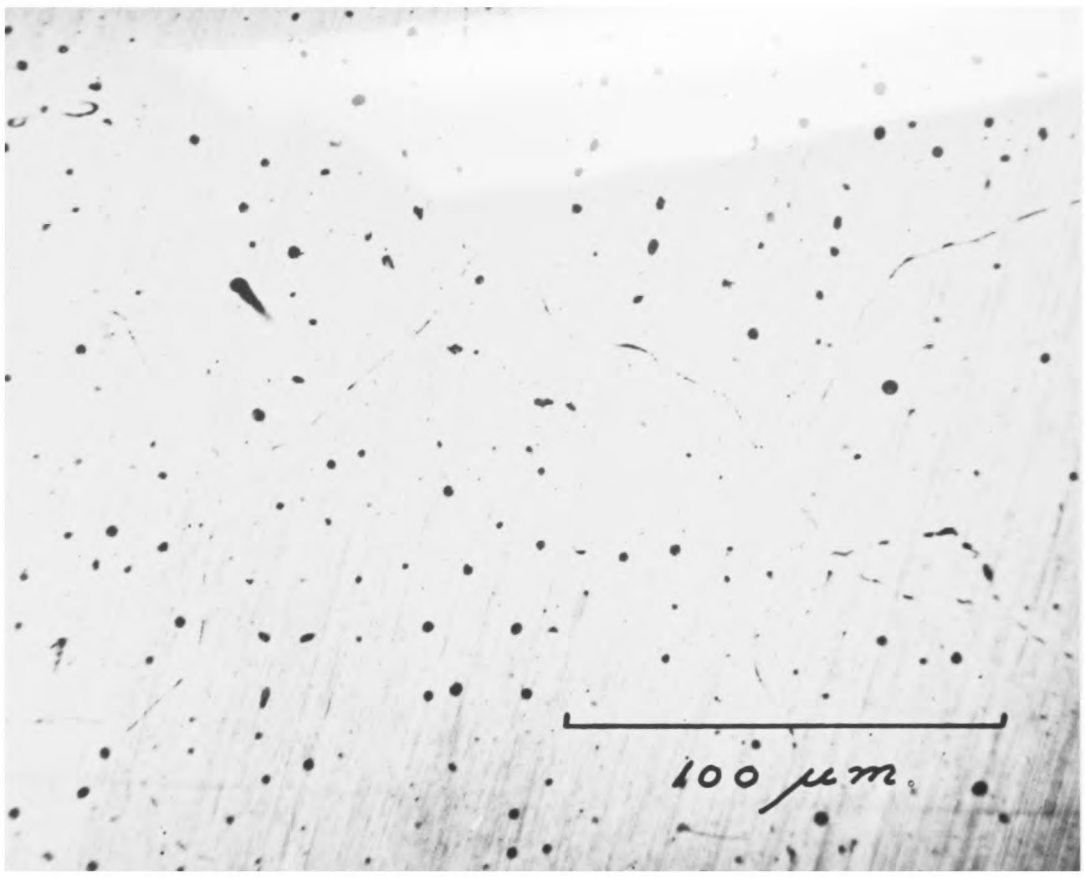
100 μm

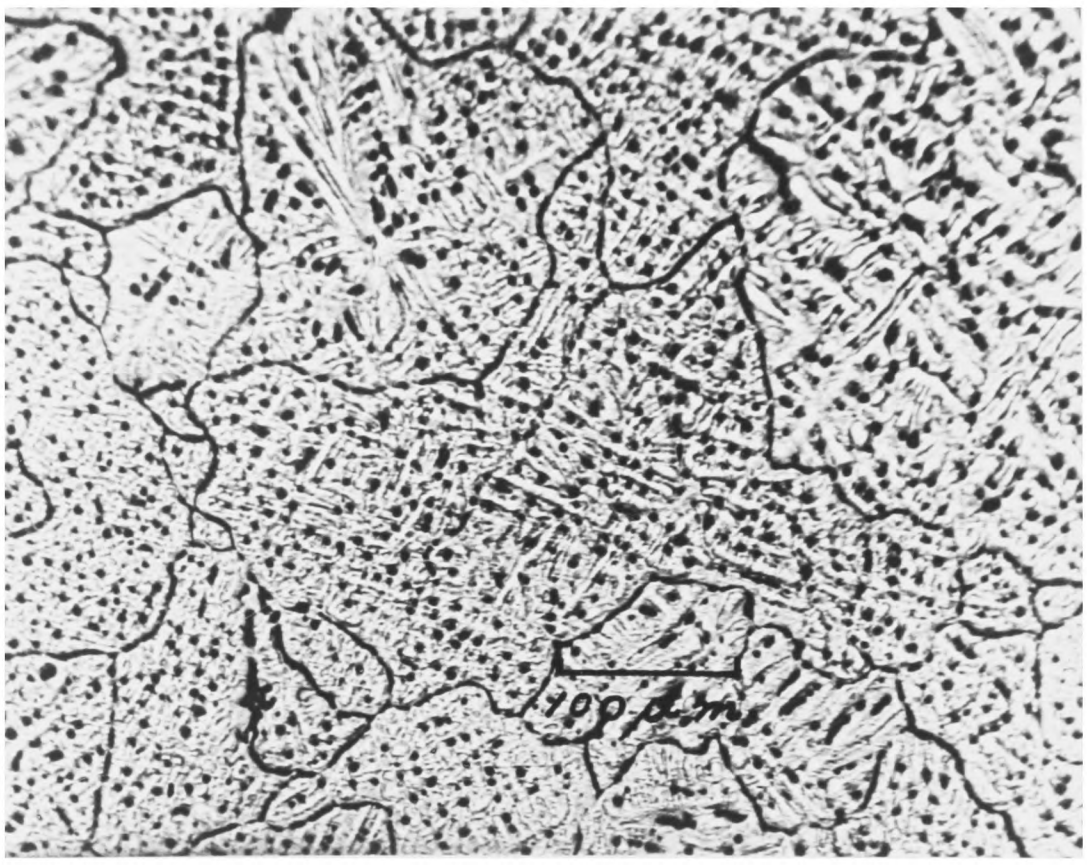
100 μm



Plate 3.17

Homogenized BD8; As Cast Alloy held for 16hrs. at 530°C. (Optical Micrograph; Keller's Etch).

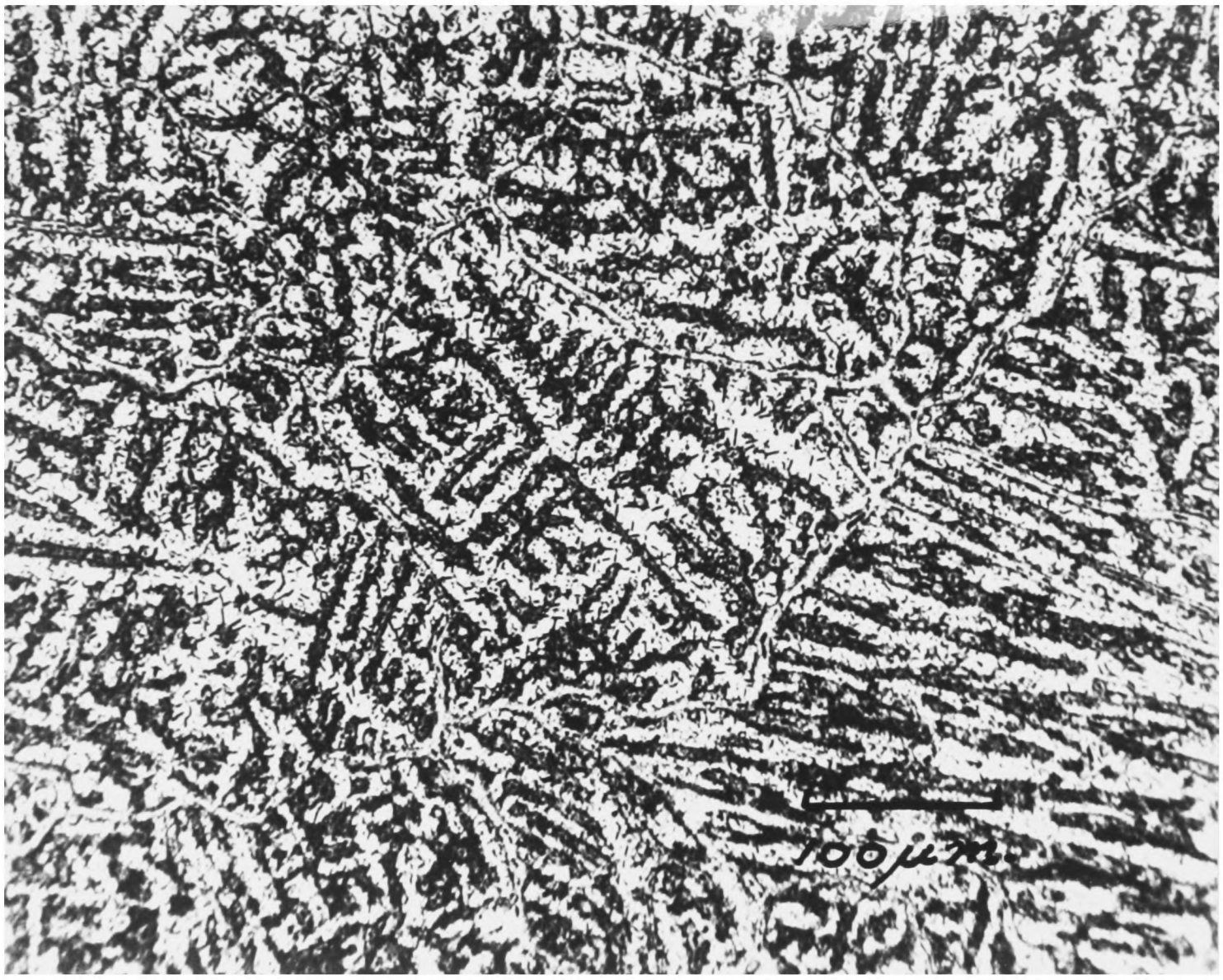
100 µm

Plate 3.18

Phase diagram of Al-Mg-Si - the limits of solid solubility.

(Reproduced from 'Equilibrium Diagrams of Al-Alloy Systems' (A.D.A.) edited by H. W. L. Phillips, 1961).

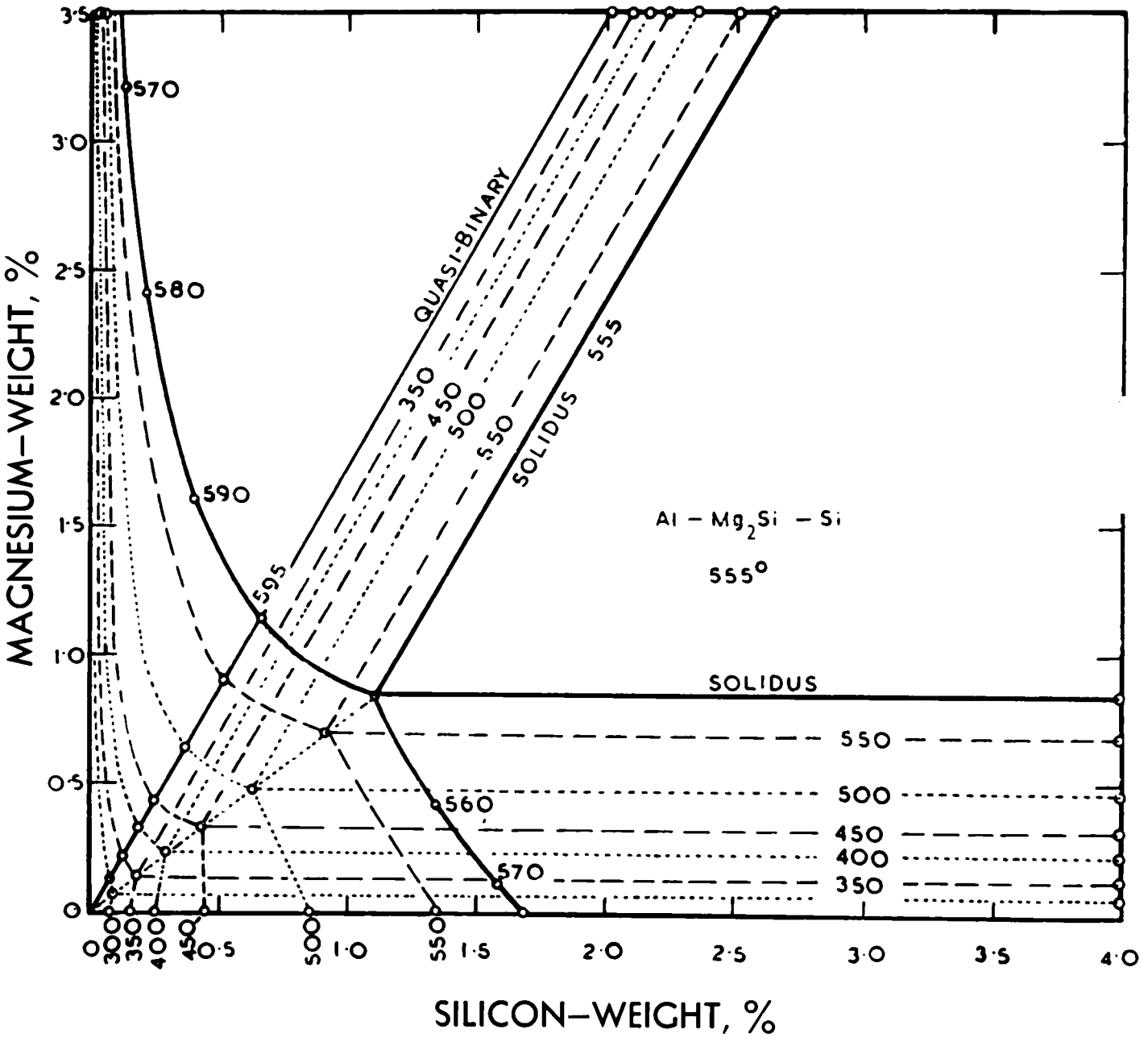
MAGNESIUM–WEIGHT, %
SILICON–WEIGHT, %
Al – Mg2Si – Si
555°
QUASI-BINARY
SOLIDUS
SOLIDUS
570
580
590
595
560
570
350
450
500
550
555
550
500
450
400
350
0
0·5
1·0
1·5
2·0
2·5
3·0
3·5
4·0

Plate 3.19

T.E.M. of Homogenized BD8. (16hrs. at 530°C).

Plate 3.20

T.E.M. of Homogenized BD8 after Solution Heat Treatment at 560°C for 30 minutes.

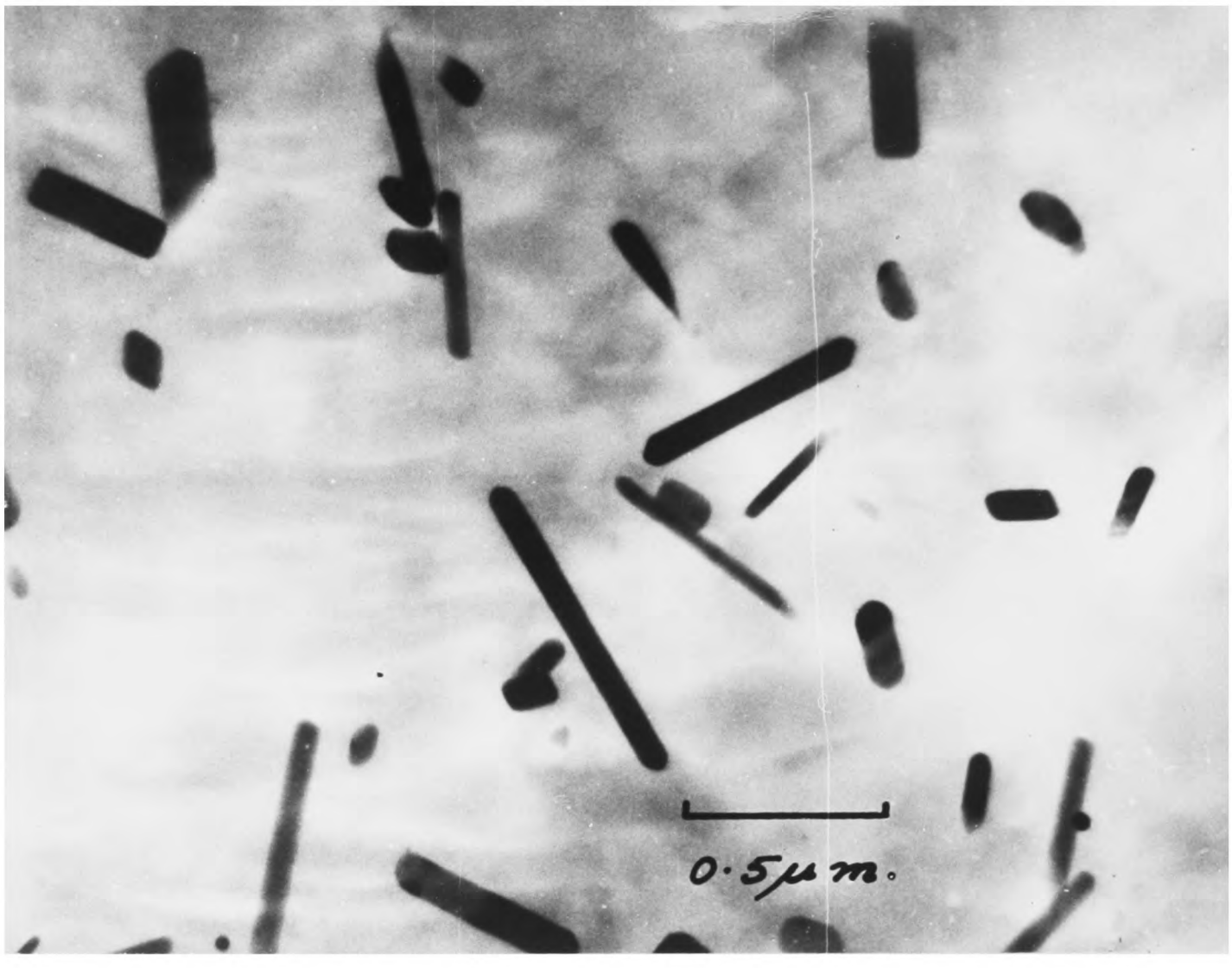
0·5μm.

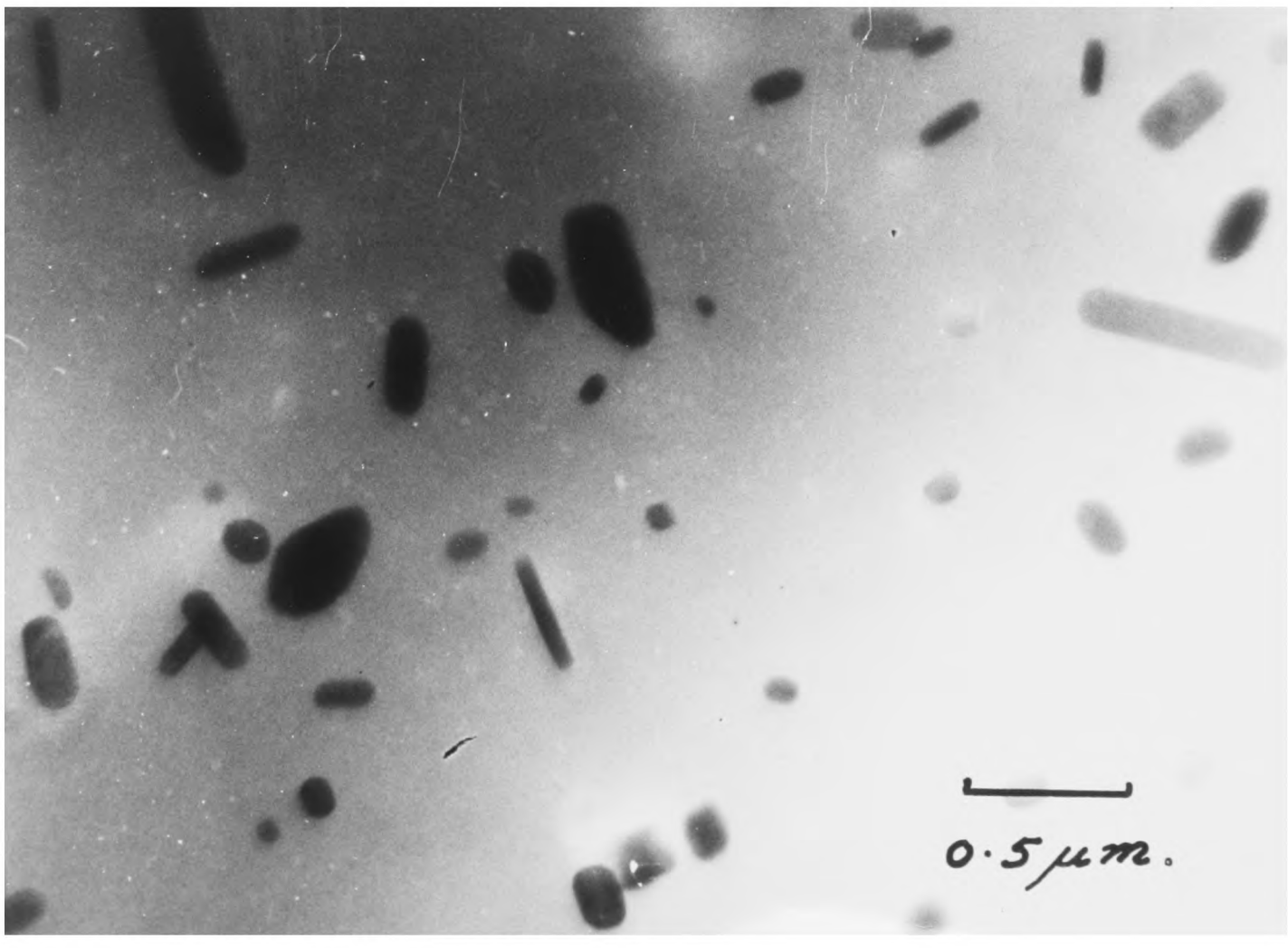
0·5μm.

Plate 3.21

Homogenized BD8 after a solution Heat Treatment at 560°C for 30 minutes. (Optical Micrograph; Keller's Etch).

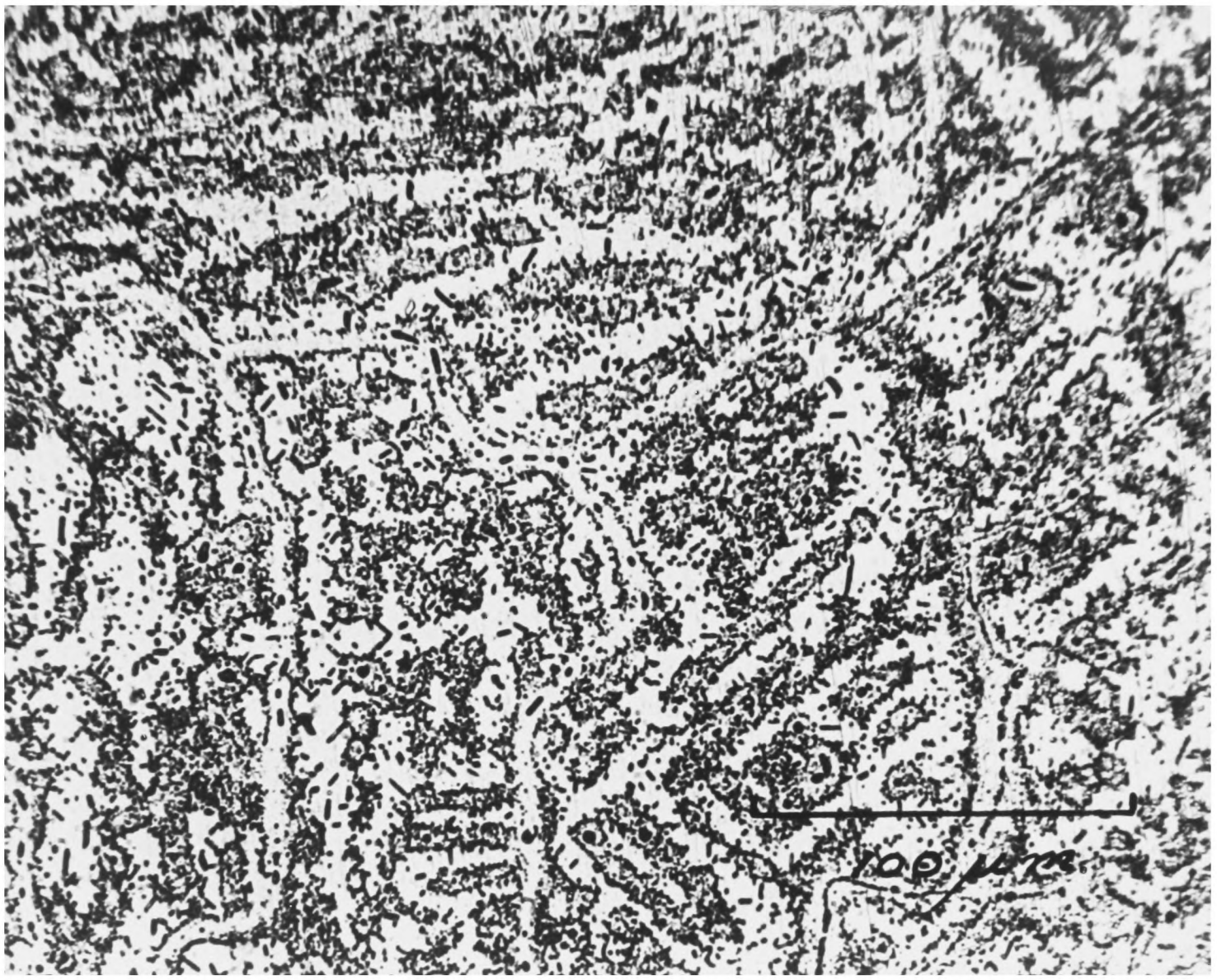
100 μm

Plate 3.22

T.E.M. of Cast BD8 after 1 minute at 530°C.

Plate 3.23

T.E.M. of Cast BD8 after 3 minutes at 530°C.

Plate 3.24

T.E.M. of Cast BD8 after 3 minutes at 530°C.

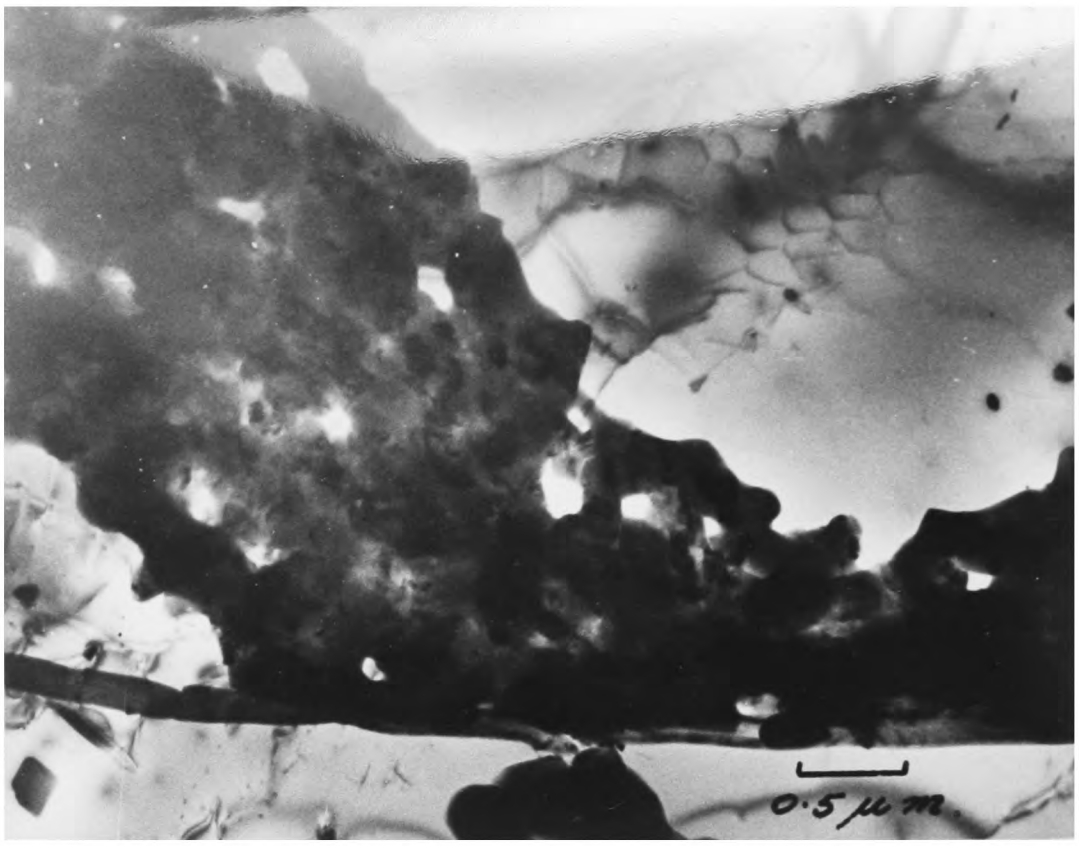
0·5 μm.


0·5 μm.


0·5 μm.

Plate 3.25

T.E.M. of Cast BD8 after 5 minutes at 530°C.

Plate 3.26

T.E.M. of Cast BD8 after 5 minutes at 530°C.

Plate 3.27

T.E.M. of Cast BD8 after 30 minutes at 530°C.

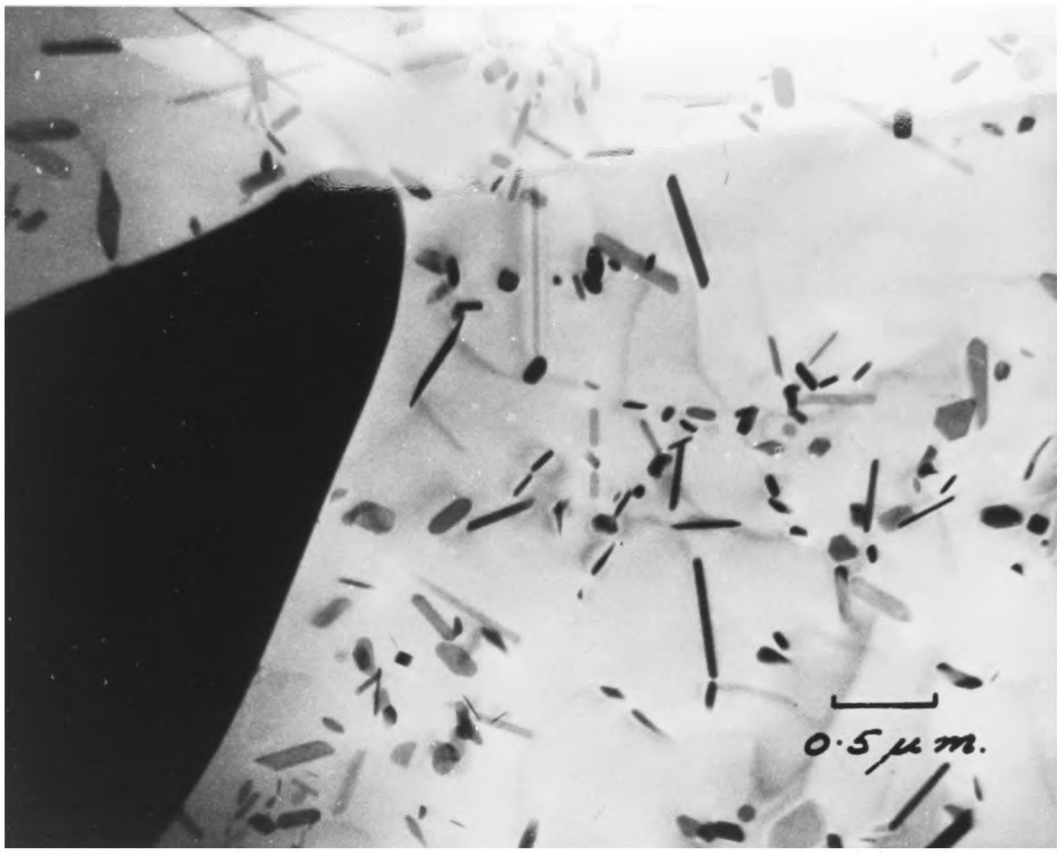
0·5μm.

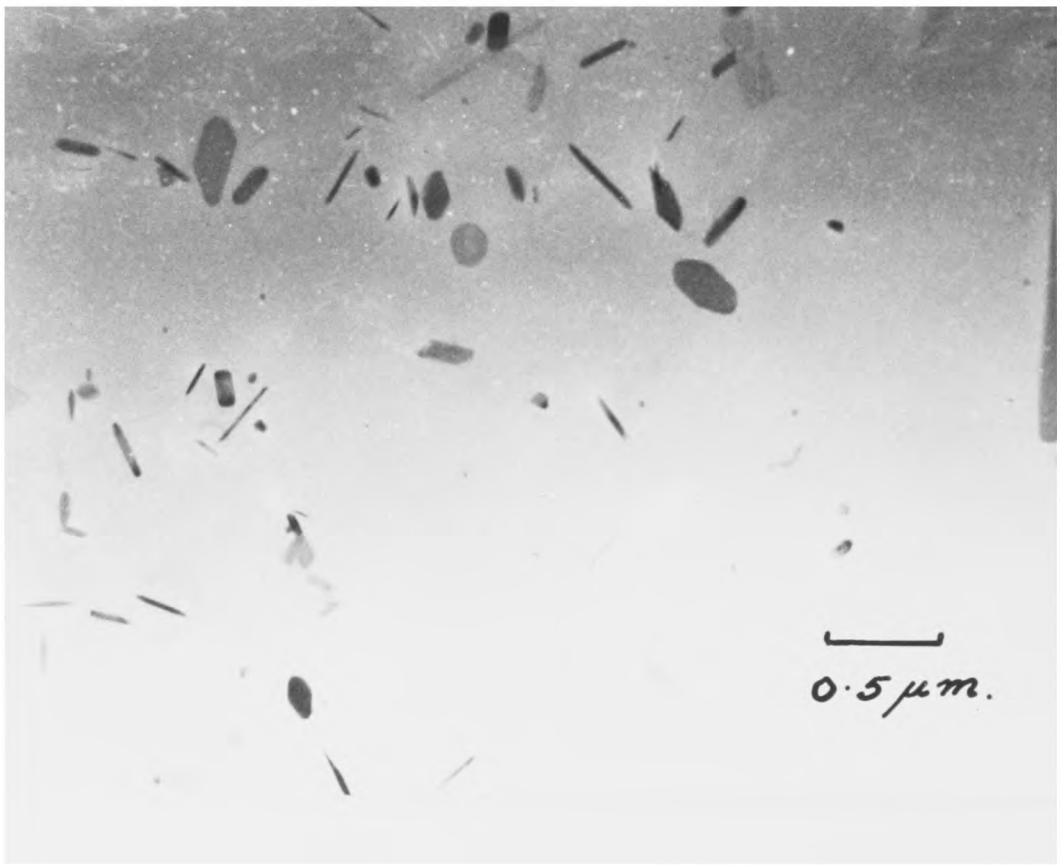
0·5μm.

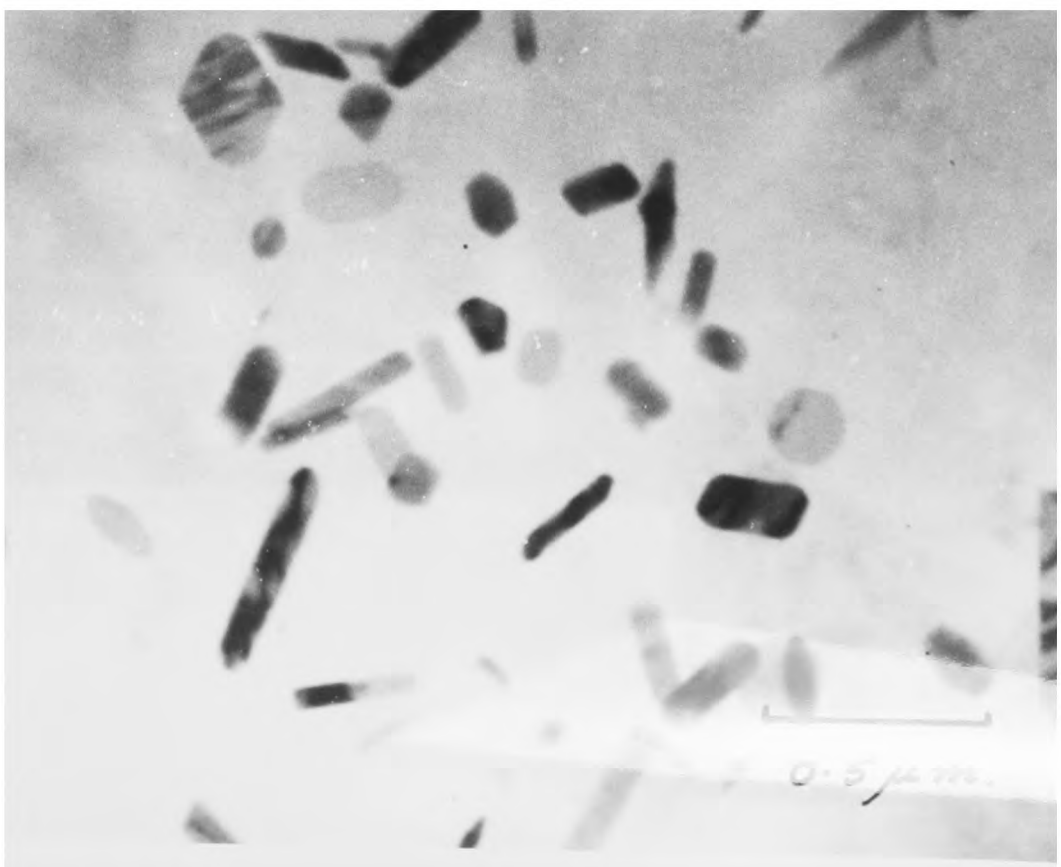
0·5μm.

Plate 3.28

T.E.M. of Cast BD8 after 30 minutes at 447°C.

Plate 3.29

T.E.M. of Cast BD8 after 30 minutes at 447°C, followed by solution heat treatment at 560°C for 30 minutes.

Plate 3.30

T.E.M. of Cast BD8 after 10 minutes at 581°C.

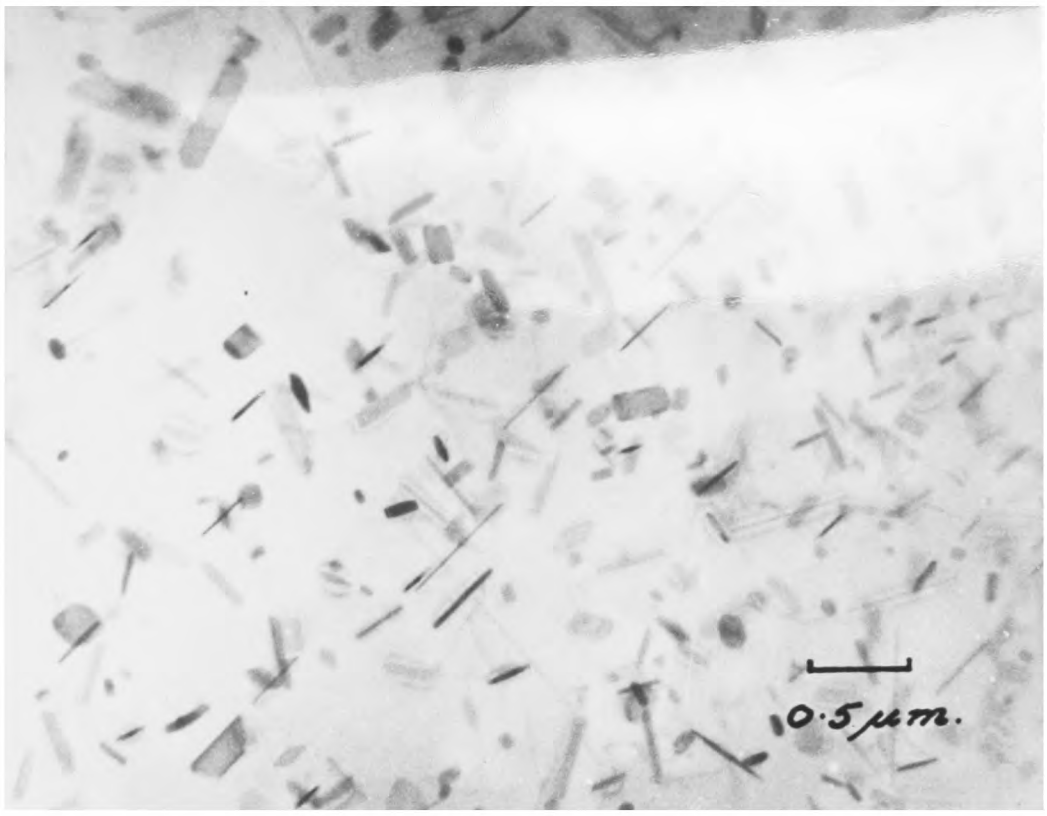
0·5μm.

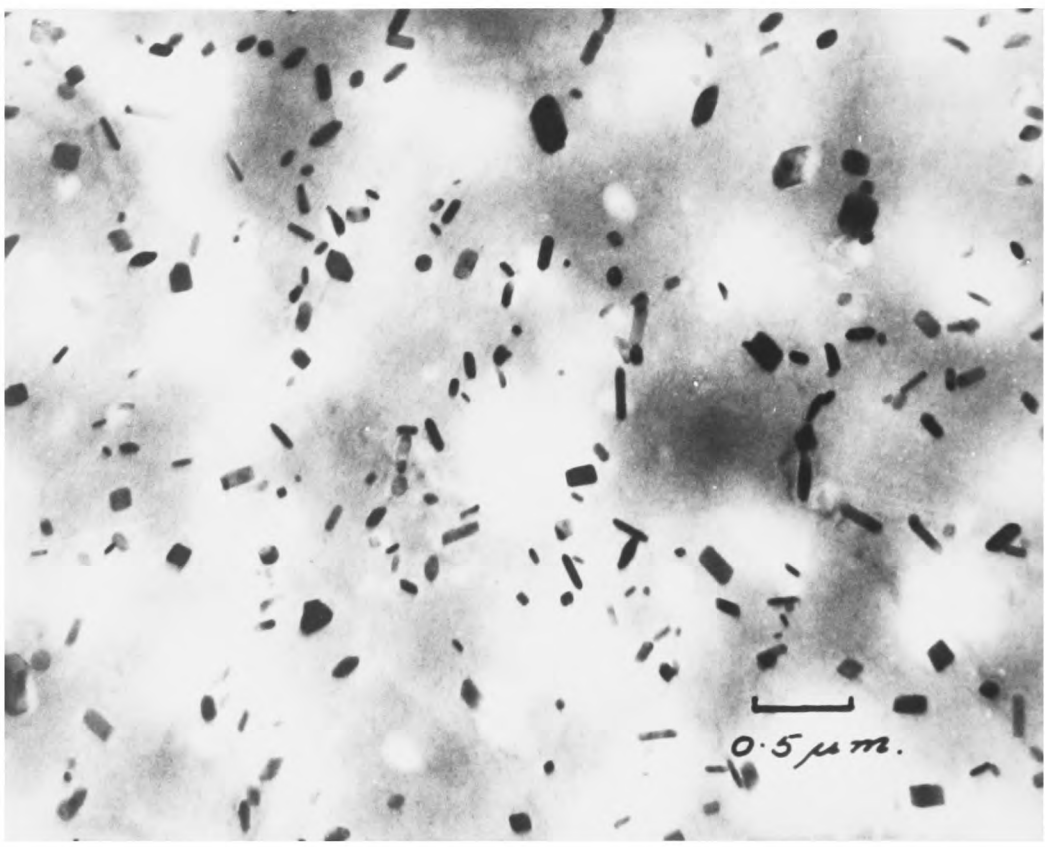
0·5μm.



Plate 3.31

Phase diagram of Al-Mg-Si - Solidus Surface.

(Reproduced from 'Equilibrium Diagrams of Al-Alloy Systems' (A.D.A.) editor H. W. L. Phillips, 1961).

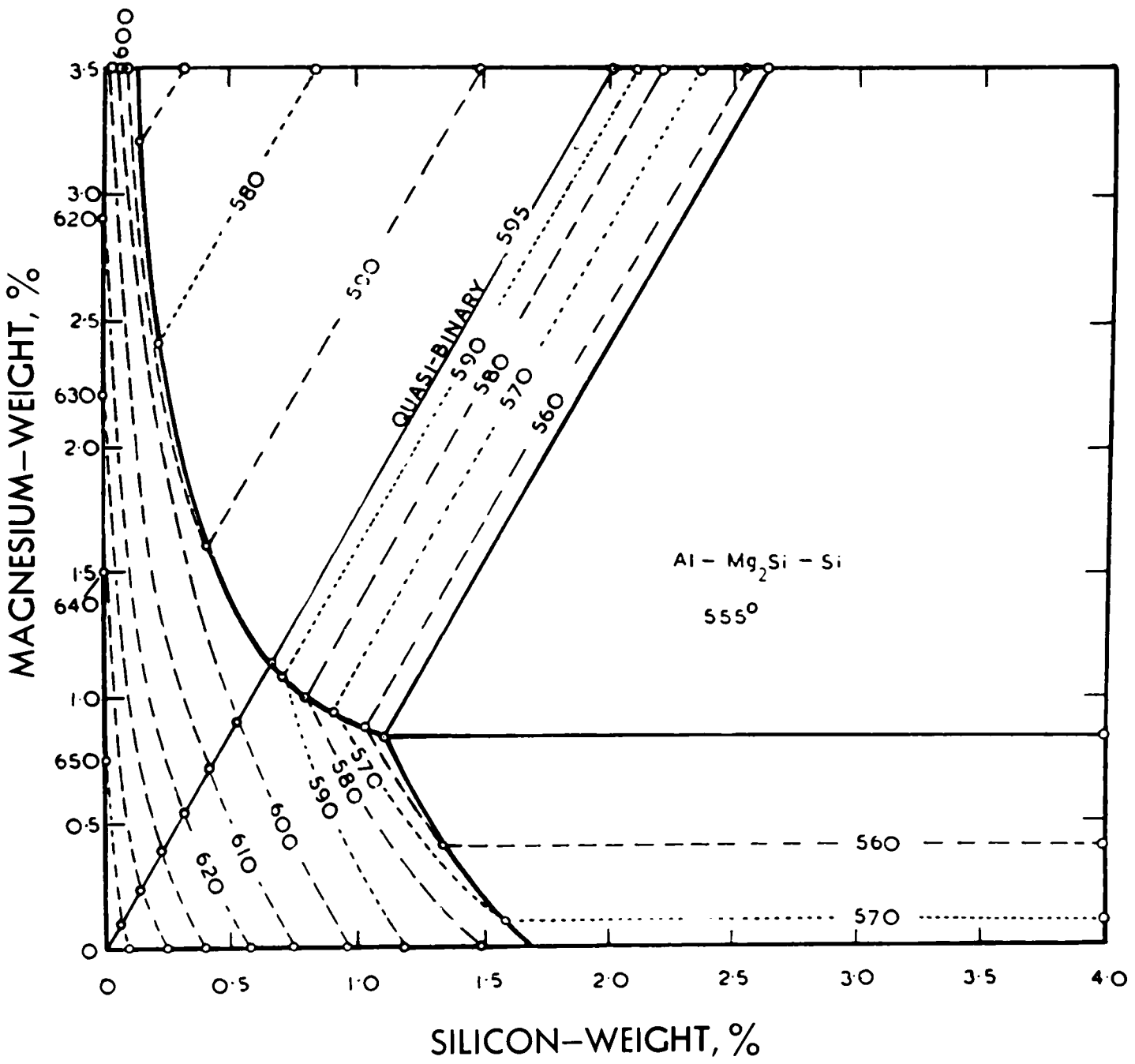
MAGNESIUM–WEIGHT, %
SILICON–WEIGHT, %
600
3·5
3·0
620
2·5
630
2·0
1·5
640
1·0
650
0·5
0
0
0·5
1·0
1·5
2·0
2·5
3·0
3·5
4·0
580
590
600
610
620
570
580
590
QUASI-BINARY
595
590
580
570
560
Al – Mg2Si – Si
555°
560
570

CHAPTER 4
DEFORMATION MECHANISMS

4.1. INTRODUCTION

The metallographic observations have provided some information about the microstructure of the three alloys. In this chapter, their mechanical behaviour is explored in order to detect any differences in dislocation distribution after deformation and to see how these may affect the fracture nucleation processes. Tensile behaviour at elevated temperatures is studied and this leads to a better understanding of crack propagation and failure in the alloys.

Propagation was also examined by optical metallography of work hardened specimens.

4.2. COMPRESSION TESTS

4.2a Results and Discussion of Work Hardening Behaviour

The stress-strain curves for the three alloys are shown in Fig. 4.1. The yield stresses of the alloys are similar and this is to be expected from the ageing data where the peak hardness values are also similar.

The initial work hardening rate (0.01% strain) for BD8 is about 1.30kg/mm^2; BD6 has work hardening rate of 0.86kg/mm^2 which is little higher than in BD3 (~ 0.84kg/mm^2). Two important factors which can alter the work hardening rate are grain size and dispersion size and distribution. Theoretically, using the equations of Ashby, 1970, (see Section 1.6a), the ratio of observed work hardening rates at a constant strain, for materials of different grain size is given by

$$\left(\frac{d\sigma}{d\bar{e}}\right)_1 : \left(\frac{d\sigma}{d\bar{e}}\right)_2 = \left(\frac{d_2}{d_1}\right)^{\frac{1}{2}} \qquad 4.1$$

where d_2 and d_1 are the grain size of the two materials. Using equation 4.1, the work hardening ratio of BD8 (d = 70μm) to BD6 (d = 100μm), ignoring any contribution from the particles, is 1.19, whereas comparison of the experimentally determined rates gives a value of 1.5. When the work hardening ratio is calculated in terms of particle radius, r, and volume fraction, F_V (Ashby, 1970), i.e.

$$\left(\frac{d\sigma}{de}\right)_1 : \left(\frac{d\sigma}{de}\right)_2 = \left(\frac{F_{V_1}}{r_1} \times \frac{r_2}{F_{V_2}}\right)^{\frac{1}{2}} \qquad 4.2$$

the ratio for BD8 ($F_V = 1.1 \times 10^{-2}$, r = 0.05μm) to BD6 ($F_V = 0.4 \times 10^{-2}$, r = 0.05μm) is 1.7, which is closer to the experimental value than the value based on the grain size difference.

The higher work hardening rate in BD8 indicates that the manganese intermetallic particles are tending to cause dislocation debris to be formed at the particles so that the slip bands will work-harden, thus causing slip bands to form elsewhere. In BD3, the dislocations will cut through the Mg_2Si precipitates and produce local softening of the slip plane and subsequent dislocations will glide preferentially along this path. However, this local hardening in BD8 must be a subtle effect, because if the intermetallic particles in BD8 raised the rate of work hardening excessively, then the strength of the grain interiors would be high in comparison with the grain boundaries, which contain precipitates, and this would lead to intergranular decohesion after small strains.

4.2b T.E.M. of Deformed Alloys

T.E.M. of foils prepared from compression specimens shows that initially all three alloys contain slip bands. For a given strain, the average spacing is highest in BD3 and smallest in BD8. The

spacing in BD3 does not change much with strain, but in BD6 and BD8 the spacing decreases with increasing strain. Fig.4.2 illustrates these results graphically. Eventually, it might be expected that BD6 and BD8 will no longer contain resolvable slip bands and the dislocation distribution will be homogeneous. This was, in fact, observed in BD8 after a compressive strain of ~ 9%, Plate 4.1. In BD6, after a similar strain, there was still evidence of slip in bands but these were not very distinct, Plate 4.2 and near the grain boundaries the dislocation distribution was uniform, Plate 4.3. In contrast, BD3 contained well defined slip bands and the inter-band regions were free of dislocations, Plate 4.4. The explanation of these effects is as stated in the previous paragraph.

The grain boundaries of BD6 and BD8 showed no signs of marked local distortion at strains up to 9%, Plates 4.3 and 4.5, but in BD3 there was some indication that the grain boundaries could be distorted, Plate 4.6, and this implies that the slip bands produce high localised stress concentrations at the boundaries.

4.2c Observations and Discussion of Slip Distribution

Since initially the three alloys contain slip bands, localised stress concentrations should arise in all three. An estimation of the relative stress concentrations can be made using Stroh's model (1954) for the two dimensional stress at the end of a thin slip band (McLean, 1975). For such a band meeting a grain boundary at an angle θ, the tensile stress, σ_s, normal to the boundary is

$$\sigma_s = 3\,\alpha\,\mathrm{Sin}\,\theta\,\mathrm{Cos}\,\frac{\theta}{2} \qquad 4.3$$

where

$$\alpha = \frac{\tau}{2}\left(\frac{d}{r}\right)^{\frac{1}{2}} \qquad 4.4$$

and τ is the applied shear stress, d the length of the slip band and r the distance from the point of contact. If d is taken to be the grain diameter then, all other things being equal, a slip band in BD3 will produce a local stress concentration at a boundary twice that in BD6 or BD8 due to the difference in grain size alone:-

$$\text{grain size of BD3} = 400\mu m;\quad d^{\frac{1}{2}} = 20\mu m^{\frac{1}{2}}$$

$$\text{grain size of BD6} = 100\mu m;\quad d^{\frac{1}{2}} = 10\mu m^{\frac{1}{2}}$$

$$\text{grain size of BD8} = 70\mu m;\quad d^{\frac{1}{2}} = 8.5\mu m^{\frac{1}{2}}$$

Slip band length is not the only factor which is important in fracture nucleation at boundaries. Equation 4.4 holds when the slip bands are narrow and also assumes a comparable slip band width in each case, which will not be true for the three alloys, where not only does the slip band spacing change from one alloy to another at a constant strain, but also the slip band width will be broadened by the presence of the manganese intermetallic particles tending to disperse the slip.

Evenson et al, 1975, have shown that the stress concentration for a slip band of width, W, can be expressed in terms of resistance to plastic flow within the band, σ_o, and the critical stress σ_{crit} required to nucleate fracture. If this is induced by the action of the applied stress, σ_{app}, and the stress concentration, ϕ, at the grain boundary, then for fracture nucleation

$$\sigma_{app} + \phi\,(\sigma_{app} - \sigma_o) > \sigma_{crit} \qquad 4.5$$

or

$$\sigma_{app} > \frac{\sigma_o + (\sigma_{crit}/\phi)}{1 + (1/\phi)} \qquad 4.6$$

If the slip band length is d (this can be taken as the grain diameter) and W is the slip band width

$$\phi \simeq \left(\frac{d}{W}\right)^{\frac{1}{2}} \qquad 4.7$$

and provided ϕ is much greater than unity,

$$\sigma_{app} > \sigma_o + \frac{1}{d^{\frac{1}{2}}} \left(\sigma_{crit} W^{\frac{1}{2}}\right) \qquad 4.8$$

Equation 4.8 gives a qualitative description of the effect of slip band width on stress concentration; slip confined in a narrow band will be more deleterious than when the slip is dispersed in a broad band. As the authors point out, the extent of slip band broadening depends not only on the microstructure of the grains but also on the slip distribution within the grains. Thus in BD3, where there are no non-deformable particles, it is reasonable to assume that the slip bands are narrow with a high dislocation density within them but in BD6 and BD8 the dislocation distribution within the bands is not so simple. Here the slip band spacing is smaller, so that for a given strain the dislocation density per band will be different from BD3, and the intermetallic particles will cause lateral spreading of the dislocation array. Hence the actual magnitude of σ_{crit} is not determinable for the alloys, but from the above reasoning it is probable that the stress concentrations at the head of a slip band will be smaller in BD6 and BD8 than in BD3, where it will be high, and this is supported by the observed grain boundary displacements.

These arguments can be rationalised in a semi-quantitative way in terms of the observed slip band spacing. Maximum stress concentration is produced by narrow bands, i.e. a minimum W, which is when the slip band spacing is a maximum. Minimum stress concentration occurs when slip is fully homogenized, i.e. when the slip band spacing is a minimum. This suggests that the slip band width, W,

can be expressed as

$$W \propto \frac{1}{\text{slip band spacing}} = \frac{1}{p} \qquad 4.9$$

Substituting this in equation 4.7, the stress concentration is now

$$\phi \propto (dp)^{\frac{1}{2}} \qquad 4.10$$

Using the values of p shown in Fig.4.2, $(dp)^{\frac{1}{2}}$ can be calculated for the three alloys at different strains. The values of $(dp)^{\frac{1}{2}}$ are given in Fig.4.3. The ratio of $d^{\frac{1}{2}}$ for BD3 : BD6 : BD8 is 1 : 0.5 : 0.41, but at any given strain the ratio of $(dp)^{\frac{1}{2}}$ always gives values for BD6 and BD8 which are less than those predicted by grain size alone. At ~ 1.6% strain, the ratio is 1 : 0.48 : 0.33 and after ~ 3.9% strain the ratio is 1 : 0.33 : 0.26. These results show how important slip band distribution is when considering stress concentrations at grain boundaries.

4.2d Fracture Processes in BD3

From T.E.M., it has been shown that the grain boundaries in BD3 can be distorted by the localised stress concentrations at the head of the slip bands (Plate 4.6). Since there are P.F.Z.s adjacent to the grain boundary and these regions are soft relative to the age-hardened grain interiors, the local stress concentrations may eventually lead to decohesion at the interface between the P.F.Z. and the grain boundary precipitates, which impose constraints on the homogeneous deformation within the P.F.Z. Once the voids are formed at the grain boundary precipitates, they should extend and coalesce within the P.F.Z. under the applied stress, because the interiors of the grains are harder than the P.F.Z.

If the fracture nucleation process in BD3 is one of void nucleation at the grain boundary precipitates and this leads to fracture by void coalescence in the P.F.Z., then the work of fracture for the latter must contain not only a surface energy term, γ_s, but also a plastic work term, γ_p, for the work done in shearing the P.F.Z. Evenson et al, 1975, have studied the intergranular failure of an Al - 0.62wt%Mg - 0.39wt%Si alloy and have calculated the work of fracture, $(=\gamma_s + \gamma_p)$, using equation 1.17, i.e.

$$\sigma_F = \frac{4\mu\gamma d^{-\frac{1}{2}}}{k_f}$$

(σ_F is the fracture stress for crack growth; γ, total work per unit area needed for continual crack growth; k_f, a measure of the difficulty of transmitting slip at the grain boundaries (i.e. the slope of the Petch plot); μ, shear modulus and d, the grain diameter).

When the alloy was fully age-hardened, they found that γ was of the order of 10^4 ergs/cm^2, which is higher than theoretical grain boundary surface energies. From S.E.M., they confirmed that the fracture path was intergranular and that the grain surfaces showed evidence of ductile failure. This latter observation would account for the large value of γ because of the extra work to propagate the crack in a ductile fashion.

Thus at this stage, the experimental evidence suggests that the fracture nucleation mechanism in BD3 is one of voiding at the grain boundary precipitates. Further support for this hypothesis arises from the appearance of the fracture surfaces of BD3 and this will be discussed later in section 4.4d.

4.2e The Possibility of Inducing Intergranular Failure in BD6 and BD8

In BD6 and BD8, it has been shown that the manganese intermetallic particles may cause lateral spreading of the slip bands. Hence, the corresponding stress concentration ϕ (from equation 4.10) at the grain boundaries is much less than in BD3, where the slip band width is very narrow. The absence of grain boundary distortion in BD6 and BD8 supports this idea. As in BD3, the grain boundaries of BD6 and BD8 also contain precipitates, but earlier work (Dowling, 1972) has shown no evidence of intergranular failure in BD8. This implies that the stress concentrations produced by the broadened slip bands are insufficient to nucleate voids at the grain boundary precipitates. However, if in BD6 and BD8, deformation occurred by slip in narrow bands and this could be maintained without lateral spreading, then these alloys might also fail intergranularly and show less ductility in spite of their small grain size.

Stewart and Martin, 1975, have investigated the effect of temperature on the deformation behaviour of single crystals of an Al - 0.5wt%Si - 0.45wt%Cu alloy, which was heat treated to produce approximately spherical particles of silicon, 0.1μm - 0.6μm in diameter. After deformation at room temperature and below, they found that primary dislocations were produced at the particles and also secondary dislocations in regions above and below the particles which intersected the primary slip planes. The initial work hardening rates in this temperature range were high. Deformation at temperatures above room temperature reduced the dislocation activity on the secondary slip planes and the dislocations were confined within the primary slip planes. This process was accompanied by a sudden drop in the rate of work hardening at about 100°C, because no dislocation debris was pro-

duced at the particles, since the particles were by-passed by a local climb process.

This work suggests that BD6 and BD8, which contain similarly sized 0.1μm intermetallic particles, may show a similar change in work hardening rate at elevated temperatures and hence become intergranularly brittle, due to the slip distribution no longer being homogenized.

Tensile tests have thus been carried out on all three alloys at 150°C and 185°C, as well as at room temperature, to investigate the dislocation structures and ductility at these temperatures and these are discussed in section 4.3a.

4.3. TENSILE TESTS

4.3a Ductility and Deformation Structure

The experimental procedure for the mechanical testing of cylindrical test pieces of BD3, BD6 and BD8 at elevated temperatures has already been described in sections 2.5 and 2.5b. Fig.4.4 gives the percentage elongation and reduction in cross sectional area after deformation to fracture at room temperature, 150°C and 185°C. BD3, the intergranularly brittle alloy, shows little variation in ductility (~ 1% elongation) at temperatures above room temperature. At each temperature, the reduction in cross sectional area (R.A.) was too small to be determined with any degree of accuracy and was probably only about 1 - 2%.

There was found to be a small increase in ductility for BD6 and BD8 at elevated temperatures and this was accompanied by an increased degree of % R.A. in each case. BD8, at 185°C, showed a value of ~ 73%

R.A. with an elongation of ~ 21%, whereas at room temperature the corresponding measurements were ~ 56% and ~ 17%. BD6 shows a similar increase in ductility, but the R.A. is not so pronounced as that observed in BD8.

The initial work hardening rate could not be measured with any degree of confidence, as the initial portion of the stress-strain curves always contained displacement effects due to some slipping in the grips. Thus it was not feasible to detect if the work hardening rate decreased significantly above room temperature.

From these exploratory tests, the increased ductility of BD6 and BD8 indicated that the deformation structure in these two alloys was such that it did not give rise to grain boundary stress concentration at temperatures up to 185°C. Tensile tests at temperatures higher than 185°C were not carried out, because of the probable over-ageing and thus changing the microstructure. The peak of the age hardening curves at 185°C is relatively flat, so that the time required for a tensile test at this temperature would not substantially alter the microstructure.

In order to investigate the slip distribution in BD8 and BD6 at elevated temperatures, thin foils were prepared from the fractured test pieces and these examined using T.E.M. The dislocation structures were compared with those in BD3 at the same temperatures. In the specimen tested at room temperature, the dislocation structures of the three alloys were similar to those observed in the compression tests. BD3 contained well defined slip bands with a spacing of ~ 3μm, Plate 4.7, while BD6 and BD8 contained a homogeneous tangle of dislocations, Plate 4.8. The deformation structure of BD3 was unaltered at 185°C; the slip was still in bands, but these were fewer in number.

Despite the increased ductility seen in BD6 and BD8 at 185°C, these alloys contained well defined slip bands at elevated temperatures, Plate 4.9 and 4.10. The slip band spacing in each case is ~ 1.5μm and the regions between the bands contain a low density of dislocations, Plate 4.11. This slip band spacing is comparable to that observed at low strains at room temperature in these alloys (see Fig. 4.2).

This dislocation structure may have been the result of recovery of the deformed materials after testing. As mentioned in section 2.5b, there was always a delay between the end of a high temperature test and quenching of the fractured test pieces to room temperature. To ascertain whether this 'annealing' was sufficient to change the dislocation distribution into bands, a test piece of BD8, fractured at room temperature, was annealed for 15 minutes at 185°C and the deformation structure re-examined using T.E.M.

This annealing treatment produced little change in deformation structure. The homogeneous dislocation array still persisted, though there was some evidence of dislocation re-arrangement, Plate 4.12. However, the structure is markedly different from that seen after deformation of BD8 at 185°C, Plate 4.10. This implies that the latter deformation structure is not produced by 'annealing' effects, but results from local climb processes at the particles during deformation at 185°C. This has reduced the effectiveness of the particles in homogenizing the slip process.

In spite of these well defined slip bands in BD6 and BD8, the metallography of deformation, which is described in section 4.4b indicates that they fracture transgranularly. It can only be concluded that the stress concentrations at the head of the slip bands are

inadequate to nucleate grain boundary fracture. Presumably local stress relaxation rates will be similar in BD3 at elevated temperatures and these are seen to be inadequate to prevent intergranular cracking in that alloy.

The reduced grain boundary stresses in BD6 and BD8, in comparison with BD3, at 185°C must therefore arise from (a) the finer grain size of the former and (b) the smaller slip band spacing for a given strain as has been discussed previously when considering room temperature behaviour (section 4.2c).

Though the high temperature tests failed to induce intergranular brittleness in BD6 and BD8, they did provide some information on the fracture processes in these alloys. These, together with observations from the notch bend tests and scanning electron microscopy of the fracture surfaces, are described and discussed in the following sections.

4.3b Discussion of Conventional Stress-Strain Curves

BD3, which shows little variation in ductility at elevated temperatures (see Fig.4.4) has a lower yield stress and fracture stress at elevated temperatures, Fig.4.5, but the form of the conventional stress-strain curve does not change with increasing temperature. However, the conventional stress-strain curves of BD6 and BD8 do change with increasing temperature, Figs.4.6 and 4.7, and the salient data for these curves are tabulated in Figs.4.8 and 4.9. The lowering of the yield stress at 150°C and 185°C, seen in all three alloys, results from the decrease in Young's modulus with increasing temperature and thermal activation of dislocation processes at yield. These thermal activation processes will also lower

the general stress level of the curves of the alloys.

At a given temperature, localised deformation always starts at a lower strain in BD8 than in BD6. At room temperature, this occurs at ~ 11% elongation in BD8 and ~ 14% elongation in BD6. With increased temperature, the onset of localised deformation is shifted to lower strains.

From the compression tests, it is known that BD8 initially work hardens slightly faster than BD6 at room temperature. From Considere's criterion, a material with an overall lower work hardening rate, will reach the U.T.S. point at a strain which is smaller than that for a material with a high work hardening rate. Therefore at room temperature, BD8 is expected to reach its U.T.S. at a larger strain than BD6. The fact that BD8 reaches its U.T.S. at a smaller strain than BD6 implies that its rate of work hardening must decrease more rapidly than that of BD6.

Again, since the U.T.S. point occurs at lower strains at the elevated temperatures for both alloys, this implies that the work hardening rates of BD6 and BD8 are decreasing with increasing temperature. This is to be expected as thermal activation enables dislocations to climb around the particles in the slip planes, thus the slip planes do not work harden so rapidly.

The above explains why the U.T.S. point is earlier in BD8 than in BD6, but says nothing about the structural changes which determine the relative changes in work hardening rate.

Broek, 1972, has shown that large particles (~ 10μm) in aluminium alloys can initiate voids at strains as low as a few percent, but the alloys do not fail until ~ 25% strain. Cox and Low, 1974,

have shown that the stress to nucleate a void at a particle of diameter D is proportional to $D^{-\frac{1}{2}}$, therefore a greater stress will be required to open up voids at small particles than at larger ones. In BD6, there are fewer of the coarse ~ 5μm particles (see section 3.3) than in BD8 and these particles tend to be slightly smaller than in BD8. Therefore voids are expected to form at the coarse particles at smaller strains in BD8.

Optical examination of room temperature fractured test pieces of BD8 has shown that voids do exist at the coarse particles not only in the necked region but also in region towards the gripped end of the specimen which has only undergone uniform elongation. Voids at particles are also seen in BD6 in the region well away from the neck, but the voids are smaller and fewer than in BD8.

It is considered that the progressive formation of cavities associated with the large inclusions will effectively reduce the work hardening rate of the material. Since such voids are more prolific in BD8 than in BD6 this progressive porosity will cause the rate of work hardening in BD8 to fall below that of BD6 as the strain increases, so that the U.T.S., i.e. plastic instability, will be observed at smaller strains in BD8 than in BD6.

This model also explains why the U.T.S. occurs at lower strains at 150°C and 185°C. At these temperatures, the work hardening rate is lower so the matrix between the coarse particles is softer, therefore voids are formed at lower strains because (a) the work of decohesion is less and (b) the process is assisted by thermal activation.

Beyond the point of the U.T.S., the localised deformation strain

is more extensive in BD8 than in BD6 at a given temperature. As the temperature increases, this region of localised deformation increases in both alloys. At any temperature, the conventional stress-strain curve of BD8 drops more steeply than in BD6 except in the last 1% (approximately) strain before fracture, where the curve of BD6 drops sharply (cf Figs.4.6 and 4.7). The shape of the curves beyond the U.T.S. reflects the processes of further void formation as well as void growth and coalescence. Since these processes define important fracture parameters, they will be discussed separately in Section 4.4

4.3c Discussion of Fracture Stresses

Neglecting triaxiality effects due to the neck, when the true fracture stress (applied load/final cross sectional area) is calculated, BD8 always fractures at a higher stress than BD6 for a given temperature and the fracture stresses of both alloys decrease with increasing temperature. At room temperature, the fracture stresses are 64.6kg/mm^2 for BD8 and 43.5kg/mm^2 for BD6. At 185°C, the corresponding values are 52.5kg/mm^2 and 38.7kg/mm^2. For comparison, the fracture stresses of BD3 are 33.4kg/mm^2 at room temperature and 26.0kg/mm^2 at 185°C.

It must be remembered that these are the stresses needed to propagate an existing crack and they supply no information on the stress required to nucleate fracture. This is especially true of BD3 where fracture is initiated by internal, high, localised stresses, but the fracture stress reflects the work done in propagating fracture along the grain boundary path. As reported in Section 4.2d, Evenson et al, 1975, calculated this energy term, γ, from

$$\sigma_F = \frac{4\gamma\mu d^{-\frac{1}{2}}}{k_f}$$

and found that for a fully aged Al-Mg-Si alloy, γ was ~ $10^4 ergs/cm^2$ and k_f was $0.7MN/m^{3/2}$. These values will apply approximately to BD3. If they are assumed to be valid for BD6 and BD8, then their theoretical fracture stresses for intergranular failure can be calculated using the following relationship:

$$\sigma_F \text{ (BD3)} : \sigma_F \text{ (BD6)} = (d^{-\frac{1}{2}})_{BD3} : (d^{-\frac{1}{2}})_{BD6}$$

This gives values of 67.0 kg/mm^2 in BD6 and 79.5 kg/mm^2 in BD8. The actual fracture stresses in BD6 and BD8 are a good deal less than these calculated values, so that the alloys must fracture by an alternative mechanism. The observed intergranular fracture process is likely to be related to the presence and distribution of the intermetallic particles in the two alloys.

In the previous section, the role of the coarse, ~ 5μm particles in determining the onset of ductile fracture processes has been discussed. Since voids form at these particles at a relatively early stage in the deformation process, especially at 150°C and 185°C, and fracture takes place at much longer strains, it would seem that the coarse particles are not a very critical factor in fracture propagation processes.

Apart from the ~ 5μm intermetallic particles in BD6 and BD8, there are also the 0.1μm intermetallic particles. In BD6, the volume fraction of these particles is 0.4×10^{-2} and in BD8, it is 1.1×10^{-2} and the fracture stress in BD8 is higher than BD6. Thus it appears that increasing the 0.1μm particle volume fraction results in a higher fracture stress and it is suggested that this may arise by the 0.1μm particles having the effect of impeding crack propagation.

4.4. METALLOGRAPHY OF FRACTURE

4.4a Optical Metallographic Observations

Optical examination of the fractured test pieces of BD6 and BD8 indicated that the hypothesis of crack stopping by the 0.1μm particles holds some truth. Longitudinal sections of test pieces from all three alloys were examined after deformation at 20°C, 150°C and 185°C.

At all three temperatures, BD3 clearly fractured along its grain boundaries, Plate 4.13, and internal cracks along the grain boundaries, close to the plane of fracture, were observed. Presumably, these have not propagated because the orientations of the adjacent grain boundaries do not provide an energetically favourable path.

The room temperature fractured test piece of BD6 contained a number of coarse voids in the necked region and these were often associated with narrow cracks which lay at 45° to the tensile axis. The micrograph in Plate 4.14a shows the appearance of these voids before etching. Plate 4.14b shows one such feature at a higher magnification. It was also observed that the profile of the fracture surface was serrated, but these serrations were not of the same coarseness as seen in BD3.

BD8 also contained voids in the necked region, but these were of the coarse, spherical variety, Plate 4.15a, but at higher magnifications these voids were seen to be associated with fine, 45° cracks, Plate 4.15b. The coarse voids were frequently found adjacent to and between the coarse residual casting particles (~ 5μm in size); in BD6, these coarse voids could not be identified with the casting particles, but this might be explained by the fact that these particles are smaller than in BD8. The 45° cracks observed in BD8 have not extended to any

great extent; their length is at the most 10μm. In BD6 the lengths of the 45° cracks are between 50μm and 100μm long. The 45°cracks are only seen in the necked region.

After electrolytic etching, the 45° cracks in BD6 appeared in some cases to lie along 45° grain boundaries, but this was not always the case as seen in Plate 4.16. The grains themselves have become elongated in a direction parallel to the tensile axis. BD8, after etching, provides less information about the relative positions of the voids, Plate 4.17. BD8 necks down further than BD6 (see Fig.4.4) with the result that the grain boundaries are not easily discernible in the highly strained region of the neck.

After fracture at $150^{o}C$ and $185^{o}C$, a larger number of the coarse voids are seen in both BD6 and BD8, Plates 4.18 and 4.19. BD8 contains many smaller voids which are elongated in the direction of the tensile axis. Again these are associated with the residual casting particles, but in this case the smaller ones. These small voids are seen in BD6 too as well as the coarse voids and the 45° cracks. After etching, the alloys are similar in appearance to the room temperature test pieces, Plates 4.20 and 4.21.

4.4b Discussion of Metallographic Observations

The type of voids seen in BD6 and BD8 have been observed in other materials. Cox and Low (1974) investigating the plastic fracture of an AISI 4340 steel, observed optically that large voids were formed around the manganese sulphide inclusions in the material. These voids had coalesced by the formation of a sheet of voids which had the appearance of a thin crack and lay at 45° to the tensile axis. The voids in this sheet were thought to be nucleated at the cementite

particles which precipitated on the martensite lath boundaries.

More recently, Van Stone and Psioda, 1975, have reported on the void formation in aluminium alloys. They conclude that the fracture process consists of three stages - void initiation, void growth and void coalescence. In the first stage, large voids are nucleated at large coarse second phase particles (1 to 10μm in size) by cracking. (Hahn and Rosenfield, 1973, have shown that such coarse particles are more liable to cracking because they are large enough to contain cracks or surface defects which can initiate fracture of the particles at relatively low stresses). After further deformation, the two faces of the fractured particle separate and the void grows into the matrix. The extent of void growth increases with increasing spacing to size ratio of the void nucleating particles. The final stage in the fracture of fully aged aluminium alloys is the coalescence of the large voids by formation of void sheets. So far, the above authors have only fully investigated these features in a 2124-T851 aluminium alloy. Using optical microscopy, they show that large voids form at the coarse particles and these are connected by void sheets which are approximately at 45° to the tensile axis. The void sheets are believed to be a sheet of submicron dimples initiated at 0.1μm particles, which are present in the matrix, by interface decohesion.

These reports suggest how the voids in BD6 and BD8 are nucleated (i.e. by the coarse particles) but supply no explanation for the brevity of the 45° cracks in BD8 or the extended crack length in BD6. Returning to the argument of Van Stone and Psioda, they maintain that the extent of void growth is proportional to the ratio of spacing to size of the void nucleating particles. If this is true for these coarse particles, it should also hold for coalescence of voids at the 0.1μm particles. Writing down the proportionality

$$\text{length of void sheet} \propto \frac{\text{particle spacing}}{\text{particle diameter}} \qquad 4.11$$

it is seen that in BD6 and BD8, where the 0.1μm manganese intermetallic particle diameters are similar, but the particle spacing in BD6 is larger than in BD8, equation 4.11 correctly predicts a longer void sheet in BD6, but still no conclusions can be drawn about the mechanics of the process, except that decreasing particle spacing must reduce the length of void sheet. It appears that the 0.1μm particles impose barriers to ductile fracture propagation and their efficacy depends on the particle size and volume fraction.

4.4c Inhibition of Ductile Fracture Propagation by Small Particles

Hahn and Rosenfield, 1973, have shown empirically that the plane strain fracture toughness, K_{IC}, of a material can be expressed in terms of the particle spacing, assuming that all particles either decohere or fracture.

$$K_{IC} \approx \sqrt{2\,\sigma_y\, E\, \lambda_c} \qquad 4.12$$

where σ_y is the yield stress, E is the elastic modulus and λ_c is approximately the ligament width between the particles. Using the approximation

$$F_V \simeq \frac{D^3}{\lambda_c^3} \qquad 4.13$$

where D is the particle diameter and F_V is the volume fraction of the particles, then

$$K_{IC} \propto D^{\frac{1}{2}}\, F_V^{-1/6} \qquad 4.14$$

This implies that alloys containing particles with a large diameter

will be more resistant to fracture than those with small ones, but Cox and Low, 1974, have observed that in marraging steels, where void initiation occurs by cracking of inclusions, the stress necessary for void initiation is proportional to $D^{-\frac{1}{2}}$. Further, when the steels had virtually the same particle spacing, but different particle size, the greatest fracture toughness was observed for the smallest particle size.

In respect of these observations, Van Stone and Psioda suggest that the stress necessary for void initiation is given by

$$\sigma_{void} \propto D^{-\frac{1}{2}} \qquad 4.15$$

or

$$\sigma_{void} \propto \lambda^{-\frac{1}{2}} F_V^{-1/6} \qquad 4.16$$

Substituting the values of the mean free path, λ, and volume fraction, F_V, of the 0.1μm particles for BD8 and BD6 in equation 4.16,

$$\sigma_{void}\ (BD6) \propto (27.7)^{-\frac{1}{2}}(0.4 \times 10^{-2})^{-1/6} \simeq 0.48$$

and

$$\sigma_{void}\ (BD8) \propto (8.9)^{-\frac{1}{2}}(1.1 \times 10^{-2})^{-1/6} \simeq 0.72$$

These results are in the ratio of 1.5 : 1 for σ_{void} (BD8) to σ_{void} (BD6) and indicates that void nucleation at these small particles in BD8 requires a greater stress than in BD6.

It is interesting to note that the ratio of fracture stresses for BD8 : BD6 is 1.5 at room temperature, 1.4 at 150°C and 1.4 at 185°C. This suggests that the difficulty of void nucleation at the 0.1μm particles might be responsible for the high ductilities and fracture stresses of BD6 and BD8. It is therefore proposed that the 0.1μm particles can act as inhibitors to the propagation of

ductile fracture by the coalescence of voids formed previously at the coarser particles. The interlinking of such voids by the formation of cavities at the 0.1μm particles in the ligaments will be more difficult in BD8 than in BD6 for the above reasons, so the hypothesis can explain both the metallographic observations and the extent of localised elongation observed in the tensile curves of the alloys.

The process of void formation at sub-micron particles has been observed by Broek, 1972, during in-situ deformation of a 7075 aluminium alloy in the electron microscope. A crack, impinged on the surface of a sub-micron particle, did not produce instantaneous decohesion or cracking; further straining was required to propagate the crack around the particle. From this he concludes that the cohesive forces between matrix and intermetallic particles in aluminium alloys must be extremely large to withstand such high stresses at the particle-matrix interface.

From this, it is now understood why voids do not spread so easily in BD8. Any void trying to move forwards in BD8 will encounter a large number of particles in its path and a large increase in stress is needed to overcome these obstacles. In BD6, an extending void will meet fewer particles in its path and so a smaller stress increase is needed to propagate the void past the particles. In both alloys, the extent of void growth will be governed by the local plastic strain which,away from the narrowest part of the neck, is insufficient to propagate the void significantly.

4.4d Proposed Fracture Processes in BD6 and BD8

All this information can now be used to describe the possible

fracture processes which take place in BD6 and BD8. Initially small voids are formed at the coarse, ~ 5μm, intermetallic particles. This probably occurs at low strains prior to the onset of localised deformation. As the voids grow, the work hardening of the alloys is eventually no longer sufficient to maintain uniform elongation and localised deformation begins.

In BD8, after the U.T.S., voids continue to form at the coarse intermetallic particles and these voids will extend and coarsen along the direction of the tensile axis under the action of the applied stress. The voids do not extend in the form of 45° cracks across the specimen because of the high density of 0.1μm particles which act as a barrier to fracture propagation. As the test proceeds, the strain becomes sufficient to open up voids at smaller particles, and eventually, voids begin to form at the 0.1μm particles. When voids have formed at nearly all the 0.1μm particles, the alloy fails by breaking of the ligaments between these voids.

In BD6, after the U.T.S., voids at the ~ 5μm intermetallic particles will coarsen. The voids can extend laterally by way of 45° cracks because BD6 contains fewer 0.1μm particles and thus present a smaller barrier to an extending crack. When the strain is high enough, these cracks can rapidly extend across the narrowest part of the neck because of the paucity of 0.1μm particles and the alloy fails suddenly.

The voiding at the 0.1μm particles must take place very close to the final rupture. Broek, 1972, has investigated the fracture processes in thirteen aluminium alloys and has observed void formation at the sub-micron particles in only a few cases, even in the highly strained state. BD6 and BD8 were examined in T.E.M. to see if voids

could be detected in highly strained material, but without success. Some cracked particles were seen, Plate 4.22, but in all cases these were excessively elongated or large particles. Broek has seen only a few cracked particles and these were in two aluminium alloys, where the dispersoid particles had an elongated habit. This paucity of voids at sub-micron particles, either by decohesion or particle rupture, he suggests is due to the process requiring high stresses or strains such that conditions for coalescence are fulfilled simultaneously.

This latter condition of high stresses or strains must be important, because at 150°C and 185°C the region of localised deformation in BD6 and BD8 dominates the nominal stress-strain curve. The optical metallography has shown that at these temperatures the necked regions of the two alloys contain a higher density of coarse voids than is seen after fracture at room temperature. This emphasises how resistant the 0.1μm particles are to crack propagation and void formation.

In summary, therefore, since BD8 and BD6 show similar total elongation to fracture (yet an earlier plastic instability in BD8), the role of the various inclusions may be stated:

a) Coarse, ~5μm particles nucleate ductile rupture. This occurs earlier in BD8 because the volume fraction of coarse particles is larger than in BD6.

b) Fine 0.1μm particles act as inhibitors to fracture until a very late stage of deformation. Since BD8 contains a higher volume fraction of 0.1μm particles than BD6, this accounts for the greater degree of localised deformation observed.

4.4e Fractography of BD3, BD6 and BD8

If the proposed models for fracture in BD6 and BD8 are correct, then their fracture surfaces should show fractographic differences. As reviewed by Broek (cit.loc.), ductile shear is characterised by shallow parabolic dimples, while ductile rupture produces equiaxed, deep, dimples. Therefore in BD6, where the fracture process has been suggested to be predominantly one of shear, the fracture surface should consist of parabolic dimples, whereas in BD8, where fracture would seem to occur by rupture of ligaments between the manganese particles, the dimples will be equiaxed. BD3, which fractures intergranularly, will have an atomically smooth surface if the boundaries are broken open by cleavage, but if fracture proceeds by void formation around the grain boundary particles then the grain surfaces should be covered with dimples.

Reports of the fracture surfaces of BD8 and BD3 after room temperature deformation have been given previously (Dowling, 1972). Since then, further S.E.M. examinations have been carried out and particular attention was given to the nature of the surface dimples in the three alloys.

At low magnifications, the fracture surface of BD3 is typical of a material which has failed intergranularly, Plate 4.23. The grain boundary surfaces appear smooth and planar and the sharp ridges reflect the equiaxed grain structure seen in the polished, optical sections. Some debris is seen, usually at the junction of two steeply inclined boundary planes. This probably arises because it is easier for the advancing crack to shear across a grain corner rather than follow the grain boundary path through a sharp angle. On the right hand side of the micrograph, there can be seen one such

grain which has been sheared across its corner.

At higher magnifications (~ 5000 times), the grain surfaces no longer appear featureless, Plate 4.24. They are covered with shallow dimples which are slightly parabolic and vary in diameter between 0.5μm and 1μm. These measurements correspond closely to the average spacing of the grain boundary precipitates in BD3, ~0.5μm. Broek has also analysed dimple spacing in aluminium alloys and found that there is roughly one to one correspondence between dimple diameter and particle spacing. (He defined the average inclusion distance, $\bar{s}$, as $\bar{s} = (N/A)^{-\frac{1}{2}}$ where N was the number of particles in an area A of a thin foil. Thus $\bar{s}$ is the inclusion distance in a flat sheet of the thickness of the electron microscope specimen. This is essentially, therefore, a 'mean planar' spacing, which may well not be the appropriate parameter in the context of ductile fracture - see later). Therefore each dimple should correspond to a void formed round a single particle. However the dimple size tended to be larger than the particle spacing and Broek concluded that this would result where void initiation does not occur at every inclusion.

Thus fracture in BD3 must take place by void formation at the grain boundary particles and the shearing of the ligaments between the voids. This process can take place at a low stress level, because the matrix adjacent to the grain boundary is the soft region of the P.F.Z. and deforms more easily than the precipitation-hardened grain interiors.

Plates 4.25 and 4.26 show micrographs of the room temperature fracture surfaces of BD6 and BD8. Compared with BD3, BD6 shows certain similarities - the surface is faceted with ridges - but BD8 has a fibrous appearance with a high density of voids. At a slightly

higher magnification, the voids and dimples in BD8 are more clearly seen. They can be divided roughly into three groups - very coarse and deep ones, ~10μm across, intermediate, equiaxed dimples, ~ 2μm across and shallow ones, also ~ 2μm across. The latter are not resolvable at this magnification. Plates 4.27 and 4.28 contain examples of the three dimple types.

The very coarse dimples seen in Plate 4.27 must correspond to the large voids seen in the optical examination of the fractured test pieces. These are formed at the very coarse intermetallic particles and spread laterally and longitudinally. On the surface of these large dimples, smaller dimples, ~ 2μm in diameter can be seen. These must be produced by voids formed at some of the 0.1μm manganese particles. Plate 4.28 shows their equiaxed shape and the diameter is between 1 and 2μm which is consistent with their being associated with some of the 0.1μm particles whose nearest neighbour distance, Δ_3, is 0.3μm in BD8. In the 'foreground' of this micrograph, the dimples are very shallow and indicative of a shear process. This probably occurs in the final moments before fracture, when nearly all the material in the neck has fractured by ductile rupture, leaving only a few regions intact.

The fracture surface of BD6 contains the large dimples (~ 10μm diameter) corresponding to voids being nucleated at coarse (~ 5μm diameter) particles. The surface facets which are 50 - 100μm across, are not smooth. There are small ridges on these 'flat' regions and at high magnifications, shallow dimples are seen in some of these areas and these are ~ 3μm in diameter, Plate 4.29. It should be noted that the shallow dimples seen in Plate 4.29 may not be typical of the fracture surface of BD6, since dimples were not resolvable

on many of the 'flat' areas. Such relatively smooth regions might be expected in BD6 where fracture takes place by propagation of voids, which meet few 0.1μm particles in their paths. The nearest neighbour distance of the 0.1μm particles in BD6 is 0.5μm and this implies that the dimples are again formed at a proportion of the manganese particles. The absence of deep equiaxed dimples produced by ductile rupture confirms the hypothesis that fracture proceeds by shear in BD6.

It is probably unwise to attempt to establish a close quantitative correlation between rupture dimples on the fracture surface of a ductile material with the distribution of the inclusions in the material prior to deformation. During the final plastic parting, very high local plastic strains take place and the narrowing of the neck itself will have the effect of bringing particles closer together. For example in BD8, where the reduction in cross sectional area is ~ 56% at room temperature, reduction of the interparticle spacing by a factor of $\frac{1}{2}$ appears likely in the narrowest part of the neck. This makes correlation between dimple diameter and the originally observed particle spacings, (either the mean free path or the nearest neighbour distance) of uncertain validity.

4.4f Crack Propagation in Notch-Bend Tests

These fractographic observations seem to support the proposed fracture mechanisms for BD3, BD6 and BD8. In conclusion, it is instructive to consider the deformation processes as cracks are slowly propagated across the alloys. The notch bend tests were devised to produce information on the path which a crack followed. The experimental details have been described in section 2.5c.

Plate 4.30 shows how, in BD3, the crack originates in the grain boundary which is most favourably orientated in the stress field. In this case, the preferred grain boundary is at right angles to the bending shear. The crack then moves away from the notch as the strain is increased, selecting those boundaries which provide the easiest path. Of course, the polished section only shows the grain boundary profile and this gives no information about the orientation of the grain surface within the bend specimen. Thus in the early stages where the crack appears to change its direction by ~ 90°, this is probably because the grain surfaces are suitably orientated for de-cohesion within the bulk material. The final photograph in this sequence shows that the grain boundaries can shear along each other to accommodate the increasing strain. Plate 4.31 shows the complete crack after extensive strain. There is only a small plastic strain field around the crack and the slip bands are quite distinct. Several subsidiary cracks can be seen near the main crack. These have not grown because either they are not in the region of highest stress or because the orientations of the adjacent grain boundaries do not provide an energetically favourable path.

BD6 and BD8 provide less detailed information about their fracture paths, because the process of crack propagation is accompanied by large amounts of plastic strain which cause distortion of the surface. Plate 4.32 shows the first stages of crack propagation in BD6. The crack does not start to form until there is a high plastic strain in the notch region and, as in BD3, selects a path which follows the regions perpendicular to the shear strain. Plate 4.33 shows the fully propagated crack. The region of plastic strain around the crack tip is larger than in BD3 and the slip lines are only discernible well away from the fracture path. BD8, Plate 4.34,

behaves in a similar way to BD6, but the nucleation and the propagation of the crack evidently requires a greater degree of local plastic deformation. The slip lines are not easily detectable and Plate 4.35 shows that there are few if any subsidiary cracks associated with the main crack, whereas in BD6 there are a number of secondary cracks branching from the main crack. The latter confirms the suggestion that cracks can spread more easily in BD6 where the density of manganese particles is low.

Fig.4.1

Conventional stress-strain curves for fully-aged alloys, BD3, BD6 and BD8. (Compression).

FIG. 4.1

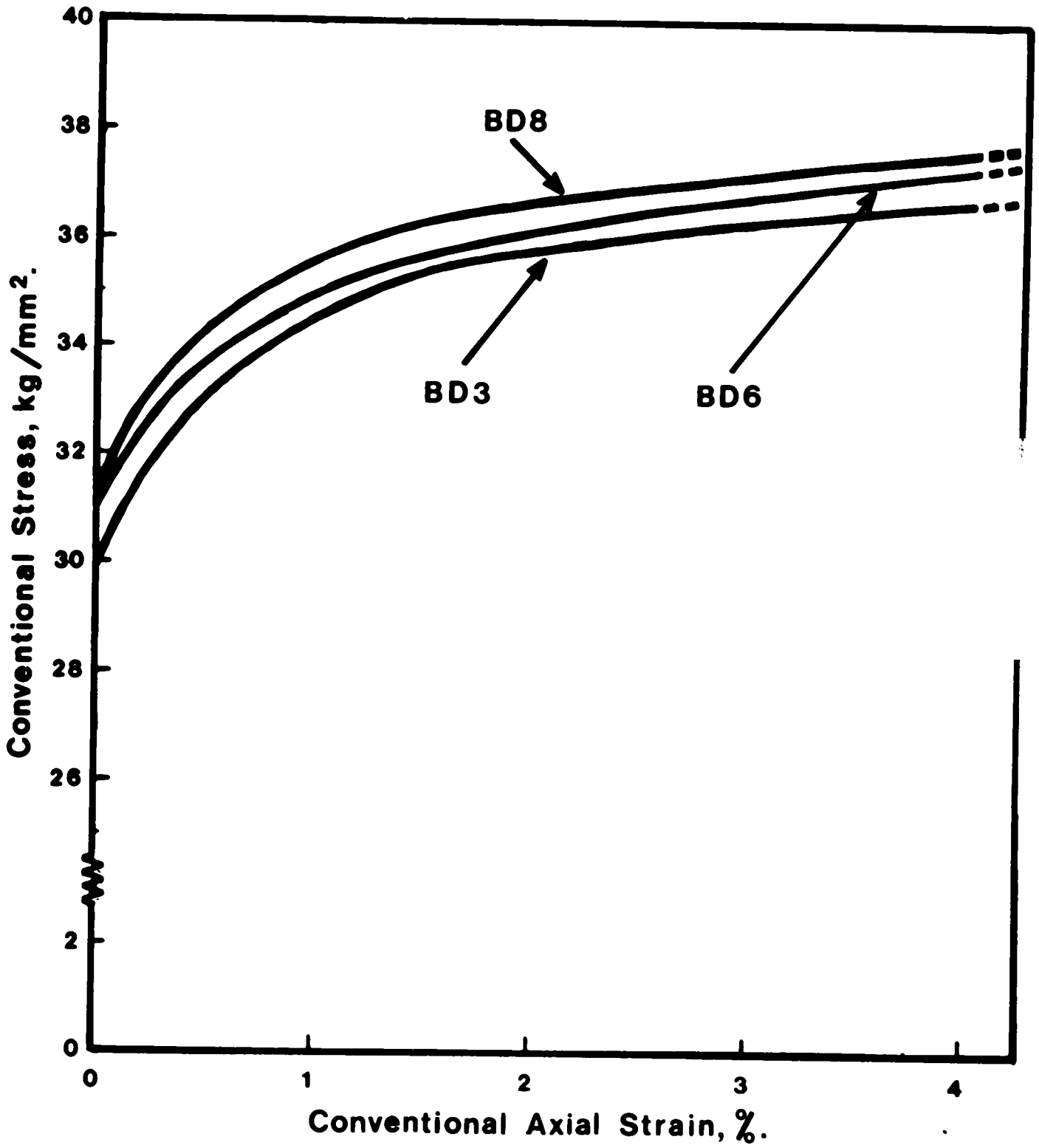
40
38
36
34
32
30
28
26
2
0
BD8
BD3
BD6
Conventional Stress, kg/mm².
0
1
2
3
4
Conventional Axial Strain, %.

Fig.4.2

Slip band spacing in BD3, BD6 and BD8 as a function of conventional compressive strain.

FIG. 4.2

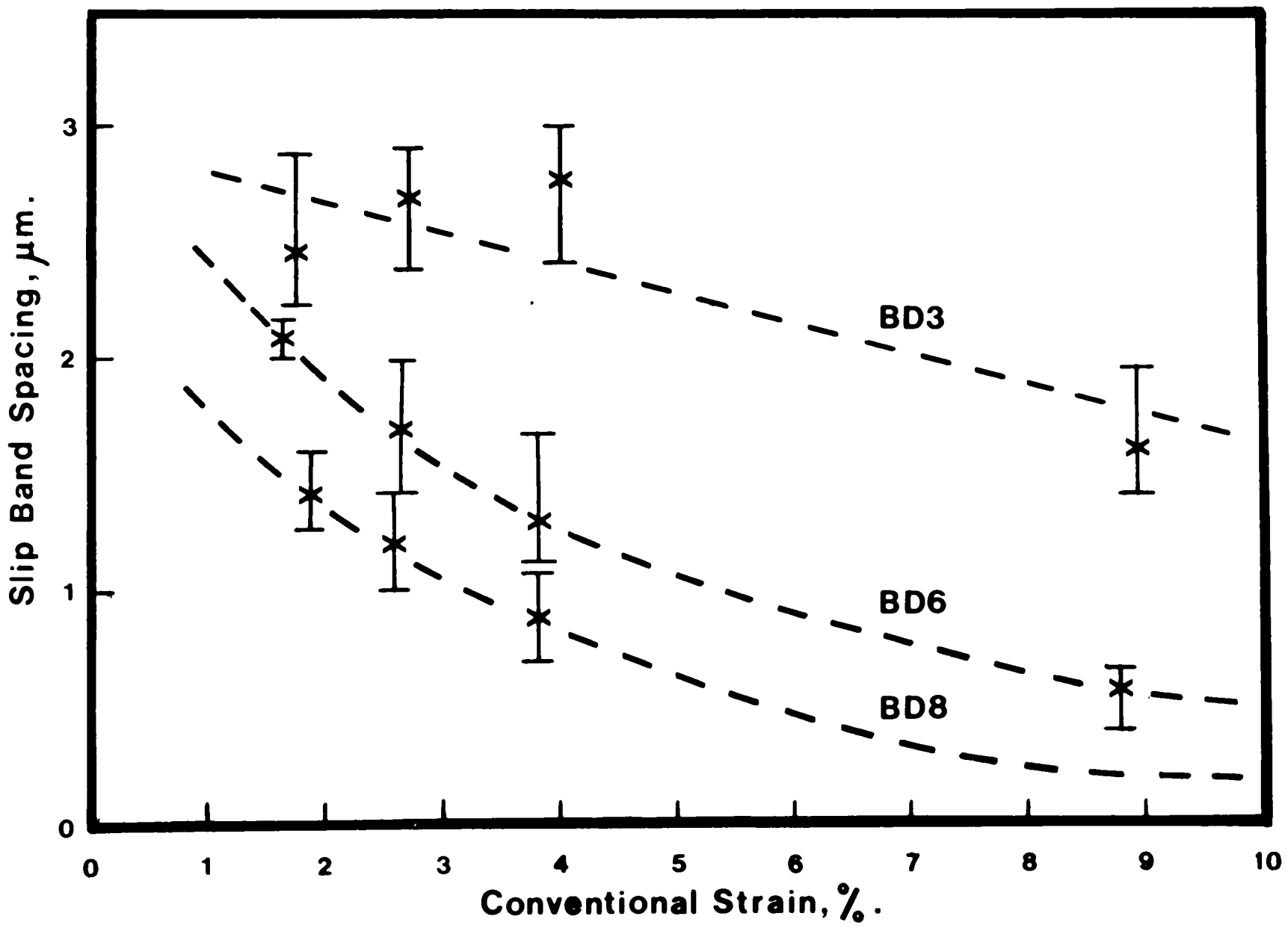
Slip Band Spacing, μm.
3
2
1
0
BD3
BD6
BD8
0
1
2
3
4
5
6
7
8
9
10
Conventional Strain, %.

Fig.4.3

EFFECT OF SLIP BAND WIDTH ON GRAIN BOUNDARY STRESS CONCENTRATION IN ALLOYS BD3, BD6 AND BD8.

Ratio of stress concentration factor, ϕ, calculated at various strains in terms of the slip band spacing, ρ, and grain diameter, d,

$$\phi \simeq \frac{d}{W}^{\frac{1}{2}} \propto (d^{\frac{1}{2}} \rho^{\frac{1}{2}})$$

where W is the slip band width. (See section 4.2c).

a) ~ 1.8% elongation

b) ~ 2.6% elongation

c) ~ 3.9% elongation

d) ~ 9.0% elongation

Fig.4.3

(a)

ALLOY	d,μm	$d^{\frac{1}{2}}$,$\mu m^{\frac{1}{2}}$	$p^{\frac{1}{2}}$,$\mu m^{\frac{1}{2}}$	$d^{\frac{1}{2}}p^{\frac{1}{2}}$	Ratio ($d^{\frac{1}{2}}p^{\frac{1}{2}}$)
BD3	400	20	1.52	30.4	1
BD6	100	10	1.46	14.6	0.49
BD8	70	8.4	1.18	9.95	0.33

(b)

ALLOY	d,μm	$d^{\frac{1}{2}}$,$\mu m^{\frac{1}{2}}$	$p^{\frac{1}{2}}$,$\mu m^{\frac{1}{2}}$	$d^{\frac{1}{2}}p^{\frac{1}{2}}$	Ratio ($d^{\frac{1}{2}}p^{\frac{1}{2}}$)
BD3	400	20	1.65	33.0	1
BD6	100	10	1.3	13.0	0.4
BD8	70	8.4	1.1	9.25	0.28

continued overleaf.

Fig.4.3 (Contd.)

(c)

ALLOY	d,μm	$d^{\frac{1}{2}}$,$\mu m^{\frac{1}{2}}$	$p^{\frac{1}{2}}$,$\mu m^{\frac{1}{2}}$	$d^{\frac{1}{2}}p^{\frac{1}{2}}$	Ratio ($d^{\frac{1}{2}}p^{\frac{1}{2}}$)
BD3	400	20	1.67	33.4	1
BD6	100	10	1.12	11.2	0.33
BD8	70	8.4	0.95	8.35	0.26

(d)

ALLOY	d,μm	$d^{\frac{1}{2}}$,$\mu m^{\frac{1}{2}}$	$p^{\frac{1}{2}}$,$\mu m^{\frac{1}{2}}$	$d^{\frac{1}{2}}p^{\frac{1}{2}}$	Ratio ($d^{\frac{1}{2}}p^{\frac{1}{2}}$)
BD3	400	20	1.27	25.4	1
BD6	100	10	0.74	7.4	0.29
BD8	70	8.4	-	-	-

Fig.4.4

TABLE OF % ELONGATION AND % R.A. AT FRACTURE AT $20^{o}C$, $150^{o}C$ and $185^{o}C$.

ALLOY BD3	$20^{o}C$	$150^{o}C$	$185^{o}C$
% ELONGATION $(\ell f-\ell o)/\ell o$	1 ± 1	1 ± 1	1 ± 1
% R.A. $(A_o-A_f)/A_o$	-	-	-

ALLOY BD6	$20^{o}C$	$150^{o}C$	$185^{o}C$
% ELONGATION $(\ell f-\ell o)/\ell o$	16 ± 1	21 ± 1	21 ± 1
% R.A. $(A_o-A_f)/A_o$	26 ± 1	52 ± 1	$62 \pm$ -

ALLOY BD8	$20^{o}C$	$150^{o}C$	$185^{o}C$
% ELONGATION $(\ell f-\ell o)/\ell o$	17 ± 1	18 ± 1	21 ± 1
% R.A. $(A_o-A_f)/A_o$	56 ± 1	70 ± 1	73 ± 1

Fig.4.5

Typical conventional stress-strain curves for fully-aged BD3 at $20^{o}C$, $150^{o}C$ and $185^{o}C$.

FIG. 4.5

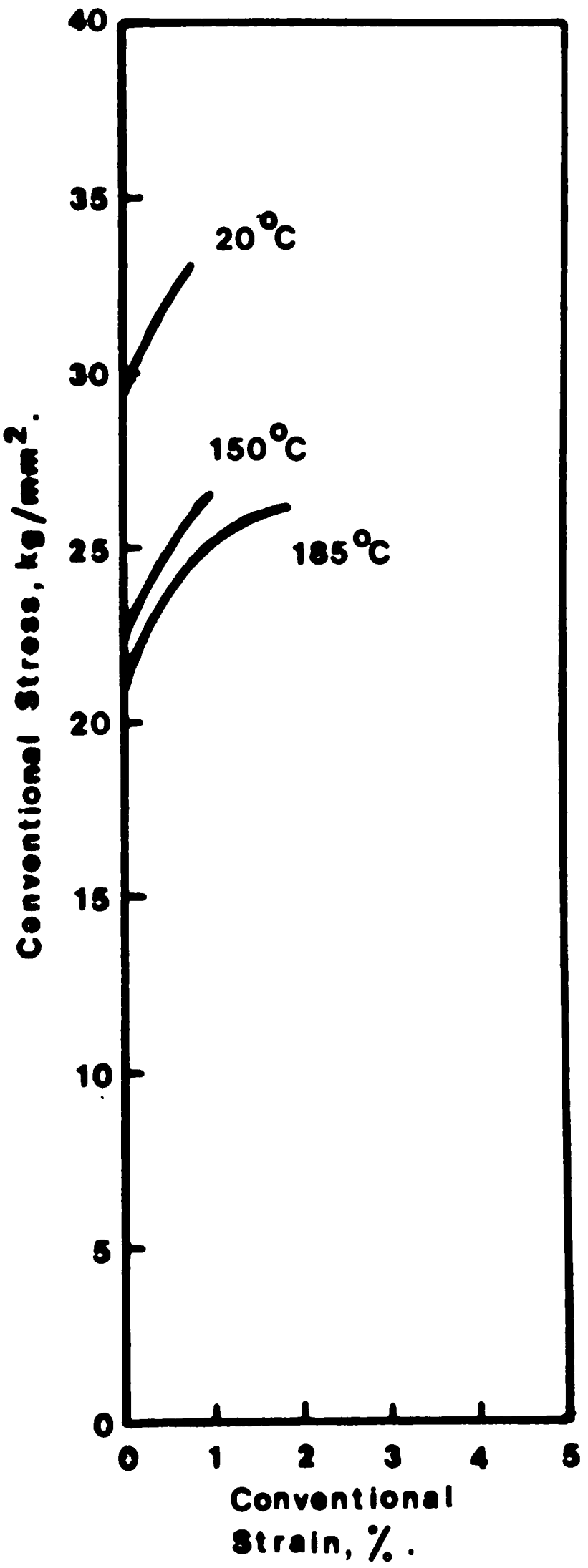
40
35
30
25
20
15
10
5
0
0
1
2
3
4
5
20°C
150°C
185°C
Conventional Stress, kg/mm².
Conventional Strain, %.

Fig.4.6

Typical conventional stress-strain curves for fully aged BD6 at $20^{o}C$, $150^{o}C$ and $185^{o}C$.

FIG. 4.6

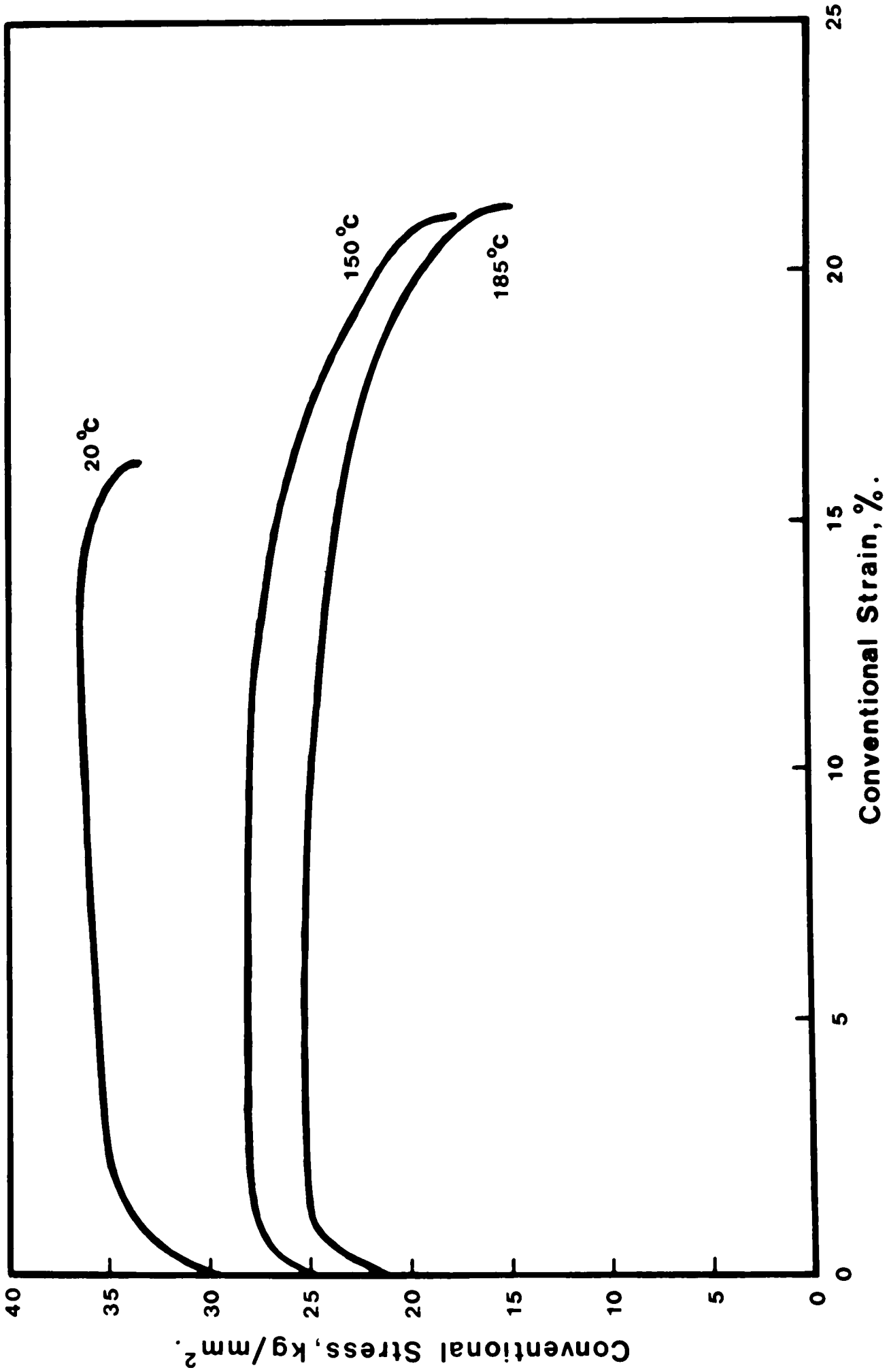
20°C
150°C
185°C
Conventional Stress, kg/mm².
0
5
10
15
20
25
30
35
40
Conventional Strain, %.
0
5
10
15
20
25

Fig.4.7

Typical conventional stress-strain curves for BD8 at $20^{o}C$, $150^{o}C$ and $185^{o}C$.

FIG. 4.7

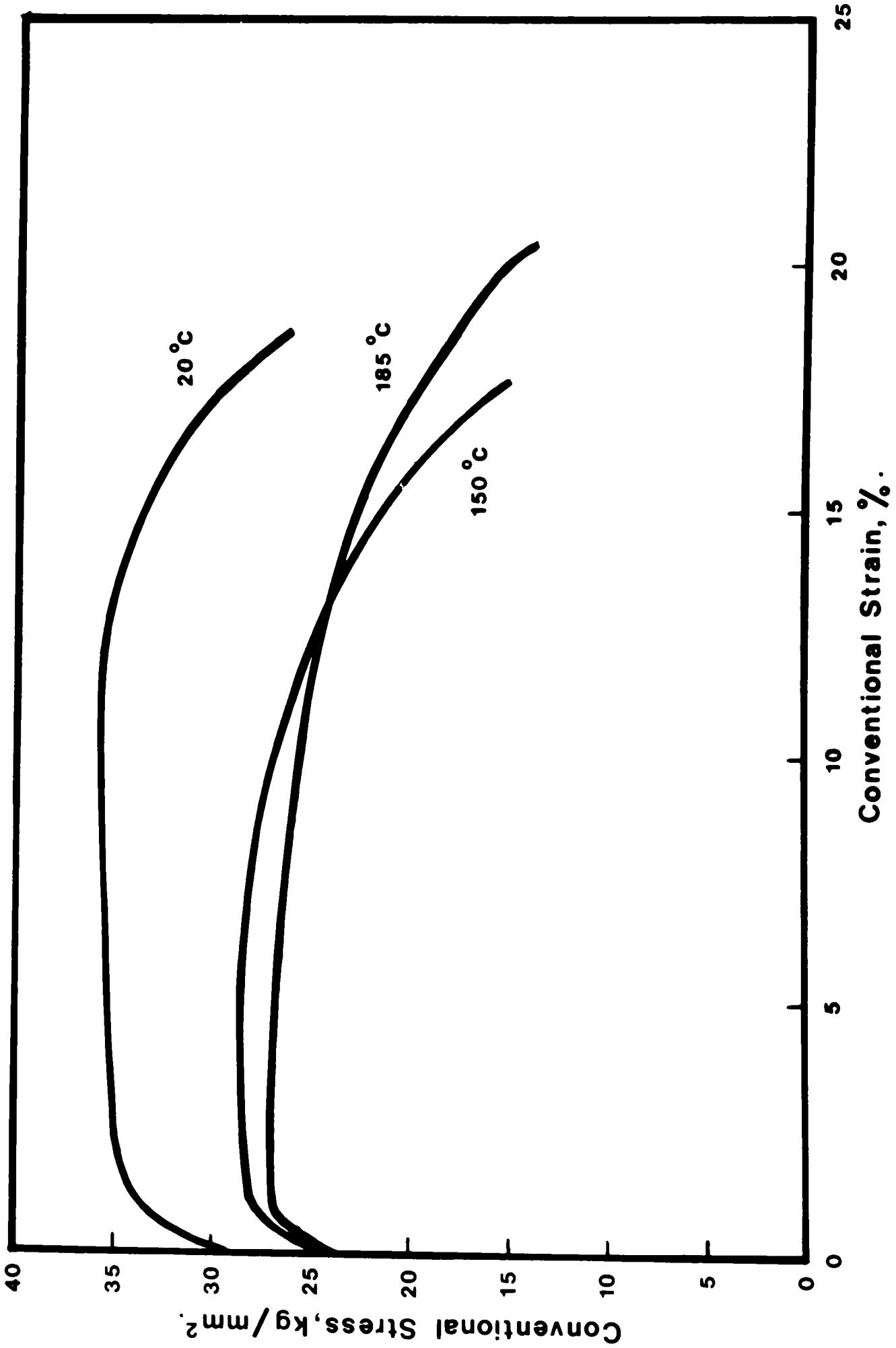
20 °C
185 °C
150 °C
Conventional Stress, kg/mm².
0
5
10
15
20
25
Conventional Strain, %.
0
5
10
15
20
25
30
35
40

Fig.4.8

DATA FOR CONVENTIONAL STRESS-STRAIN CURVES OF BD6

(SEE FIG.4.6)

ALLOY BD6	YIELD STRESS kg/mm^2	U.T.S. L_{max}/A_o, kg/mm^2	% ELONGATION $(\ell_f-\ell_o)/\ell_o$, AT U.T.S.	FRACTURE STRESS L_f/A_f, kg/mm^2	% ELONGATION $(\ell_f-\ell_o)/\ell_o$,	% R.A. $(A_o-A_F)/A_o$
20^oC	29.6	36.4	14	43.5	16	23
150^oC	25.0	28.1	9	39.7	21	56
185^oC	21.1	25.4	7	38.7	21	62

Fig.4.9

DATA FOR CONVENTIONAL STRESS-STRAIN CURVES OF BD8
(SEE FIG.4.7)

ALLOY BD8	YIELD STRESS kg/mm^2	U.T.S. L_{max}/A_o kg/mm^2	% ELONGATION $(\ f\ \ o)/\ o$, AT U.T.S.	FRACTURE STRESS L_f/A_f, kg/mm^2	% ELONGATION $(\ f-\ o)/\ o$	% R.A. $(A_o-A_f)/A_o$
20^oC	30.5	35.5	11	64.6	18	55
150^oC	23.5	28.3	6	53.4	18	71
185^oC	23.6	27.1	4	52.5	21	73

Plate 4.1

T.E.M. of Peak-Aged BD8 after ~ 9% compressive strain.

Plate 4.2

T.E.M. of Peak-Aged BD6 after ~ 9% compressive strain.

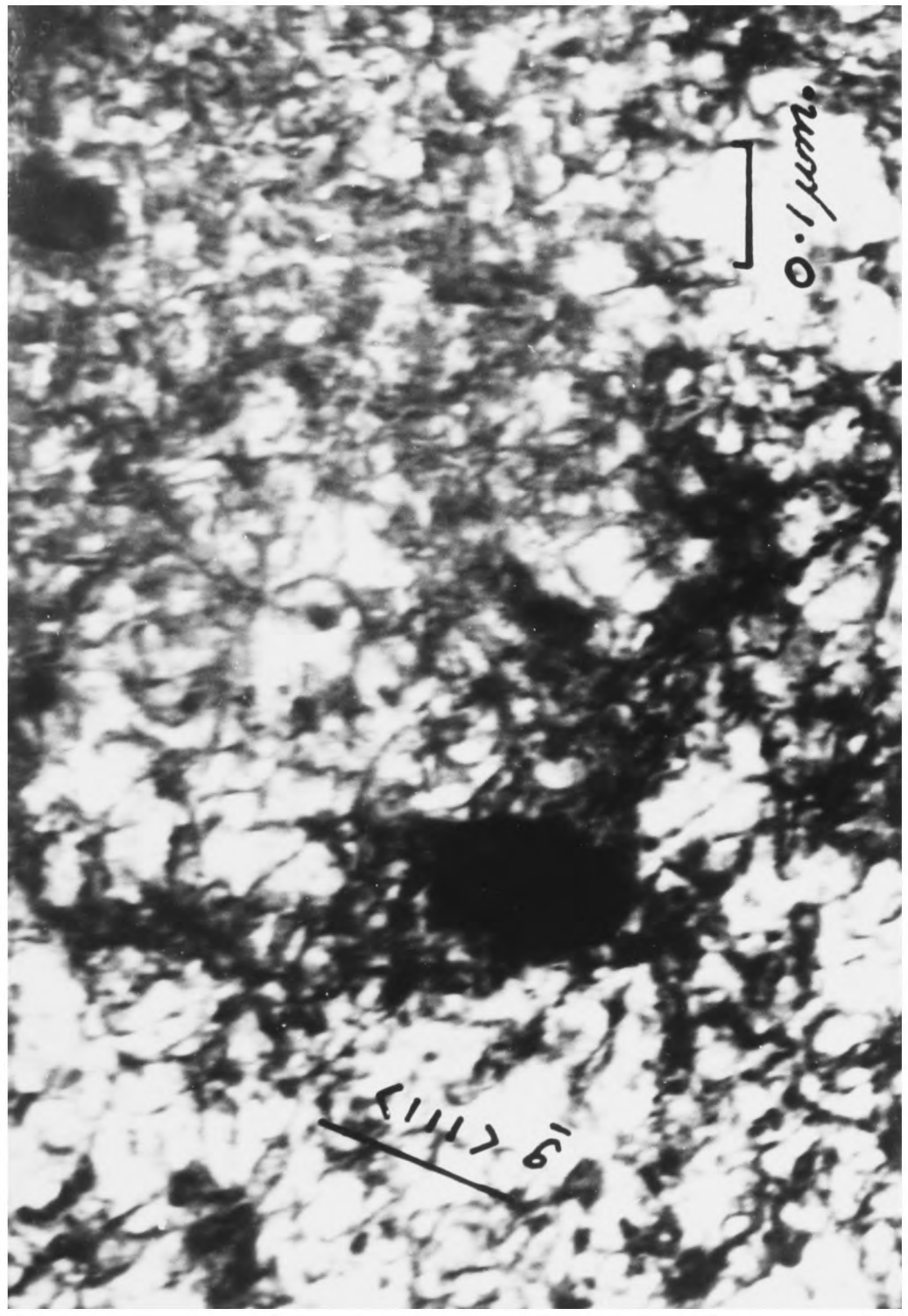
0.1 μm.
g, <111>

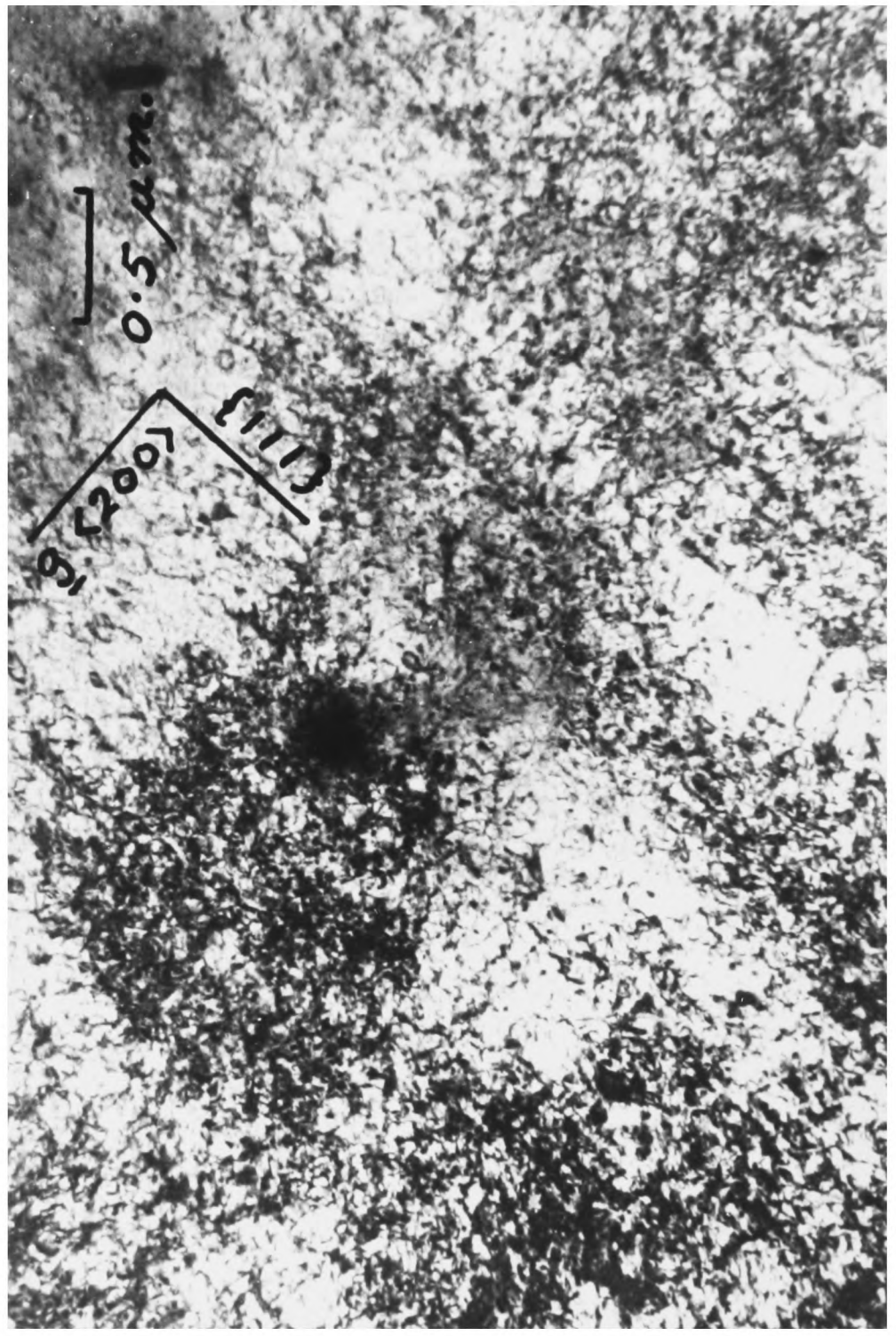
0.5 μm.
g, <200>
<111>

Plate 4.3

T.E.M. of Peak-Aged BD6 after ~ 9% compressive strain. Grain boundary region.

Plate 4.4.

T.E.M. of Peak-Aged BD3 after ~ 9% compressive strain


g <200>
0·1 μm.

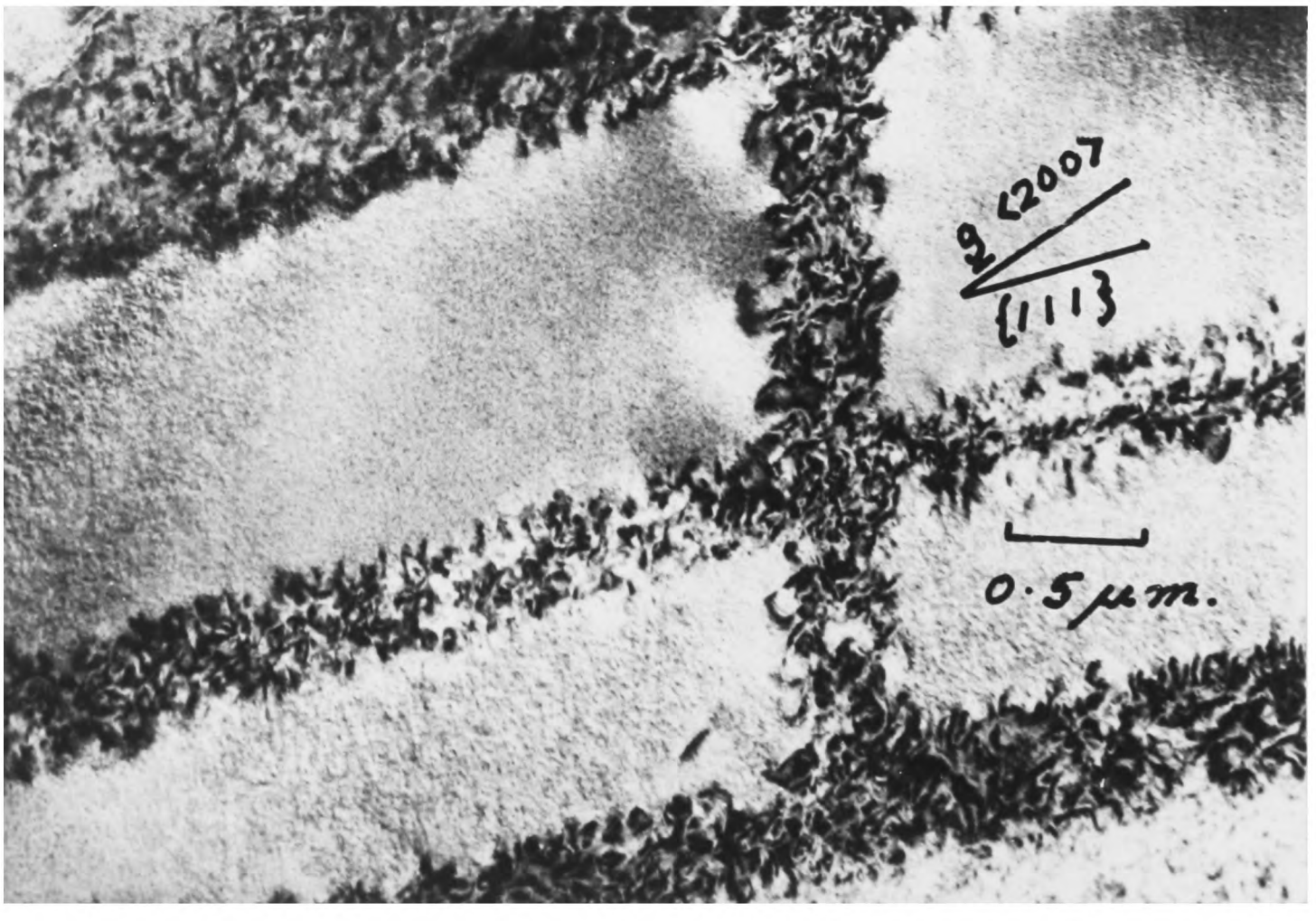
g <200>
{111}
0·5 μm.

Plate 4.5

T.E.M. of Peak-Aged BD8 after ~ 9% compressive strain. Grain boundary region.

Plate 4.6

T.E.M. of Peak-Aged BD3 after ~ 9% compressive strain. Grain boundary distortion.

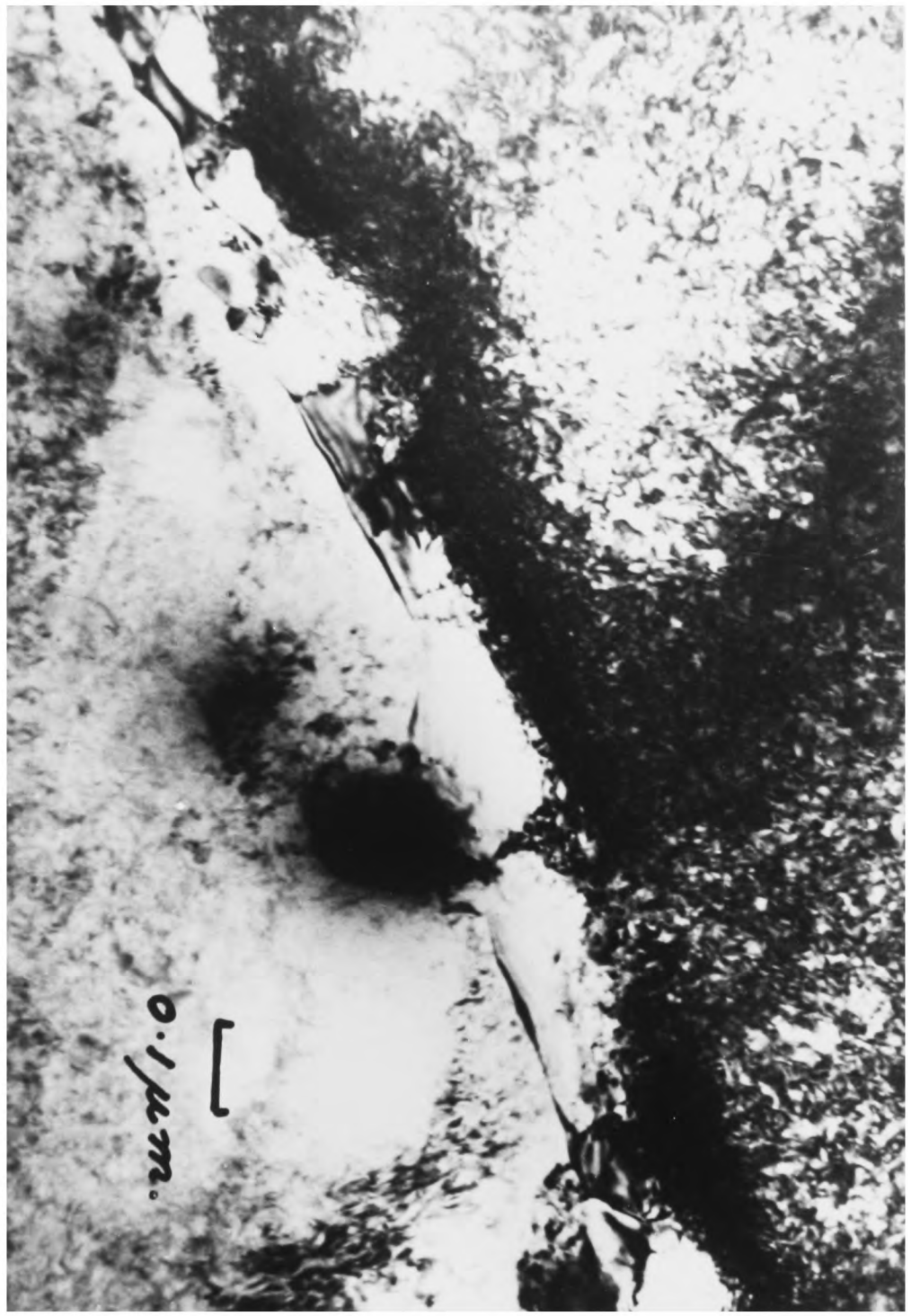
0.1 μm.

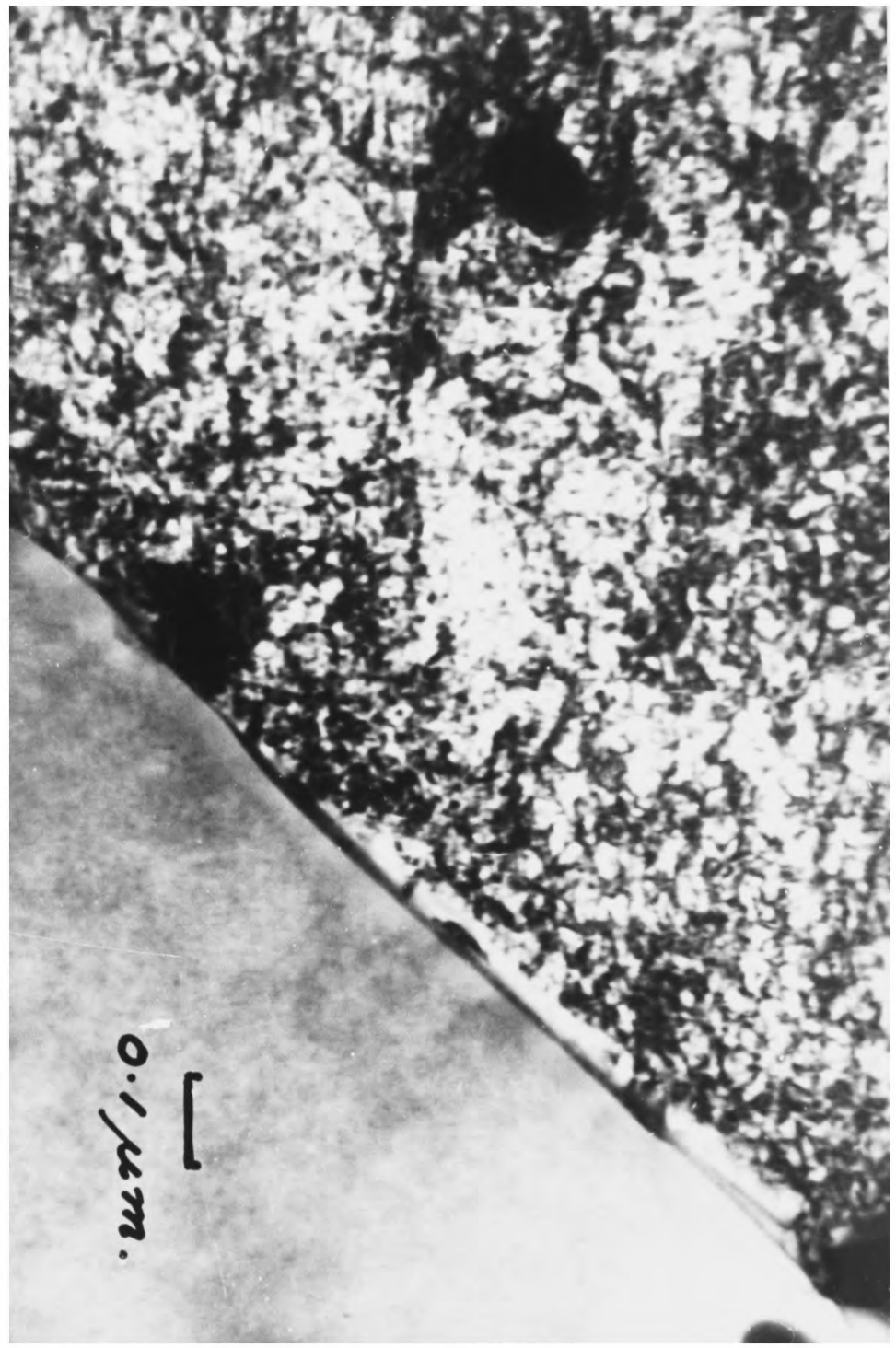
0.1 μm.

Plate 4.7

T.E.M. of a section from a tensile test piece of BD3 after fracture at 20°C.

Plate 4.8

T.E.M. of a section from a tensile test piece of BD6 after fracture at 20°C (BD8 is similar).


{111}
<200>
{111}
1 μm.

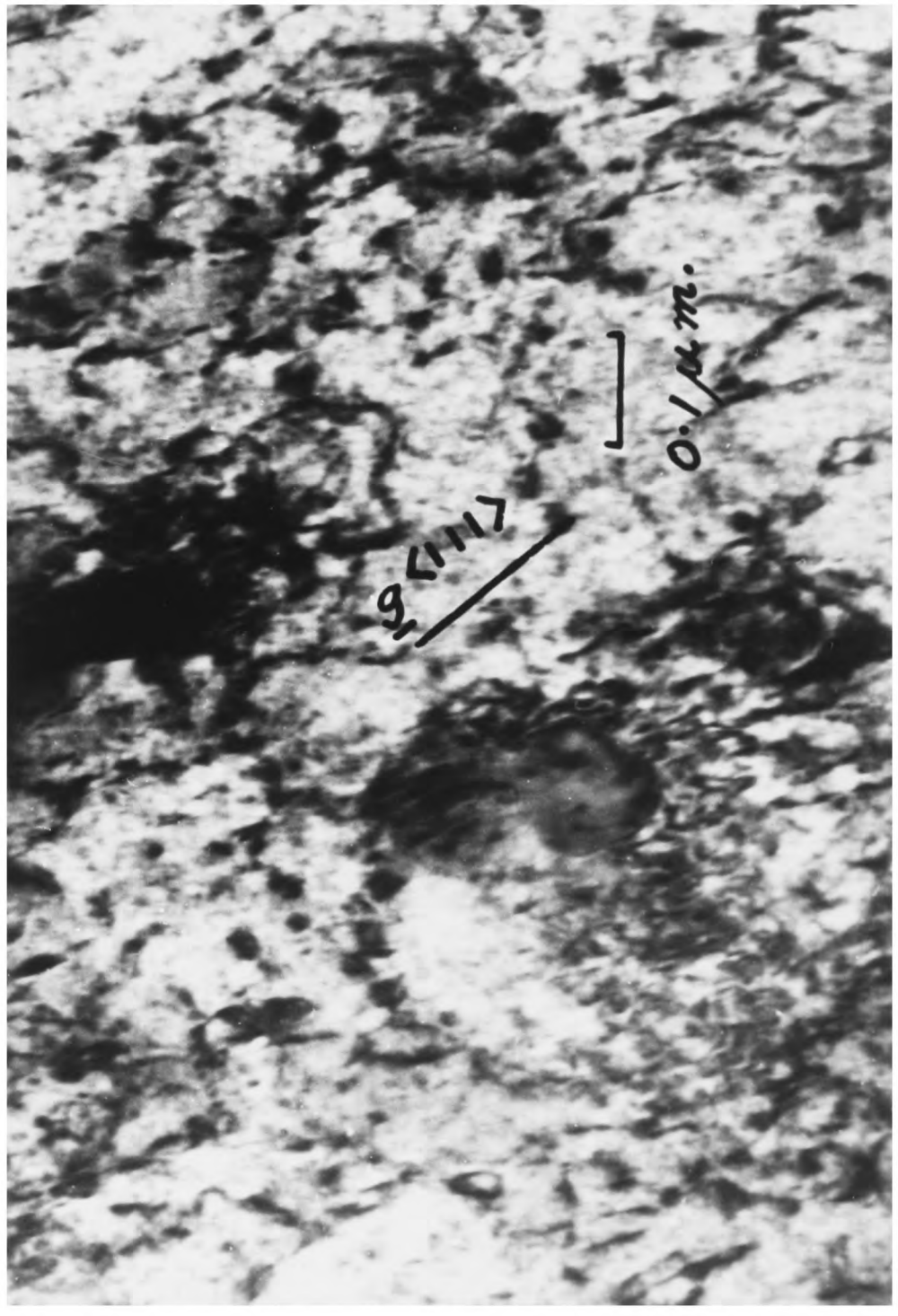
g<111>
0.1 μm.

Plate 4.9

T.E.M. of a section from a tensile test piece of BD6 after fracture at 185°C.

Plate 4.10

T.E.M. of a section from a tensile test piece of BD8 after fracture at 185°C.

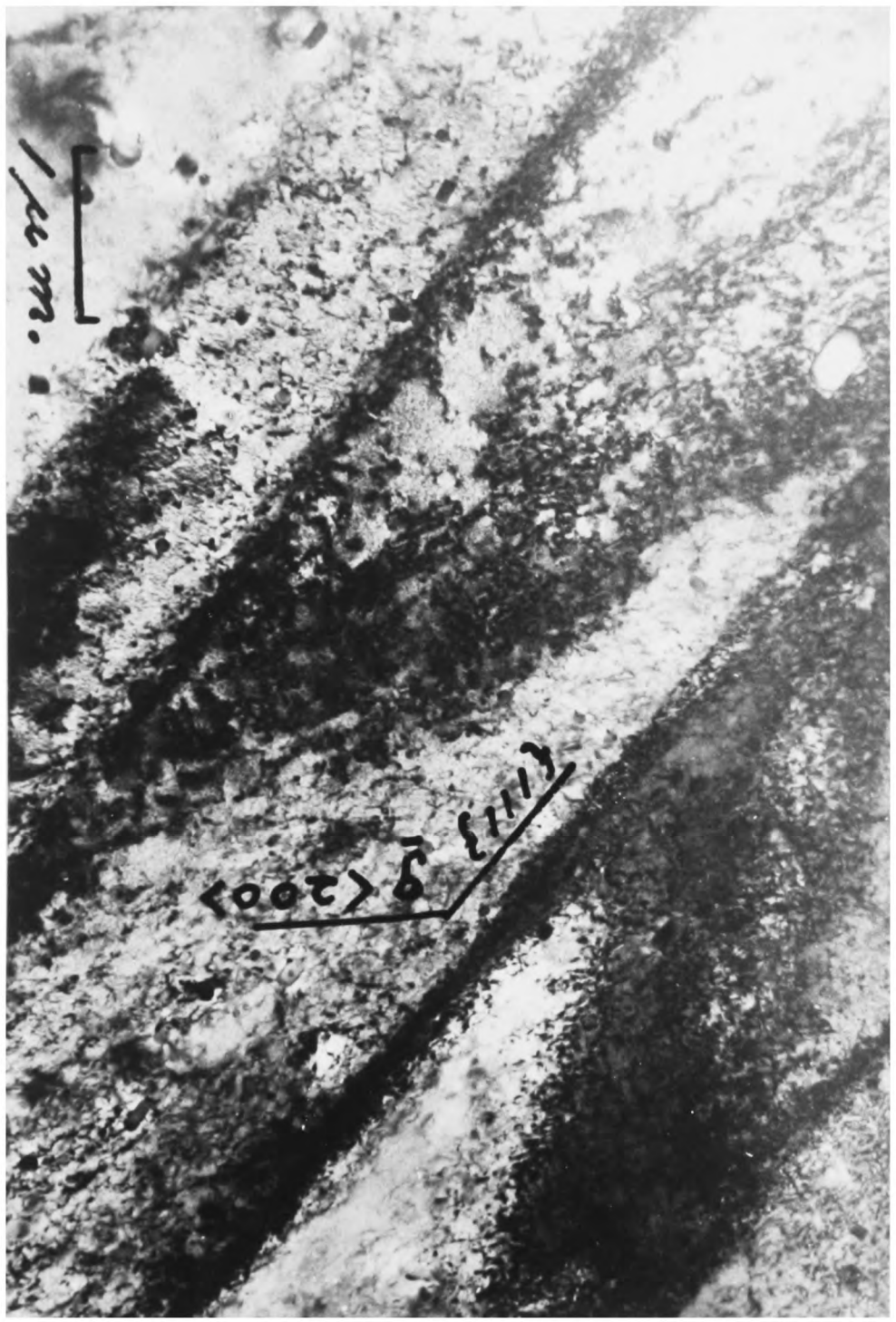
1 μm.
g ⟨200⟩
{111}

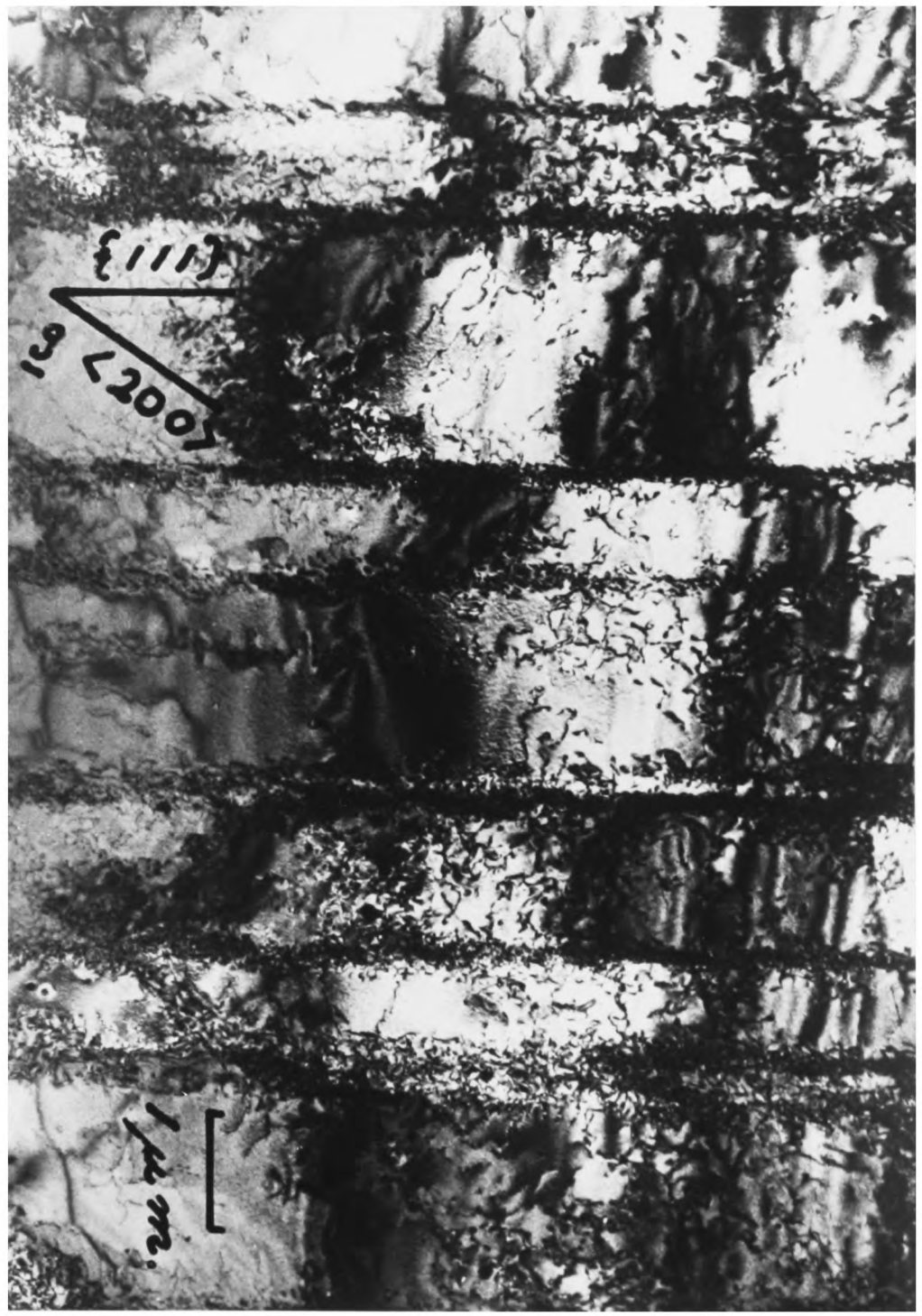
{111}
g ⟨200⟩
1 μm.

Plate 4.11

Plate 4.10 at a higher magnification, showing the dislocation distribution between the slip bands.

Plate 4.12

T.E.M. of a test piece of BD8 fractured at $20^{o}C$ and then annealed for 15 minutes at $185^{o}C$. (c.f. Plate 4.8 and 4.11).

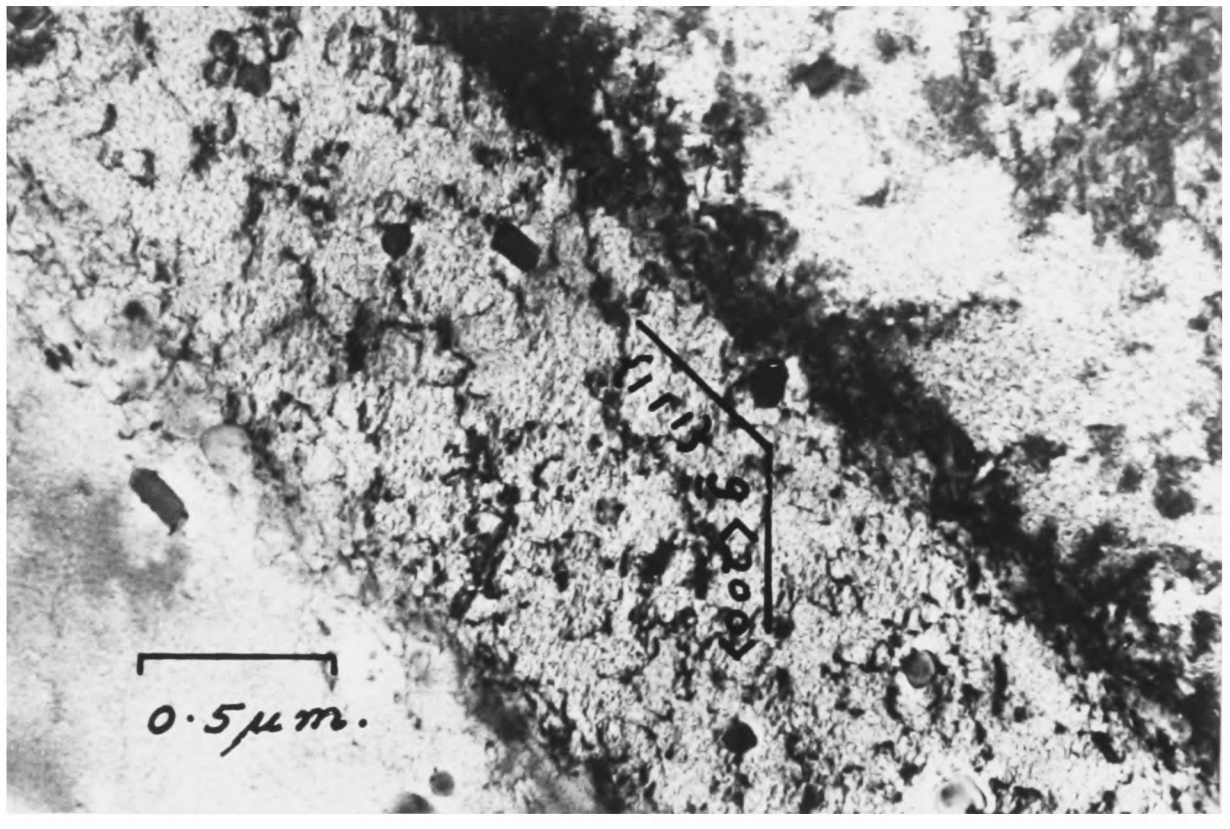
{111}
0·5μm.

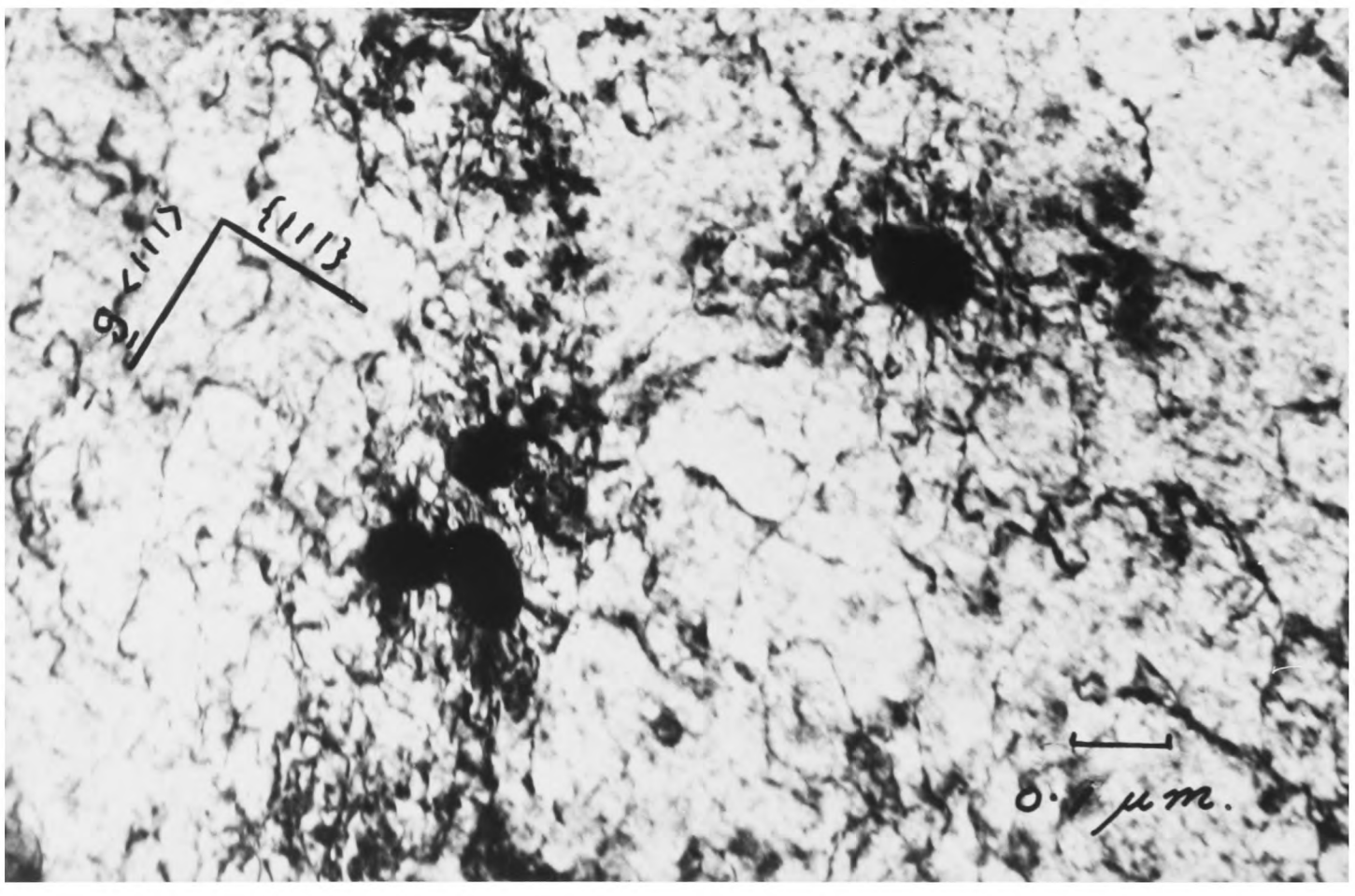
{111}
0·5μm.

Plate 4.13

Longitudinal section of tensile test piece of BD3, fractured at room temperature. (Optical micrograph; electro-chemical etch).

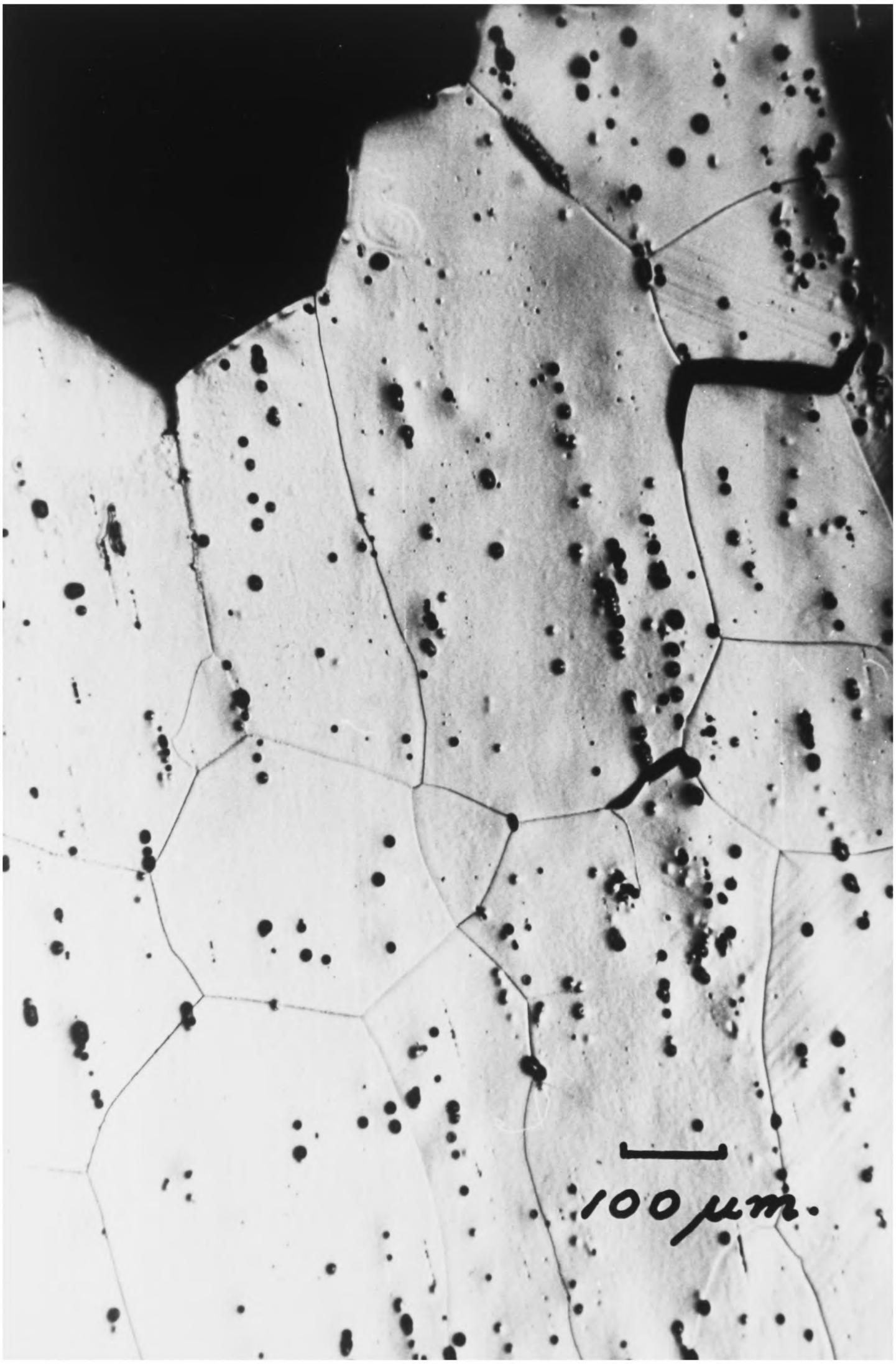
100 μm.

Plate 4.14

(a) Longitudinal section of a tensile test piece of BD6, fractured at room temperature. (Optical micrograph; unetched).

(b) High magnification : void sheet in BD6.

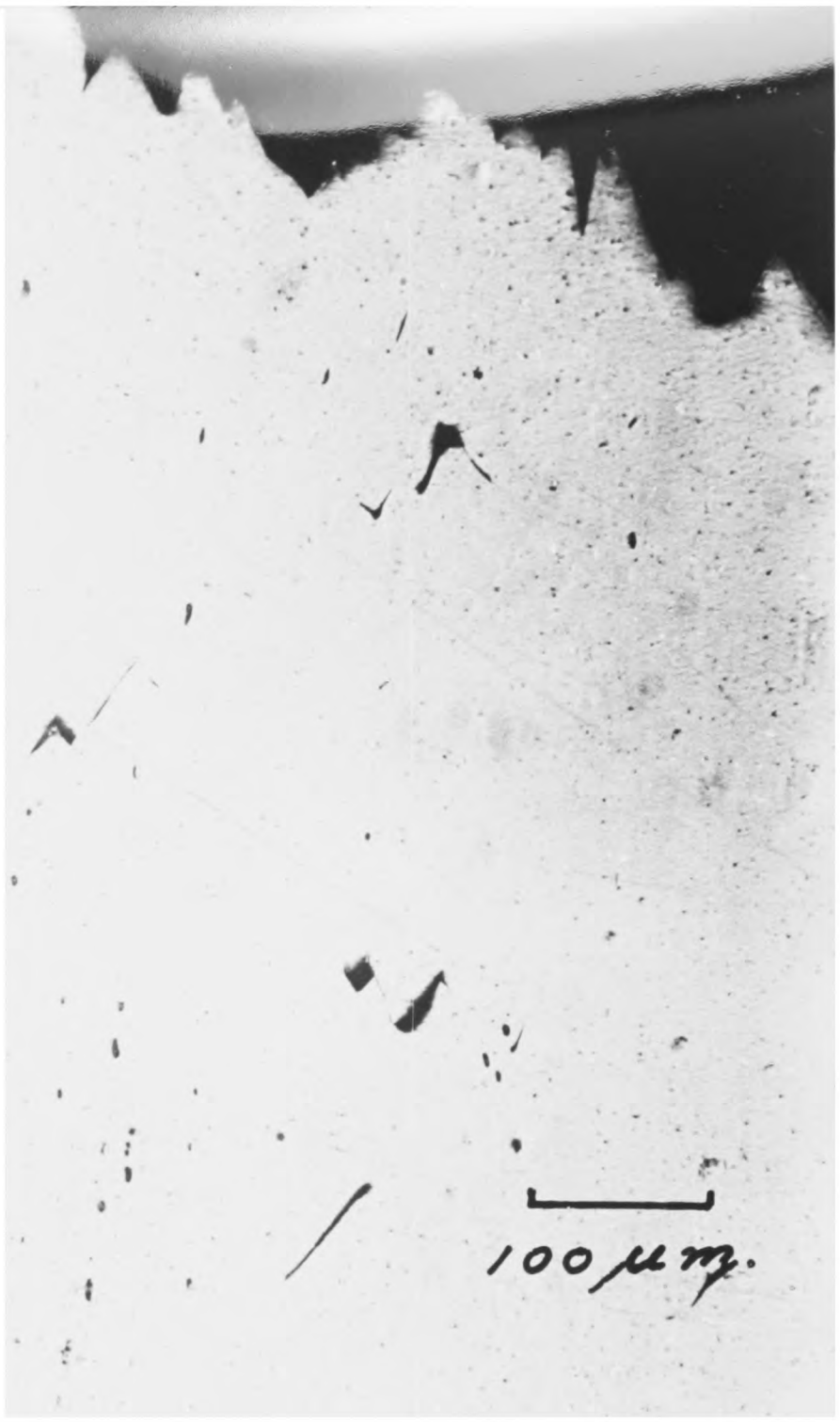
100 μm.

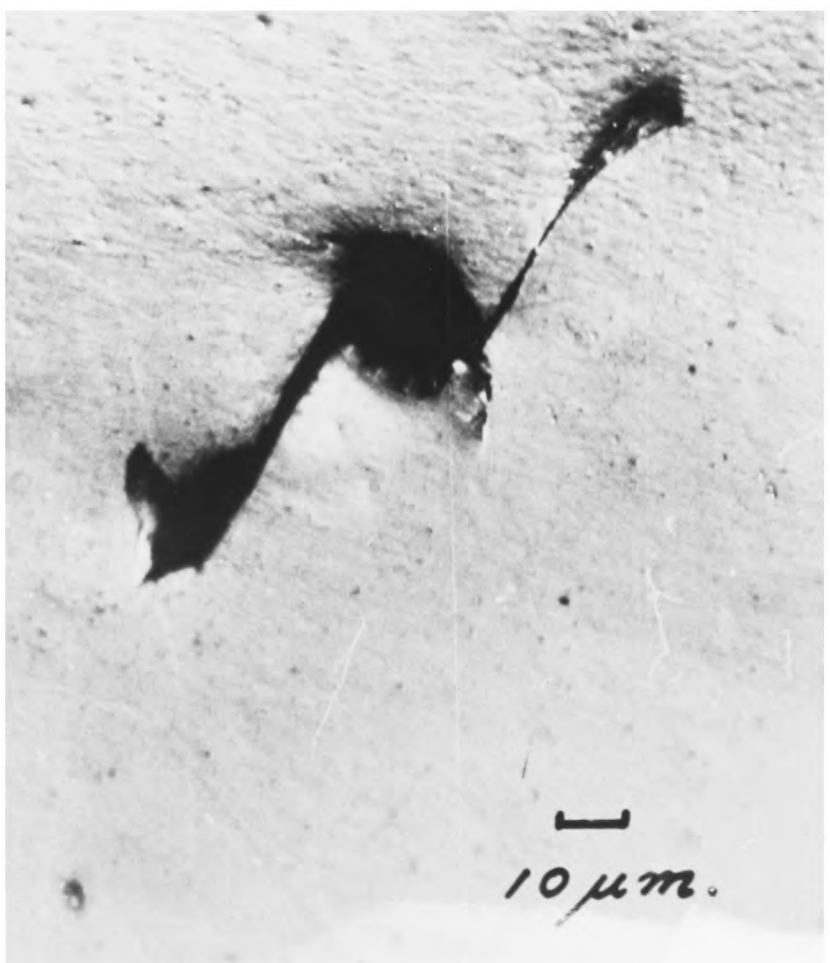
10 μm.

Plate 4.15

(a) Longitudinal section of a tensile test piece of BD8, fractured at room temperature. (Optical micrograph, unetched).

(b) High magnification : voids nucleated at the coarse, ~ 5μm, $\alpha(Al_{12}Mn_3Si)$ particles.

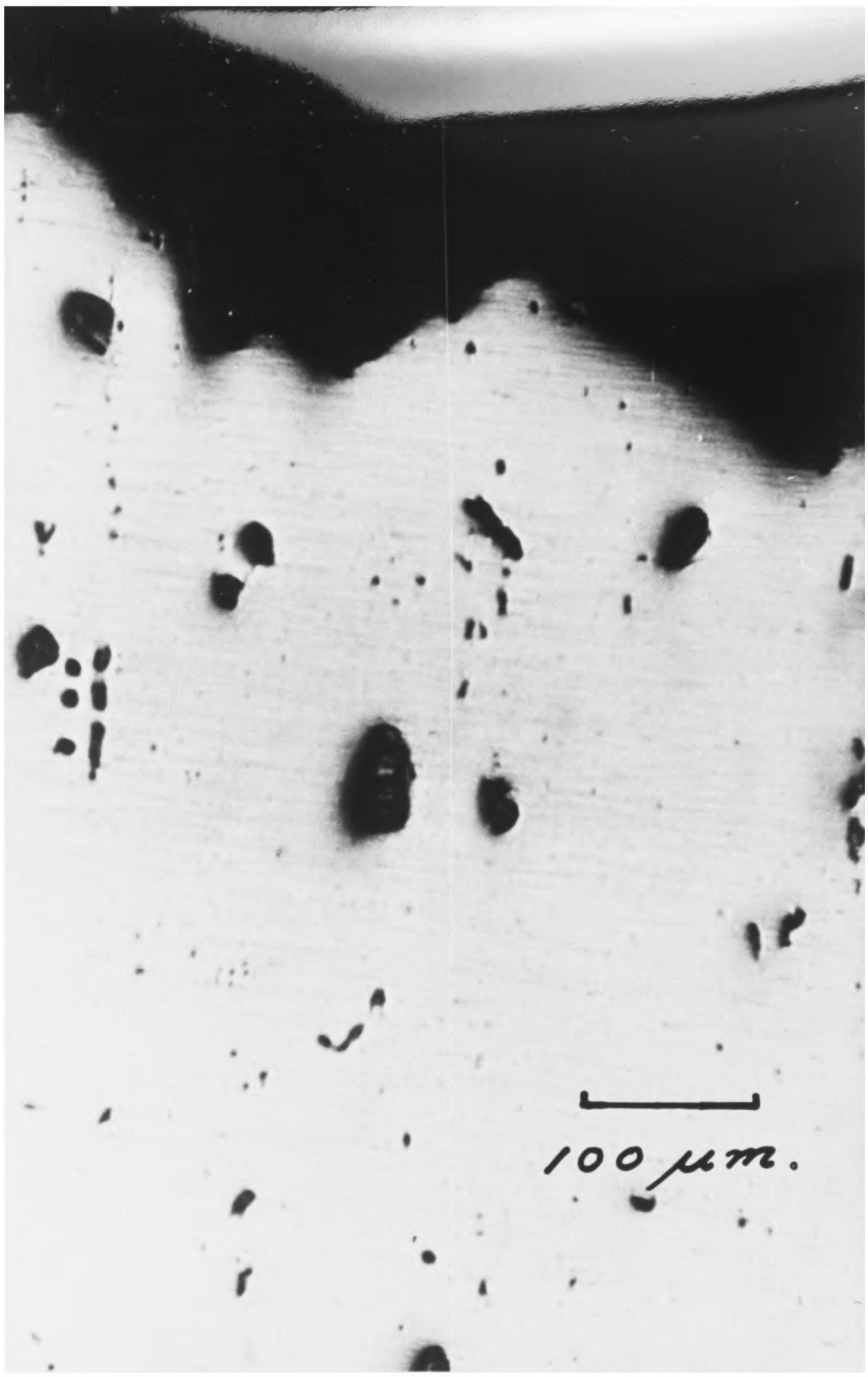
100 μm.


10μm.

Plate 4.16

Longitudinal section of a tensile test piece of BD6, fractured at room temperature. (Optical micrograph; electro-chemical etch).

Plate 4.17

Longitudinal section of a tensile test piece of BD8, fractured at room temperature. (Optical micrograph; electro-chemical etch).

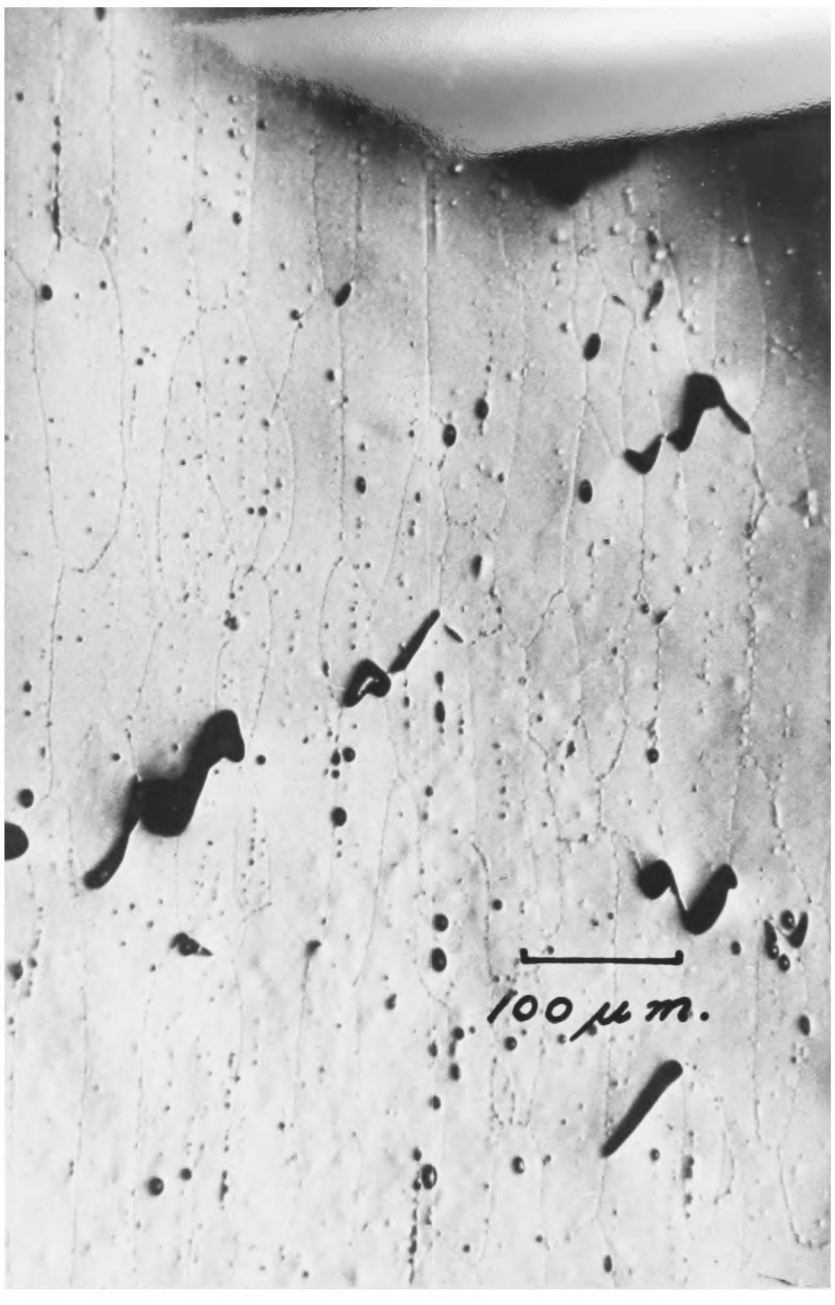
100 μm.


100 μm.

Plate 4.18

Longitudinal section of a tensile test piece of BD6, fractured at 185°C. (Optical micrograph; unetched).

Plate 4.19

Longitudinal section of a tensile test piece of BD8, fractured at 185°C. (Optical micrograph; unetched).


100 μm.

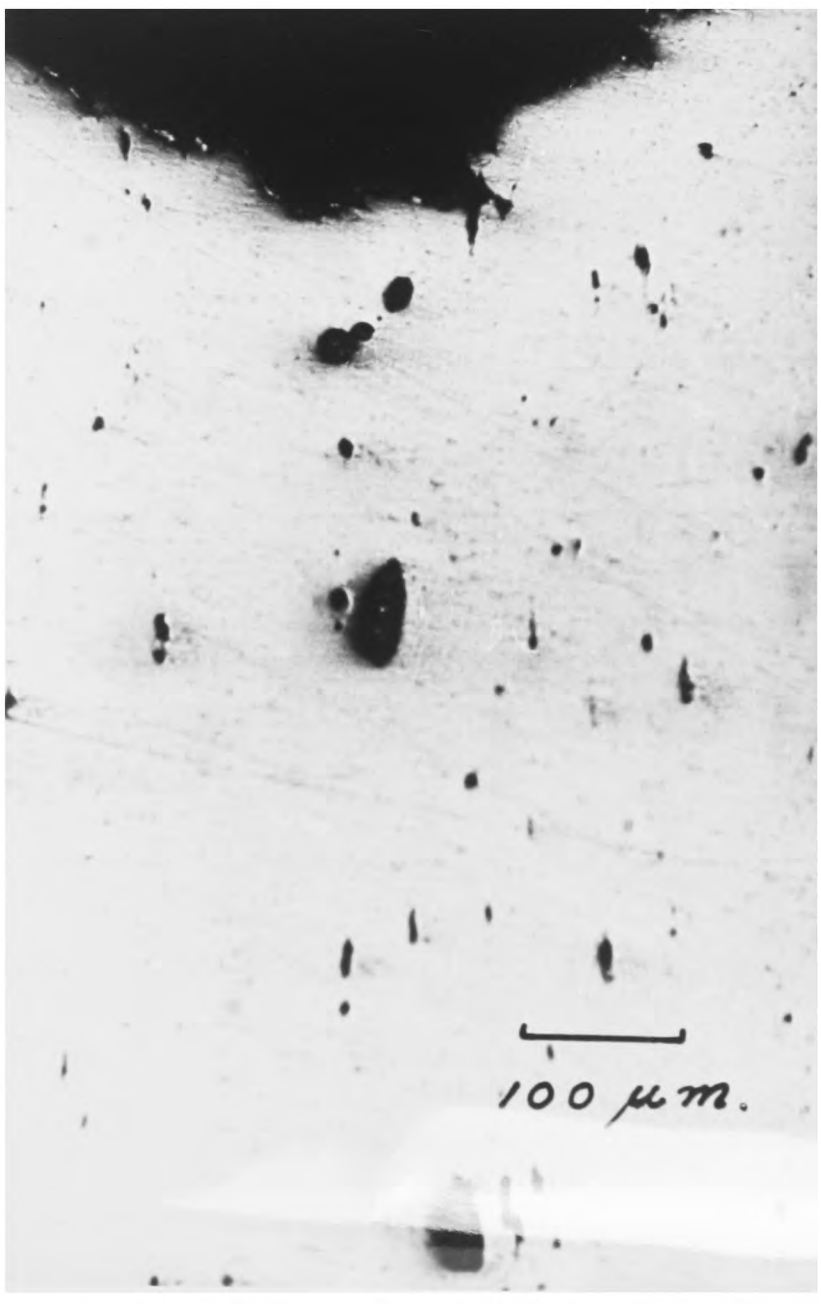
100 μm.

Plate 4.20

Longitudinal section of a tensile test piece of BD6, fractured at 185°C. (Optical micrograph; electro-chemical etch).

Plate 4.21

Longitudinal section of a tensile test piece of BD8, fractured at 185°C. (Optical micrograph; electro-chemical etch).

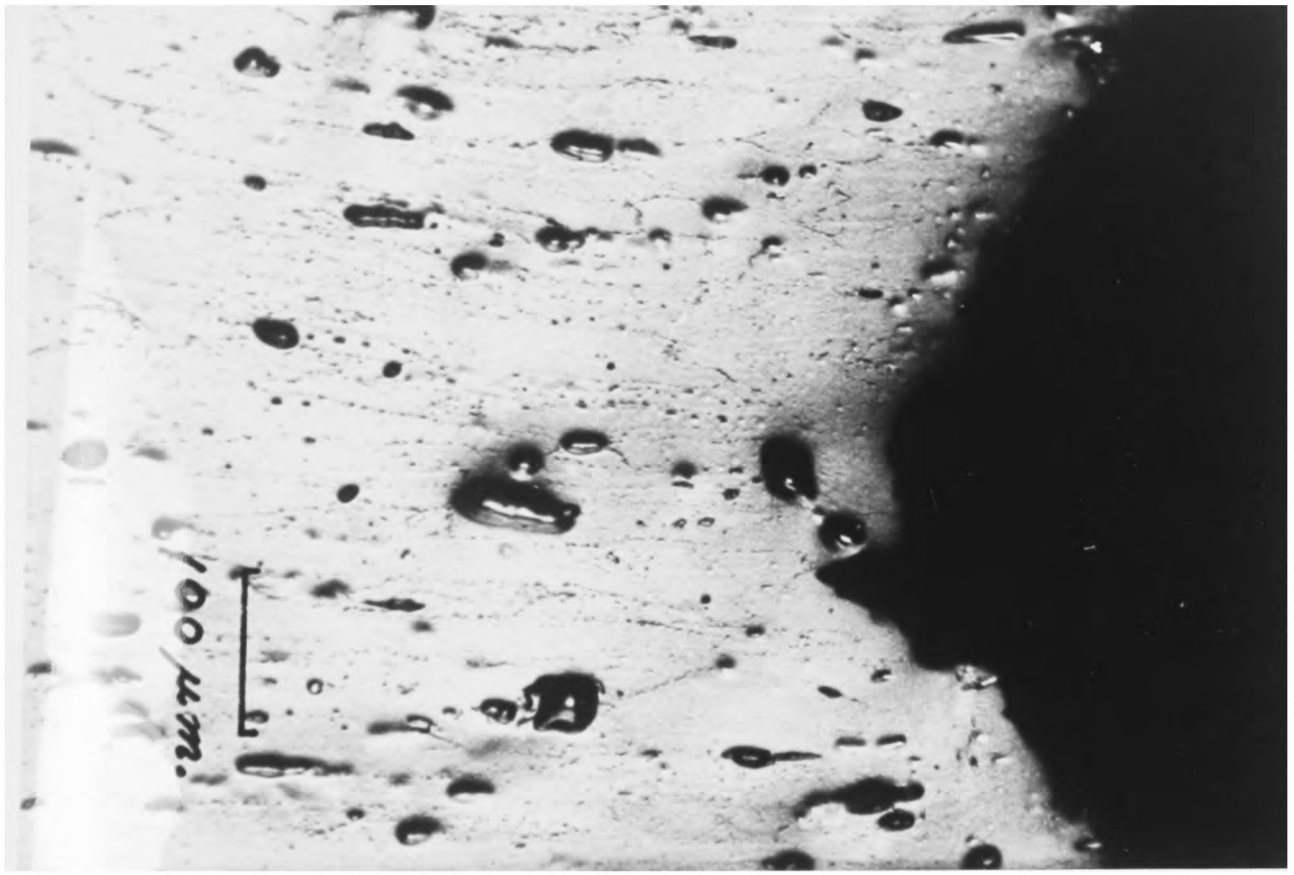
100 μm.

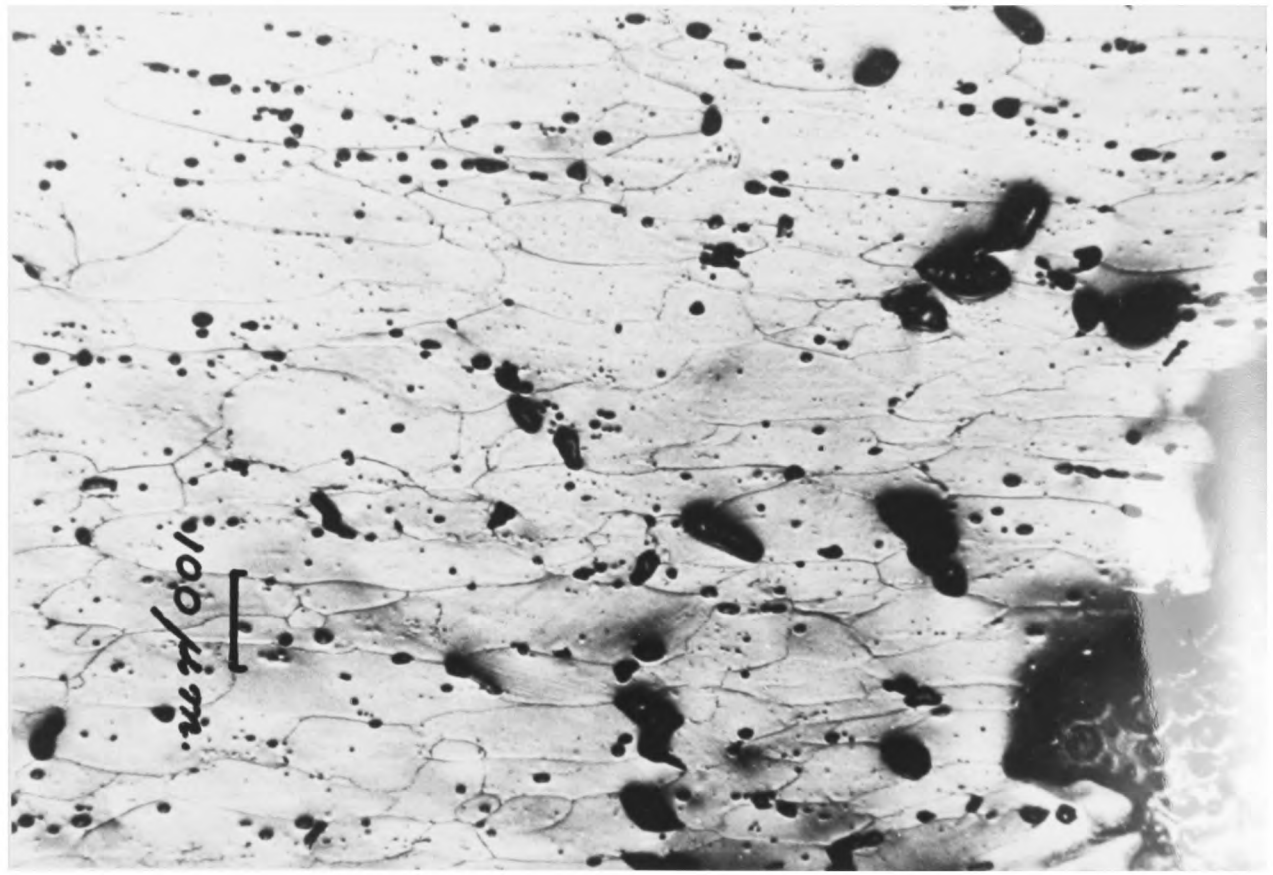
100 μm.

Plate 4.22

Two examples of cracked, ~ 0.1μm, particles in BD8. (T.E.M.)

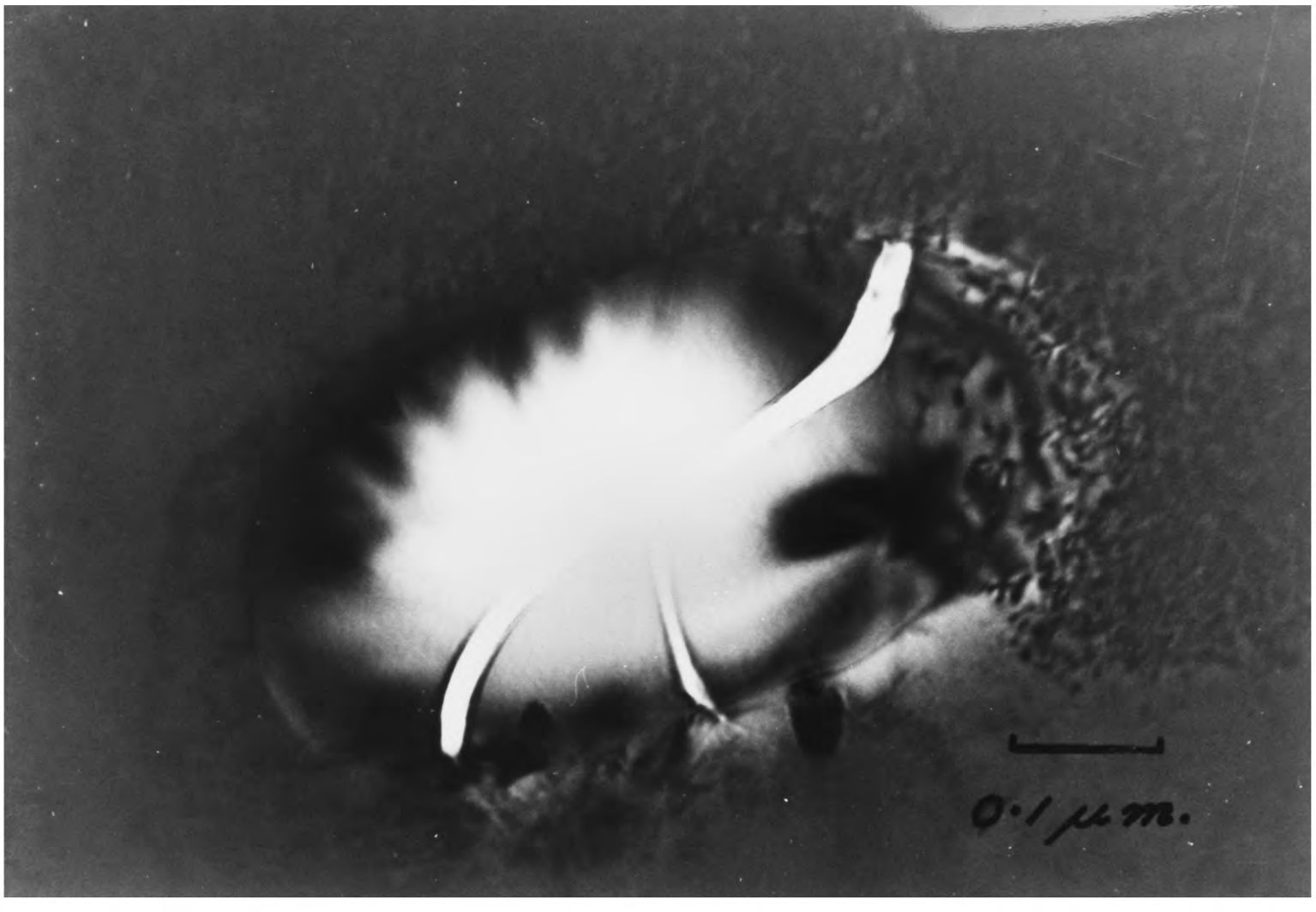
0·1 μm.

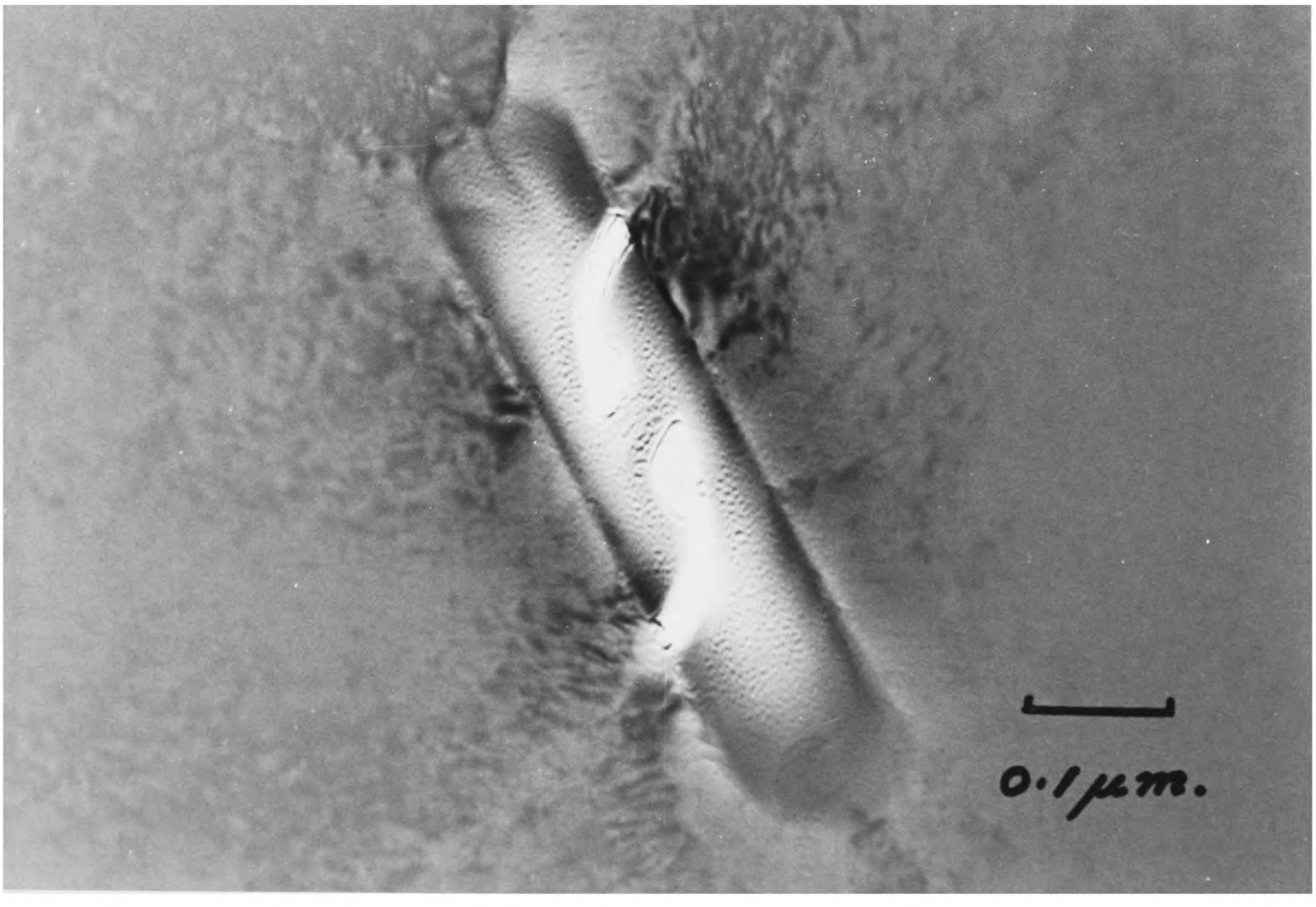
0·1 μm.

Plate 4.23

S.E.M. of the fracture surface of peak-aged BD3. (Low magnification).

Plate 4.24

Dimpled surface of a grain boundary in BD3 (S.E.M.).

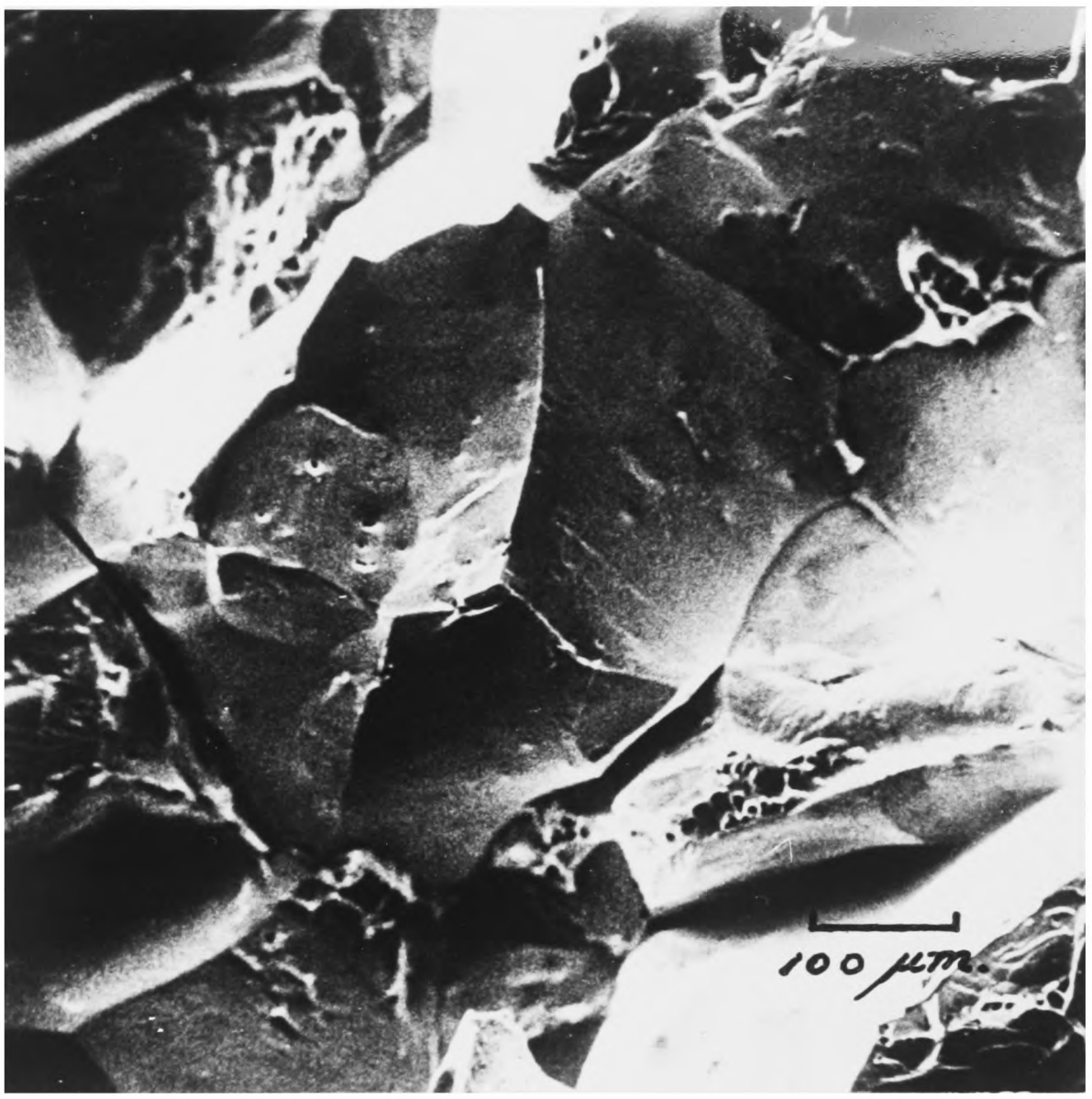
100 μm.

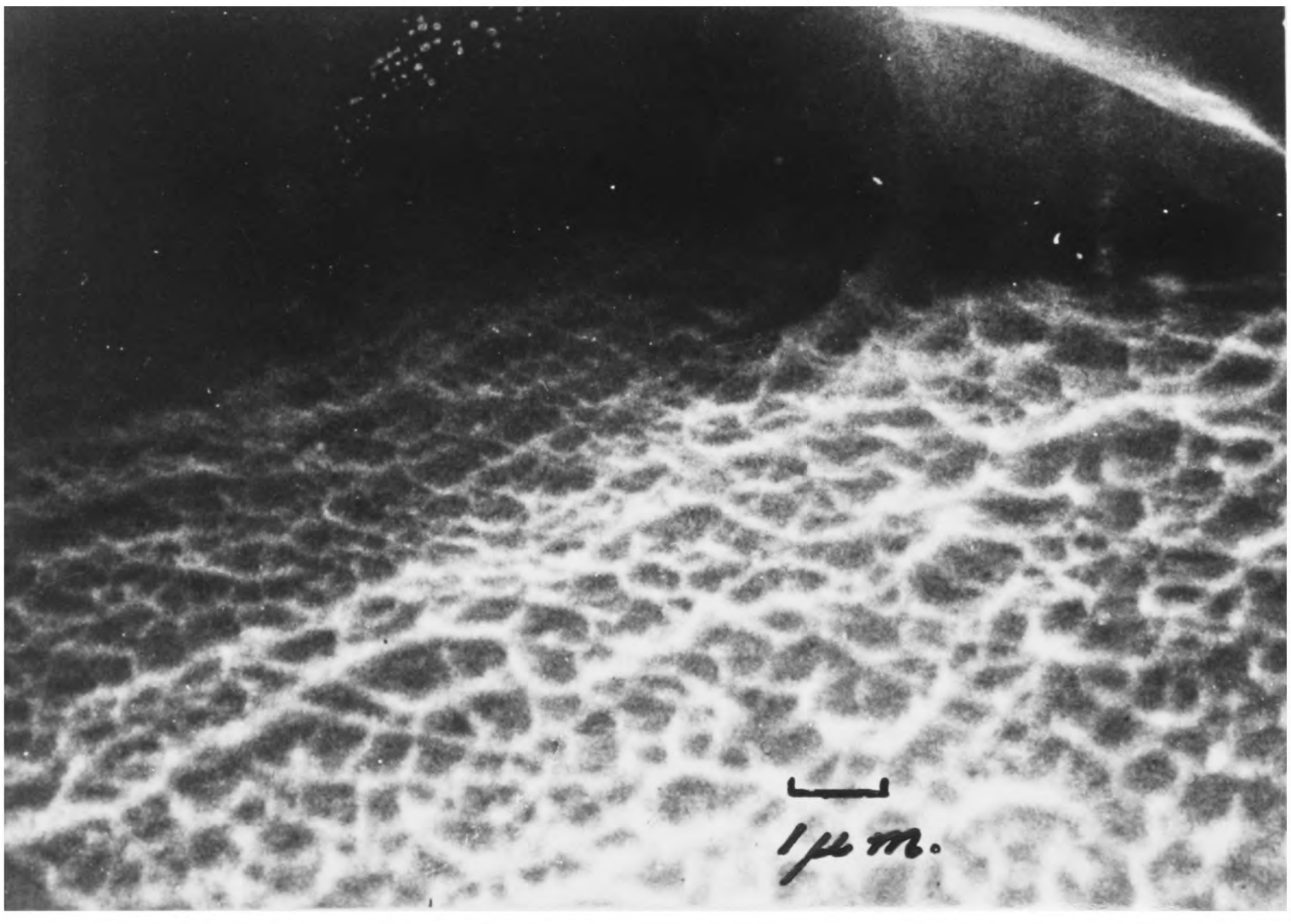
1 μm.

Plate 4.25

S.E.M. of the fracture surface of peak-aged BD6. (Low magnification).

Plate 4.26

S.E.M. of the fracture surface of peak-aged BD8. (Low magnification).


100 μm


100 μm.

Plate 4.27

S.E.M. of fracture surface of peak-aged BD8. (High magnification).

Plate 4.28

S.E.M. of the fracture surface of peak-aged BD8. (High magnification).


10 µm.


1 µm

Plate 4.29

S.E.M. of the fracture surface of peak-aged BD6. (High magnification).

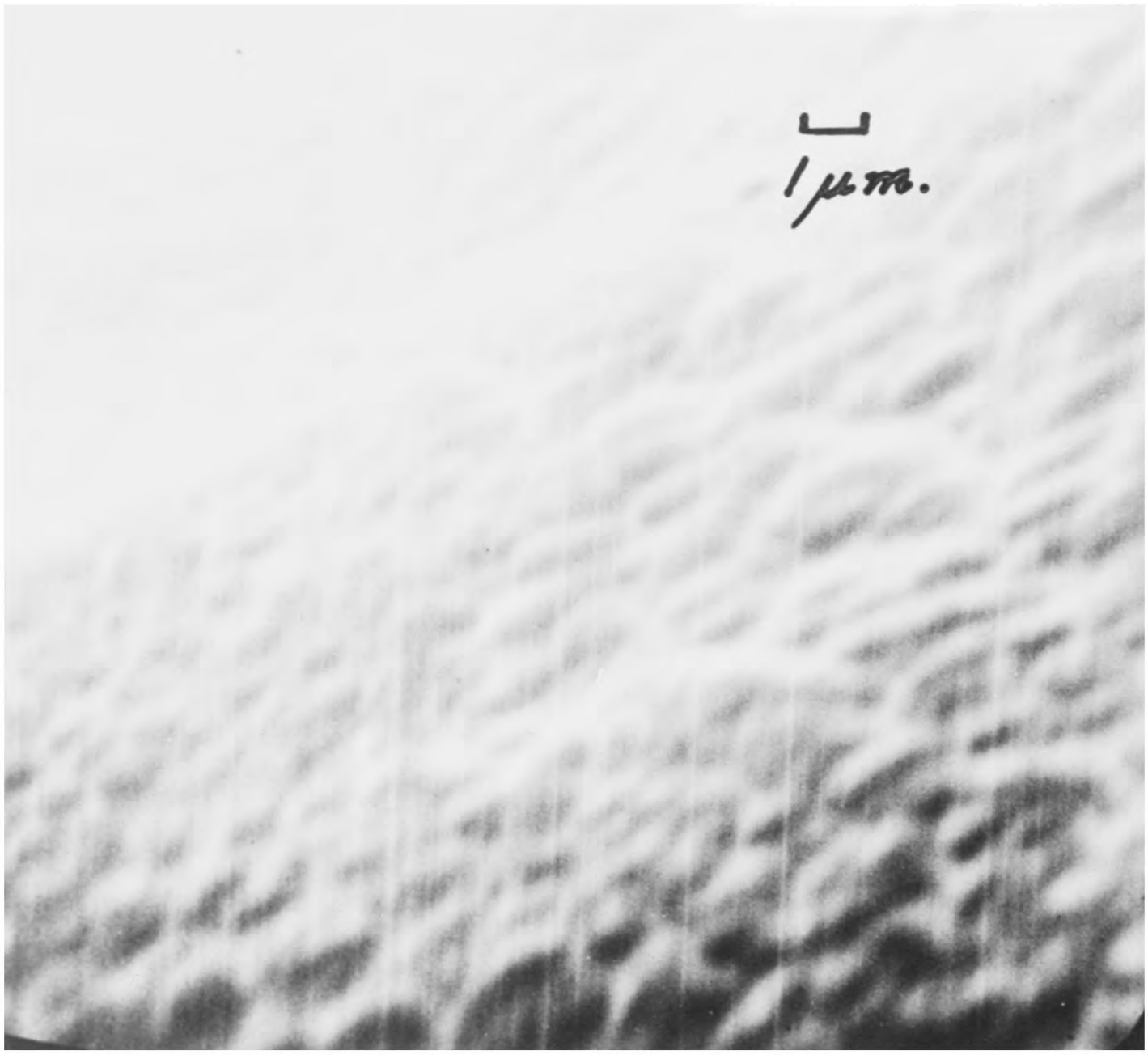
1 μm.

Plate 4.30 (a, b, c, d and e)

Crack Propagation in BD3
(Notch bend test)

(a) Before straining

(b) After a small strain

(c) After further straining, a grain boundary opens up at the root of the notch

(d) and (e) overleaf


100 μm.

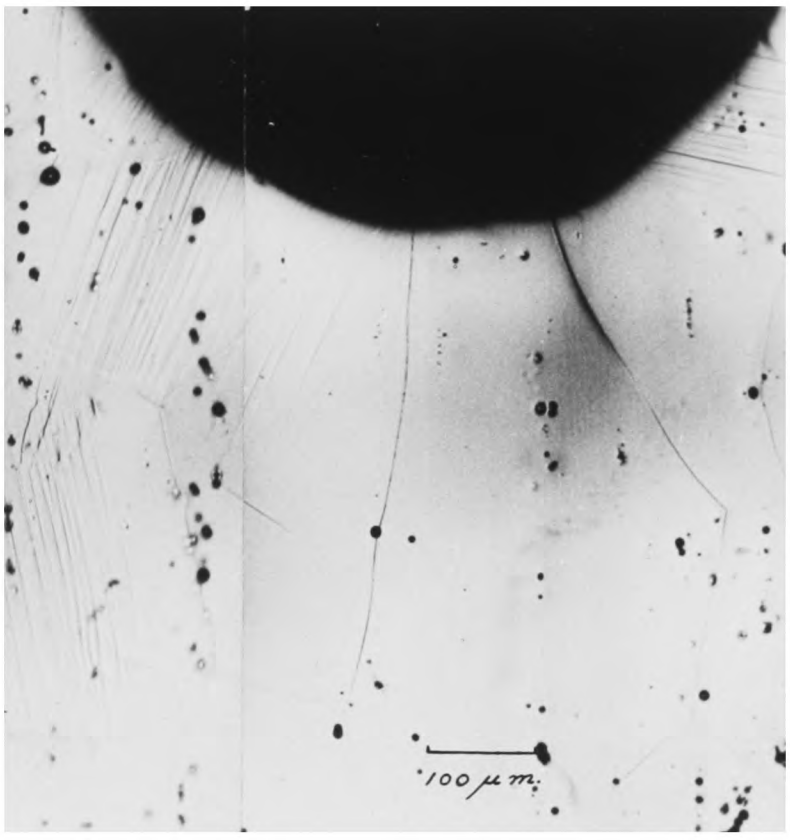
100 μm.

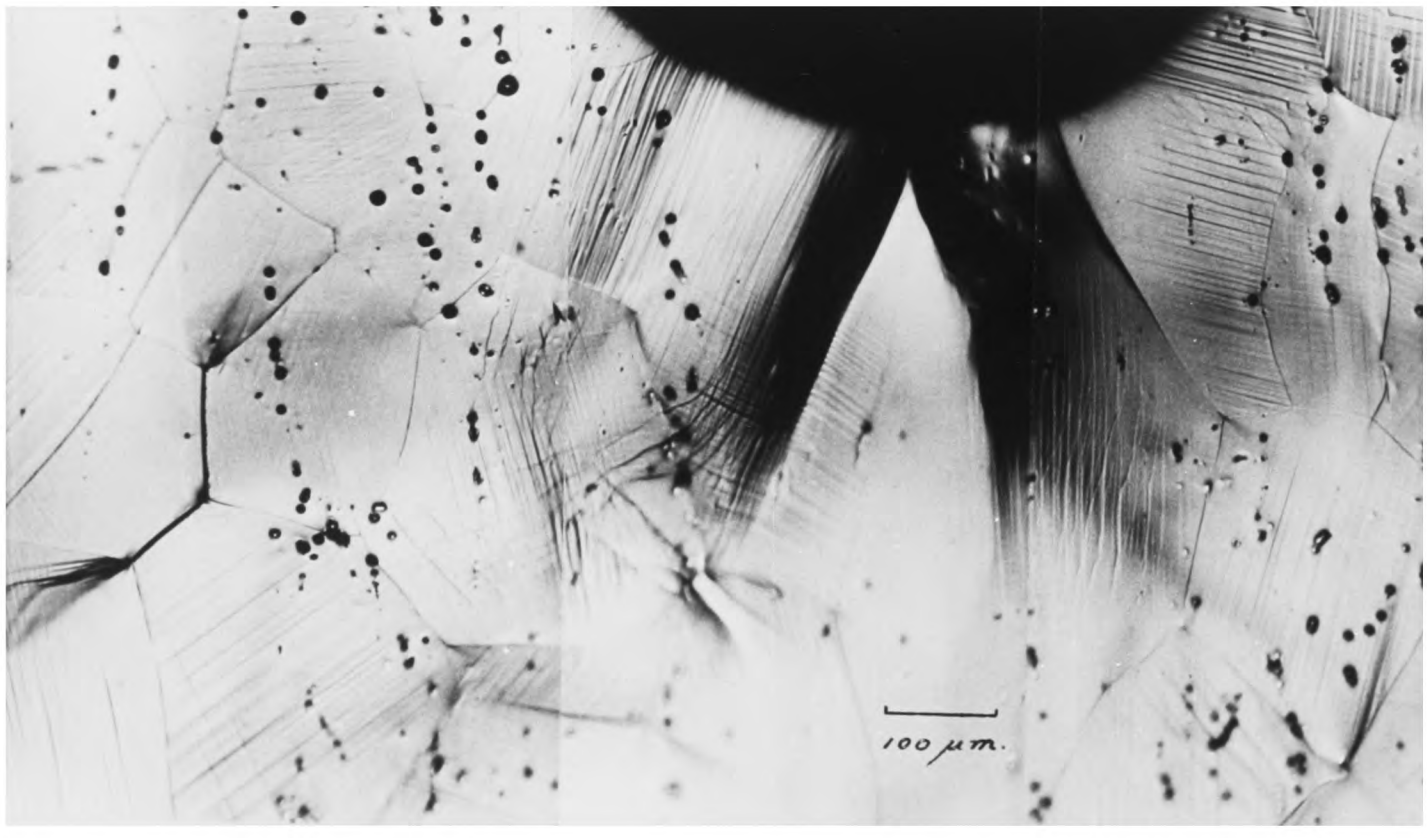
100 μm.

Plate 4.30 (contd.)

(d) Increasing the strain after stage (c), the crack has propagated well into the specimen. Two grain surfaces have started to slide across one another.

(e) After large amounts of strain, the two grain boundaries, which had started to slide across one another in (d), have now completely separated.

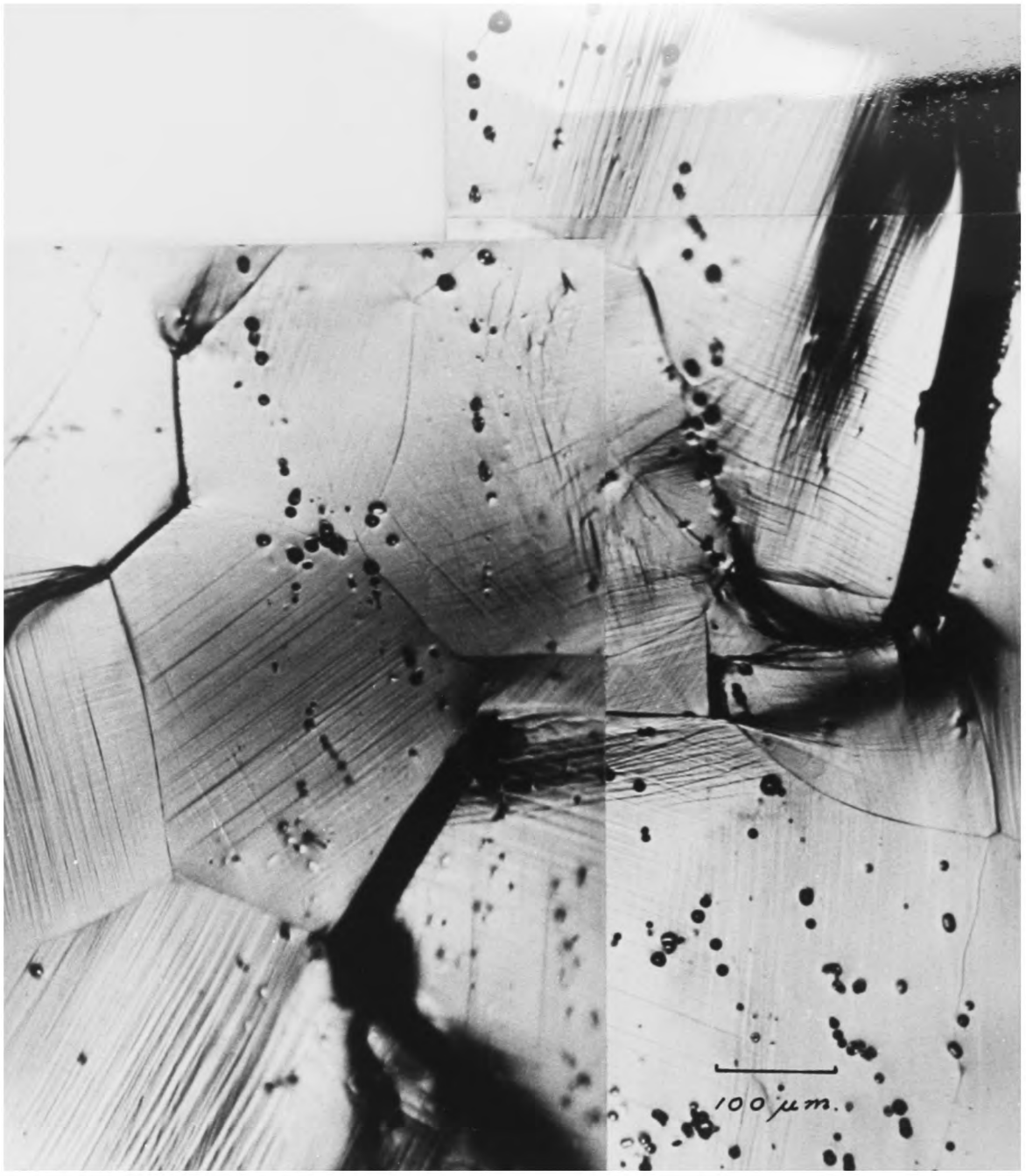
100 µm.


100 µm.

Plate 4.31

The appearance of the crack at the end of the notch bend test of BD3.


500 μm.

Plate 4.32 (a, b, c and d)

Crack propagation in BD6
(Notch bend test)

(a) Before straining

(b) After a small strain

(c) and (d) overleaf

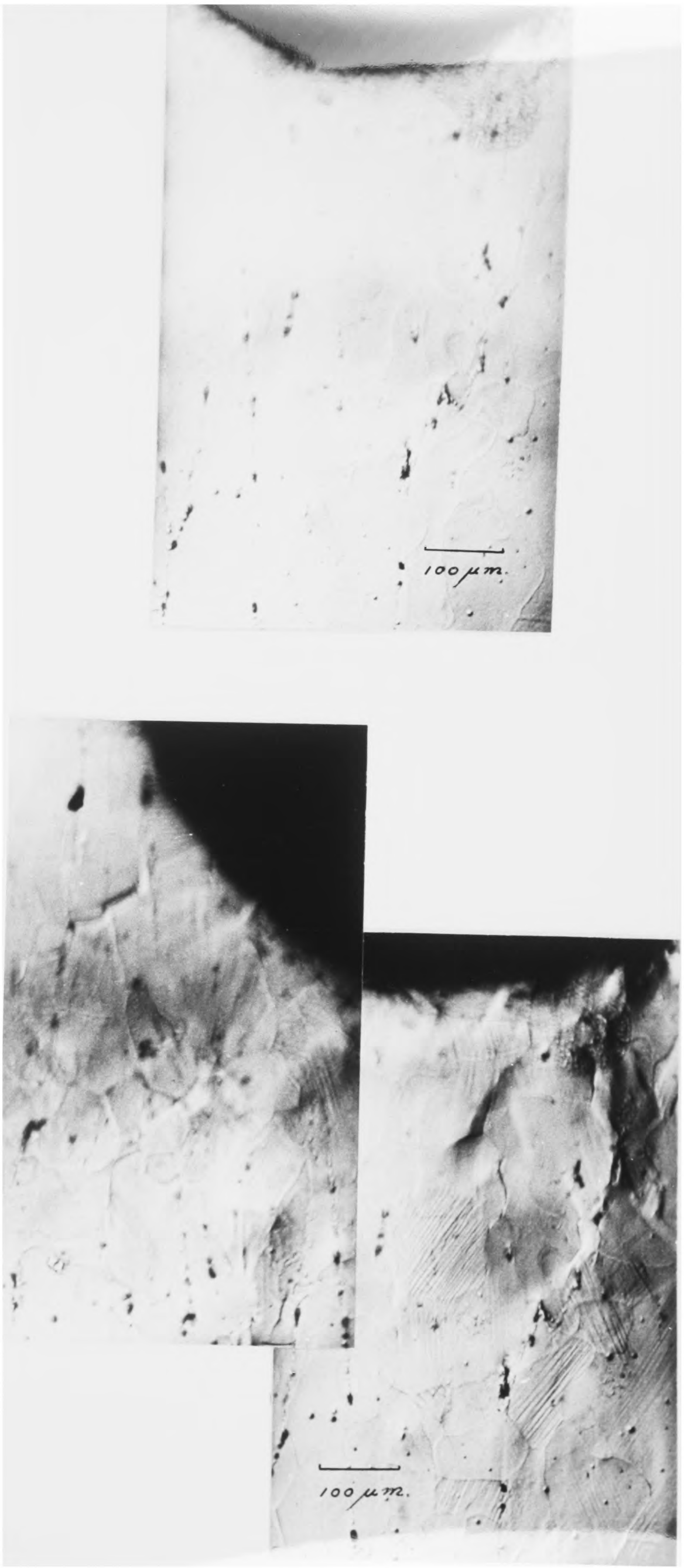
100 μm.
100 μm.

Plate 4.32 (contd.)

(c) After further straining, several cracks form at the notch

(d) After large strains, one crack (X) is successfully propagated across the specimen

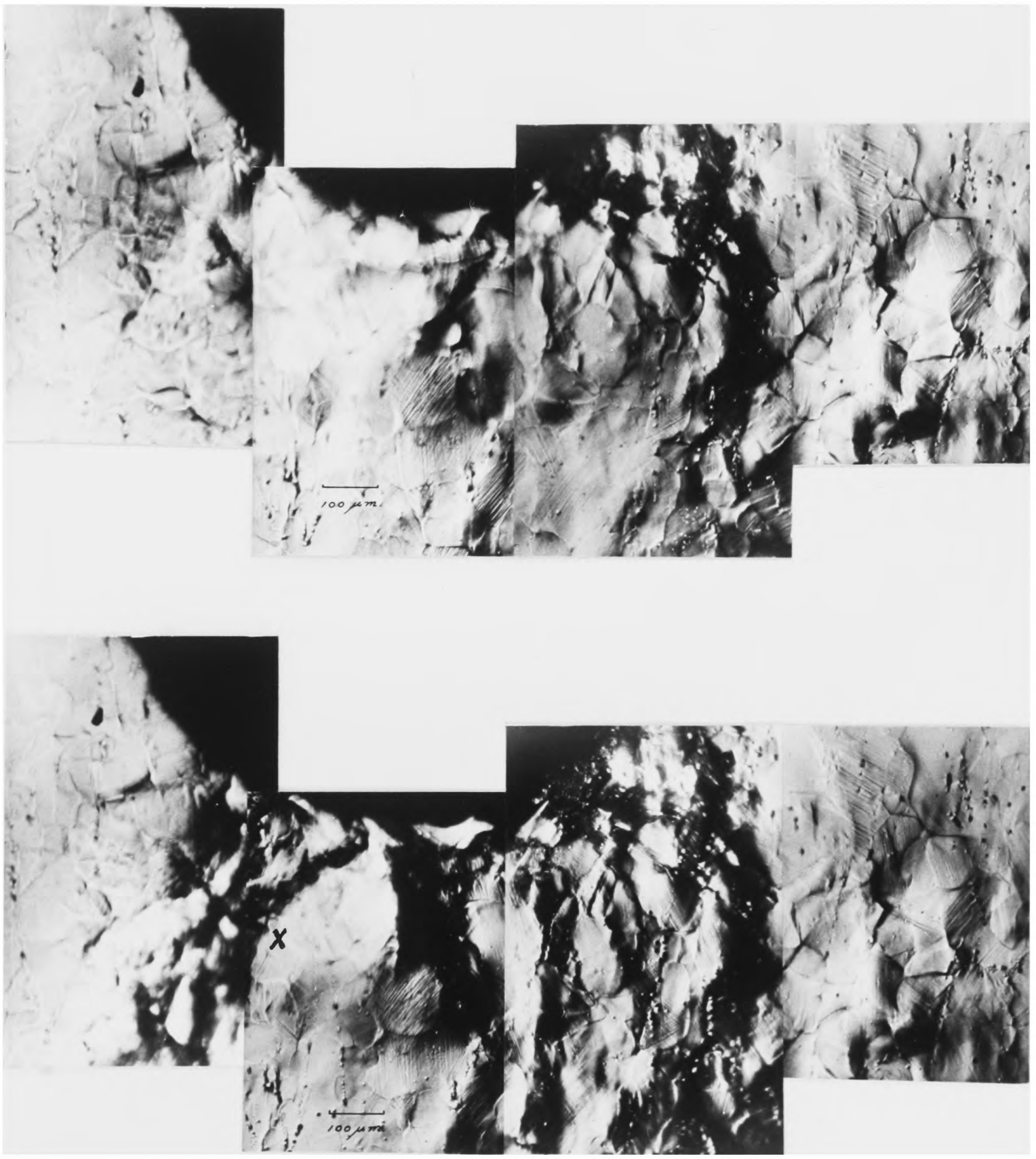
100 μm
X
100 μm

Plate 4.33

The appearance of the crack in BD6 at the end of the notch-bend test

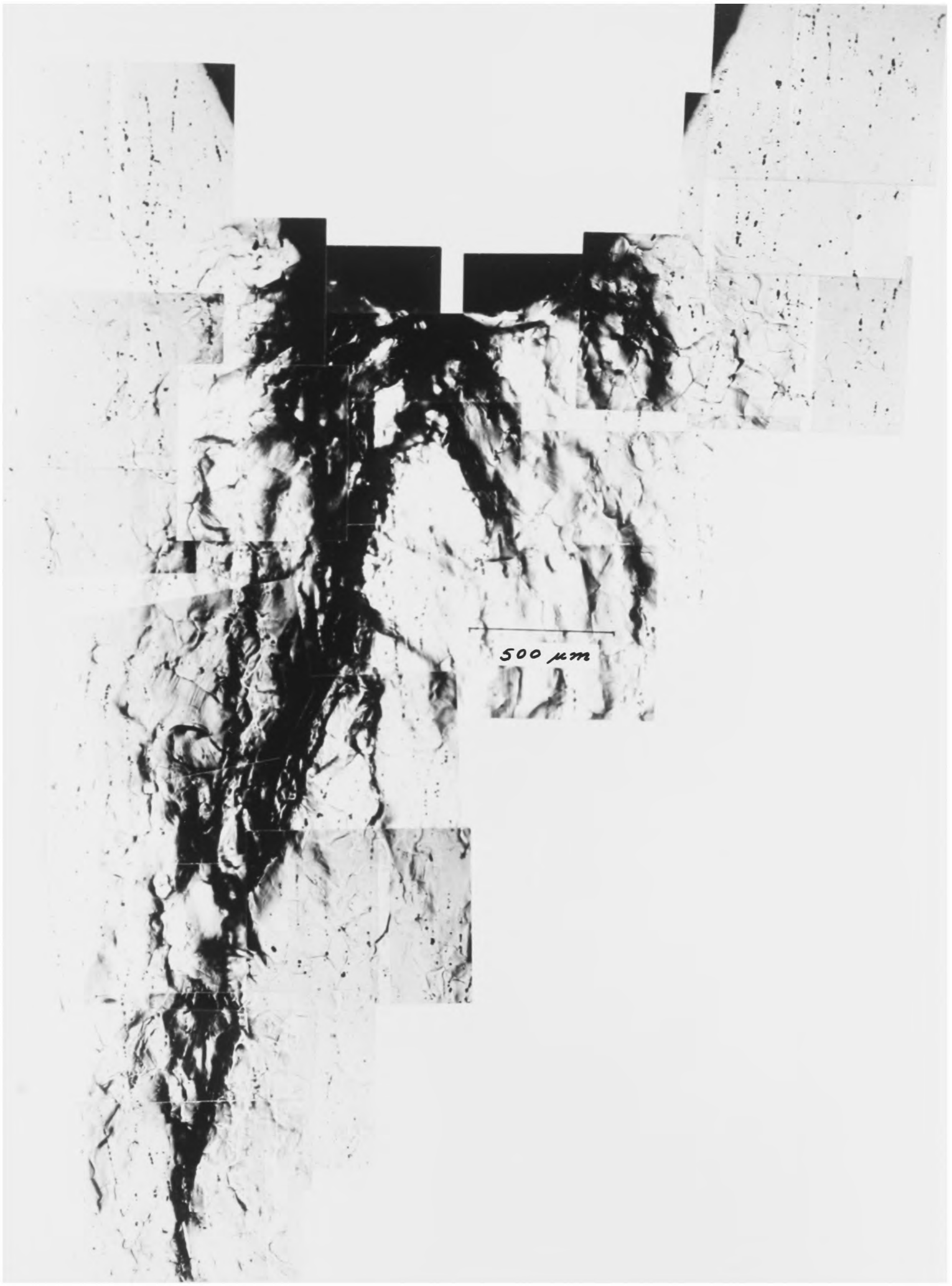
500 μm

Plate 4.34

Crack propagation in BD8
(Notch-bend test)

(a) Before straining

(b) After a small strain, a crack forms at the notch

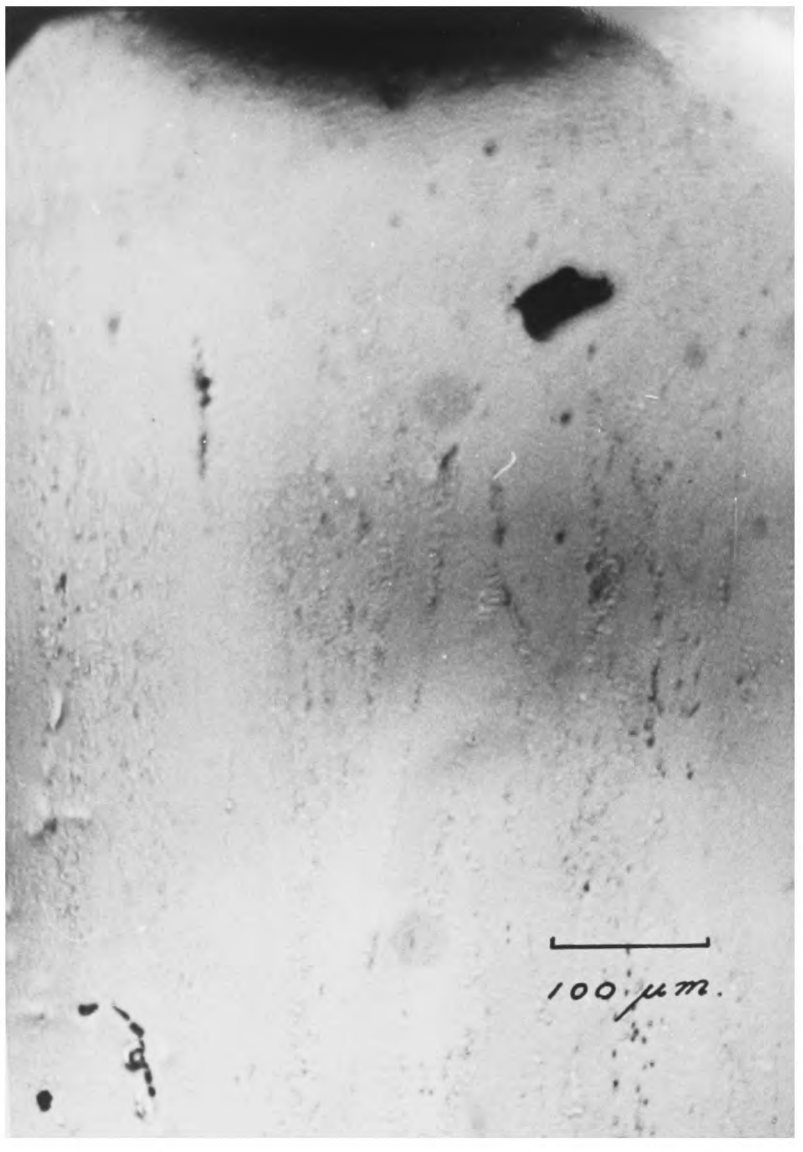
100 μm.

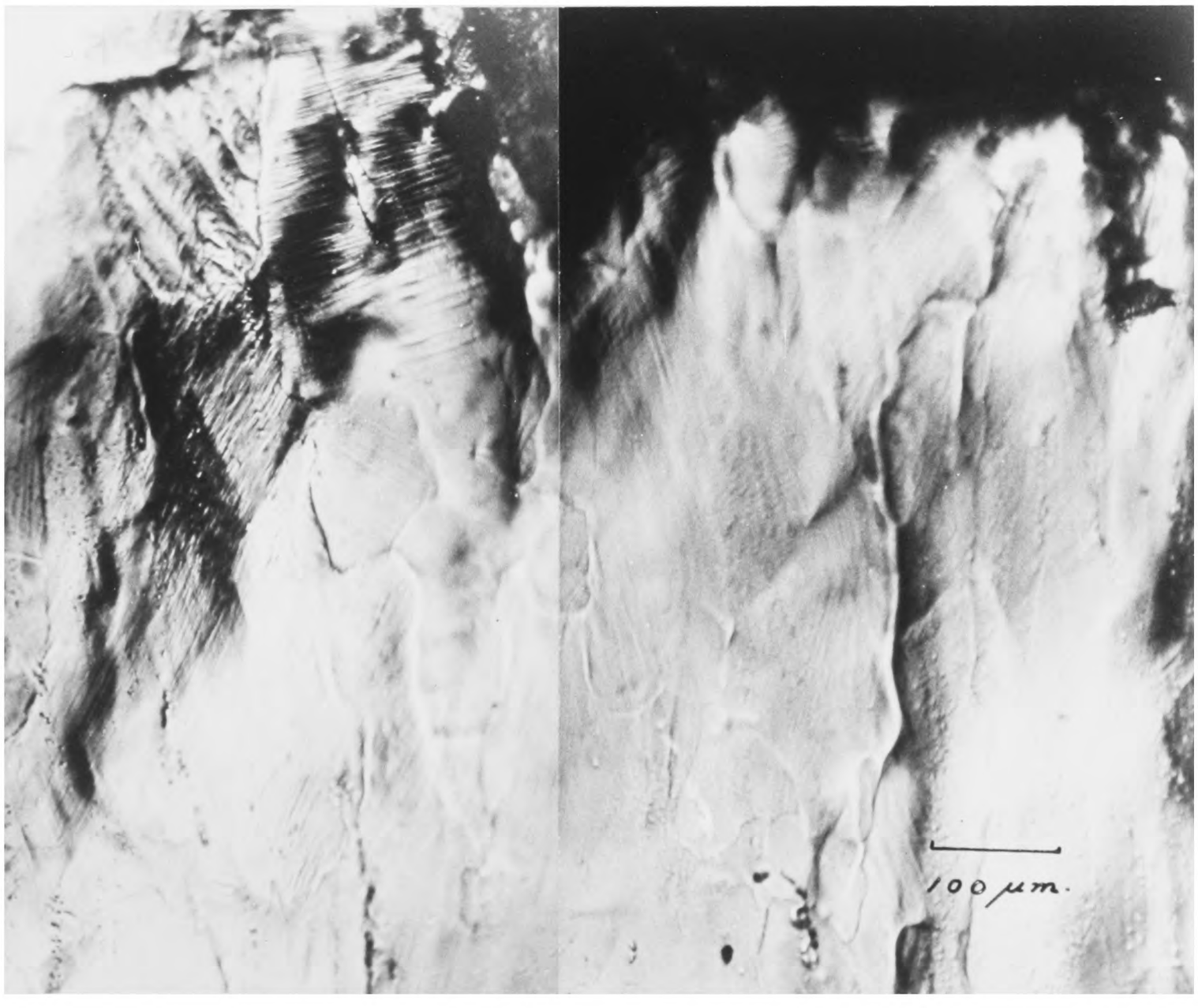
100 μm.

Plate 4.35

The appearance of the crack in BD8 at the end of the notch-bend test.

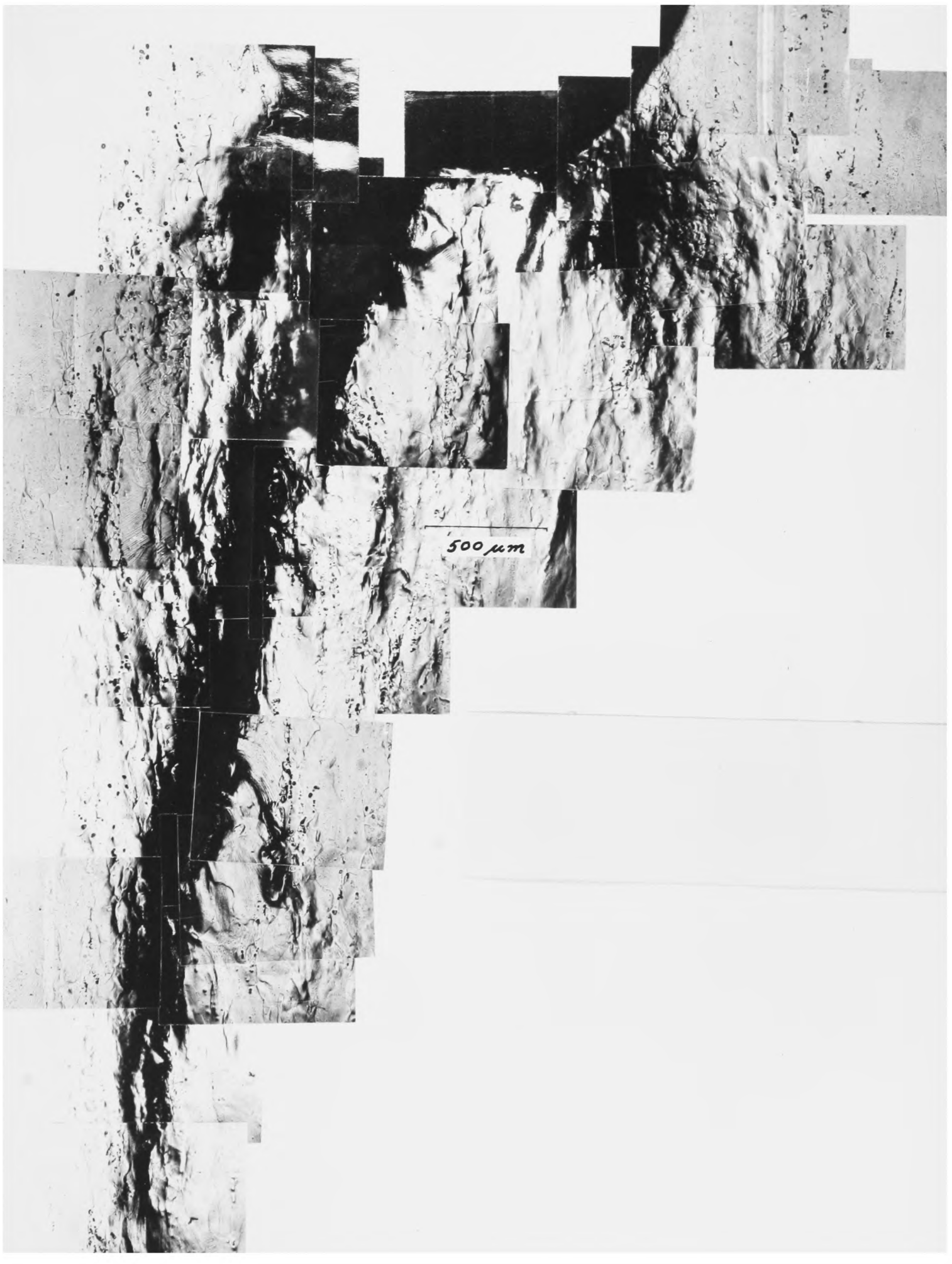
500 μm

CHAPTER 5

SUMMARY, FINAL DISCUSSION AND CONCLUSIONS.

5.1. RELATION OF MICROSTRUCTURES TO THE THERMO-MECHANICAL PROCESSING OF THE ALLOYS

As mentioned in Section 2.2, the aluminium alloys investigated had undergone a sequence of heat treatments and rolling processes to produce sheet of 3mm thick. In light of the precipitation studies of BD8, the microstructural changes which these processes produce are now more easily understood.

i In the as cast state, the alloys all contain residual casting precipitates of Mg_2Si. In addition, the manganese-bearing alloys contain coarse residual particles, ~5μm, of $\alpha(Al_{12}Mn_3Si)$.

ii After homogenization at 530°C, a large proportion of the residual casting precipitates of Mg_2Si go back into solution. In the manganese-bearing alloys, the 0.1μm $\alpha(Al_{12}Mn_3Si)$ particles are produced during this heat treatment.

iii The casting is hot rolled at 530°C followed by cold rolling to produce plate 3mm thick.

iv The sheet is solution treated at 560°C. The cold worked alloys recrystallise and any Mg_2Si precipitates go back into solution.

v The alloys are then aged for 5 minutes at room temperature prior to artificial ageing at 185°C. In all three fully-aged alloys, this sequence produces a fine precipitate structure of β" Mg_2Si needles (~ 100Å long) within the grains, a P.F.Z. ~ 1000Å wide and grain boundary precipitates of Mg_2Si.

5.2. DEFORMATION AND FRACTURE MECHANISMS IN BD3 (Al-0.58wt%Mg-1.02wt%Si)

i In the fully aged condition, the alloy has an equiaxed grain size of ~ 400μm. Apart from the β" Mg_2Si precipitates in the grain interiors and the grain boundary precipitates, there were no other particles present.

ii When the alloy is deformed to fracture in tension at room temperature the material failed intergranularly at low strains of ~ 1%. At 150°C and 185°C, there was little change in ductility and intergranular fracture persists.

iii The metallography of tensile deformation showed that the grains contain well defined slip bands. Optical examination of the longitudinal sections of the fractured test pieces showed that there were several grain boundary cracks close to the fracture surface.

iv In compression, BD3 could withstand strains of at least 9%. T.E.M. of the deformed material after various strains up to 9% revealed that the alloy contained well defined slip bands. The slip band spacing decreases slightly with increasing strain.

v It is concluded that this banded deformation structure is responsible for the observed lower work hardening rate in BD3 (compared with BD6 and BD8). At yield, the dislocations shear through the β" Mg_2Si precipitates and produce local softening of the slip planes. Subsequent dislocations glide preferentially along this path rather than creating new slip planes, thus the work hardening rate is low.

vi The slip bands in BD3 produce high localized stress con-

concentrations at the grain boundaries and these produce grain boundary distortions. The high stress concentrations are due both to the large grain size of BD3 and also to the narrowness of the slip band width.

vii These high stress concentrations are believed to nucleate voids at the grain boundary precipitates by decohesion of the particle - P.F.Z. interface. Because the P.F.Z. is soft relative to the precipitate - hardened matrix, the voids extend in the P.F.Z. and fracture takes place by coalescence of these voids within the P.F.Z. This hypothesis is supported by the appearance of the fracture surface of BD3 in S.E.M. At low magnifications, the surface is typical of intergranular failure; the surface is faceted and the facets correspond to the grain surfaces of the large equiaxed grain structure of BD3. At high magnifications, small dimples are seen on the grain boundary surfaces and their size corresponds to the observed spacing of the grain boundary particles.

viii It is therefore concluded that intergranular failure of BD3 occurs at low strains because slip is concentrated in narrow bands. These result in large localized stress concentrations at the grain boundaries and leads to decohesion at grain boundary precipitates. Fracture takes place by coalescence of these voids within the P.F.Z.

5.3. MICROSTRUCTURES OF BD6 (Al-0.58wt%Mg - 0.99wt%Si - 0.21wt%Mn and BD8 (Al - 0.57wt%Mg - 0.95wt%Si - 0.50wt%Mn)

i The manganese bearing alloys have a smaller grain size than BD3, ~ 100μm in BD6 and ~ 70μm in BD8. The grain structure tends to be elongated in the rolling direction.

ii There are coarse, ~ 5μm, particles of $\alpha(Al_{12}Mn_3Si)$ which are formed during casting and are visible in the optical microscope.

These are arranged in strings parallel to the rolling direction. These coarse particles are smaller and fewer in BD6.

iii The age hardened microstructures of these alloys are similar to that in BD3, except that the alloys contain the 0.1μm rod-shaped $\alpha(Al_{12}Mn_3Si)$ precipitates which are formed during homogenization at 530^oC. The volume fraction, F_V, of these particles is 0.4×10^{-2} in BD6 and 1.1×10^{-2} in BD8.

iv The 0.1μm intermetallic particles impede recrystallisation at 560^oC. As predicted by Zener's equation for the retarding force, Pr, exerted on a grain boundary of energy σ_b, by spheres of radius r and volume fraction F_V

$$P_r = \frac{3F_V \sigma_b}{2r}$$

the grain size of BD8 is smaller than BD6 because BD8 has a higher volume fraction of the 0.1μm particles.

5.4. DEFORMATION STRUCTURES OF BD6 and BD8 AT LOW STRAINS

i The compression tests showed that BD6 and BD8 have a slightly higher work hardening rate than in BD3. At small compressive strains, BD6 and BD8 contained slip bands of slightly smaller spacing than those in BD3, but as the strain increased the slip band spacing decreased, so that by 9% strain, slip bands were no longer resolvable in BD8. In BD6, there was still evidence of slip in bands at this strain, but these were not very distinct. These observations, coupled with the measured increase in work hardening rate, suggest that the interaction between the dislocations and the 0.1μm manganese intermetallic particles in the slip plane is producing dislocation debris at the particles. The slip bands then work harden and thus cause slip bands to form elsewhere.

This increase in work hardening rate above that in BD3 must be a subtle effect, because if there is a large increase in work-hardening in BD8 or BD6, the grain boundaries will become weaker relative to the matrix and intergranular failure would occur.

ii The presence of the 0.1μm manganese particles therefore causes lateral spreading of the slip bands and this is an important effect when considering the stress concentrations in BD6 and BD8. Since the stress concentration, ϕ, at the head of a slip band is given by

$$\phi = \left(\frac{d}{W}\right)^{\frac{1}{2}}$$

where W is the slip band width and d is the grain diameter, the stress concentrations at the head of a slip band in BD6 and BD8 are much smaller than in BD3. Experimentally, this is supported by the lack of grain boundary distortion in BD6 and BD8. Therefore, even though slip bands are formed in the early stages of deformation, the associated stress concentrations are not sufficient to produce grain boundary distortion or decohesion. This is because both the small grain size of BD6 and BD8 and the broad slip band width reduce the stress concentration factor, ϕ. Thus intergranular failure at low strains is suppressed in the manganese-bearing alloys.

5.5. VOID NUCLEATION IN BD6 AND BD8

i When the alloys are deformed to fracture in tension, their nominal stress-strain curves show certain differences. The onset of localized deformation occurs earlier in BD8 than in BD6. After this point the nominal stress-strain curve drops more steeply in BD8 than in BD6, except just before fracture where the stress-strain curve of BD6 drops sharply. Comparable values of total elongation to fracture were obtained in both alloys.

ii Between yield and the point of plastic instability, small voids are formed at the coarse particles. The ease of this void formation is proportional to the size of the coarse particles and their density. Therefore in BD8, voids form at the coarse particles earlier than in BD6, because BD8 contains more of the coarse particles and these are larger than in BD6. The effect of the voids on the flow stress when there are large numbers of them, out-weighs the work hardening effects and localised deformation eventually sets in. Because the coarse particles are smaller and fewer in BD6, a higher strain is required to nucleate voids and their population is lower so that the U.T.S. occurs later in BD6.

5.6. FRACTURE PROCESSES IN BD6 AND BD8

i After the onset of plastic instability, the voids in the region of localised deformation continue to grow. Further voids will form at the smaller of the coarse particles as well. In BD8, the voids do not extend laterally by means of 45° cracks or void sheets because the high density of 0.1μm manganese particles impedes void extension. In BD6, where the volume fraction of the 0.1μm particles is lower, the voids at the large particles can extend into 45° cracks because there are insufficient 0.1μm particles to hinder void growth. This difficulty of crack propagation is related to the high stress σ_{void} needed to extend a crack by cavitation at the 0.1μm particles, i.e.

$$\sigma_{void} \propto \lambda^{-\frac{1}{2}} F_V^{-1/6}$$

where λ is the particle spacing and F_V is the volume fraction of the small particles. The absolute magnitude of the stress is dependent upon factors including the particle-matrix binding energy.

ii As the test proceeds, the increasing local stress enables voids to be opened up at progressively smaller particles. Eventually, a few voids start to form at the 0.1μm particles.

iii Once the voids start to form at the 0.1μm particles, the 45° cracks in BD6 extend rapidly across the specimen as there are fewer 0.1μm particles and it fails catastrophically.

iv In BD8, where there are many more 0.1μm particles, straining continues until voids have formed at nearly all the particles and the alloy then fails by breaking of the ligaments between the voids.

v This voiding process at the 0.1μm particles takes place very close to fracture, because voids are not seen at the 0.1μm particles even in highly strained materials. Some cracked particles have been seen, but these are usually excessively elongated particles. Thus it is concluded that the binding energy between the matrix and particle is very high. The particle shape is important too in respect of particle cracking. If the particles are excessively elongated they can be easily broken due to stress concentration, but equiaxed sub-micron particles will be more resistant to cracking. Therefore the equiaxed sub-micron particles are more efficient crack stoppers, providing their binding energy with the matrix is high.

vi S.E.M. of the room temperature fracture surfaces supports the proposed model of fracture of BD6 and BD8. The fracture surface of BD8 contains both large dimples corresponding to the voids nucleated at the coarse particles and small equiaxed dimples with a size similar to the spacing of the 0.1μm particles. BD6 also contains the large dimples, and these are connected by planar areas covered with very shallow dimples, which reflect the ease of propagation of the 45° cracks across

the alloy.

vii The mechanical behaviour of BD6 and BD8 at 150°C and 185°C supports the suggested fracture processes as does the metallography of crack propagation in the notch bend tests.

5.7. FINAL DISCUSSION AND CONCLUSIONS

From the summary and discussion of the deformation and fracture processes of the three alloys, BD3, BD6 and BD8, it can be concluded that the presence of the 0.1μm manganese intermetallic particles are very important in controlling the deformation mechanisms in BD6 and BD8. Not only do the 0.1μm particles disperse slip, thus preventing intergranular failure at low strains, but they also appear to be effective in impeding crack propagation.

Their efficacy in both these processes depends on their volume fraction, their size and their spacing. Thus qualitatively, it is possible to identify the microstructural conditions which will produce an alloy with good mechanical properties.

i Volume Fraction

The volume fraction of the sub-micron particles must be sufficient to produce slip homogenization so that stress concentrations at the grain boundaries are reduced and intergranular failure is suppressed at low strains. Too high a volume fraction of sub-micron particles should be avoided, because this would lead to a very high initial work hardening rate and the grain boundaries then become weak relative to the matrix leading to intergranular failure.

To impede crack growth, a fairly high volume fraction of sub-

micron particles is required. If the volume fraction is too low, cracks can extend easily. Therefore there is a minimum volume fraction, below which crack extension takes place very easily and this will lead to fracture at low stresses and strains.

ii Particle Size and Shape

Small particles, being more perfect, tend to be more resistant to cracking than large ones, so the volume fraction of coarse particles should be kept as low as possible. If the volume fraction of the coarse particles (~ 5μm) dominates the microstructure, the alloy will fracture at low strains corresponding to the ease of cracking the large particles.

The shape of the small particles should be approximately equiaxed. Excessively elongated sub-micron particles have a low resistance to cracking. Thus in an alloy with elongated particles, void nucleation at these sub-micron particles will take place at relatively low applied stresses and strains. The alloy is then expected to fail at a lower level of applied stress than an alloy containing equiaxed particles.

iii Particle Spacing

This parameter is linked via the volume fraction to the particle size, but for a given size of sub-micron particles, widely spaced particles are less effective at stopping cracks than particles which are close together.

iv Particle-Matrix Binding Energy

A high particle-matrix binding energy reduces the ease of decohesion of the particle from the matrix. Not only does this increase the stress

required to nucleate voids at the particles but it also makes propagation of a crack past the particle more difficult.

v Inhibition of Grain Growth

Second phase particles can retard extensive grain growth. If the 0.1μm particles can be precipitated before recrystallisation of the cold worked alloy, the final grain size of the material will be small. A small grain size will reduce the stress concentration at the head of a slip band in comparison with a large grained material. Therefore the 0.1μm particles also contribute to increased ductility indirectly by reducing the grain size and thus local grain boundary stress concentrations. In large grained alloys such concentrations can initiate intergranular fracture at low strains.

Although the contribution of these parameters can be stated qualitatively, it is probable that the optimum structures have not yet been obtained in practice. Further research is clearly needed to provide a more quantitative basis for alloy design in this context.

REFERENCES

Armstrong, R. W., Codd, I., Douthwaite, R. M., Petch, N. J.,
1962, Phil.Mag., 7, 45.

Ashby, M. F.,
1966, Acta.Met., 14, 679.

Ashby, M. F.,
1970, Phil.Mag., 21, 399.

Ashby, M. F., Ebeling, R. E.,
1966, Irans.AIME, 236, 1396.

ASTM,
E112-60T 'Tentative Methods for Estimating the Grain Size of Metals'.

Beevers, C. J., Honeycombe, R. W. K.,
1959, 'Fracture', editors Averbach, B. L. et al, (M.I.T. Press, Wiley and Sons, New York), 474.

Brichet, C., Wyon, G., Lacombe, P.,
1970, Mem.Sci.Rev.Metal., 67, 691.

Broek, D.,
1972, 'Some Contributions of Electron Fractography to the Theory of Fracture', N.L.R. Report No. TR72029U, National Aerospace Laboratory (N.L.R.), The Netherlands.

Brown, L. M., Ham, R. K.,
1971, 'Strengthening Methods in Crystals', editors Kelly, A. and Nicholson, R. B., (Applied Science Publishers Ltd., England), 12.

Byrne, J. G., Fine, M. E., Kelly, A.,

1961, Phil.Mag., 6, 1119.

Ceresara, S., Di Russo, C., Fiorni, P., Giarda, A.,

1969/70, Mat.Sci.and Eng., 5, 220.

Chadwick, R., Muir, N. B., Grainger, H. B.,

1953/54, J.I.M., 82, 75.

Chatterjee, D. K., Entwhistle, K. M.,

1973, J.I.M., 101, 53.

Corti, C. W., Cotterill, P., Fitzpatrick, G. A.,

1972, 'The Evaluation of Interparticle Spacing in Dispersion Alloys', Review article from Department of Metallurgy and Materials Technology, University of Surrey. (Now printed in Int.Met.Rev., 1974, 19, 77).

Cox, T. B., Low, J. R.,

1974, Met.Trans., 5, 1457.

Dehoff, R. T., Rhines, N. R. (editors),

1968, 'Quantitative Microscopy' (McGraw-Hill, New York, 239 and 243).

Dew-Hughes, D., Robertson, W. D.,

1960, Acta.Met., 8, 147.

Dowling, J. M.,

1972, Thesis submitted for the Honour School of Metallurgy and Science of Materials, Part II.

Dunwoody, B. J., Moore, D. M., Thomas, A. T.,

1973, J.I.M., 101, 172.

Embury, J. D.,

1971, 'Strengthening Methods in Crystals', editors Kelly, A. and Nicholson, R. B., (Applied Science Publ. Ltd., London), 331.

Embury, J. D., Nicholson, R. B.,

1965, Acta.Met., 13, 403.

Evenson, J. D., Ryum, N., Embury, J. D.,

1975, Mat.Sci.and Eng., 18, 221.

Federighi, T., Thomas, G.,

1962, Phil.Mag., 7, 127.

Foreman, A. J. E., Makin, M. J.,

1966, Phil.Mag., 14, 911.

Fullman, R. L.,

1953, Trans.AIMME, 197, 447.

Geisler, A. H.,

1951, 'Phase Transformations in Solids', Wiley and Son, 387.

Glieter, H., Chalmers, B.,

1972, 'High Angle Grain Boundaries', Progress in Materials Sci., Vol.16, (Pergamon Press, Oxford).

Greetham, G., Honeycombe, R. W. K.,

1959/60, J.I.M., 89, 13.

Guinier, A.,

1952, Acta Cryst., 5, 121.

Guinier, A.,

1956, Trans.AIMME, 206, 673.

Guinier, A., Lambot, H.,

1948, Comptes Rendus, 227, 74.

Gurland, J.,

1968, 'Quantitative Microscopy', editors Dehoff, R. T. and Rhines, N. R., (McGraw-Hill, New York), 278.

Hahn, G. T., Rosenfield, A. R.,

1973, 5th Annual Spring Meeting of the Metallurgical Society of AIME', 'Metallurgical Factors Affecting Fracture Toughness of Al-Alloys'.

Hardy, H. K.,

1948/49, J.I.M., 75, 707.

Harris, I. R., Varley, P. C.,

1953/54, J.I.M., 82, 379.

Hart, E. W.,

1953, 'Relation of Properties to Microstructure', (A.S.M.), 95.

Higgins, G. T.,

1974, Metal Science, 8, 143.

Hirsch, P. B., et al, (editors),

1965, 'Electron Microscopy of Thin Crystals', (Butterworths, England).

Hirsch, P. B., Humphreys, F. J.,

1969, 'Physics of Strength and Plasticity', editors Argon, A. S., (M.I.T. Press, Cambridge, Mass.), 189.

Humphreys, F. J., Martin, J. W.,

1967, Phil.Mag., 16, 927.

Jacobs, M. H.,

1972, Phil.Mag., 26, 1.

Jacobs, M. H., Pashley, D. W.,

1968, Symposium on 'The Mechanism of Phase Transformations in Crystalline Solids', (I. of M. Monograph, Published 1969), 43.

Jeffries, Z., Kline, A. H., Zimmer, E. B.,

1916, Trans.AIME, 57, 594.

Kelly, A., Fine, M. E.,

1957, Acta.Met., 5, 365.

Kelly, P. M.,

1973, Int.Met.Rev., 18, 31.

Kocks, S.,

1966, Phil.Mag., 13, 541.

Köster, U.,

1974, Metal Science, 8, 151.

Lorimer, G. W., Nicholson, R. B.,

1966, Acta.Met., 14, 1009.

Lutjering, G., Weissman, S.,

1970, Acta.Met., 18, 785.

Lutts, A.,

1961, Acta.Met., 9, 577.

Mondolfo, L. F.,

1943, 'Metallography of Al-Alloys', (Wiley and Sons, New York).

McLean, D.,

1975, Conference on 'The Mechanics and Physics of Fracture', Cambridge, England, (I.P. and Metal Soc.), 'Effective Intergranular Cohesion'.

Nicholson, R. B., Thomas, G., Nutting, J.,
1960, Acta.Met., 8, 172.

Pashley, D. W., Jacobs, M. H., Vietz, J. T.,
1967, Phil.Mag., 16, 51.

Pashley, D. W., Rhodes, J. W., Sendorek, A.,
1966, J.I.M., 94, 41.

Phillips, H. W. L. (editor),
1961, 'Equilibrium Diagrams of Al-Alloy Systems',
(Aluminium Development Association).

Price, R. J., Kelly, A.,
1964, Acta.Met., 12, 159.

Scharf, G., Gruhl, W.,
1969, Z.Metallkde, 60, 413.

Smithells, C. J. (editor),
1967, 'Metals Reference Book', (Butterworths, London).

Stewart, A. T., Martin, J. W.,
1975, Acta.Met., 23, 1.

Stroh, A. N.,
1954, Proc.Roy.Soc., A223, 404.

Thomas, G.,
1959, Phil.Mag., 4, 1213.

Thomas, G.,
1961, J.I.M., 90, 57.

Thomas, G.,

1966, 6th International Conference on Electron Microscopy, Volume I, (Maruzen Co. Ltd., Tokyo), 389.

Thomas, G., Nutting, J.,

1959/60, J.I.M., 88, 81.

Underwood, E. E. (editor),

1970, 'Quantitative Stereology', (Addison-Wesley, Reading, Mass.), 82.

Unwin, P. N. T., Lorimer, G. W., Nicholson, R. B.,

1969, Acta.Met., 17, 1363.

Van Horn, K. R. (editor),

1967, 'Aluminium - Vol.I, Properties, Physical Metallurgy, Phase Diagrams', (A.S.M.), 359 and 365.

Van Stone, R. H., Psioda, J. A.,

1975, Met.Trans., 6A, 669.

Wahi, R. P., Von Heimendahl, M.,

1974, Phys.Stat.Sol.(a), 24, 607.